Residual stress and fatigue crack growth life prediction in fastener holes cold-worked by uniform indentation in 2024-T351 aluminium alloy

Thesis

Faculty of Technology

Department of Materials Engineering

Residual Stress and Fatigue Crack Growth Life Prediction in Fastener Holes Cold-Worked by Uniform Indentation in 2024–T351 Aluminium Alloy

by

Jeffrey Meng–Lee Tan

April 2006

A THESIS SUBMITTED TO THE DEPARTMENT OF MATERIALS ENGINEERING OF THE OPEN UNIVERSITY FOR THE DEGREE OF DOCTOR OF PHILOSOPHY

DATE OF SUBMISSION : 7 JULY 2006
DATE OF AWARD : 31 JANUARY 2007


RUAG
IABG

Frontispiece: A Swiss Armed Forces F/A-18 Hornet at the structural testing facility of RUAG Aerospace. The full scale fatigue test programme is part of stringent structural integrity assessment of the duration of its service life according to the highest standards of flight safety. The Swiss configuration has a unique reinforced structure of titanium bulkheads with additional cold-worked holes.

Interference fitting and cold-working of fastener holes have been cautiously implemented to increase the fatigue durability of mechanical joints under severe operating conditions. Interference fitting with very tight tolerance is capable of inducing a greater amount residual stress, and has been widely applied to the structural joints at the lower sections of the aircraft. It was found that 12 to 16 times life improvement factor can be gained in close tolerance fitting of holes alone.

Preliminary fatigue coupon results indicates that incorporating the cold-working and interference fit in metallic joints together may even increase the fatigue life enhancement factor dramatically.

Jeffrey Meng–Lee Tan
The Open University

Ph.D. Thesis
April 2006

Residual Stress and Fatigue Crack Growth Life Prediction in Fastener Holes Cold-Worked by Uniform Indentation in 2024–T351 Aluminium Alloy

ABSTRACT

This thesis concerns primarily the residual stress characterisation in fastener holes cold-worked by a novel StressWave process, and the prediction of the fatigue crack growth under the influence of such residual stress. Aerospace 2024–T351 aluminium alloy plate of 6.35 mm thickness containing a nominal Ø6.35 mm hole was used.

Using neutron and laboratory X-ray diffraction measurements, a large compressive residual stress was found in StressWave and split-sleeve cold-worked holes. Detailed stress mapping indicates that a StressWave hole contains a highly symmetric residual stress field with a wider compressive region. Conversely, the split-sleeve technique generates a complex asymmetric stress variation through the specimen thickness and around the hole. Independently, a comprehensive finite element study was conducted to reveal the residual stress development associated with the two distinct cold-working techniques at various stages. Favourable agreement was achieved between the experiment and simulations. The deformation mechanism associated with the cold-working process is decisive to the behaviour of the residual stress field created.

The symmetric crack growth behaviour observed in StressWave specimens permits a through-thickness crack geometry to be considered. Accordingly, Green's functions for a single crack and two symmetric cracks originating from the edge of a circular hole were developed. These solutions were verified using weight function and finite element analysis and are therefore appropriate for subsequent study of fatigue crack growth.

A theoretical framework was proposed to explicate the interaction of residual stress with the superimposed loading at the crack tip, which was mathematically expounded as a function of stress intensity factor and stress ratio. This analytical framework provides a reasonable correlation between the mean stress and crack closure criteria. As a demonstration, a finite-width plate containing a centre hole with a single crack, with surface residual stress measured by X-Ray diffraction was analysed. It was revealed that for a predictive task, both the mean stress and crack closure definitions necessitate different requirements of material database and parametric definitions.

Next, the fatigue testing suggested that the fatigue durability of fastener holes treated by the StressWave method generally outperformed those observed for split-sleeve samples. Prediction according to the unified theory produced encouraging results matching the experimental fatigue crack growth measurement. Detailed analysis showed that suitable parametric calibration and the appropriate use of crack models were imperative to achieve reliable prediction. Future efforts necessary for accuracy of prediction work for StressWave cold-worked holes are discussed.

ACKNOWLEDGEMENT

Without the immeasurable help of so many generous people, it is difficult to imagine how this piece of work could have ever been completed. A few words of appreciation from the bottom of my heart are now offered.

My co-supervisors, Professor Lyndon Edwards and Dr. Michael E. Fitzpatrick, assisted me greatly from the time I arrived at OU. Both are unique individuals anyone could have the pleasure of knowing. The excellent guidance and benevolence that they offered has encouraged and inspired me to explore further. I am truly grateful to them leaving me to adventure my own leeway in uncharted horizons.

The inspiring technical discussion and cold-working of specimens using the patented StressWave process played a crucial role to the success of this endeavour. My warmest acknowledgement and appreciation to the Eric Easterbook, Dr. Taeksun Nam and Michael Landy from the StressWave, Inc, Seattle, USA, in every possible aspects to help my understanding of the novel cold-working technique. I could still remember vividly how my first e-mail enquiry four and half-years back had been replied favourably by Eric. Surprisingly, our regular discussion for several months eventually opened a door of opportunity of my PhD research later in OU.

No man is an island; no man stands alone. My personal perspective on life has been much enriched by the constant interaction and friendship with many individuals at OU. My grateful thanks are due to Olivier Zanellato, Dr. Sumit Pratihar, Dr. Jon James, Dr. Mark Turski, Dr. David Bacon, Dr. Supriyo Ganguly, Dr. Nadri Brahim, Dr. Ying Zhang, Dr. Salih Gungor, Colin Gagg, Dr. Mark Endean, Iestyn Jowers, Mehmet Kartal, Joao Gomes, Monshiur Rahman, David Sefton, Mulyadi and Dr. David Liljedahl. My special thanks also to Professor Mark Daymond, Dr. Javier Santisteban and Dr. Ed C. Oliver for providing instrument and data analysis support regarding my experiment at ISIS, Oxford.

I am deeply grateful for the technical assistance provided by the members of research laboratory and workshop in the this department, particularly to Stan Hiller, Pete A. Ledgard, Tim Gough, Ian Norman, Gordon Imlach and Dr. Jim Moffatt. Not least to mention the helping hands from Rehana Malik and Debbie Derbyshire in my official

engagements with the university. I will also always remember the numerous timely assistances from Sonja Odell and Carol Vallis to fix up my PC for various reasons.

Elsewhere, many friendships have also blossomed and endure during my life in this city. Jessica and I enjoy immensely meeting people from The Church of Christ The King at Kents Hill, Milton Keynes Malaysian Club, our house group and Young Adult Fellowship. I would like to extend my thanks to each of them in providing every advice, love and prayer we needed to become better persons.

The entire work is devoted to my family and God. Firstly, I dedicate this to my loving wife and steadfast companion, Jessica. Her unfailing care and encouragement gave me strength to achieve my best in life, even under difficult circumstances. Likewise, she was always happy to share the joy of little celebrations along the way. Secondly, I offer this to my grandparents, parents, sister and brothers in Malaysia. They reminded me the sincere struggle and determination to hope for better life. I cast my final words of thanks and praises to Jesus Christ. Without his blessings and love, my achievement would not have gone this far.

陈明旅

Jeffrey M.–L. TAN
April 2006

AUTHOR'S DECLARATION

This thesis is submitted for the degree of Doctor of Philosophy of The Open University, United Kingdom. The work described in this thesis was performed in the Department of Materials Engineering, Faculty of Technology, between October 2002 and April 2006, under the supervision of Professor Lyndon Edwards and Dr. Michael Edward Fitzpatrick.

It is entirely the work of the author except where clearly referenced. None of this work has been submitted for a degree or other qualification at this or any other university.

The views and opinions represented in this thesis are solely those of the author, and not The Open University.

Jeffrey M.–L. TAN
April 2006

TABLE OF CONTENTS

NOMENCLATURE

Symbol	Description
Roman	
2D	Two dimensional
3D	Three dimensional
A	Cross-sectional area
A_k	Fitting parameter in ($K_{critical}$ / K_{IC}) versus thickness relation in NASGRO–3.0 equation
A_0, A_1 , A_2, A_3	Coefficients of Newman crack opening function
a	Crack; lattice parameter for a cubic unit cell
B	Specimen half width; external boundaries that interact with crack geometry
B_k	Fitting parameter in ($K_{critical}$ / K_{IC}) versus thickness equation in NASGRO–3.0 equation
b	Lattice parameter for a cubic unit cell; combined hardening parameter that defined the rate at which the size of the yield surface changes as plastic straining develops
C	Crack growth rate constant in Paris equation; linear kinematic hardening modulus
CC	Crack closure method
CH	Combined hardening
$\underline{\underline{C}}$	Elastic stiffness (or modulus) tensor
CE	Cold expansion of hole
CW	Cold-working
$CTOD$	Crack tip opening displacement
C_{ijkl}	Elastic stiffness relating the stresses in the ij-direction to the strain in the kl-direction in an anisotropic system
c	Crack length; lattice parameter for a cubic unit cell
c_{ij}	Independent component in an elastic compliance (or constant) tensor reduced for isotropic system
C_{th}	Threshold coefficient in NASGRO–3.0 equation
D_{major}	Mandrel major diameter
d	Lattice spacing of a stressed crystalline

da/dN, dc/dN	Fatigue crack growth rate
d_0	Lattice spacing of an stress-free crystalline
e	eccentricity of hole from the edges or centre
E	Energy; Young's or elastic modulus
EDM	Electric discharge machine
EPFM	Elastic-plastic fracture mechanics
FCG	Fatigue crack growth
FE	Finite element
FTI	Fatigue Technology, Inc.
F_B	Compliance function that accounts for the interplay between external boundaries with the internal crack
F_S	Standard reference function of stress intensity factor
F_ϕ	Geometry compliance function in cracked hole specimen
f	Newman crack opening function; frequency
GF	Green's function
H	Specimen half length
h	Planck's constant
{ *hkl* }	Family of crystallographic planes
IH	Isotropic hardening
I_a	Interference ratio or amount of hole expansion in cold-working
J	J-integral
K	Stress intensity factor
KH	Kinematic hardening
KGF	Kernel Green's function
K_I, K_{II}, K_{III}	Stress intensity factor of mode-I, II and III loadings, respectively
K_C	Fracture toughness for mode-I plane stress case; effective fracture toughness for the part-through-the-thickness crack
K_{IC}	Fracture toughness for mode-I plane strain case
k	Boltzmann's constant; dummy suffix summing over all k in generalised Hooke's law
k_i	Vector of incident X-ray
k_f	Vector of diffracted X-ray
L	Total time-of-flight distance; total length of specimen
LEFM	Linear elastic fracture mechanics
LHS	Left hand side

LIF	Life improvement factor
$\underline{L}_i$	Laboratory (X-ray) coordinate system
L_1	Time-of-flight distance from moderator to sample
L_2	Time-of-flight distance from sample to detector
L_{entry}	Length of the entry section of the tapered mandrel
L_{exit}	Length of the exit section of the tapered mandrel
L_{major}	Length of the major section of oversized mandrel
MS	Mean stress method
M_n	Stress intensity magnification factor for n-degree polynomial term
m	Mass of fundamental particle; gradient of $d_{\phi\psi}$ versus $\sin^2\psi$ plot in X-ray diffraction
N	Number of cycles elapsed; number of crack emanating from the hole edge
n	Integer in Bragg's law; degree of polynomial function; Material constant in Paris equation given by the slope of logarithmic plot of da/dN versus ΔK relation
O	Origin of reference axis
P	Point load
PSB	Persistent slip bands
p	Exponent in NASGRO–3.0 equation
Q	Scattering vector corresponds to strain direction
Q_∞	Combined hardening parameter that represents the maximum change in the size of the yield surface
q	Exponent in NASGRO–3.0 equation
R	Stress ratio (= $\sigma_{max}/\ \sigma_{min}$ or $K_{max}\ /\ K_{min}$); hole radius
RP	Reference point of a rigid body in finite element method
RHS	Right hand side
R_{hi}	Upper bound of R-shift in da/dN versus ΔK plot
R_{lo}	Lower bound of R-shift in da/dN versus ΔK plot
RI_1 , R_2I_2, R_4I_4	Exact integral functions in analytical kernel Green's function
r	Radial distance to the crack tip in polar coordinate; radial distance measured from the hole edge
r_c	Cyclic plastic zone at crack tip
r_p	Crack tip plastic zone, i.e. $r_p = 2\ r_y$
r_y	Crack tip plastic radius

S	Fatigue stress in Newman crack opening function; alternating stress
$\underline{\underline{S}}$	Elastic compliance (or constant) tensor
SIF	Stress intensity factor
SSM	Split-sleeve mandrel
SW	StressWave
S_{ijkl}	Compliance relating the strains in the *ij*-direction to the stresses in the *kl*-direction in an anisotropic system
$\underline{S}_i$	Specimen coordinate system
s	Normalised crack size, $(=c/(R+c)=\xi/(1+\xi))$
s_{ij}	Independent component in a elastic stiffness (or modulus) tensor reduced for isotropic system
T	Temperature; specimen thickness
TOF	Time of flight
t	Time of flight of neutron; thickness of split-sleeve; normalised crack size$(=R/(R+c)=1/(1+\xi))$
u_r	Crack opening profile
u_z	Permanent axial deformation
v	Velocity of neutron
W	Specimen width ($W = 2w$)
WF	Weight function
w	Specimen half-width
X, Y, Z	Global Cartesian coordinates
x, y, z	Local Cartesian coordinates; horizontal, vertical and normal axes
Z	Atomic number / number of protons of an atom

Greek

α	Angular aperture of detector banks in ENGIN–X instrument; crack tip constraint in Newman stress opening function
α_T	Linear coefficient of thermal expansion
$\alpha_1, \alpha_2, \alpha_3$	Divergences/ collimation angles in a monochromatic system
β	Compliance function taking account of the geometry effect in relation to the crack size, c
γ	Combined hardening parameter that determines the rate at which the kinematic hardening modulus, C, decreases with increasing plastic

	deformation
ε	Strain; true strain; effective strain
$\underline{\underline{\varepsilon}}$	2nd rank strain tensor
$\varepsilon^{p}_{\text{true}}$	True plastic strain
Δ	Difference; range; applied indentation in StressWave technique
ΔK_0	Threshold stress intensity factor range at stress ratio, $R = 0.0$ in NASGRO–3.0 equation
δ	Kronecker's delta function: $\delta_{ij} = \{1, \text{ for } i = j \ ; \ 0, \text{ for } i \neq j$; residual depth of after StressWave indentation
ζ	Normalized crack length over distance (= x/c)
η	Mosaic spread of crystal monochromator
θ	Angle; angle between the incident beam and diffracting planes; radial angular of polar coordinates in relation to the crack tip
2θ	Angle between incident beam and diffracted beam for a stressed crystal
λ	Wavelength; ratio of in-plane biaxial loading (= σ_x / σ_y)
μ	Coulomb isotropic coefficient of friction
ν	Poisson ratio
ξ	Normalized crack length over hole radius (= c/R)
σ	Stress; true stress; effective stress
$\underline{\underline{\sigma}}$	2nd rank stress tensor
σ_o	Material flow stress, taken to be average of the yield stress and ultimate stress
$\sigma\vert_0$	Combined hardening parameter representing the equivalent stress that defines the size of yield surface at zero plastic strain
σ_{true}	True stress
τ_{xy}	Shear stress componet
$\emptyset$	Hole diameter (= $2R$)
ϕ, ψ	Angles of diffracting lattice plane normal (rotation and tilt) relative to a fixed coordinate system
ω	Rotation; angle of rotation

Superscript

M	Monochromator
p	Plastic component

Subscript

0	Reference state; initial
1, 2, 3	Principal directions
apply	applied by remote action
eff	Effective
f	Final
hkl	Miller indices
i	Initial
i, j	Matrix index; measured components relative to chosen axes in specimen
int	Internal
m	Moderator; number of external boundaries in cracked hole specimen
max	Maximum
min	Minimum
n	Neutron
o	Reference state
op	Crack opening
p	Proton
ref	Reference
res	Residual stress
th	Threshold value
θθ, rr, zz	Hoop, radial and axial direction in polar coordinates
tot	Total
u	Ultimate tensile strength
Y	Yield stress
$\perp$	Perpendicular; normal
∞	Infinite; remote

Dimensions

Å	Angstrom, i.e. 1×10^{-10}

CHAPTER 1: INTRODUCTION

This chapter provides a general overview of the issues of fatigue cracking susceptibility of fastener holes in aircraft structures subjected to fatigue loading, and how the problem can be mitigated by the application of residual stress through cold-working. A comprehensive description of commercial cold-working techniques, i.e. split-sleeve, split-mandrel and StressWave, currently used by the aerospace industry is presented. The damage tolerance guidelines presently adopted by aircraft manufacturers, regarding the application and integration of cold-working effect on fatigue life analysis of aircraft are then discussed. Finally, the research motivation and the outline of the thesis are stated.

1.1 Background

In metallic airframe manufacturing, mechanical joints incorporating fastener holes, such as rivets, bolts, pins and lug attachments, are the dominant means of component assembly and dismantling, as well as transferring or distributing loads across the structure. However, due to their inherent geometry discontinuity that concentrates stress, fastener holes are susceptible to fatigue crack initiation and propagation that often cause premature failures in aero-structures. Typically, for a wide-bodied civil aircraft the average number of fastener holes is about 3 to 4 million, and approximately 10 % of them are situated at critical locations of fatigue cracking [1].

Figure 1.1.1(a) illustrates a test coupon containing numerous fatigue cracks emanating from multiple holes, which classically represents multiple site damage normally encountered in-service for aero-structures. Fatigue loading imposed on the test coupon, such as constant amplitude load normally used in laboratory study (Figure 1.1.1(b)), or

load spectrum experienced actually during the flight (Figure 1.1.1(c)), is equally capable of promoting crack damages around the holes.

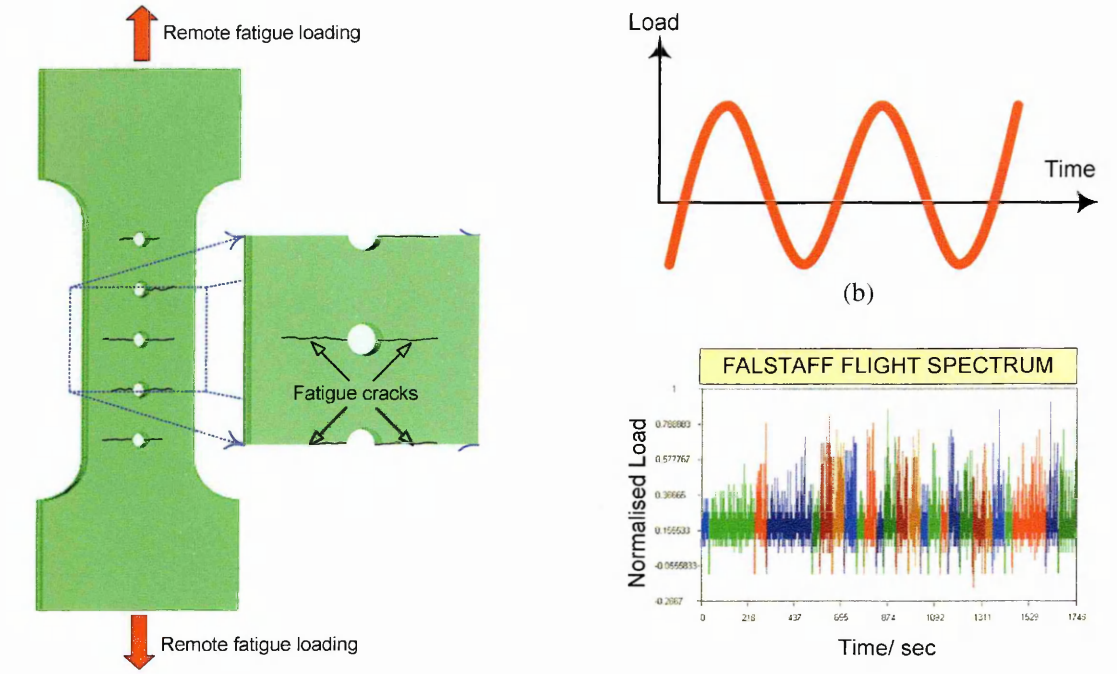

Figure 1.1.1 (a) Multi-site damage in fatigue coupon (b) Constant amplitude loading (c) Aircraft service loading.

In response to the fatigue issues related to fastener holes, various fatigue life enhancing techniques have been devised, e.g. hole cold-working/cold-expansion [2], interference fitting [3], split-mandrel expansion [4], spherical mandrelling [5], roller burnishing [6], ballising [7], coining [8], permanent-installed bushing [9] and shot peening [10].

Among the techniques proposed, perhaps cold-working of fastener holes by radial expansion is the most widely acceptable practice employed to prolong the fatigue performance of aerospace structures. Historically, tight interference fitting, cold-expansion or the combination of both methods was originally integrated into the design and manufacturing of high performance fighter aircraft to meet stringent safety demands. Realising the remarkable fatigue improvement that could be potentially gained, these techniques have been subsequently extended as part of airframe fabrication and maintenance in civil aircraft industry [11]. Champoux [12] has provided a broad overview

to evaluate the merits and limitations of various local enhancement techniques centred on the hole expansion mechanism.

1.1.1 Benefits of hole cold-working

The main idea behind hole cold-working is the introduction of a controlled region of compressive residual stress in the material surrounding the hole, as depicted in Figure 1.1.2. The beneficial effect of compressive residual stress against fatigue loading is schematised in Figure 1.1.3. When combined with tensile fatigue loading, the compressive stress is effective in counteracting the detrimental effect of tensile stress induced at the hole edge. Also, this indirectly reduces the stress concentration effect associated with the hole.

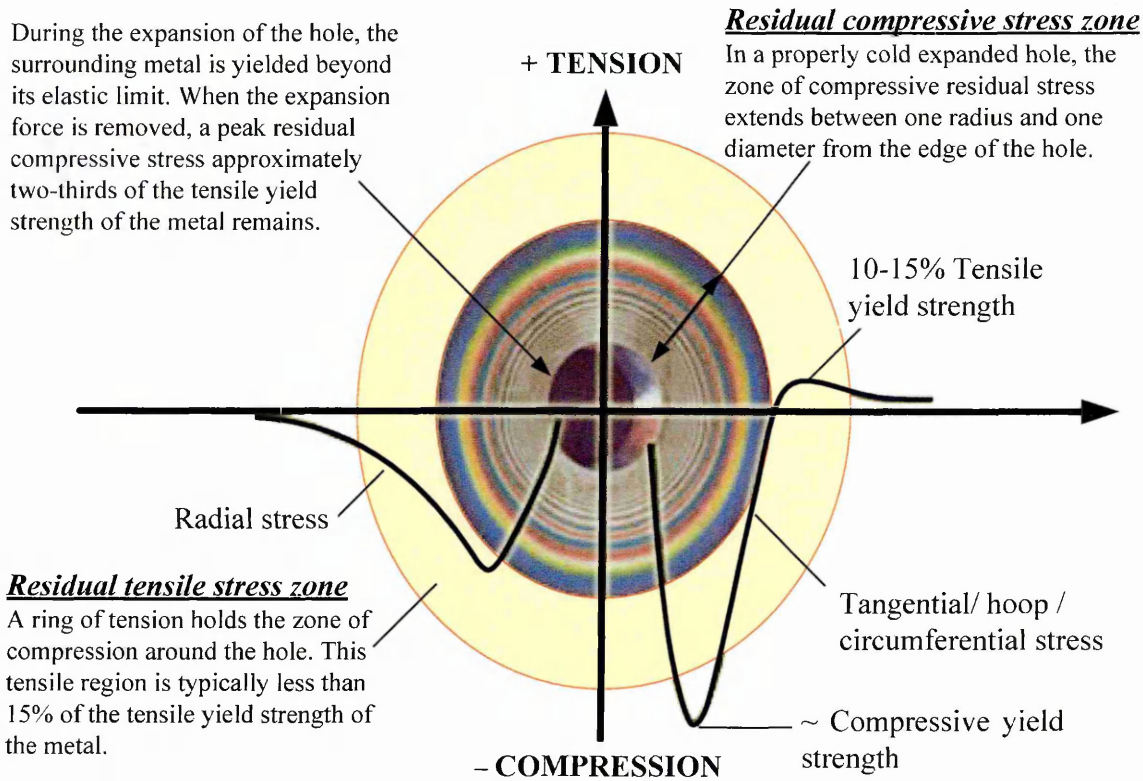

Figure 1.1.2 Residual stress field generated in a cold-worked hole. The coloured bands radiating from the hole show the residual compressive stress created by FTI's split-sleeve cold-expansion system. The bands are made visible by viewing a bi-refringent plastic thorough a polarizing filter. The plastic was epoxy bonded to the metal prior to being cold expanded. Adapted from [13]

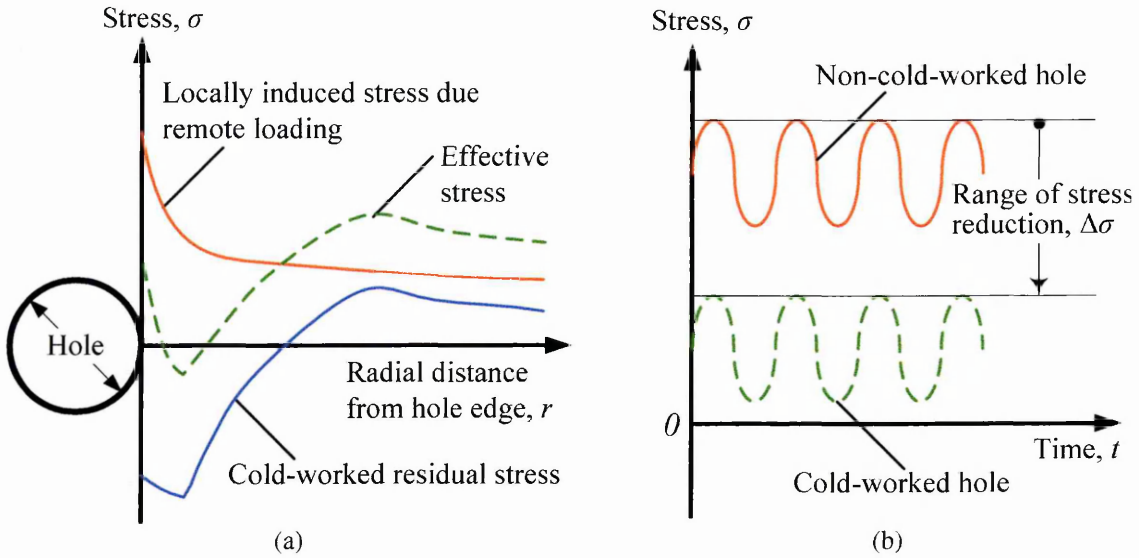

Figure 1.1.3 The influence of compressive hoop residual stress around a cold-worked hole: (a) offsetting effect of compressive stress resulting in peak stress reduction; (b) mitigation of material damage on under high magnitude of tensile fatigue load.

Similarly, even in the presence of fatigue flaws subjected to remote tension, the compressive residual stress is capable of locally suppressing the crack opening. According to the fracture mechanics approach this equivalent reduction of crack tip opening can be mathematically related to the decrease of stress intensity factor acting at the crack tip [14], as illustrated in Figure 1.1.4. Again, this condition is responsible for the delay of the rate of fatigue crack propagating from the hole.

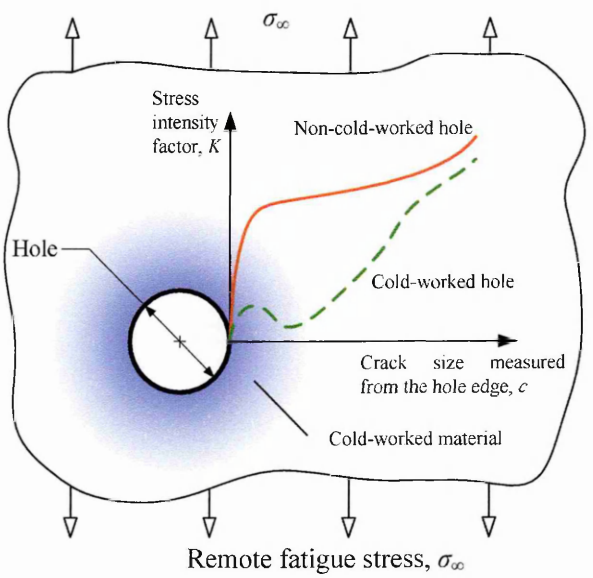

Figure 1.1.4 The reduction of a stress intensity factor at crack tip in cold-worked hole [14].

The cold-expansion methodology offers several technological benefits to aero-structures. First, fatigue problems can normally be reduced in airframes with thicker components or change of material specification; however, the redesign process inevitably is at the expense of weight and cost. Thus, cold-working is an alternative means to improve the fatigue resistance of critical assemblies without incurring such penalties.

Second, fatigue crack initiation and growth from cold-worked holes has significant impact on the procedures of structural inspection, repairs and maintenance. In practice, the physical and practical limitations of any non-destructive inspection (NDI) technology employed could possibly overlook the presence of small or shallow cracks at certain joint locations [15]. However, the "grace period" associated with cold working would guarantee operational safety before these unnoticed cracks grow to some detectable size in recurring inspections. Timely maintenance or repair is still feasible before these cracks reach critical size, and therefore results in considerable cost savings. For that reason, the hole cold working techniques have been extensively used by manufacturers to provide additional assurance on the safety of wide-bodied and combat aircrafts.

1.2 Process Descriptions of Mandrelizing Cold-Woking Systems

Currently, in the aerospace industry the most popular and efficient hole cold-working is carried out by drawing oversized mandrels through tight-tolerance, pre-sized starting holes. Such process of fastener hole treatment by mechanical pre-stressing can be accomplished either using the split-sleeve [16] or split-mandrel [17] cold-expansion systems.

A schematic summary of both cold-working procedures is given in Figure 1.2.1. The summary provides an overview of the systematic flow of various process controls necessary to attain acceptable quality of cold-worked holes in metallic components.

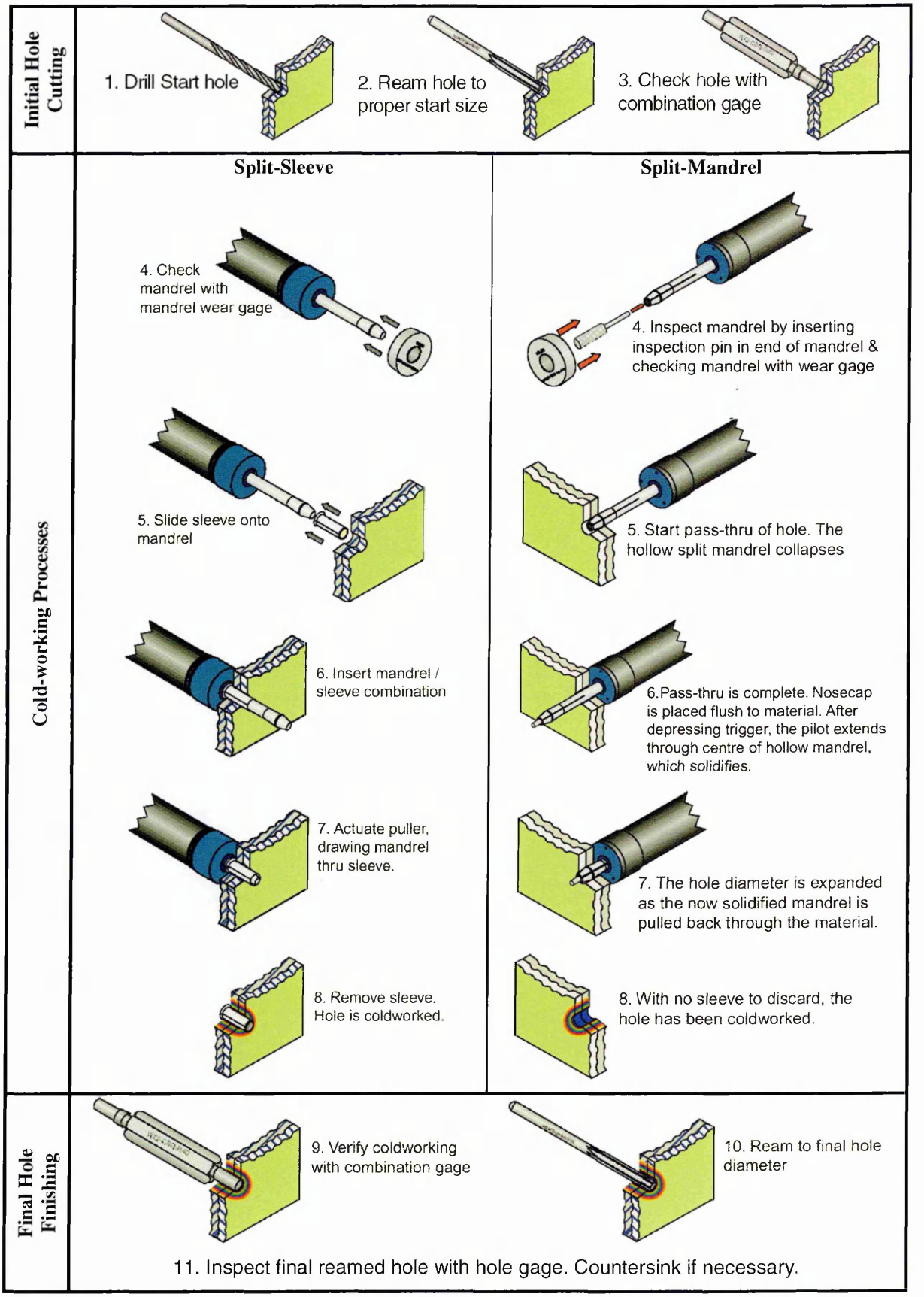

Figure 1.2.1 Complete cold-working procedures of holes required by split-sleeve and split-mandrel methods [17].

1.2.1 Split-sleeve cold-expansion

The split-sleeve cold-working system was developed by the Boeing Company in the early 1970s [2] and then improved and marketed by Fatigue Technology Inc., Seattle, USA [16]. This technique involves pulling a high strength solid mandrel in combination with an internally pre-lubricated split-sleeve fully engaged in the starting hole. The mechanism of hole cold-working effective in split-sleeve technique can be described by the progressive spread the yielded zone in the material along the hole bore, as illustrated in Figure 1.2.2.

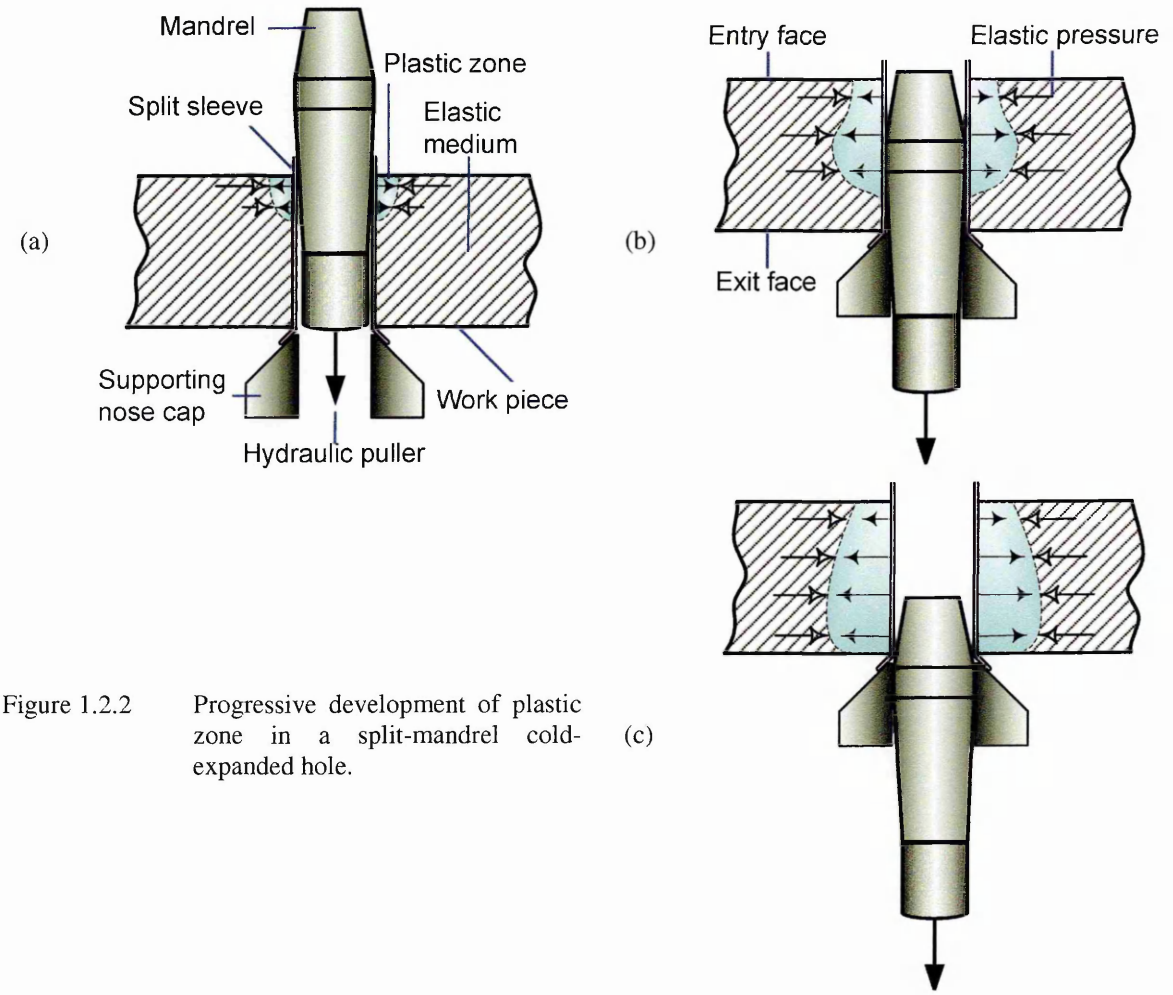

Figure 1.2.2 Progressive development of plastic zone in a split-mandrel cold-expanded hole.

The advantage of split-sleeve system is that it can be completed by hydraulic puller from any side of the hole convenient to the operator. Figure 1.2.2 (a) shows the side of the work piece where the mandrel enters subject to the first development of plasticity starting from the entry hole bore. The creation of yielded zone is immediately counterbalanced by the pressure from the surrounding material which is still in elastic condition.

Since the metallic plasticity is an irreversible process that cause permanent material deformation, this state of "misfit" persists even after the hole is unloaded from radial expansion. The relaxation of the cold-worked material enables a new equilibrium of elastic-plastic condition establishes in the work piece. As the outer rim of elastically deformed region springs back to attain its original position, the elastic pressure renders the majority of inner rim of plastically deformed material into compression, and this in turns leaves the elastic region in tension. The amount of plastic zone increases to full radial enlargement occurs by an amount equal to the combined thickness of the sleeve and oversized section of the mandrel.

In Figure 1.2.2 (b), as the tapered mandrel is drawn through the hole the plastic zone closes to the mandrel entry face relaxes from previous full cold-expansion, whereas at the mid-bore the hole is now fully expanded. This process continues until the removal of the mandrel gives rise an internal region of compressive residual stress field is formed around the permanently enlarged hole (Figure 1.2.2 (c)).

The mechanism of radial plastic deformation in single-sided split-sleeve mandrelizing process occurs successively along the hole bore, rather than simultaneously, which causes an asymmetric plastic zone forms through the thickness of the plate. This asymmetric plasticity effect becomes even more pronounce with the presence of axial deformation along the plate thickness due to increase flows of material pile up.

The asymmetric through-thickness plastic deformation can be explained by the existence of extrusion-type frictional force in the mandrel–sleeve–hole interfaces during mandrel passage through the hole wall. The problem is further complicated by the gradual transition of material constraint from plane stress at the hole entry and exit faces to plane strain at the mid-thickness in mandrelizing process. Also, the extrusion behaviour of mandrel drawing

process is manifested by the creation of surface upset called the "volcano effect" around the cold-expanded hole, as illustrated in Figure 1.2.3. The increase of material surface thickness is attributed to the fact that hole region near to the hole is more likely to flow in the thickness (i.e. axial) direction when subjected to plastic radial pressurisation [18].

As will be discussed later in Section 1.5, the characteristic of the plastic zone imparted has a direct influence on the three-dimensional distribution of residual stress and crack shape formation at split-sleeve cold-expanded hole.

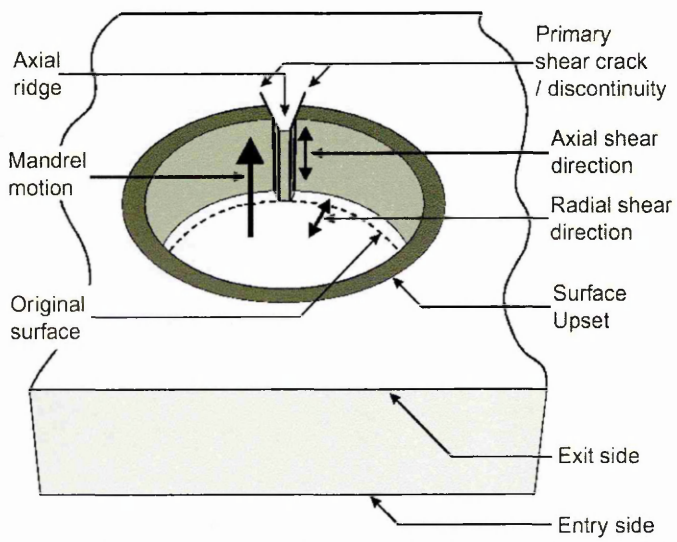

Figure 1.2.3 Shear cracking at split sleeve axial ridge [4].

A pip or axial ridge can be seen as a result of the gap in the split-sleeve (Figure 1.2.3). It has been shown that this feature can be a site of premature crack growth due to local shear tearing [4, 19]. However, in practice, this undesirable geometry is removed by final reaming prior to installation of fastener. The original working dimension of the sleeve is severely altered by cold-working, and consequently the used sleeve must be discarded.

1.2.2 Split-mandrel cold-expansion

A closely similar technology developed later in 1983 by West Coast Industries is the sleeveless split-mandrel method [17], which cold works hole also by plastic radial enlargement but without the use of disposable sleeve. The split-mandrel system utilizes an axially split, collapsible, tapered mandrel which is automatically lubricated by liquid acetyl alcohol (BOULUBE™). By pushing a small pilot through the internal slot of the split-

mandrel, the oversized section of the mandrel expands in a solid position as it is retracted back through the hole. The process consequently enlarges the hole, and also minimises the formation of the axial ridge in permanently enlarged hole seen in Figure 1.2.3 [20]. Although split-mandrel expansion is mechanically accomplished by a slightly different mechanism, the underlying principle is same as to those reported for split-sleeve method. Therefore, the residual stress field generated by the split-mandrel technique is virtually identical to the split-sleeve system.

As shown in Figure 1.2.4, both the split-sleeve and split-mandrel systems are both effective in delaying the fatigue damage process of metals [4, 21], with some evidence that holes treated with the split-mandrel technique achieved an even greater improvement in fatigue durability than the split-sleeve method, particularly at low levels of stress.

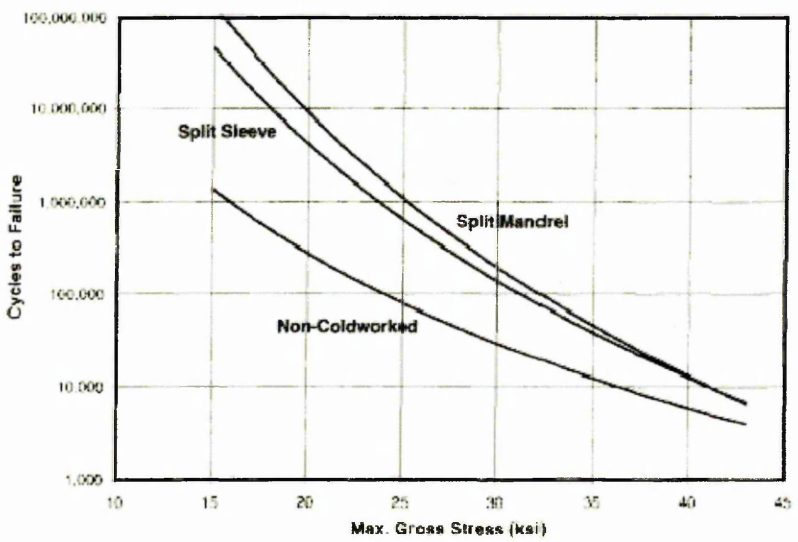

Figure 1.2.4 Comparison of fatigue results for 6.35 mm diameter in Al 2024 plate cold-worked with split-sleeve and split-mandrel processes, and non-cold worked holes [4].

However, the common feature of these systems is the requirement of various pre- and post-processing production steps, significant tooling, and tight tolerances of hole sizes for optimum cold-working (Figure 1.2.1). Since the entire operation is labour-intensive, implementing these cold-working systems for automation of mass production can be highly complex and expensive, although some success has been obtained in automating the split-mandrel systems [20, 22-24].

1.3 Process Descriptions of Indentation Cold-Woking Systems

This section explains a novel cold-working method in the form elastic-plastic indentation in metallic work piece performable either under quasi-static mode, or dynamic mode. The quasi-static indentation can be easily accomplished by force or displacement control modes, and hence accessible to any laboratory equipped with conventional material testing machines. However, the quasi-static indentation also requires high indenting load attributed to overcome the near incompressibility of metal under compression.

An alternative to solve the requisite of high static load is the use of dynamic indentation taken at a prescribed impact velocity yet at a much lower dimpling load. The obvious discrepancy is that the phenomenon of stress wave scattering is triggered in the target material under high strain rate loading, which is not normally seen in quasi-static application. The magnitude of impact, as a function of indenter size, dimple depth and material type, can be controlled precisely by electromagnetic impulsive actuator.

Amongst the metals used in aerospace industries, the mechanical properties of steels and titanium alloys are noticeably susceptible to high strain rates but remain fairly negligible for strain-rate insensitive metallic such as aluminium alloys [25, 26]. In general, as far as the range of impact velocities and strain rates concern, for the same indentation depth considered the dynamic indentation can equally deliver comparable degree of cold-working shown in the quasi-static case. Also the mechanical properties of material altered by high strain rates are mostly localised on the dimpled sites, and the material at these locations are normally removed afterwards by hole drilling and reaming.

The subsequent explanation is divided into three sections. Section 1.3.1 concerns mainly the basic process steps and the history of elastic-plastic deformation associated with the

novel indentation technique. The information reported in Section 1.3.1 is generic to quasi-static and dynamic cold-indentations.

Other Sections 1.3.2 & 1.3.3 are related to the dynamics aspects material subjected to effect of elastic-plastic stress wave. In Section 1.3.2, the historical background on the stress wave application is provided. Account on the previous works in the development of cold-working of fastener hole involving stress wave is also given. The qualitative and quantitative description of stress waves produced in solids is treated in Section 1.3.3.

1.3.1 Cold-working of metals by indentation technique

The StressWave (SW) method has been recently developed to overcome the principal limitations of current cold-expansion techniques [27]. The novel technique uses local cold-indentation in metal at the prospective hole locations prior to hole machining. Residual stress is generated within the material around the prospective location without using a starting hole.

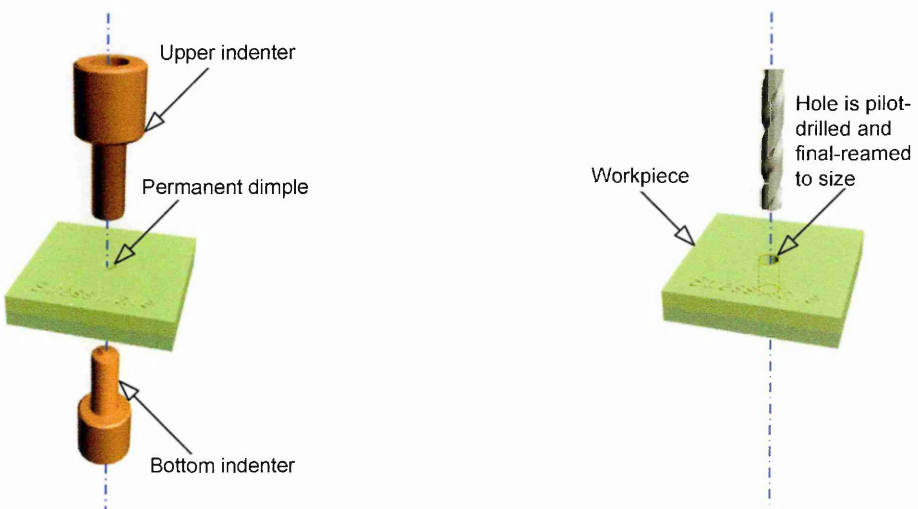

(a) Step-1: Cold-working by indentation (b) Step 2: Hole machining

Figure 1.3.1 StressWave cold-working procedures of holes [28].

Figure 1.3.1 demonstrates the two basic steps of the hole cold-working procedure using the SW technique. The process involves pressing a pair of co-axial indenters onto the work piece (Figures 1.3.1 (a)) to create permanent dimples on each side of the material (Figure

1.3.1 (b)). At sufficiently deep indentation, the indenter generates a symmetric material flow emanating from the dimples causing elastic-plastic deformation.

Figure 1.3.1 is further expanded into Figure 1.3.2 to clarify the transformation of material states arise during the SW treatment. The cold-working mechanism of SW indentation capitalises the near incompressibility of metal when undergoing plastic deformation [29].

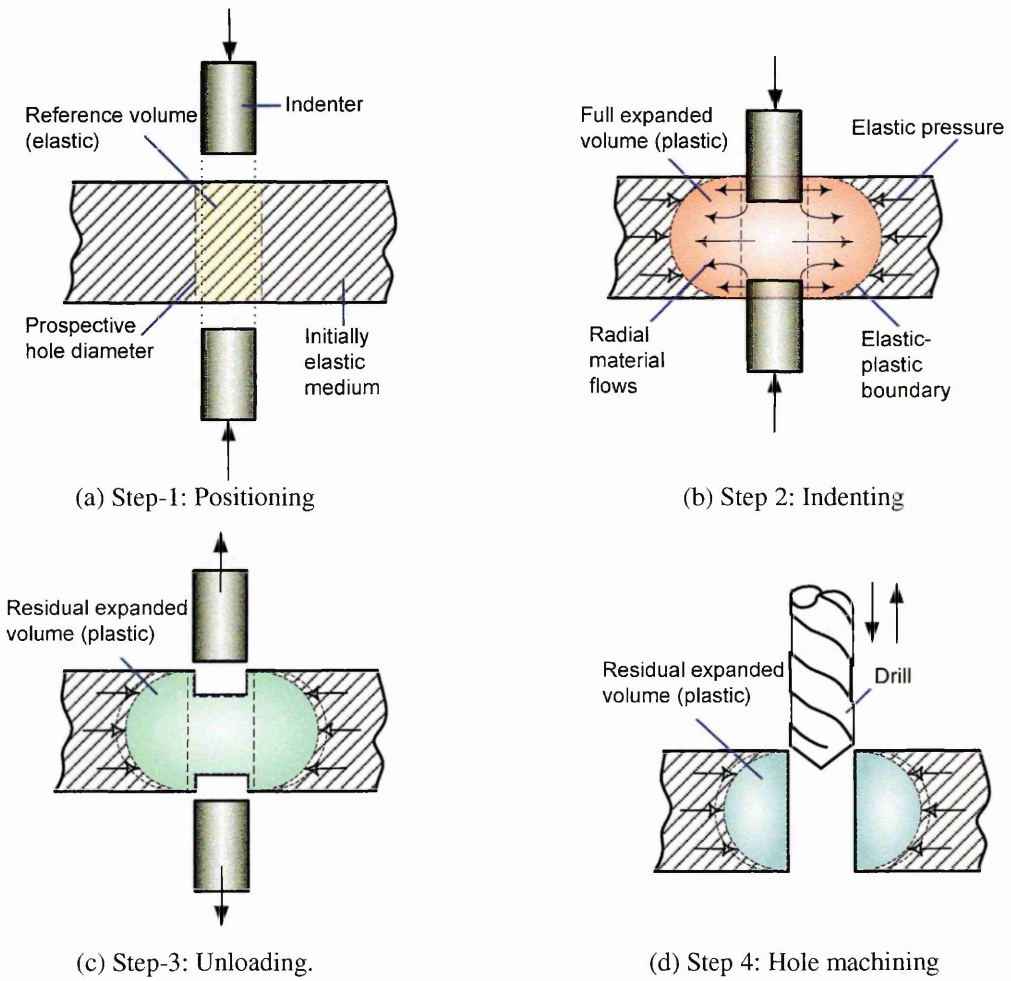

(a) Step-1: Positioning

(b) Step 2: Indenting

(c) Step-3: Unloading.

(d) Step 4: Hole machining

Figure 1.3.2 Mechanism of StressWave cold-working technique.

Figure 1.3.2 (a) shows a standard SW system that firstly involves the alignment of a pair of co-axial indenters positioned at some axial distance perpendicular to the target. The diameters of the dimples created by the indenters are smaller than the final hole size. Specialised electromagnetic devices are frequently employed to deliver enough kinetic energy to drive the indenters to the desired depth into the target material, as shown in Figure 1.3.2 (b).

Under high axial compression the reference volume of elastic material in Figure 1.3.2 (a) is now forced to deform radially from the pinched locations that involve high degree of plastic flows. The expansion of the elastic volume into plastic state in Figure 1.3.2 (b) can be visualised as "barrelling effect" in monotonic compression test of round solid cylindrical metals [29]. The volume of yielded material is shown by the elastic-plastic boundary. Likewise to the mandrelizing method (see Figure 1.2.2), the formation of plastic region must be counteracted by the pressure field of elastically deformed volume away from the SW dimples in Figure 1.3.2 (b).

In Figure 1.3.2 (c), the removal of indenters allows the first equilibrium state of elastic-plastic deformation to establish, accompanied by a nominal shrinkage of the plastic volume under external elastic pressure. A subsequent hole drilling process in Figure 1.3.2 (d) eliminates the cylindrical volume of plastic region (including the undersized permanent dimples) concentric to the hole centre. The loss of material constraint during the hole cutting process allows a relatively higher elastic pressure to act on the inner rim of remaining plastic zone. Given this circumstance, a second stage of material static equilibrium may induces higher magnitude of compressive residual stress at the hole edge.

The indentations result in voluminous material plastic flow concentrates near to the mid-thickness plane, compared to those near to the surface. This mechanism in combination with smaller indenter is capable to confine the "volcano effect" only within the dimpled sites, and the problem of surface upset can be also minimised by optimising the design of indenter tip. In practice, the surface upset in SW specimen can be easily removed by machining a final hole of diameter larger than that of the dimple (see also Figure 1.3.5 (b)).

1.3.2 Historical background of stress wave technique

High strain rate machining that generates stress wave has found many industrial applications, such as manufacturing of metal parts, processing and new materials synthesis, explosive joining and bonding [30, 31]. The stress wave incident is considered negligible when the force application is low and the rate of loading is slow (quasi-static). However, the effect of stress wave becomes increasing evident if the loading rate is high with large load application. Upon contact with the target surface of a solid, the impulsive loading creates a disturbance that is generated travels through the solid as stress waves, which are analogous to sound waves propagating through air [32]. Table 1.3.1 provides a summary of the classification of dynamic characteristics for various manufacturing processes of metal forming [33]. The type of stress wave to cold-work joint hole in metals falls within the category of high strain rate application (column *IV*).

Characteristic time scale (s)	10^{6} 10^{6}	10^{2} 10^{0}	10^{-2} 10^{-4}	10^{-6}	10^{-8}
Strain rates (s^{-1})	10^{-8} 10^{-6}	10^{-4} 10^{-2}	10^{0} 10^{2}	10^{4}	10^{6}
	Creep rates	*Quasi-static rates*	*Intermediate strain rates*	*High strain rates*	*Very high strain rates*
	I	***II***	***III***	***IV***	***V***
Primary load environment	High or moderate temperatures	Slow deformation rates	Rapid loading or low velocity impact	High velocity impact or loading	Very high velocity or hypervelocity impact
Usual method of loading	Constant load or constant stress machines	Conventional hydraulic or mechanical machines	Fast-acting hydraulic or pneumatic machines, cam plastometers, low impact devices	High velocity impact devices, expanding-ring technique, high speed metal cutting	Light gas gun or explosively accelerated plate or projectile impact
Dynamic considerations in testing	Strain versus time	Constant-strain-rate test	Machine stiffness wave effects in specimen & testing machine	Elastic-plastic wave propagation	Shock wave propagation, fluid-like behaviour
Thermodynamics characteristic	← Isothermal →		← Adiabatic →		
Dynamic effect of mass	← Inertia force neglected →		← Inertia force important →		

Table 1.3.1 Classification of dynamics regime; adapted from [33].

In the context of present work, I shall only concentrate on the fastener holes cold-working technique for metallic structures encountering stress wave event. The working principle is that during dynamic impact the energy transmission between contact bodies in the form of stress wave can be very intense. Consequently, this stress wave process has been found effective to deform metals at greater speed but at lower working load.

The practical usage of impact at contact to ease fastener installation and cold-working were recorded in the work of Leftheris [34, 35]. Leftheris [34], based on his earlier patented work in this area [31], conceived the idea of converting electromagnetic energy into a stress wave fastening system. The stress wave is conditioned, focussed and imparted to one end of interference-fit fastener to drive the fastener into a hole. Later, Leftheris *et al.* [35] extended the fastening system to incorporate sleeveless mandrelizing technique for straight bore or tapered bore holes. The invention is aimed to cold-expand fastener holes at high velocity, while control the geometrical sizing and the quality of hole bore surface finishing simultaneously. Nevertheless, as these processes [34, 35] demand the use of precision starting holes, they all suffers similar production difficulties inherent to the split-sleeve and split-mandrel cold-expansion system described in Section 1.2 earlier.

In present attempt, the dynamics indentation method used was developed lately by Easterbrook [36] centred on the instantaneous local indentation in solids that is accompanied by stress wave. The termed "stress wave" has been afterwards adopted as the process commercial name called StressWave (SW), and is also subsequently used in this thesis to refer to the method investigated.

Easterbrook's technique [36] is an improvement of the idea proposed by Wong & Rajic [37] that used a local impression on the surface of a solid. The advantage of Wong & Rajic's invention is the elimination of starting hole requirement to cold expand a hole, and

also a close tolerance hole can be easily machined as the created dent size is smaller than the final hole diameter. However, under quasi-static mode the process entails relatively high load to indent or cold-work the material, and can only be accomplished in high capacity machinery such as hydraulic or power presses. This major shortcoming of Wong & Rajic invention prohibits an extensive adoption of their technique in automated fastening systems.

Nonetheless, by introducing the working principle of stress wave in combination with indentation, the dynamic working load reduces considerably when compared to the quasi-static load required to produce same amount of cold-working. The low load indentation associated with stress wave process enable better implementation of the technique into airframe manufacturing procedure.

1.3.3 Principle of stress wave in solids

The propagation of dynamic stress waves through finite medium of varying geometry is a complex event, and can become even more complicated for heterogeneous material. For generality, the discussion onwards will be confined only to infinite isotropic body subject to local indentation at high speed.

At the instant of impact onto the target the indenter imparts three principal modes of compressive stress waves with different velocities and vibration characteristics: dilatational, distortional and Rayleigh waves. Both the dilatational are distortional waves are categorized by the direction of particle motion with respect to the propagation direction of the disturbance, or the wave front, as demonstrated in Figure 1.3.3.

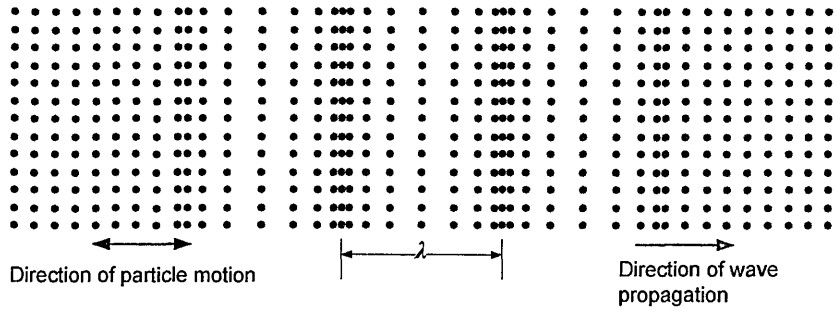

(a) Dilatational wave (*P*-wave).

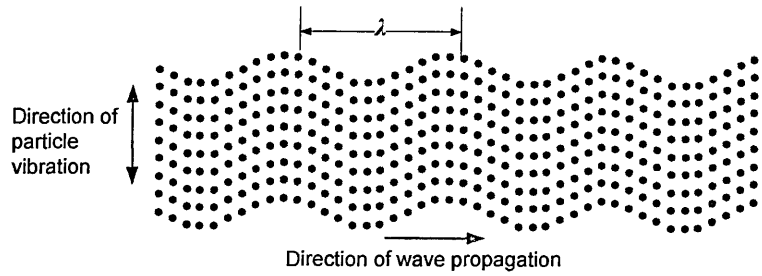

(b) Transverse wave (*S*-wave).

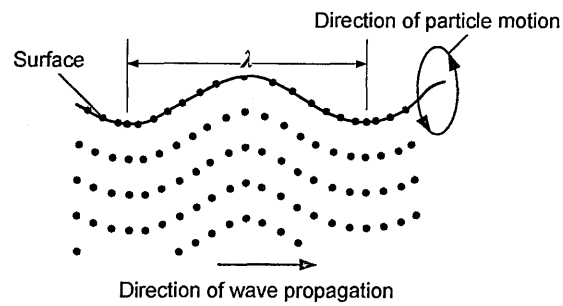

(c) Rayleigh wave (*R*-wave).

Figure 1.3.3 Directions of particles motion associated with different type of stress wave in solids. λ = wavelength [38]

Dilatational wave is also referred to as compression waves or *P*-waves, as the particle motion is parallel to the propagation direction (Figure 1.3.3 (a)). Dilatational wave propagates in all kinds of media associated with normal stress or pressure. Distortional wave is also known as shear waves or *S*-waves. Distortional wave causes particles to vibrate perpendicular (i.e. transverse) to the propagation direction (Figure 1.3.3 (b)), and hence give rises to shearing stress effect. Distortional wave occurs only in media with shear stiffness, i.e. solids. Rayleigh wave is also termed as surface wave or *R*-wave, which propagation limited only to particles on the surface of a solid because it attenuates rapidly with depth (Figure 1.3.3 (c)). The trajectories of particle motion for Rayleigh wave are in elliptical shape.

The wave front defines the leading envelope of stress wave at different time as it propagates through a medium, and may assume three idealised shapes: planar, spherical and cylindrical. The profiles of the *P*-, *S*-, and *R*-wave fronts are governed by the conditions of the disturbance. Closely related to current problem, by striking a rigid rod normal to a point on the surface of a solid, the *P*- and *S*- waves propagate in hemispherical wave fronts (see Figure 1.3.4 (a)). The *R*-wave, on the other hand, travels away from the indented point in a cylindrical wave front, as schematised in Figure 1.3.4 (b).

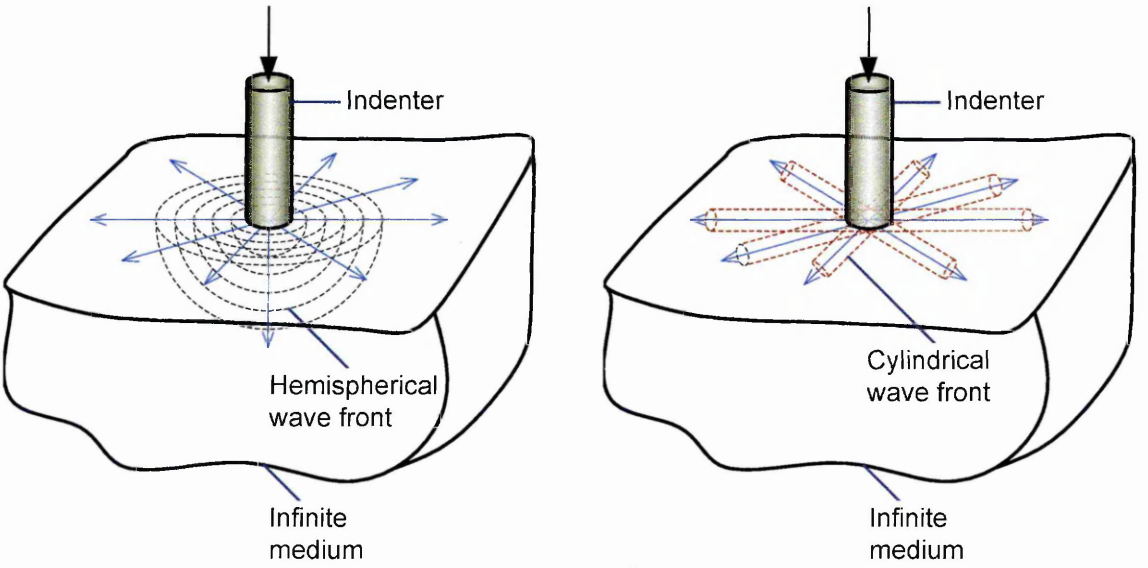

(a) Shape of *P*- & *S*-wave front. (b) Shape of *R*-wave front.

Figure 1.3.4 Spatial wave fronts generated by dynamic indentation of an isotropic infinite solid.

From the theory of wave scattering in infinite, isotropic, elastic body, the *P*-wave possesses the highest travelling speed:

$$\text{Dilatational: } C_P = \sqrt{\frac{E(1-\nu)}{\rho(1+\nu)(1-2\nu)}} \tag{1.3.1}$$

where E is the Young's modulus, ν is the Poisson's ratio, and ρ is the material density. The propagation speed of *S*-wave in infinite solid is given by:

$$\text{Distortional: } C_S = \sqrt{\frac{G}{\rho}} = \sqrt{\frac{E}{2(1+\nu)\rho}} \tag{1.3.2}$$

where G is the shear modulus of elasticity. The *R*-wave propagates at the slowest speed that can be approximated by [39, 40]

$$\text{Surface: } C_R = \left(\frac{0.87+1.12\nu}{1+\nu}\right) C_S \tag{1.3.3}$$

For aerospace aluminium 2024-T351 alloy used in present study (elastic constants $E = 71.9$ GPa, $\nu = 0.32$ and $\rho = 2780$ kg/m^3 (see Section 3.3.6)), the speeds of different stress wave calculated from Equations 1.3.1–1.3.3 are $C_P = 6.084 \times 10^3$ m/s, $C_S = 3.13 \times 10^3$ m/s and $C_R = 2.913 \times 10^3$ m/s. In other words, the *S*-wave is 51% of *P*-wave speed, whereas *R*-wave speed is about 93% of *S*-wave speed, or 48% of the *P*-wave speed. The estimated values of C_P and C_S for Al 2024–T351 alloy are in agreement with the values from the literature in Table 1.3.2.

Material	C_P	C_S
	m/s x 10^3	
Aluminium	6.15	3.10
Brass	4.24	2.14
Copper	4.27	2.15
Gold	3.14	1.17
Iron	5.06	3.19
Lead	2.12	0.74
Magnesium	6.44	3.09
Nickel	5.59	2.93
Silver	3.45	1.57
Steel	5.71	3.16
Tin	2.96	1.49
Tungsten	7.78	2.64
Zinc	3.86	2.56

Table 1.3.2 Propagation velocities of stress wave, C1, C2 for various materials. Nominal values calculated from data on elastic constant (E, ν) and density, ρ [38].

Under a rigid impact that is sufficient to initiate plasticity, the elastic waves described in Equation 1.3.1–1.3.3 is followed by the spread of compressive plastic waves [41]

$$\text{Plastic: } C_{plas} = \sqrt{\frac{K}{\rho}\left[\frac{1+H'(\varepsilon)/3K}{1-H'(\varepsilon)/9K}\right]} \tag{1.3.4}$$

Where the bulk modulus or modulus of compression, $K = E/\left[3(1-2\nu)\right]$; $H'(\varepsilon)$ is the tangent modulus calculated from the plastic stress-strain curve $\sigma = \sigma_Y + H(\varepsilon)$; σ_Y is the material yield stress and ε represents the total strain. To reduce the complexity in Equation

1.3.4, Easterbook [36] considered an approximated formulation proposed by Kolsky [32] to describe the plastic wave speed for SW technique:

$$\text{Plastic: } C_{plas} = \sqrt{\frac{E_p}{\rho}} \tag{1.3.5}$$

A useful feature of stress wave is that for a given input energy its intensity may be amplified to produce a highly focused energy output [32, 42]. For indentation-type cold-working, this requirement can be met by specially tailor the design of stress wave focuser (i.e. indenter) as exemplified in Figure 1.3.5 (a). The indenting device receives the input energy from the larger (bottom) end, and transmits the energy out at the indenter tip (top) into the material.

This arrangement has the benefits of rendering elastic-plastic deformation more easily onto the dimple, with further prospect of reduced applied load. In addition, the design of indenter tip shown in Figure 1.3.5 (a) is also intended to optimise for greater material radial flow (i.e. increase cold-working) and to minimise surface upset around the dimple in Figure 1.3.5 (b).

Indenting force, F = 64.5 kN (14.5 kips)

(a) Indenter

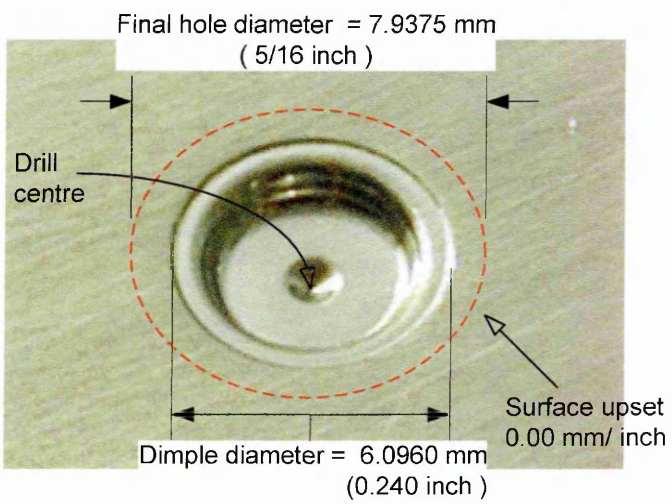

Dimple depth, δ = 0.89 mm (0.035 in.) per side

(b) Dimple

Figure 1.3.5 Formation of permanent dimple on the surface of Al 2024-T3 plate by StressWave proprietary indenter [28].

The SW method ensures that material flows radially from the dimple as there is a high degree of axial compression in the through thickness direction. The symmetry of the SW method ensures that the resulting residual stress is even both around the hole and through the thickness of the sample.

When compared to split-sleeve and split-mandrel methods, this distinct cold-working mechanism lends the SW process more readily to automation of mass production of fatigue-resistant fastener holes. The SW process is also highly adaptable into existing automated fastened assembly and other manufacturing devices. This suggests that the SW method may achieve better economic efficiency in the aircraft industry. SW fatigue data also suggest that the method produces a comparable or even superior fatigue performance compared to conventional practise (Figure 1.3.6).

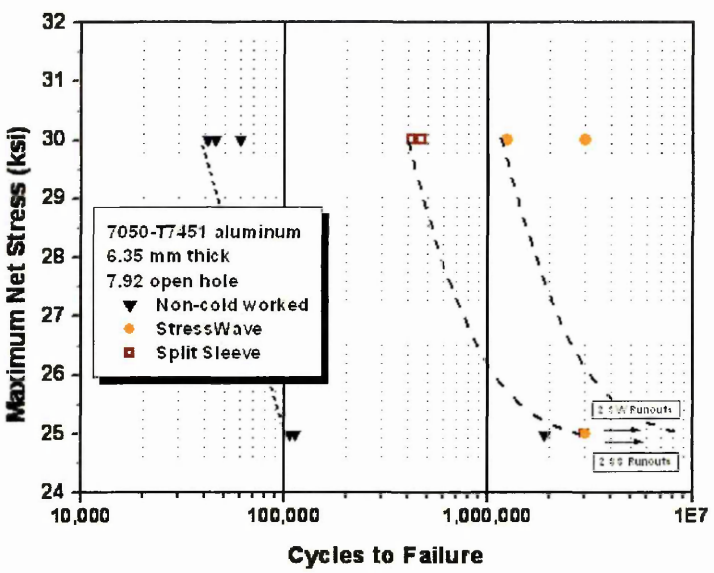

Figure 1.3.6 S-N curve comparing the fatigue enhancement attained in cold-worked holes pre-stressed by split-sleeve and StressWave processes [43].

1.4 Quality assurance of cold-expansion systems

The degree of effectiveness of mandrel methods in providing sufficient amount of hole cold-working depends primarily on the dimensional tolerance of the working tools (e.g. sleeve, mandrel and expanding pilot) and work piece (e.g. hole diameter and straightness of hole wall). The procedure involves stringent checking of the hole sizes at starting, post-

worked and post-reamed stages of cold-working using a combination gage, whereas the mandrel dimension must be verified using a wear fixture before cold-expansion. These techniques are very sensitive to manufacturing variables and often operator proficiency.

In contrast to mandrel methods, the permanent dimple is the principal metric of quality control of the SW technique (Figure 1.3.5 (b)). The residual depth of the dimple, δ, is an observable and directly measurable property that is well-correlated to the degree of cold-working introduced into the materials. Accordingly, the shape and depth dimple is a reliable indication of effectiveness of SW process. The qualities of dimple created in Figure 1.3.5 (b), along with the appropriate level of applied indenting force (Figure 1.4.1) are principally used to ensure that optimum process control can be obtained. Of course, the prospective location of the hole must be well-aligned before pilot drilling and reaming, so that compressive stress can be evenly distributed around the hole periphery.

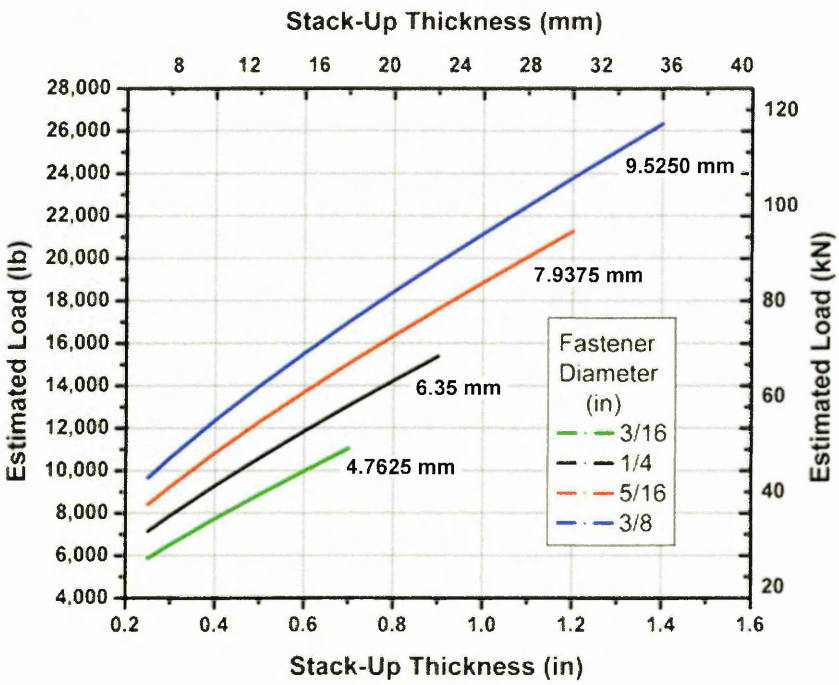

Figure 1.4.1 Indenting force requirement chart for aluminium alloy plate, as a function of stack-up thickness and fastener diameter [28].

The present work considers SW specimens cold-worked under static force-control mode, using the relations of "indenting load versus stack-up thickness and final hole diameter" obtained under quasi-static finite element simulations (Figure 1.4.1.) The dimensions of the

plate specimens are 6.35 mm thick with 6.35 mm final hole diamter, and therefore requires about 38.7 kN (i.e. 87,000 lb) of indenting force to achieve a nominal 4% cold expansion.

The quasi-static load required is well within the capacity of the manufacturer's press machine, and also due to the fact that no electromagnetic fastening machine were not accessible for dynamics process at that time. The complexity of stress wave propagation is further reduced in view that aluminium 2024–T351 alloy is known to be fairly insensitive to range of high strain rates catagorised in column *IV* of Table 1.3.1 [44].

1.5 Damage Tolerance of Mechanical Joints

1.5.1 Current state of design guidelines

A typical wide-bodied aircraft contains more than 3 million cold-worked fastener holes, which implies substantial time and cost involved in the manufacturing phase alone [45]. Despite the attractiveness and benefits offered by cold hole expansion methods, unfortunately to date regulations do not allow the beneficial contributions of the cold-expansion process to be incorporated in design optimisations and fatigue endurance calculations [46, 47].

At present, cold-expansion is merely regarded as an extra safety feature to ensure that the intended design life of aircraft can be obtained. One major obstacle to fully embrace the benefits of cold-expansion in airframe design is the fact that the prediction of accurate fatigue life of cold-expanded fastener holes is non-trivial. In practice, the fatigue life prediction is highly sensitive to the residual stress field and the resultant crack shape formation.

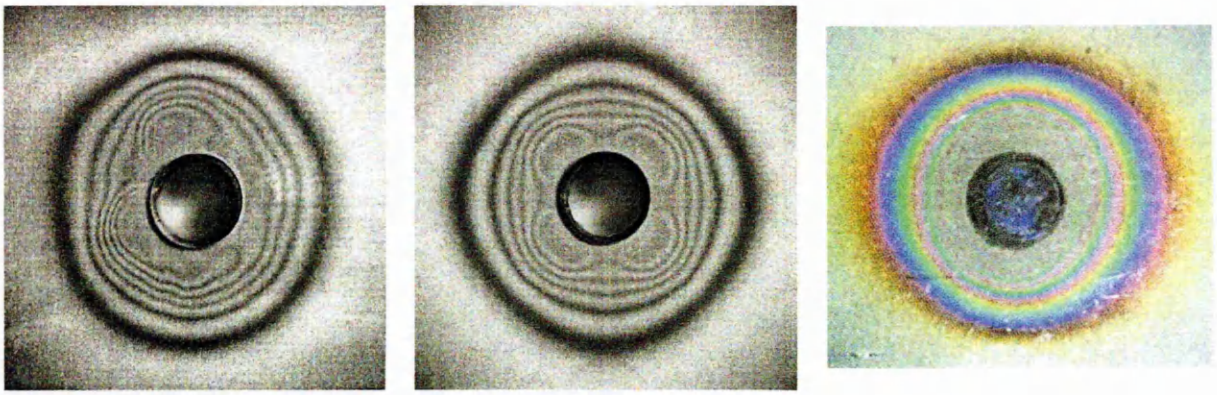

(a) Split Sleeve [4] (b) Split Mandrel [4] (c) StressWave [48]

Figure 1.5.1 Photo-elastic images show the region of surface compressive residual stress around holes induced by three different cold-working processes.

The relative degree of residual stress field around the hole is illustrated by Figure 1.5.1 which juxtaposes photo-elastic profiles of two-dimensional surface residual stress field imparted by different methods of cold-working. Clearly, the SW attains a high degree of concentric stress field compared to the traditional split-sleeve and split-mandrel methods (Figure 1.5.1(c))). Near the hole border, asymmetrical stress patterns of 'heart shape' (Figure 1.5.1(a)) and 'cloverleaf' Figure 1.5.1(b)) are visible before blending gradually into circular pattern away from the hole. These uneven stress fields reveal that there is a lack of uniform radial expansion of material around the hole periphery, which is due to the gap or slot geometry present in the split-sleeve and split-mandrel.

(Information on the residual stress field and fatigue crack shape for split-mandrel holes is not currently available in the literature, and so only a limited account on the cold-working method is given here.)

Earlier research [49-60] has confirmed that the traditional split-sleeve mandrelizing technique inevitably introduces asymmetric three-dimensional compressive residual stresses along the planar and through thickness directions at the hole. In particular, the residual stress induced on the entry side of the mandrel passage is somewhat less than exists both at the mid-thickness and exit side. As a result, a complex crack shape has been

frequently observed in single cold-expanded hole, in which the crack length at the entry face is constantly greater than the exit side (Figures 1.5.2 (a) & 1.5.2 (c)) [61]. Although partial improvement of crack symmetry has been recently reported for hole cold-expanded twice in reverse directions (Figures 1.5.2 (b) & 1.5.2 (d)) [61], it is unlikely that the method is appropriate for an actual manufacturing environment. Extra cost of disposable tooling, additional operating time and limitation of access of both sides of the fastener holes at restricted areas are the major drawbacks of this method.

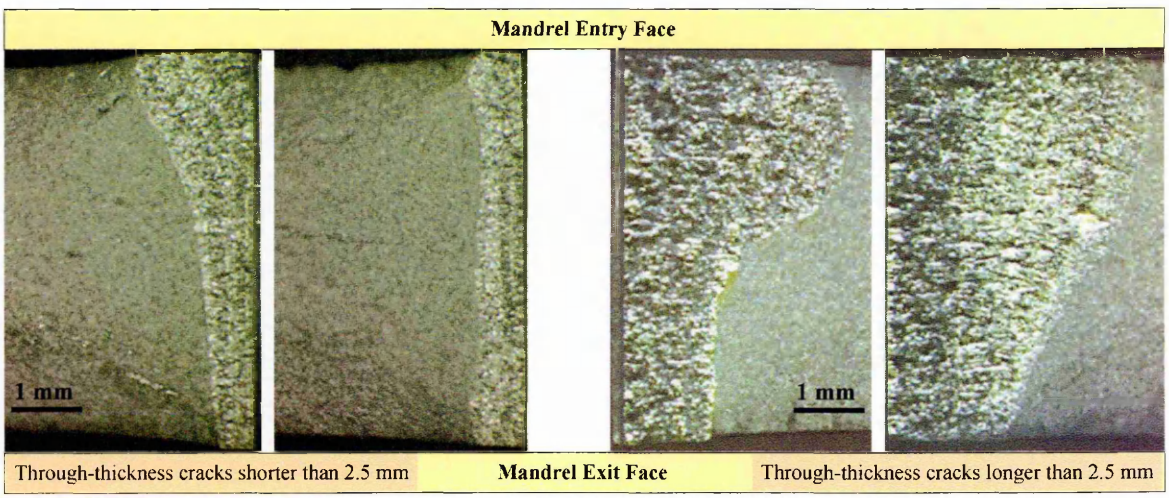

(a) SCE (b) DCE (c) SCE (d) DCE

Figure 1.5.2 Crack shape evolution in single cold-expanded (SCE) and double cold-expanded (DCE) hole [61] revealing the through-thickness effect of non-uniform expansion process.

The eccentric nature of the residual stress in the planar direction, when acted under uni-axial cyclic load, is manifested by the fact that a secondary crack follows at the opposite side of the hole after the main fatigue crack has grown to several mm (Figure 1.5.3). In order to predict the fatigue life of a cold-expanded hole, any calculation must include the evolution of the residual stress, and the double eccentricity of the crack along with the appropriate geometry factors of work piece. This unavoidably requires more measurement data to constantly follow up changes in fatigue crack growth behaviour for cold-expanded holes [62]. At present, it is still not possible to perform reliable damage tolerance analysis accounting for the complicated crack behaviour shown in Figure 1.5.2 & 1.5.3. This is mainly due to the absence of appropriate stress intensity factor solutions to model the

interaction between multiple cracks under the influence of a complex three-dimensional residual stress field.

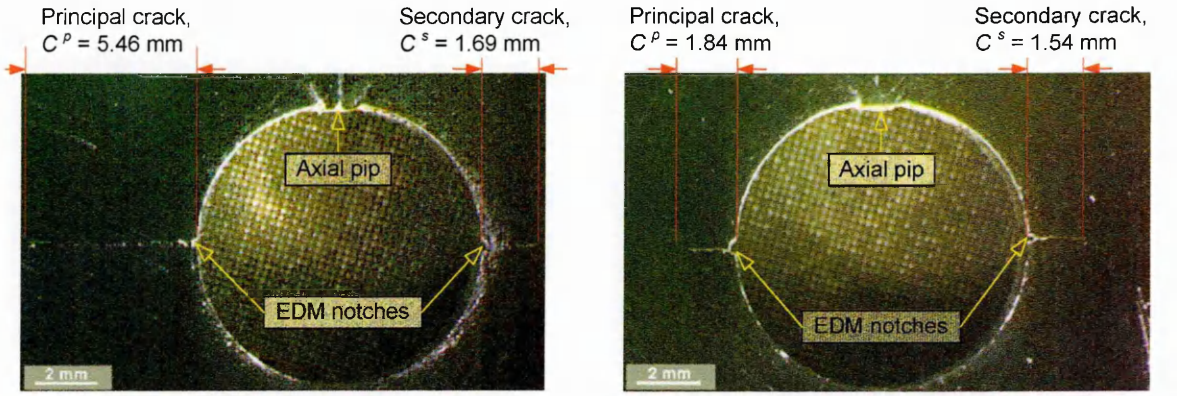

(a) Mandrel entry face (b) Mandrel exit face

Figure 1.5.3 Evolution of primary and secondary cracks from a split-sleeve cold-expanded hole.

Furthermore, consistent realisation of the benefits of life enhancement techniques requires exceptionally high quality process control of materials, which is not always obtained during manufacture (Section 1.2) [63]. It is therefore unwarranted that all fatigue enhancement techniques can be effectual in delaying crack growth under all circumstances. Consequently, in order to maximise flight safety and to reduce the impact of manufacturing errors, the regulating documents such as JSSG-2006 [47] stipulate that damage tolerance requirements should be met without taking account for the favourable effects of particular joint design and assembly process.

1.5.2 Fatigue crack growth from cold-worked holes

A comprehensive experimental work has been carried out by Lamb *et al.* [64] to compare the fatigue crack growth behaviour of baseline, split sleeve and SW specimens. Part of their fatigue data is presented in Figure 1.5.4 indicating that the nature of residual stress field induced around the hole, as a consequence of cold-working technique used, has a significant influence on the characteristics of surface cracks propagating in the specimens.

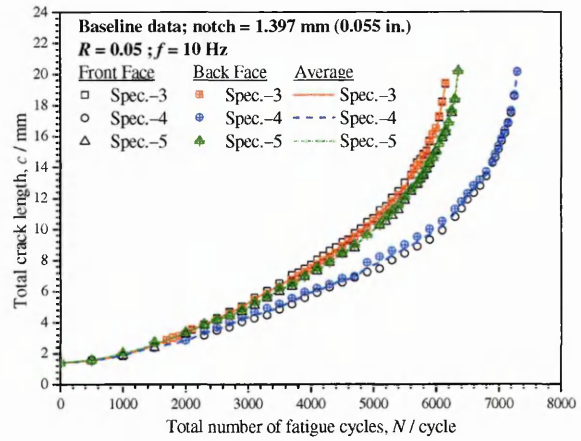

(a) Baseline data

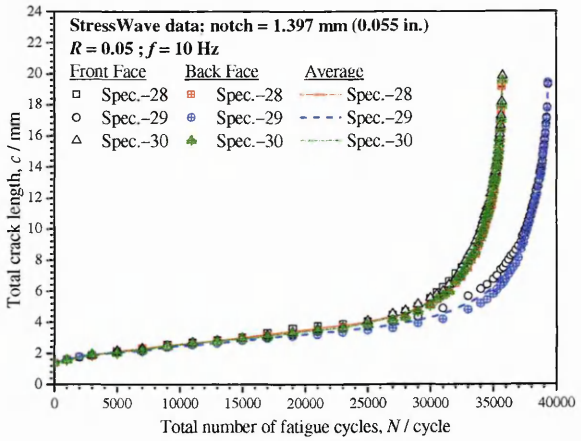

(c) StressWave data

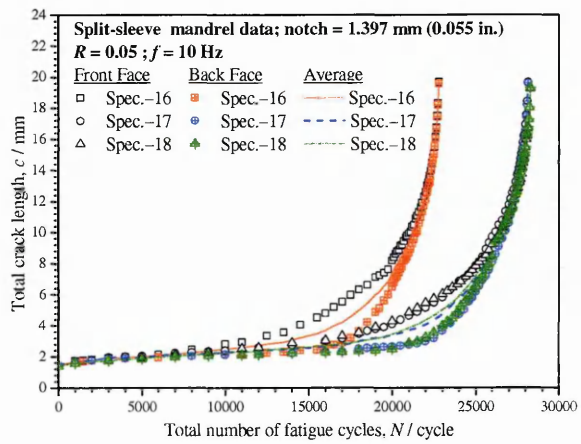

(b) Split-sleeve mandrel data

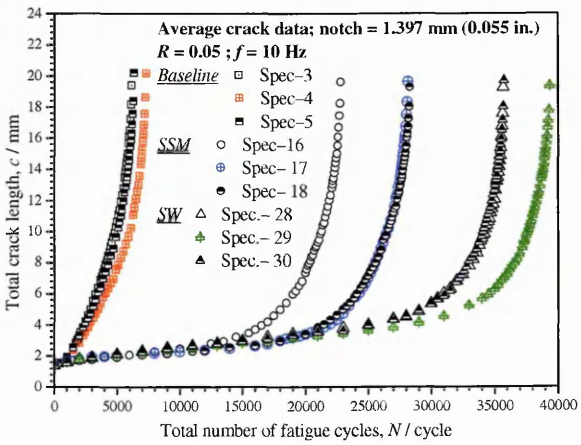

(d) Composite data

Figure 1.5.4 Fatigue crack growth data for baseline (non-cold-worked), split-sleeve and StressWave specimens. Cracks were grown from single through-thickness EDM notches installed at hole edges. Plate material: Al 2024-T3; plate thickness T = 6.35 mm (0.25 in); hole diameter, Ø = 7.874 mm ~ 7.9248 mm (0.310 in ~ 0.312 in); maximum cyclic stress, σ_{max} = 172 MPa (25 ksi) [65].

In split-sleeve specimens (Figure 1.5.4 (b)), the crack growth rate at front-face (mandrel entry) is consistently more rapid than at the back-face (mandrel exit). Such crack asymmetry disappears gradually when both the surface cracks have grown to sizes longer than 12 mm. It can be deduced that the region around the mandrel exit face experiences a greater amount of compressive residual stress, which is responsible for the significant retardation of crack growth compared to that of the mandrel inlet face.

In contrast, it can be seen in Figure 1.5.4(c) that substantial improvements in crack symmetry on both sides of the hole have been achieved using the SW method. Additional fatigue life improvement is also seen in SW holes compared to split-sleeve samples. In

damage tolerance analysis, the simplicity of the symmetric crack geometry should make it possible to develop a stress intensity factor solution accurate enough to incorporate the influence of residual stress in prediction. For that reason, it is anticipated that greater prediction reliability of fatigue life can be achieved in SW holes compared to split-sleeve holes.

1.6 Motivations of Present Research

Considerable cost and resources must be invested in hole cold working associated with airframe production, structural maintenance, inspection and down-time of aircraft. Additionally, conservatism in damage tolerance design inevitably introduces a weight penalty resulting in additional fuel consumption. If the benefits of cold hole working are to be fully utilised, the process reliability of manufacturing metallic joints together with fatigue life prediction methods must be improved. Ideally, the allowance of the damage tolerance analysis to include the cold-working effect in cracked holes would permit lighter structures and optimal structural design to be used.

Amongst the cold-working methods reviewed earlier, SW has shown promising applications that can meet both the stringent process requirements and the production of fatigue-resistant fastener holes in aero-structures. However, while there have been numerous papers published about the mandrel cold-working techniques (especially for the split-sleeve technique), comprehensive knowledge regarding the SW process and its associated damage tolerance analysis is lacking. The associated residual stress field induced by cold-indentation of material is not well-understood. This information is crucial to the optimisation of beneficial residual stresses, and the process parameters such as indenter shape, dimple sizes, material types, thicknesses, and hole sizes need presently to be developed for each new application.

Additionally, the *S-N* curve approach does not allow one to distinguish the degree of contribution of cold-working at different stages of cracking damage occurring at the hole. Nevertheless, for the damage tolerance philosophy currently adopted in aircraft structure safety design, an ability to analyse fatigue crack propagation from initial defects in cold-worked holes is essential [66]. This tool is crucial to provide guidance to the appropriate level of damage detection and inspection procedure conducted for in-service aircraft. The objective must be that effective repair/rework can be carried out in time to restore the strength and fatigue resistance of structure back to optimum design state [66, 67]. In this case, reliable prediction of fatigue crack growth life in SW holes relies very much on accurate knowledge of residual stress field and the proper understanding of interaction mechanism of the residual stress with the fatigue crack.

In response to these requirements, the present work is undertaken to explore the residual stress formation mechanism in the SW process along with the role of its residual stress on the fatigue life enhancement process. This research will use a high strength 2024-T351 aluminium alloy commonly adopted in airframe construction of civil aircraft. A detailed plan of the present work is given in Section 1.7.

1.7 Structure of Thesis

The thesis consists of several chapters that are presented in the following manner:

Chapter 2 provides a literature overview of background knowledge in the context of the research work performed in the succeeding chapters. This includes residual stress and its measurement techniques using diffraction techniques; fracture mechanics and the fatigue behaviour of metallic materials.

Chapter 3 discusses the experimental investigation of residual stress in specimens cold-worked by SW and split-sleeve methods, using non-destructive neutron and laboratory X-ray diffraction measurement. A three-dimensional stress mapping technique was employed to reveal the characteristic of residual stress distribution through the plate thickness in holes treated with the two different methods.

A detailed investigation of an axisymmetric finite element simulation of residual stress development in both cold-working processes is presented in Chapter 4. To achieve reliable outcomes from the numerical work, various conditions in the modelling were considered, such as the elastic-plastic response of the material, tool dimensions, plate supporting constraints and contact definition of surfaces. The accuracy of the numerical work is validated using the experimental data presented in Chapter 3.

Chapter 5 describes the development of a stress intensity factor solution for two symmetric radial cracks originating from the edge of a circular hole. Centred on the Green's function approach and superposition principle, a closed-form model taking account of both the crack tip singularity and hole geometry is derived. Application of the model to a cold-expanded hole is made, and the computed result is validated using weight function and finite element methods.

Based on the concept of linear elastic fracture mechanics, the next two Chapters 6 and 7 are devoted to the theoretical treatment, along with the laboratory fatigue study and fatigue crack growth life prediction, of a SW hole. Chapter 6 concerns the inclusion of the experimentally measured residual stress data into the calculation of the stress intensity factor. Here, finite-width plates containing a centre hole with single crack were studied, and accordingly the Green's function approach of Chapter 5 was extended to construct a stress intensity factor model representative to the crack geometry considered. A systematic

study of the interaction of stress intensity factor due to the residual stress effect and remote loading is also assessed, using both the mean stress and crack closure criteria proposed.

An experimental evaluation of the fatigue durability and the modelling of crack growth life of SW specimens are presented in Chapter 7. Besides the discussion on fatigue testing, a comprehensive investigation to improve the prediction work in line with the experimental observation is also given. This includes parametric studies according to the mean stress and crack closure definitions, and the comparison of different solutions of stress intensity factor on the predictive reliability.

Finally, Chapter 8 provides a summary of conclusions of present work, and suggestions of further research.

1.8 References

1. Fatigue Technology Inc., The Anatomy of Fatigue Enhancement, Materials Testing. 1989, 401 Andover Park East, Seattle, WA 98188-7605 USA.
2. Phillips, J.L. Fatigue improvement by sleeve coldworking. in National Aerospace Engineering & Manufacturing Meeting. 1973. Los Angeles, CA: Society of Automotive Engineers.
3. Lam, Y.C., A comparative study on the effects of interference fit and cold expansion on the fatigue life of cracked holes. Scripta Metallurgica et Materialia, 1993. 28(2): p. 191-195.
4. Leon, A., Benefits of split mandrel coldworking. International Journal of Fatigue, 1998. 20(1): p. 1-8.
5. Maximov, J.T. and Kalchev, G.M., Modelling of spherical mandrelling manufacturing resistance. International Journal of Machine Tools and Manufacture, 2004. 44(1): p. 95-100.
6. Ozdemir, A.T. and Hermann, R., Effect of expansion technique and plate thickness on near-hole residual stresses and fatigue life of cold expanded holes. Journal of Materials Science, 1999. 34(6): p. 1243-1252.

7. Lai, M.O., Nee, A.Y.C., and Oh, J.T., Effect of residual stress on the fatigue performance of the surface of a ballised hole. Journal of Materials Processing Technology, 1992. 29(1-3): p. 301-309.
8. Speakman, E.R., Fatigue life improvement through stress coining methods, in Achievement of High Fatigue Resistance in Metals and Alloys, ASTM Special Technical Publication 467. 1970, American Society for Testing and Materials: Philadelphia, PA. p. 209-227.
9. Rufin, A.C., Extending the fatigue life of aircraft engine components by hole cold expansion technology. Journal of Engineering for Gas Turbines and Power, Transactions of the ASME, 1993. 115(1): p. 165-171.
10. Bozdana, A.T., On the mechanical surface enhancement techniques in aerospace industry – a review of technology. Aircraft Engineering and Aerospace Technology, 2005. 77(4): p. 279-292.
11. Mann, J.Y. and Jost, G.S., Stress fields associated with interference fitted and cold-expanded holes. Metals Forum, 1983. 6: p. 43–53.
12. Champoux, R.L., An Overview of Cold Expansion Methods, in Fatigue Prevention and Design, J.T. Barnby, Editor. 1986, Cameloen Press: London. p. 35-52.
13. Fatigue Technology Inc., World Leaders in Cold Expansion Technology, Commercial pamphlet. 1999.
14. Cathey, W.H. and Grandt, A.F., Fracture Mechanics Consideration of Residual Stresses Introduced by Cold working Fastener Holes. J. Eng. Mats Tech., 1980. 102: p. 85-91.
15. Farahmand, B., Bockrath, G., and Glassco, J., Fatigue & Fracture Mechanics of High Risk Parts: Application of LEFM & FMDM Theory. 1997: Kluwer Academic Publishers.
16. Fatigue Technology Inc., FTI Process Specification 8101C Cold Expansion of Holes Using the Standard Split Sleeve System and Countersink Cold Expansion™ (CsCx™). 1994: 401 Andover Park East, Seattle, WA 98188-7605 USA.
17. West Coast Industries, Expendable Tooling Section, WCI Coldwork Tooling Catalog. 1996, Seattle, Washington.
18. Nadai, A., Chapter 33: Theory of plastic deformation of flat rings or disks, in Theory of Flow and Fracture of Solids. 1950, McGraw-Hill: New York. p. 458–471.
19. Reid, L. and Easterbrook, E. Evaluation of Shear Tears Found at Cold Expanded Holes in 7178-T6 Extrusions - KC-135 Laboratory Teardown Inspection. in 1996 USAF Aircraft Structural Integrity Program Conference. 1996. San Antonio, Texas, USA.

20. Weigel, M.J. and Leon, A. Shear crack issues addressed by split mandrel and automated coldworking. in SAE Aerospace Automated Fastening Conference & Exposition (Aerofast) 1996. 1996. Seattle, Washington: Society of Automotive Engineers.
21. Leon, A. and Weigel, M. Benefits of Split Mandrel Coldworking of Large Fastener Holes. in First International Conference on Fatigue Damage in Structural Materials. 1996. Hyannis, Massachusetts: Engineering Foundation.
22. Leon, A. and Weigel, M. Greater manufacturing efficiency through automated split-mandrel, Paper No. AIAA-1996-5513. in 1st SAE/AIAA World Aviation Congress and Exposition. 1996. Los Angeles, California: Society of Automotive Engineers.
23. Weigel, M.J. and Shaw, R.L., Automated split mandrel coldworking - Toward greater manufacturing efficiency. SAE Transactions Journal of Aerospace, Section 1, 1994. 103: p. 1931-1935.
24. Leon, A. and Hempstead, B. Developments in fastener coldworking in next generation automated production units, SAE Paper No. 1999-01-3441. in SAE Aerospace Automated Fastening Conference & Exposition (Aerofast) 1999. 1999. Nashville, Tennessee.
25. ASM Handbook. Volume 20: Materials Selection and Design, ed. G.E. Dieter and S. Lampman. Vol. 20. 1997, Materials Park, OH: ASM International. 901.
26. ASM Handbook. 10 ed. Volume 8: Mechanical Testing and Evaluation, ed. J. Newby and K. Mills. Vol. 8. 2000, Materials Park, OH: ASM International. 998.
27. Easterbrook, E.T., Flinn, B.D., Meyer, C., and Juhlin, N. The StressWave™ Fatigue life Enhancement Process. in SAE Aerospace Automated Fastening Conference and Exhibition, Proceedings of 2001 Aerospace Congress, Paper No. 2001-01-2578. 2001. Seattle, USA: Society of Automotive Engineers.
28. StressWave Inc., New Technology For Aircraft, Commercial Presentation & Report. 2005.
29. Kulkarni, K.M. and Kalpakjian, S., A study of barrelling as an example of free deformation. ASME Journal of Engineering for Industry, 1969. 91: p. 743-754.
30. Shock Waves for Industrial Applications, ed. L.E. Murr. 1988, New Jersey: Noyes Publications.
31. Leftheris, B.P., Method and apparatus for deforming metal, Patent No. 3,824,824. 1974, Grumman Aerospace Corp. (Bethpage, NY): United States.
32. Kolsky, H., Stress Waves in Solids. 2 ed. 1963: Dover Publications. 213.
33. Blazynski, T.Z., Chapter 16.2: Metal forming, in Mechanical Engineers Reference Book, E. H.Smith, Editor. 1998, Butterworth-Heinemann: Oxford. p. 1248.

34. Leftheris, B.P., Method and apparatus for driving interference-fit fasteners, Patent No. 3,945,109. 1974, Grumman Aerospace Corp. (Bethpage, NY): United States.
35. Leftheris, B.P., Mainhardt, J.H., and Schwenk, W., Method and apparatus for working a hole, Patent No. 4,129,028. 1977, Grumman Aerospace Corp. (Bethpage, NY): United States. p. 7.
36. Easterbrook, E.T., Method and apparatus for producing beneficial stresses around apertures by use of focused stress waves, and improved fatigue life products made by the method, Patent No. 6,230,537. 2001, StressWave Inc, Kent, WA: United States. p. 40.
37. Wong, A.K. and Rajic, N., Improving fatigue life of holes, World Intellectual Property Organisation Publication Number WO 93/09890. 1993: Australia.
38. Graff, K.F., Chapter 5: Waves in infinite media, in Wave Motion in Elastic Solids. 1975, Dover Publications: New York. p. 649.
39. Graff, K.F., Chapter 6: Waves in semi-infinite media, in Wave Motion in Elastic Solids. 1975, Dover Publications: New York. p. 649.
40. Viktorov, I.A., Rayleigh & Lamb Waves: Physical theory and applications (Ultrasonic Technology), translated by W.P. Mason. 1967, New York: Plenum Press. 154.
41. Hopkins, H.G., Dynamic expansion of spherical cavities in metals, in Progress in Solid Mechanics, I. Sneddon and R. Hill, Editors. 1960, North Holland: New York. p. 85–164.
42. Porubov, A.V., Amplification of Nonlinear Strain Waves in Solids. 2003, Singapore: World Scientific Publishing. 228.
43. StressWave Inc, Technical Report AL-07, Fatigue Testing of 7050-T7451 Aluminum (Mar. 1, 2002). 2002: 6644 South 196th Street, Suite T-106, Kent, WA 98032. p. 3.
44. Lesuer, D.R., Experimental Investigationsof Material Models for Ti-6Al-4V Titanium and 2024-T3 Aluminum, Report No. DOT/FAA/AR-00/25. 2000, Lawrence Livermore National Laboratory: Livermore, CA. p. 41.
45. Jupp, J.A. and Price, H.A., Transport aircraft - a challenge for aluminium alloys for the 21st century. The Aeronautical Journal, 1998. 102(N.1014): p. 181-188.
46. Özdemir, A.T., Cook, R., and Edwards., L. Residual stress distributions around cold expanded holes. in Durability and Structural Integrity of Airframes, Proceedings of ICAF '93, (International Committee on Aircraft Fatigue). 1993. Stockholm, Sweden: EMAS, Cradley Heath, West Midlands.
47. JSSG-2006- Joint Service Specification Guide - Aircraft Structures. 1998: US Department of Defence.

48. StressWave Inc., New Technology For Fatigue Enhancement, Commercial pamphlet. 2001.
49. Pavier, M.J., Poussard, C., and Smith, D.J., A finite element simulation of the cold working process for fastener holes. The Journal of Strain Analysis for Engineering Design, 1997. 32(4): p. 287-300.
50. Bernard, M., Bui-Quoc, T., and Burlat, M., Effect of re-coldworking on fatigue life enhancement of a fastener hole. Fatigue & Fracture of Engineering Materials & Structures, 1995. 18(7-8): p. 765-775.
51. de Matos, P.F.P., Moreira, P.M.G.P., Pina, J.C.P., Dias, A.M., and de Castro, P.M.S.T., Residual stress effect on fatigue striation spacing in a cold-worked rivet hole. Theoretical and Applied Fracture Mechanics, 2004. 42(2): p. 139-148.
52. Forgues, S.A., Bernard, M., and Bui-Quoc, T., 3-D axisymmetric numerical analysis and experimental study of the fastener hole cold working process, in Computer Methods & Experimental Measurements for Surface Treatment Effects, M.H. Aliabadi and C.A. Brebbia, Editors. 1993, Computational Mechanics Publications. p. 61–70.
53. Kang, J., Steven Johnson, W., and Clark, D.A., Three-dimensional finite element analysis of the cold expansion of fastener holes in two aluminium alloys. Journal of Engineering Materials & Technology, Transactions of the ASME, 2002. 124(2): p. 140-145.
54. O'Brien, E.W., Beneficial residual stress from the cold expansion of large holes in thick light alloy plate. Journal of Strain Analysis for Engineering Design, 2000. 35(4): p. 261-276.
55. Papanikos, P. and Meguid, S.A., Three-dimensional finite element analysis of cold expansion of adjacent holes. International Journal of Mechanical Sciences, 1998. 40(10): p. 1019-1028.
56. Papanikos, P. and Meguid, S.A., Elasto-plastic finite-element analysis of the cold expansion of adjacent fastener holes. Journal of Materials Processing Technology, 1999. 92-93: p. 424-428.
57. Poussard, C., Pavier, M.J., and Smith, D.J., Analytical and finite element predictions of residual stresses in cold worked fastener holes. Journal of Strain Analysis for Engineering Design, 1995. 30(4): p. 291–304.
58. Zhang, Y., Edwards, L., and Fitzpatrick, M.E. Finite element simulation of hole cold expansion process in EN8 steel plates. in Proceedings of the Sixteenth ABAQUS UK User Group Conference. 2002. Warrington, UK.

59. Ozdemir, A.T. and Edwards, L., Measurement of the three-dimensional residual stress distribution around split-sleeve cold-expanded holes. Journal of Strain Analysis for Engineering Design, 1996. 31(6): p. 413-421.
60. Wang, D.Q. and Edwards, L. Neutron diffraction determination of the complete 3D residual stress distribution surrounding a cold expanded hole. in Proceedings of the 4th European Conference on Residual Stresses (ECRS4). 1998. Cluny en Bourgogne, France: Nancy J de Physique.
61. Stefanescu, D., Experimental study of double cold expansion of holes. The Journal of Strain Analysis for Engineering Design, 2003. 38(4): p. 339-347.
62. Stefanescu, D., Edwards, L., and Fitzpatrick, M.E., Stress intensity factor correction for asymmetric through-thickness fatigue cracks at holes. Int. J. Fatigue, 2003. 25(7): p. 569-576.
63. Ofsthun, M., When fatigue quality enhancers do not enhance fatigue quality. International Journal of Fatigue, 2003. 25(9-11): p. 1223-1228.
64. Lamb, G.J., Jr., A.F.G., and Easterbrook, E.T. Fatigue Performance of an Advanced Hole Cold Working Method. in 2001 USAF Aircraft Structural Integrity Program Conference. 2001. Williamsburg, VA.
65. Lamb, G.J., Fatigue Performance of an Advanced Fastener Hole Cold Working Method, M.Sc Thesis, in School of Aeronautics and Astronautics. 2002, Purdue University: West Lafayette, Indiana, USA.
66. Wang, Z. and Zhang, X., Predicting fatigue crack growth life for cold-worked holes based on existing closed-form residual stress models. International Journal of Fatigue, 2003. 25(9-11): p. 1285-1291.
67. Reid, L., Incorporating Hole Cold Expansion to Meet Durability and Damage Tolerance Airworthiness Objectives, SAE Paper No. 972624. SAE Transactions Journal of Aerospace, Section 1, 1997. 106: p. 1242-1249.

CHAPTER 2: RESIDUAL STRESS, FRACTURE MECHANICS AND FATIGUE OF MATERIALS

This chapter describes the background knowledge specifically required for the research work in the subsequent chapters. The topics covered include residual stress; non-destructive measurement and analysis of residual stress using X-ray and neutron diffraction; fracture mechanics and fatigue behaviour of cracked solids under loading.

2.1 Introduction

This chapter is divided into several topics, and the outline is arranged as follows. Section 2.2 discusses the classifications and origins of residual stresses in materials and their role in fatigue crack damage based on a length-scale viewpoint. Next, the elastic theory of solids related to crystallographic strain/stress measurement is briefly presented in Section 2.3. Then the idea of non-destructive stress measurement in materials using the X-ray and neutron diffraction techniques, together with their respective analysis methodologies, is explored separately in Sections 2.4 and 2.5. This is followed by a discussion of the principles of fracture mechanics in solids containing defects or cracks in Section 2.6. Finally, in Section 2.7 several aspects of fatigue crack formation and growth, along with fatigue life prediction in cracked components, are presented.

2.2 Residual Stress

2.2.1 Types and origins

Residual stresses are self-equilibrating stresses within a stationary solid body in the absence of externally applied forces. Residual stresses arise due to shape misfits or incompatibilities, occasionally termed 'eigenstrains', between the unstressed shapes of different parts, regions or phases of the material; their magnitude and origin depends on the

length-scale perspective of the investigation, as shown in Figure 2.2.1 [1-3]. Accordingly, residual stresses are conveniently divided into three classes as a function of the geometrical scale over which they vary and are self-equilibrated: Type I, II, and III stresses.

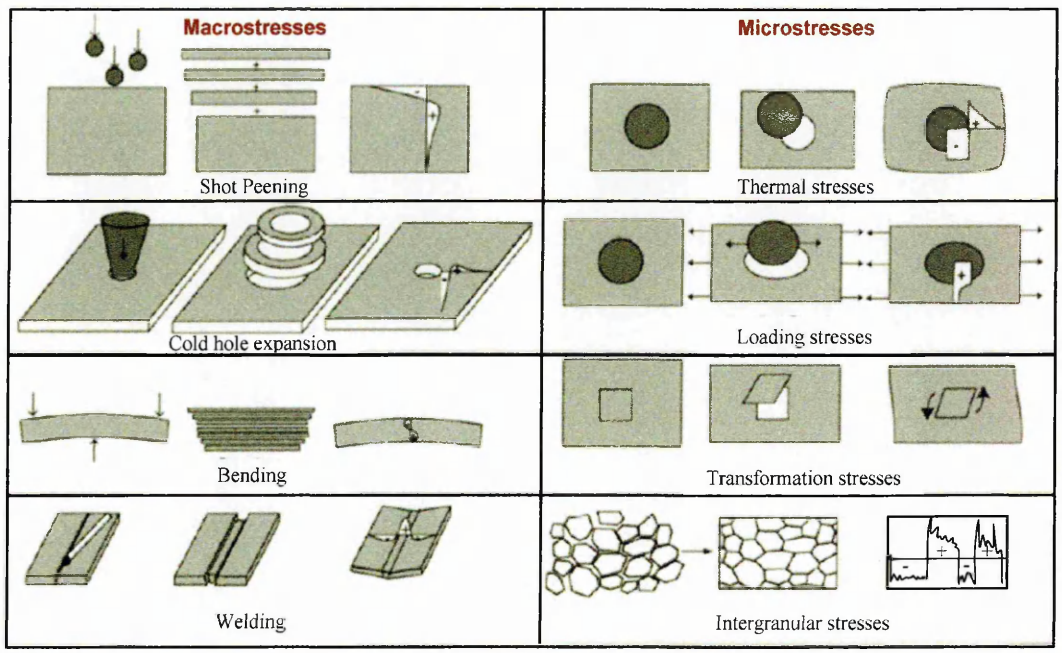

Figure 2.2.1 Residual stresses arise from misfits, either between different regions of a material or between different phases within the material. Examples of different types of residual macro- and micro-residual stress are illustrated schematically. In each case, the process is indicated on the left, the misfit in the centre, and resulting stress pattern on the right [1].

Type I residual stresses, also known as macrostresses, are homogeneous over many crystal domains in a material i.e. at the macroscopic scale of the structure. The internal forces and moments associated with macrostresses are equilibrated and balanced in all planes and axes of the volume. Typically, macrostresses present in materials are generally caused by non-uniform plastic deformation or thermal gradients.

Conversely, Type II and III residual stress, collectively defined as microstresses, act at microscopic and sub-microscopic levels. Type II residual stresses are homogeneous within a small crystal or intergranular scale of the material (a distinct grain or phase), typically 3~10 × grain size. A low level of type II residual stresses always exists in polycrystalline materials because the elastic and thermal properties of surrounding grains at different orientations are dissimilar. More substantial grain-scale stresses arise if the microstructure

consists of several distinct phases or if phase transformations occur. The internal forces associated with type II stresses are balanced between dissimilar grains or phases.

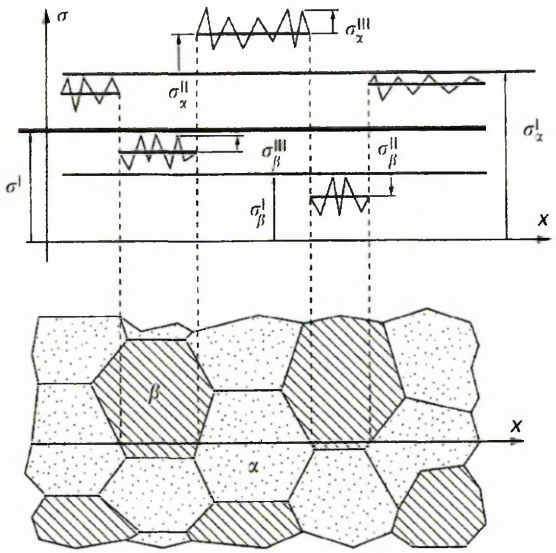

Figure 2.2.2 Three orders of residual stresses in multi-phase or composite materials. σ_α and σ_β are the stresses in phases α and β [4].

Type III residual stresses are homogeneous on the smallest crystal domain, over a few inter-atomic lengths, and consequently the internal forces coupled to type III stresses are equilibrated at subatomic domains (smaller than a grain size). Type III residual stresses are typically related to defects in crystals e.g. coherency at interfaces, dislocations, interstitials and vacancies. In Figure 2.2.2, the actual state of residual stress at a particular location inside the material may be determined from the superposition of 1st, 2nd and 3rd order stresses. Figure 2.2.2 also reveals the variation of type I, II and III residual stresses within the microstructure of multi-phase or composite materials as perceived at different order of length scales.

2.2.2 Residual stresses in engineering materials

Mechanical	Thermal	Chemical	Combination
Practically, cold working processes induce non-uniform plasticity flow in materials. 1. Surface working: • Surface rolling • Polishing • Cold expansion • Shot peening • Roller burnishing • Laser shocking • Autofrettage 2. Drawing 3. Rolling 4. Grinding & machining 5. Forming	Arising from thermal gradient alone or coupled with phase transformation. 1. Thermal gradient • Quenching • Casting • Welding 2. with phase transformation • Quenching of direct hardening or carburizing steels • Surface/induction hardening • Laser- heat treatment	Causing spalling, warping or dimensional stability of materials. 1. Oxidation 2. Corrosion 3. Electroplating 4. Deposition 5. Anodizing	The residual stresses developed might not be readily interpretable due to combined effects. 1. Abusive grinding 2. Non-thermal-induced transformation 3. Assemblies using weldments and castings 4. Flame cutting 5. Rapid cooling of cold drawn material

Table 2.2.1 Sources and categories of residual stresses generated in materials [5, 6].

Residual stresses may develop in any stage of a manufacturing process or in-service history that introduces permanent inhomogeneous deformation into materials; this is commonly as a result of mechanical, thermal or chemical mechanism, or combined mechanisms (Table 2.2.1) [5, 6]. The suitable application and continuous assessment of the knowledge and technology of residual stresses is of paramount importance to the static and fatigue performance of materials. Generally, compressive residual stress near the surface can inhibit crack formation or prolong the period for crack initiation and growth, and hence is beneficial to fatigue life and stress corrosion. In contrast, tensile residual stresses at the surface layer tend to increase the total load experienced and hence are detrimental to the fatigue behaviour of the materials [6].

2.2.3 Residual stresses in multi-scale fatigue damage

The requisite detailed knowledge of type I, II and III residual stress as to be incorporated in engineering design depends primarily on the degree of influence or dominance of such stresses on the functions of the components. Type II and III stresses are usually considered in particle reinforced materials such as metal matrix composites (MMC). The Type II stresses from thermal mismatch associated with reinforcing particles and Type III stresses due to local dislocation density associated with plasticity in crack growth affect the stiffness, yield strength, fracture toughness and fatigue crack growth behaviour of MMCs [7, 8]. Microstresses are also increasingly receiving attention as they initiate damage in materials, e.g. type II stresses responsible for crack branching or bridging, microcracking, subcritical crack growth and stress-induced phase transformation, whereas type III stresses have decisive roles in hardness and tribology behaviour [9-11]. Vasudevan and Sadananda [12] summarised some sources of internal (residual) stresses affecting the conditions of fatigue crack damage developed at diverse length scales in materials, as shown in Figure 2.2.3. The applied stresses acting on a macro/microscopic crack would interact with the local residual stress gradient to result in propagation, retardation or arrest of crack growth.

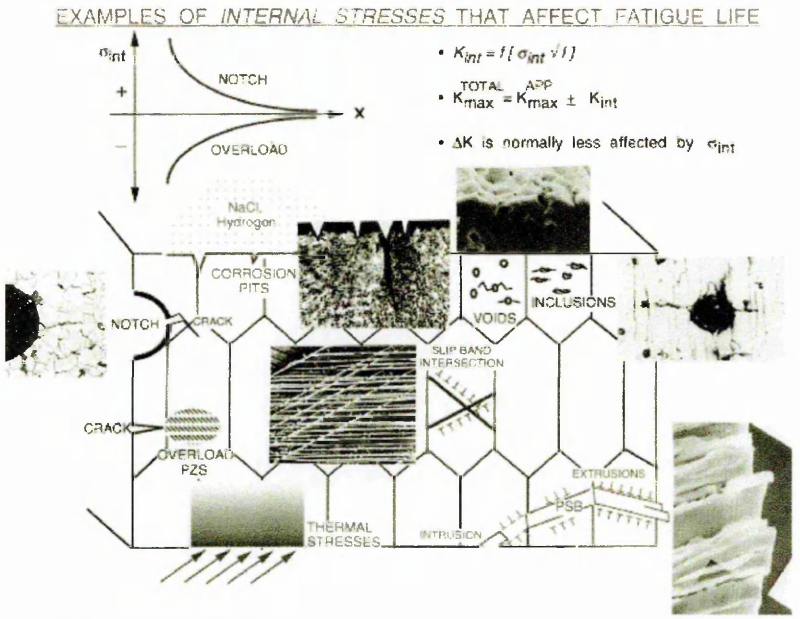

Figure 2.2.3 Examples of various types of internal stresses that affect K_{max} [12].

The present work requires only 1st order macrostress to be investigated as the large domain of residual stress imparted by the cold working process around the hole in Al 2024-T351 is produced by bulk plastic deformation. In line with the principles of continuum fracture mechanics and from the point of view of damage tolerant assessment, it is the Type I stresses that ultimately affect the entire mechanical response of an aluminium alloy structure, rather than the microstresses inside the individual crystalline grains. Furthermore, previous laboratory and theoretical investigations have inferred that only the long-range stresses have a noticeable effect on the crack driving force, K in metallic materials [12, 13]. Moreover, the type II and III stresses are more susceptible to attenuation by continuous cyclic plasticity in the crack tip zone when compared to type I stresses [2, 14, 15].

2.3 Elasticity Theory of Solids

2.3.1 Introduction to stress & strain tensors

In an anisotropic system, the stress $\underline{\underline{\sigma}}$ and strain $\underline{\underline{\varepsilon}}$ are 2nd rank tensors unified to one another by the elastic stiffness (i.e. modulus) tensor $\underline{\underline{C}}$, and the elastic compliance (i.e. constant) tensor $\underline{\underline{S}}$ [16]:

$$\varepsilon_{ij} = S_{ijkl}\sigma_{ijkl} \quad \text{or} \quad \sigma_{ij} = C_{ijkl}\varepsilon_{ijkl} \tag{2.3.1}$$

where $\underline{\underline{S}} = \underline{\underline{C}}^{-1}$, C_{ijkl} are the elastic stiffnesses relating the stresses in the *ij*-direction to the strain in the *kl*-direction, and S_{ijkl} are the compliances relating the strains in the *ij*-direction to the stresses in the *kl*-direction. $\underline{\underline{\sigma}}$ and $\underline{\underline{\varepsilon}}$ have 3×3 components, 6 of which are independent. $\underline{\underline{C}}$ and $\underline{\underline{S}}$ consist of 3 × 3 × 3 × 3 components; depending on the concurrent loading state of the component, as many as 36 members in $\underline{\underline{C}}$ and $\underline{\underline{S}}$ can be independent. An energy approach of a strained crystal may further trim down the number of independent stiffness constants and compliance from 36 to 21. The presence of symmetry in crystal reduces still further the number of independent s_{ij} and c_{ij} [16, 17]. For a cubic monocrystal, only three independent constants are necessary to describe its elastic behaviour [18].

2.3.2 Generalised Hooke's law in an isotropic continuum

Equation (2.3.1) implies that the conversion of the measured strain components to stress is inherently a complex task because it involves the practicality of measuring the strain at a point in various directions, the need to consider texture problems, the difficulty of separating macro-stress and inter-granular stress effects from the measured lattice strain, and elastic and plastic anisotropy effects in crystals [1].

Nonetheless, for simplicity most engineering measurements rely on isotropic continuum mechanics. Subsequently, the elastic stiffness tensor $\underline{\underline{C}}$ can be represented in terms of just two independent elastic components, e.g. Young's modulus, *E*, and Poisson's ratio, *v*. Subsequently, the generalized Hooke's law for isotropic materials is given by

$$\varepsilon_{ij} = \frac{1+\nu}{E}\sigma_{ij} - \delta_{ij}\frac{\nu}{E}\sigma_{kk} \qquad \text{or} \qquad \sigma_{ij} = \frac{E}{1+\nu}\varepsilon_{ij} + \delta_{ij}\frac{\nu E}{(1+\nu)(1-2\nu)}\varepsilon_{kk} \tag{2.3.2}$$

where $i, j = 1, 2, 3$ denote the components relative to chosen axes; k is the dummy suffix summing over all k (i.e. $\varepsilon_{kk} = \varepsilon_{11} + \varepsilon_{22} + \varepsilon_{33}$); δ is Kronecker's delta function:

$$\delta_{ij} = \begin{cases} 1, \textit{for } i = j \\ 0, \textit{for } i \neq j \end{cases}.$$

2.4 X-Ray Diffraction

2.4.1 Introduction

X-ray diffraction is a non-destructive method extensively used in the automotive and aerospace industries for rapid quantification of the surface residual stress field induced by numerous treatments e.g. cold-working, shot peening, grinding, carburizing, etc. The technique simply relies on the fact that values of the d-spacing of the atomic planes of crystalline materials are altered by the internal intend stresses. Hence, by measuring the strain given by the change of d-spacing via the angular position 2θ of a diffracted X-ray beam, the stress state can be subsequently deduced [5, 19-21].

2.4.2 X-Ray Diffraction in crystalline materials

The photons of an incident X-ray beam collide with the atomic fundamental particles, i.e. electrons and nuclei, in the crystal structures and scatter in every direction. Most collisions occur with the electron clouds shielding the nuclei. The collisions with electrons can be elastic or inelastic depending on the momentum transfer between the colliding photons and electrons. In elastic collisions, there is no momentum transfer and the scattered X-ray photons are coherent with the incident beam; in inelastic collisions the scattered X-ray beam is incoherently radiated due to the momentum lost by the incident photons.

For any given lattice spacing between crystal planes, d, and wavelength of incident X-ray beam, λ, the periodic orientation of atomic planes can give rise to constructive, or destructive, interference of the coherent component of the reflected radiation from the individual atoms. The magnitude of the X-ray's wavelength is typically of the same order as atomic separations in

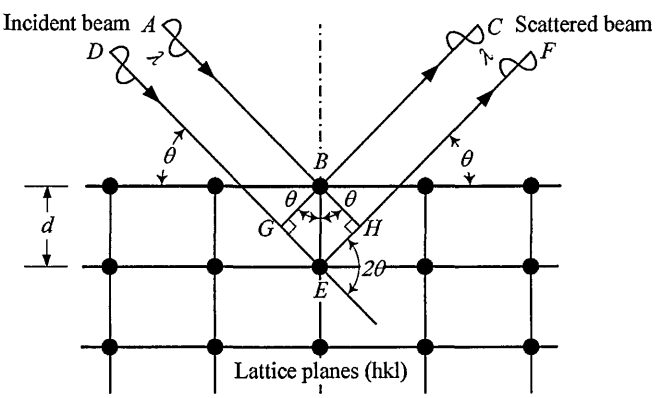

Figure 2.4.1 Reflection of an X-ray or neutron ray at the lattice planes of crystalline materials. *ABC* and *DEF* will be in phase and mutually reinforce if the path difference *GEH* is an integral multiple, n, of radiation wavelength, λ.[1, 21]

a crystal. For a particular family of crystallographic planes $\{hkl\}$, constructive interference promotes mutual reinforcement of the coherent scattered beam to produce substantial diffracted intensity, which occurrence is governed by the Bragg's Law (Figure 2.4.1):

$$2d_{hkl}\sin\theta_{hkl} = n\lambda_{hkl} \tag{2.4.1}$$

where d_{hkl} is the atomic distance between lattice planes; θ_{hkl} is the angle between the incident beam and diffracting planes$\{hkl\}$; λ is the X-ray wavelength and n is an integer.

2.4.3 Strain calculation in X-ray diffraction

For any deformed polycrystalline solid, the locally induced stress introduces an equivalent change in d-spacing, as manifested by Bragg's angle shifting to a new position, θ. From Bragg's law, this change in inter-planar spacing (d- d_o), relative to its un-deformed condition d_o, may be resolved into strain:

$$\varepsilon = (d - d_o)/d_o = \Delta d/d_o \tag{2.4.2}$$

Otherwise, the strain may also be calculated by a shift in the scattering angle (θ - θ_o) in relation to its initial state θ_o. For a given monochromatic beam of wavelength λ, differentiating Bragg's law (2.4.1) with respect to its reference states d_o and θ_o of the unstressed material gives:

$$\begin{aligned} &2d_o\cos\theta_o\Delta\theta + 2\sin\theta_o\ \Delta d = 0 \\ &\therefore \varepsilon = \Delta d/d_o = -\Delta\theta\cdot\cot\theta_o \end{aligned} \tag{2.4.3}$$

Now, for determining surface strain $\varepsilon_{\phi\psi}$ acting in a particular direction, an orthogonal coordinate system must be used to relate the specimen surface, $\underline{S}_i$ and laboratory (X-ray) $\underline{L}_i$ systems (Figure 2.4.2). In theory, strain measurement using X-Ray scattering involves several measurements of the inter-planar spacing $d_{\phi\psi}$ of a crystallographic planes $\{hkl\}$ at several orientations $S_{\phi\psi}$ to the normal of the specimen surface. This is accomplished by tilting (ψ) and rotating (ϕ) the specimen with respect to the incident beam. By fixing $\underline{S}_1$, $\underline{S}_2$

and $\underline{L_2}$ on the sample surface, the orientations $S_{\phi\psi}$ are defined by the angular coordinate ψ and ϕ. $\underline{L_3}$ is normal to the family of planes (*hkl*) whose *d*-spacing or strain is measured.

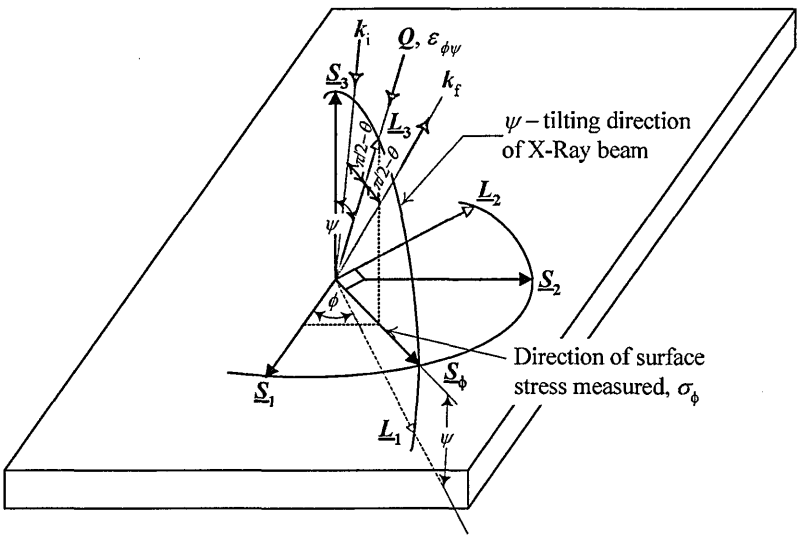

Figure 2.4.2 Definition of the sample *S* and laboratory *L* coordinate systems [1, 21].

$\underline{S_i}$: Specimen surface system

$\underline{L_i}$: Laboratory system

i : 1, 2 or 3

k_i : vector of incident X-ray

k_f : vector of diffracted X-ray

Q : scattering vector / strain

For a given $d_{\phi\psi}$–spacing, the strain along $\underline{L_3}$ is expressed by

$$\varepsilon_{\phi\psi} = \left(d_{\phi\psi} - d_o\right)/d_o \tag{2.4.4}$$

The arrangement in Figure 2.4.2 allows us to specify $\varepsilon_{\phi\psi}$ along the direction of scattering vector $\boldsymbol{Q}$ parallel to $\underline{L_3}$ as a function of strain components, ε_{ij} in the sample coordinate system. Using the direction cosines between the orthogonal sample coordinate, $\underline{S_i}$ and the laboratory coordinate, $\underline{L_i}$ systems [22], and defining $\underline{L_3} \equiv S_{\phi\psi}$, $\varepsilon_{\phi\psi}$ can be expressed as the strain ε_{ij} in the sample coordinate system, via the tensor transformation [1, 16, 21].

$$\begin{aligned}\varepsilon_{\phi\psi} = {} & \varepsilon_{11}\cos^2\phi\sin^2\psi + \varepsilon_{12}\sin 2\phi\sin^2\psi \\ & + \varepsilon_{22}\sin^2\phi\sin^2\psi + \varepsilon_{33}\cos^2\psi \\ & + \varepsilon_{13}\cos\phi\sin 2\psi + \varepsilon_{23}\sin\phi\sin 2\psi\end{aligned} \tag{2.4.5}$$

This basic strain equation for X-Ray diffraction in essence is a function of six unknown strains. ε_{ij} and hence $\varepsilon_{\phi\psi}$ can be computed provided the $d_{\phi\psi}$ along the six independent orientations $S_{\phi\psi}$ is measured for a fixed ϕ corresponding to the intended surface stress vector σ_ϕ. Equation (2.4.5) also exhibits three basic characteristics of $d_{\phi\psi}$ versus $\sin^2\psi$ plots normally encountered in X-Ray strain measurement (Figure 2.4.3) [5, 21]:

– In principal strain directions, $\varepsilon_{13} = \varepsilon_{23} = 0$ which gives rise to a linear curve (Figure 2.4.3(a)).

– The presence of out-of-plane shear components, $\varepsilon_{13} \neq 0$ and/or $\varepsilon_{23} \neq 0$ may give rise to two straight or nonlinear branches called 'ψ–splitting' (Figure 2.4.3(b)). Such split is due to the term '$\sin^2\psi$' associated with positive and negative ψ. A nonlinear concave/convex curved plot is usually due to substantial stress gradient through the depth of penetration of the X-rays in the surface. The ψ–splitting may also be the result of a misaligned diffractometer or an artefact of the peak fitting procedure.

– An oscillatory $d_{\phi\psi}$ versus $\sin^2\psi$ plot (Figure 2.4.3(c)) normally indicates that the material has a preferred crystallographic orientation (texture), i.e. variation of $E/(1+\nu)$ with ψ ,or sometimes a large grain size that dominates particular diffracting planes; in this case, $\varepsilon_{\phi\psi}$ cannot be derived by (2.4.5) without further mathematical treatments.

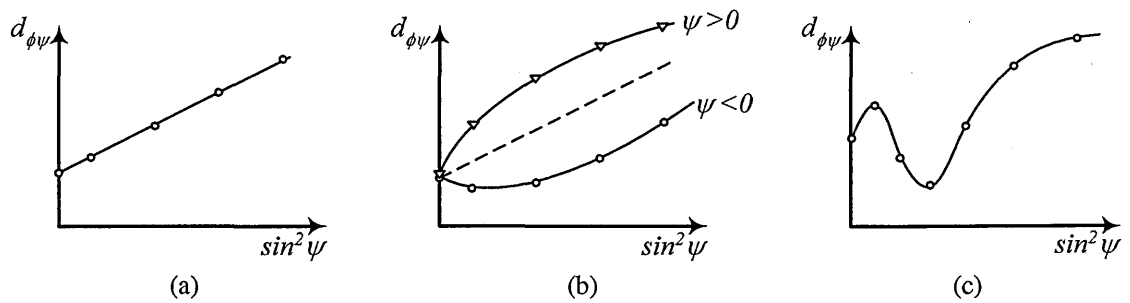

Figure 2.4.3 Types of $d_{\phi\psi}$ versus $\sin^2\psi$ plots commonly encountered in residual stress analysis of polycrystalline materials: (a) regular linear; (b) regular 'ψ–split'; (c) oscillatory [21].

2.4.4 Stress calculation in X-ray diffraction

Using the strain equation (2.4.5), the stress may be subsequently deduced according to the anticipated strain/stress state and mechanical behaviour of the material at the irradiated location. In the present work, for simplicity we assume that Al 2024-T351 alloy has the following properties: (1) macroscopically isotropic i.e. a polycrystalline material consisting of fine grains without texture; (2) linear elastic stress-strain response; (3) homogeneous state of stress/strain in the irradiated volume. Based on these conditions, the following paragraphs show how the stress may be calculated from X-ray surface measurements.

Triaxial Stress State: Employing the generalised Hooke's Law (2.3.2) into (2.4.5), the triaxial stress equation reads

$$\varepsilon_{\phi\psi} = \left(\frac{d_{\phi\psi} - d_o}{d_o}\right) = \frac{1+\nu}{E}\left(\sigma_{11}\cos^2\phi + \sigma_{12}\sin 2\phi + \sigma_{22}\sin^2\phi - \sigma_{33}\right)\sin^2\psi + \frac{1+\nu}{E}\sigma_{11} - \frac{\nu}{E}\left(\sigma_{11}+\sigma_{22}+\sigma_{33}\right) + \frac{1+\nu}{E}\left(\sigma_{13}\cos\phi + \sigma_{23}\sin\phi\right)\sin 2\psi \tag{2.4.6}$$

The presence of out-of-plane shear stress σ_{13} and σ_{23} in the measured layer will produce ψ–splitting in $d_{\phi\psi}$ versus $\sin^2\psi$ plots. Two auxiliary terms, a_1 and a_2 can be defined independently to solve the triaxial equation (2.4.6), as shown by Dolle and Hauk [1, 21]:

$$\text{Linear: } a_1 = \left[\frac{d_{\phi\psi+} + d_{\phi\psi-}}{2d_o} - 1\right] = \begin{cases} \dfrac{1+\nu}{E}\left(\sigma_{11}\cos^2\phi + \sigma_{12}\sin 2\phi + \sigma_{22}\sin^2\phi - \sigma_{33}\right)\sin^2\psi \\ + \dfrac{1+\nu}{E}\sigma_{11} - \dfrac{\nu}{E}\left(\sigma_{11}+\sigma_{22}+\sigma_{33}\right) \end{cases} \tag{2.4.7a}$$

$$\text{Nonlinear: } a_2 = \left[\frac{d_{\phi\psi+} + d_{\phi\psi-}}{2d_o}\right] = \frac{1+\nu}{E}\left(\sigma_{13}\cos\phi + \sigma_{23}\sin\phi\right)\sin|2\psi| \tag{2.4.7b}$$

For the linear term a_1, by fixing ϕ = 0°, 45°, 90° for varying ψ tilt, the stresses σ_{11}, σ_{12}, σ_{22} and σ_{33} are computed from the gradient and intercept of a_1 versus $\sin^2\psi$ plot. Whereas, the shear stresses σ_{13}, σ_{23} in the nonlinear term are resolved from the slope of a_2 versus $\sin^2\psi$ plot at ϕ = 0°, 90°. Solving the stress tensor in the sample system $\underline{\boldsymbol{S}}_i$, the stress tensor in other reference system, e.g. principal stresses and their directions, can be determined.

Biaxial Stress State: In most applications, since the penetration depth of laboratory X-rays is low i.e. only a few μm below the surface, the condition of biaxial plane stress is assumed to prevail within this thin surface layer. Consequently, the normal and out-of-plane shear components of stresses $\sigma_{33} = \sigma_{13} = \sigma_{23} = 0$ and (2.4.5) can be simplified to:

$$\varepsilon_{\phi\psi} = \left(\frac{d_{\phi\psi} - d_o}{d_o}\right) = \frac{1+\nu}{E}\sigma_\phi \sin^2\psi - \frac{\nu}{E}\left(\sigma_{11}+\sigma_{22}\right) \tag{2.4.8}$$

and the term of the measured stress σ_ϕ becomes:

$$\sigma_\phi = \sigma_{11}\cos^2\phi + \sigma_{12}\sin 2\phi + \sigma_{22}\sin^2\phi \tag{2.4.9a}$$

If the in-plane shear stress is assumed to be absent i.e. $\sigma_{12} = 0$,

$$\sigma_\phi = \sigma_{11}\cos^2\phi + \sigma_{22}\sin^2\phi \tag{2.4.9b}$$

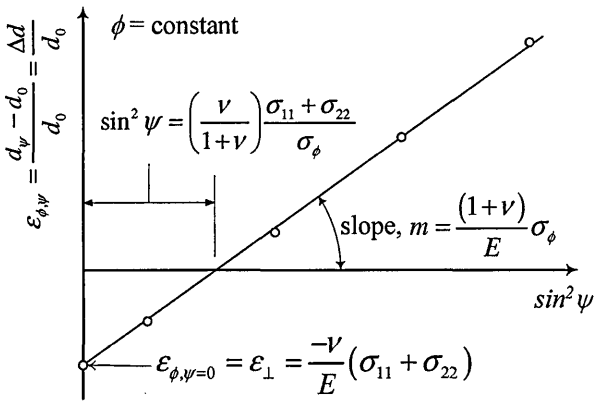

Figure 2.4.4 Illustration of a multi-angle or $\sin^2\psi$ technique for X-Ray surface stress determination. The curve is obtained directly from a least square line fitted to experimental data at several ψ. [5]

Expression (2.4.8) relates the directional strain $\varepsilon_{\phi\psi}$ or spatial lattice parameter $d_{\phi\psi}$ to the surface principal stresses σ_{11}, σ_{22} on the irradiated plane, and is a linear function of $d_{\phi\psi}$ versus $\sin^2\psi$ (Figure 2.4.4). In the present study, this technique has been entirely used to measure the surface residual stress around cold-worked holes.

Differentiation of (2.4.8) leads us to the gradient of the $d_{\phi\psi}$ versus $\sin^2\psi$ plot in Figure 2.4.4

$$m = \frac{d\left(\varepsilon_{\phi\psi}\right)}{d\sin^2\psi} = \frac{(1+\nu)}{E}\sigma_\phi \tag{2.4.10}$$

Given the elastic constants E and ν, the measured stress, σ_ϕ can be calculated as

$$\sigma_\phi = m\cdot\left(\frac{E}{1+\nu}\right) \tag{2.4.11}$$

From (2.4.9a) and (2.4.10), it is also clear that the stresses σ_{11} and σ_{22}, can be measured separately at $\phi = 0°$ and 90°. At the intercept, when $\psi = 0°$ i.e. the direction normal to the specimen surface and equation (2.4.8) becomes:

$$\varepsilon_{\phi,\psi=0} = \varepsilon_\perp = \frac{d_{\phi,\psi=0} - d_0}{d_0} = \frac{-\nu}{E}(\sigma_{11}+\sigma_{22}) \tag{2.4.12}$$

The analysis of triaxial or biaxial stress requires (1) stress-free lattice spacing, d_o, (2) elastic constants E and ν. In biaxial cases, the magnitude of Young's modulus, $E \gg \nu(\sigma_{11} + \sigma_{22})$ and consequently we can adopt $d_{\phi,\psi=0} \approx d_o$. The total error arising from this $d_{\phi,\psi=0}$ substitution is less than 0.1% in the final stress value, which is negligible compared to other sources of measurement errors [5, 21].

2.4.5 Selection of diffracting angle in X-ray stress measurement

The value of shift in d-spacing in strained material is typically given to the 3rd decimal places. Generally the diffraction peaks at higher 2θ are favoured as it gives rise to a larger

peak shift $\Delta\theta$ for a given strain, and hence is more sensitive to measure strain/stress. Referring to the strain equation (2.4.3),

$$\Delta\theta = -\varepsilon \tan\theta_o \tag{2.4.12}$$

For the same strain measured, an increase in tan θ_o for higher 2θ corresponds to noticeable changes in $\Delta\theta$. Nonetheless, it is equally important to consider the relative intensity of various diffracting peaks for satisfactory fitting of a diffraction profile [19, 21].

2.5 Neutron Diffraction

2.5.1 Introduction

The underlying principles of strain scanning by neutron and X-ray diffraction are identical. However, neutrons can penetrate into and diffract from the materials at longer depths making this technique suitable for internal strain measurement, and is normally deemed as an complement to the X-Ray method [17, 18, 20, 21]. Strain measurements in transmission and reflection can be performed for any component by positioning the corresponding direction in the sample along the bisector of the incident and scattered beams.

2.5.2 Fundamental properties of neutrons

Neutrons ($m_n \approx 1.675\times10^{-27}$ kg) are neutral subatomic particles having about the same mass as protons ($m_p \approx 1.673\times10^{-27}$ kg). The diffraction of neutrons from materials is attributed to their collision with nuclei rather than electron clouds. The neutron scattering power of an atom is weakly connected to its atomic number or number of protons, Z, unlike the X-ray and electron scattering. The fact that the neutron is chargeless leads to much lower true absorption and higher penetration than for X-rays that have strong interaction with electrons [23]. By wave-particle duality, neutrons with different energies levels E, and hence different wavelengths λ, travel at different velocities v, as described by the de Broglie's expression [1]:

$$\lambda = h/(m_n v) \tag{2.5.1}$$

where h is Planck's constant. Neutrons produced by fission reaction or spallation are not immediately suitable for strain measurement because of their high energy (normally 2~3 MeV in a fission source and 3~4 MeV for a pulsed source) associated with short wavelengths at a very high velocity [1]. For neutron scattering experiments, these energetic neutrons must be moderated by passing them through a moderator e.g. heavy water, liquid methane or graphite. Upon multiple collisions with the light atoms of the moderator, the neutrons lose energy and consequently they achieve thermal equilibrium with the moderator. The kinetic energy of the thermalised neutrons is [21, 24, 25]

$$E = \frac{1}{2} m_n v^2 = \frac{3}{2} kT_m \tag{2.5.2}$$

where k is Boltzmann's constant and T_m is the moderator temperature. From (2.5.1–2), the root-mean square wavelength of a moderated neutron beam may be predicted [23]:

$$\lambda_{rms} = \frac{h}{\sqrt{3m_n kT_m}} \tag{2.5.3}$$

The wavelength of thermal neutrons (E~10 to100meV) is comparable to the atomic d-spacing appropriate for diffraction studies of crystalline solids. For $T_m \approx 600°K$, the moderated neutrons possess energy of a few milli-electron volts (me$V$) and wavelength of around 1Å [21]. For typical stress measurement, the wavelength of neutrons used is about 1~3Å for diffraction studies using various (hkl) reflection planes in materials [1, 18].

2.5.3 Neutron sources

At present, intense neutrons beams suitable for stress/strain measurement can be principally produced from two distinct sources, namely the steady-state nuclear reactor source and the accelerator-based spallation source.

Reactor sources: For neutron research, the nuclear fission of heavy atoms of U^{235} located in a nuclear reactor produces continuous high-flux neutrons, or the order of 10^{14}~$10^{15}cm^{-2}s^{-1}$ [1]. This creates an average of 2.5 neutrons per fission with 180 MeV energy released in

the production of thermal neutrons suitable for stress/strain measurement [18]. These moderated neutrons are then guided to the strain-measuring instruments, and neutron transportation is accomplished inside borated glass tubes with Ni or Ni-C and Ti coatings on the internal wall (Figure 2.5.1).

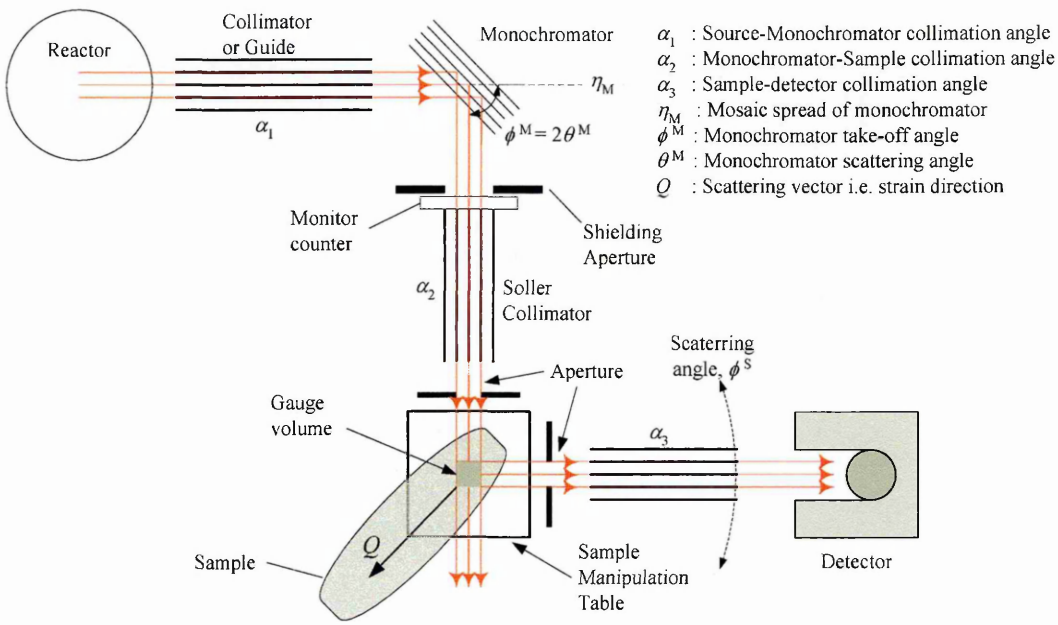

Figure 2.5.1 Schematic layout of a standard two-axis instrument for strain measurement on a reactor neutron source [1].

A white neutron beam can be monochromatized by Bragg diffraction from a single crystal monochromator, which selectively scatters the neutrons to produce the constant wavelength λ required for an experiment. A wide range of constant wavelengths can be produced by adjusting the monochromator take-off angle ϕ^M_{hkl}. Single crystals are rarely prefect because they tend to have sub-grains, each having slightly different orientation; the spread of these orientations is termed the mosaic spread. The mosaic spread of a monochromator along with the angular spread of incident beam governs the producible range of wavelengths. In Figure 2.5.1, the polychromatic/white beam transported from the neutron source (i.e. moderator) is narrowed down by Soller slits with divergence α_1 before being diffracted by the crystal monochromator. According to Bragg's law, the wavelength of the reflected neutron beams λ is governed by the interplanar spacing d_{hkl} and the take-off angle $\phi^M_{hkl} = 2\theta^M_{hkl}$ of the monochromator. The monochromatized neutron beam travels

through another Soller collimator at angle α_2, then penetrates and is diffracted by the sample according to Bragg's law; the beam diffracted by the gauge volume inside the sample subsequently arrives at the detector through a third collimator at angle α_3 [17].

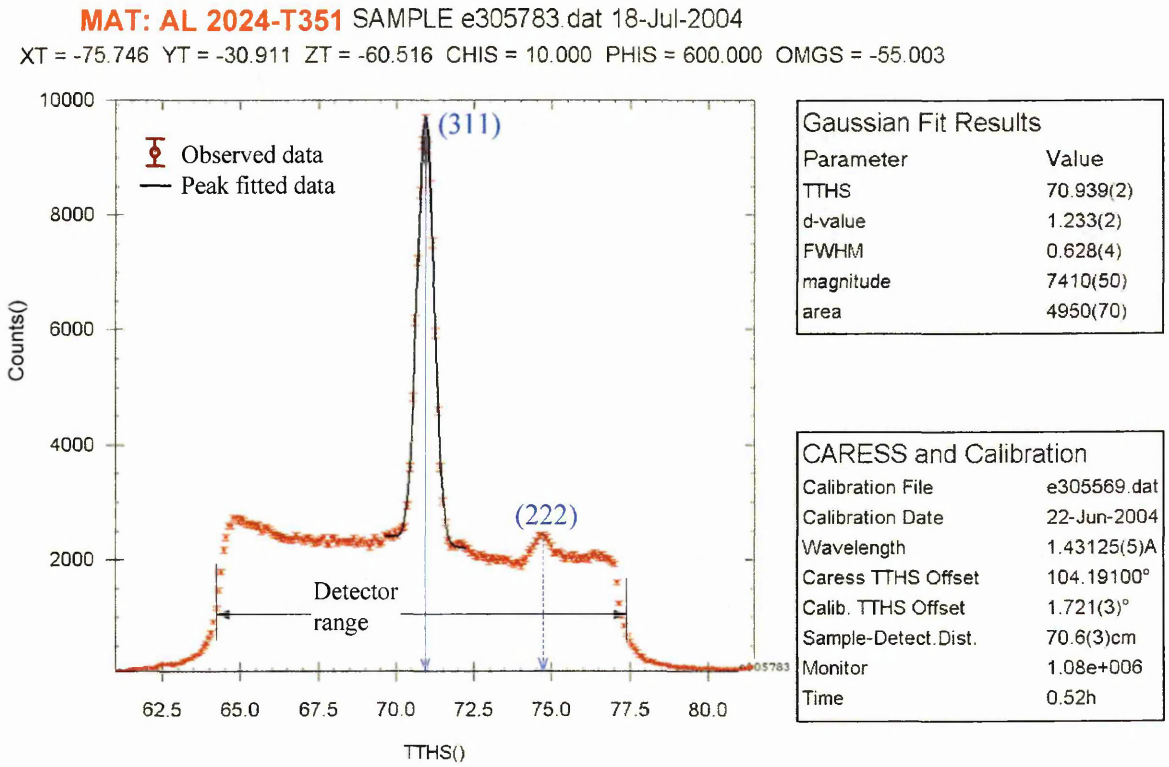

Figure 2.5.2 A diffraction profile of 2024-T351 aluminium alloy collected on reactor source E3-neutron diffractometer at Berlin Neutron Scattering Centre (BENSC), Hanh-Meitner Institute.

The specimen is mounted on an *X-Y-Z-ω* translation table permitting very accurate sample positioning during measurement. The slits placed on the incident and diffracted beam define the gauge volume inside the sample. A typical monochromatic diffraction profile from Al 2024-T351 alloy plate is presented in Figure 2.5.2.

Spallation sources: Unlike the monochromatic beam in fission sources, spallation facilities employ a white neutron beam composed of a range of wavelengths. The use of a white beam allows diffraction data to be collected fairly quickly by the concurrent detection of multiple diffraction peaks from different families of (*hkl*) reflection in the same spectrum. Spallation and fission sources differ in several aspects, e.g. spallation produces neutrons about 10 times greater by fission; whereas the heat generated by spallation is only a fraction of the energy liberated by fission for the same amount of neutrons produced. A

white neutron beam is typically produced by bombarding high energy particles from a powerful accelerator on a heavy metal target. The majority of neutron experiments reported in this thesis were performed at the ISIS facility of the Rutherford Appleton Laboratory (Oxfordshire, U.K), which currently (2005) is the world's brightest spallation source. Figure 2.5.3 is the current layout of ISIS [26].

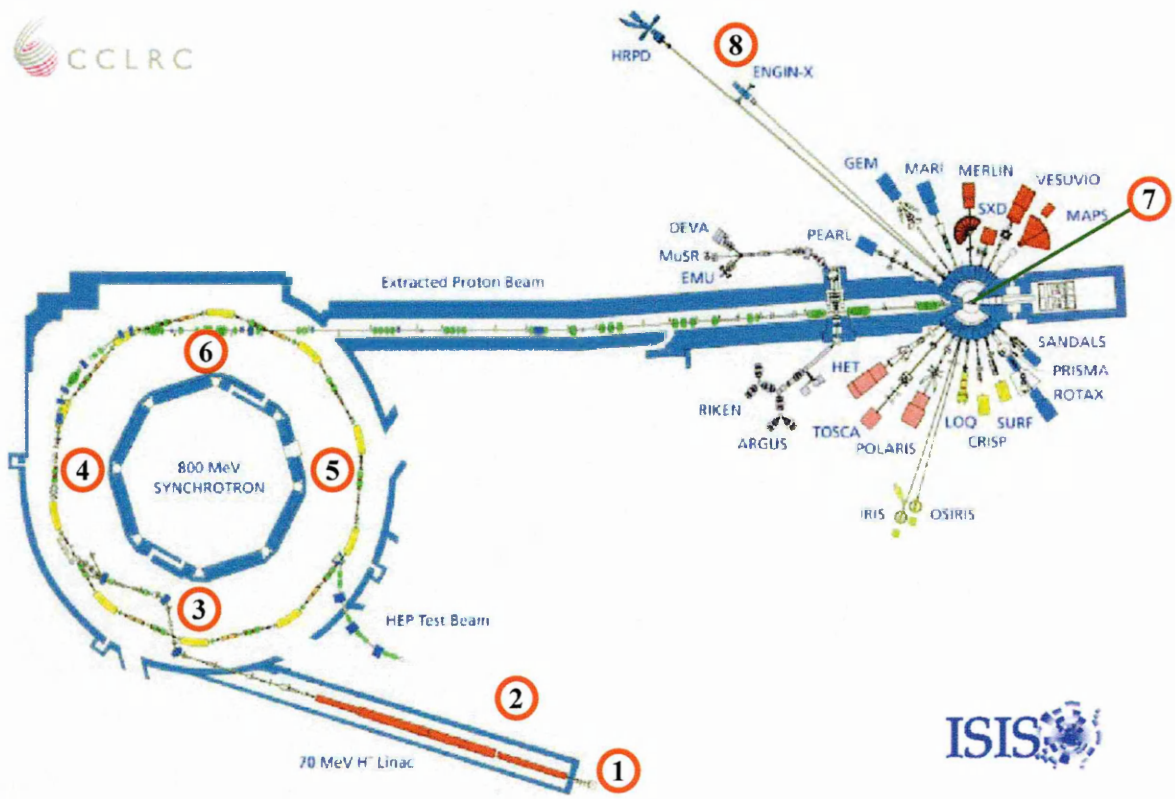

Figure 2.5.3 The ISIS pulsed-neutron source. The diameter of the synchrotron is 50m. The ENGIN-X instrument is one of the stations ([26], also adapted from [1, 18]).

The production of neutrons in ISIS is explained as follows. In the ISIS facility, through a mixture of hydrogen gas and hot caesium vapour the negative hydrogen ions (H^-) are formed by electrical discharge, are then accelerated to 665keV and injected into the linear accelerator (Location-1). At location-2, these protons are further accelerated to ~70MeV stepwise before being injected into the synchrotron. On entering the synchrotron ring, the electrons on the negatively charged hydrogen ions are removed by passage through a ~0.25μm aluminium oxide foil, leaving only bare protons (Location-3). Once the protons have been accelerated to ~800MeV in the 52m diameter proton synchrotron ring, they are extracted out by 3 fast kicker magnets giving a time-pulsed beam containing 2.5×10^{13} protons/pulse at 50Hz. Each pulse has a period of 0.4μs (Location-4). However, before

being extracted the protons will undergo approximately 10^4 revolutions in the synchrotron, driven and focused by dipole (yellow) and quadrupole (green) magnets, and accelerated by alternating voltages applied across six double-gap cavities in the ring (Location-5). The extracted proton beam then passes over the synchrotron ring (Location-6) towards the target station (Location-7). On impact with a tantalum (Ta) target, each proton produces about 15 neutrons flying in all directions. These neutrons have a broad spectrum of high energies (on average 3~4 MeV), like neutrons from reactor sources, are also subsequently moderated for use in experiments (Location-7). Various hydrogeneous moderators e.g. water at 316K, liquid methane (CH_4) at 100K and liquid hydrogen at 20K, are available in ISIS; and generally liquid methane is used. ENGIN-X, the instrument dedicated for bulk stress/strain measurement in materials is located at position-8 in Figure 2.5.3 [26].

A schematic diagram of ENGIN-X is given in Figure 2.5.4 [1, 18, 27]. The thermalised neutrons are transported from the moderator to ENGIN-X in a supermirror-coated guide, and pass through a vertical/horizontal aperture defined by a motorized incident slit system. A motorised high precision *X-Y-Z-*ω positioning table, with motion of 500mm and 370°, has the capacity to accommodate samples up to 2 tonnes in weight. The design of two large radial collimators along with the detectors fixed at Bragg angles $2\theta = \pm 90°$ to the incident beam enable two mutually perpendicular strain components to be measured simultaneously. Each detector bank consists of five vertically-stacked units of 240 scintillation elements, giving 1200 elements/bank. The detector banks cover an angular aperture $\alpha = 32°$ (or $74° < 2\theta < 106°$) on each side of the diffracted beam and therefore each element detects neutrons at a slightly different 2θ angle [27, 28]. This slight variation in path length for each detector as compared to precise $2\theta = 90°$ scattering angle is corrected by the focusing routine that integrates the data from the individual detectors [25].

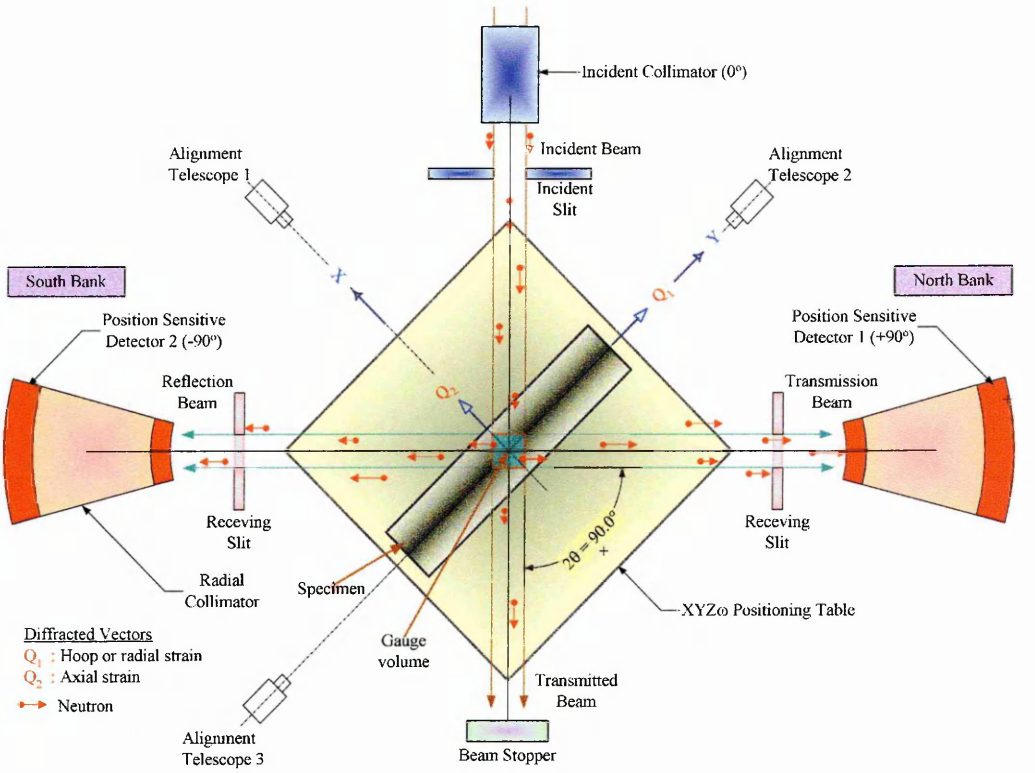

Figure 2.5.4 Schematic diagram of the ENGIN-X diffractometer at the ISIS pulsed-neutron source, Rutherford Appleton Laboratory (Oxfordshire, U.K.) (adapted from [1, 18, 27]).

The neutron beam at ISIS possesses a wavelength range of 0.5 ~ 10Å, however only those of 1~5 Å are normally required in ENGIN-X measurements. A typical time-of-flight (TOF) spectrum and equivalent *d*-spacing distribution from the Al 2024-T351 studied on ENGIN-X is given in Figure 2.5.5.

Governed by Bragg's law, the incident white beam represented by various wavelengths may be diffracted by various sets of atomic planes in crystalline materials at different 2θ; this gives rise to numerous reflection peaks as recorded by the detector banks (Figure 2.5.5(a)). Neutrons with the highest energy/velocity take the shortest time to reach and be scattered by the sample, followed by neutrons with less energy/velocity; and this gives a profile of reflection peaks with decreasing order of Miller indices (*hkl*) for each phase (Figure 2.5.5(b)). The capability of spallation source to produce numerous reflections simultaneously, even for different phases in the sample, is one of its most advantageous features over fission sources.

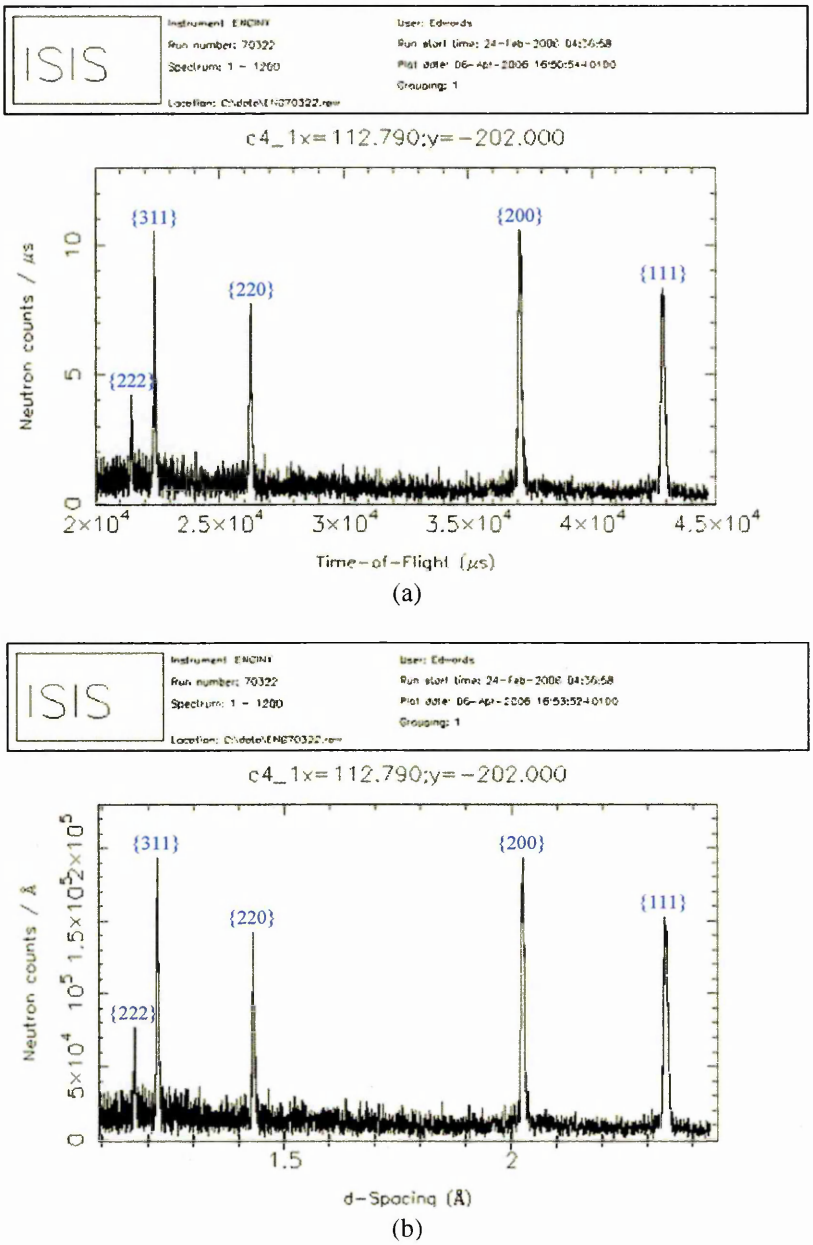

Figure 2.5.5 (a) Raw diffraction spectrum measured from a 6.35mm thick plate of 2024-T351 aluminium alloy. (b) The equivalent *d*-spacing plot showing the five most prominent peaks used in the analysis, and their values were obtained from a modified Pawley refinement routine [29].

2.5.4 Strain determination from neutron diffraction data

The essential principle of stress/strain calculation in neutron diffraction is basically the same as X-ray diffraction, as both the techniques operate on Bragg's law. However, different considerations are required on how the *d*-spacings are determined from monochromatic and polychromatic diffraction data, and this is explained below. Essentially, for the neutron techniques the reference d_o-value must be measured from stress-free materials of the same chemical composition, phase transformation, temperature, and possibly geometry to eliminate pseudo-strain due to a partially-filled gauge volume [1, 18].

Monochromatic Diffraction: For a given constant wavelength λ and selected reflection planes (*hkl*), any change in the *d*-spacing, Δd in a stressed material is manifested by a shift in the diffraction angle, $\Delta\theta$ in the reflected peak. Hence, the strain calculation for monochromatic data is straightforward according to (2.4.2–3). The values of *d*-spacing are determined from the peak fitting equations, often assuming the diffraction profile resembles a Gaussian distribution (Figure 2.5.2) with a flat, linear or parabolic background [1]. Other mathematical functions and numerical routines are also employed to increase accuracy and to deal with anomalous reflection peaks [1, 5, 17, 21].

TOF Polychromatic Diffraction: In Figure 2.5.6, the sample is positioned at fixed scattering angle, and the diffraction pattern of the time-pulsed polychromatic beam is recorded as intensity $I(t)$ as a function of time after a start signal.

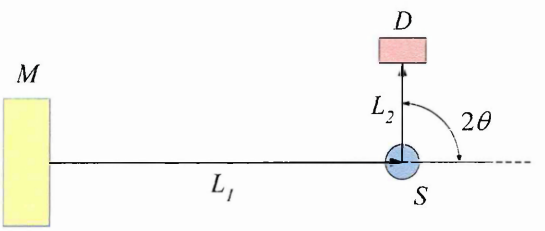

D : detector
M : moderator
S : sample
2θ : scattering angle
L_1 : moderator-to-sample distance
L_2 : sample-to-detector distance
L : total TOF distance, i.e. $L_1 + L_2$

Figure 2.5.6 The basic components of a time-of-flight diffractometer [18].

The detected neutron counts are recorded in a series of TOF channels, t_{hkl}, each related to a certain velocity v_{hkl} (Figure 2.5.5), or wavelength λ_{hkl} of a particular lattice spacing, d_{hkl}. These individual neutron velocities, v_{hkl} are then expressed as

$$v_{hkl} = \frac{L}{t_{hkl}} = \frac{h}{m_n \lambda_{hkl}} \tag{2.5.4}$$

The TOF of those diffracted neutrons that are then detected by the detector is given by

$$t_{hkl} = \frac{L\, m_n \lambda_{hkl}}{h} \tag{2.5.5}$$

When the detected neutron count is presented as a function of TOF as in Figure 2.5.5(a), it gives a series of peaks from different d_{hkl} lattice planes in the materials. By measuring the TOF (t_{hkl}) of neutrons from the moderator to detector, and knowing the diffraction angle 2θ

and flight path length L, the lattice spacing d_{hkl} for particular set of $\{hkl\}$ lattice plane can be solved. From Bragg's law (2.4.1), these individual d_{hkl} lattice planes are

$$d_{hkl} = \frac{\lambda_{hkl}}{2\sin\theta_{hkl}} = \frac{h\, t_{hkl}}{2m_n L \sin\theta_{hkl}} \tag{2.5.6}$$

In this thesis, the TOF diffraction data collected from each detector bank was visualised and analysed using Open GENIE software [30]. The data fitting technique of a Pawley-type full spectrum refinement [29] implemented in the GSAS code [31], as part of the Open GENIE package, was used to compute the bulk cell parameters a, b and c. Pawley refinement is an improvement of the earlier Rietveld method [32] which incorporates texture effects, allowing free variation of each individual reflection in the global spectrum [18]. In principle, having computed the individual d_{hkl}, the associated measured strain in sample can be simply derived as

$$\varepsilon_{hkl} = \frac{\Delta d_{hkl}}{d_{hkl,0}} = \frac{\Delta \lambda_{hkl}}{\lambda_{hkl,0}} = \frac{\Delta t_{hkl}}{t_{hkl,0}} \tag{2.5.7}$$

For an aluminium alloy, the unit cell crystal structure is of face-centre cubic (FCC) type, and is defined in the analysis codes. The Pawley-Rietveld refinement then combines all the peak information of the FCC unit cell, weighting each peak contribution towards those peaks which are most intense, and produce the most representative average lattice parameter(s), e.g. a, b and c [1]. Since $a = b = c$ for FCC material, the representative strain can then be shown analogous to (2.4.2) as

$$a = \frac{a - a_0}{a_0} = \frac{\Delta a}{a_0} \tag{2.5.8}$$

In reality, despite the presence of a certain amount of elastic and plastic anisotropy, the actual strain determined from the weighted lattice parameters of Rietveld-based refinement shows favourable agreement to the bulk microscopic strain [24, 33]. For the BCC and FCC material, the interplanar spacing, d_{hkl} in (2.4.2) can be relate to the lattice parameter, a as

$$d_{hkl} = \frac{a}{\sqrt{h^2 + k^2 + l^2}} \tag{2.5.9}$$

2.5.5 Stress calculation from neutron diffraction data

For many measurements, the principal strain directions may be deduced from the specimen geometry and/or the loading arrangements. This consequently reduces the assessable components to three principal strain directions (i.e. ε_{11}, ε_{22}, ε_{33}) and hence three principal stresses (i.e. σ_{11}, σ_{22}, σ_{33}) can be then determined from (2.4.2). It should be noted that even when the principal strain directions are not known, the direct stress calculated from these orthogonal strain components will be correct. In this case, however, they will not necessarily be the principal stresses and therefore shear stresses may also be present that act along these directions.

2.6 Fracture Mechanics

Fracture mechanics is a branch of solid mechanics that examines the behaviour of cracks or crack-like defects in materials and structures subjected to loading or stress. This involves the study of crack growth from its inception stage at flaws until the fracture of the components. Cracks or crack-like defects introduced during manufacturing, component fabrication and assembly, or developed in service due to fatigue or environmental effects may propagate to some critical size and jeopardise the overall integrity of structures in operation. Fracture mechanics is therefore regarded as an indispensable tool to prevent or delay numerous structural failures in aerospace, nuclear energy/ power generation, off-shore, medical and transport industries.

2.6.1 Fracture modes

The behaviour of a crack propagating in a solid continuum can be independently categorized into three basic modes of loading, which involve different crack surface displacements (Figure 2.6.1). In practice, it is possible to have any combination of different modes of loading that cause mixed-mode fracture. The following discussion deals mainly with mode I as it is the prime mode responsible for the majority of fracture failures in

engineering structures. However, similar mathematical treatments can readily be extended to analyse the effects of mode II and III [34-36].

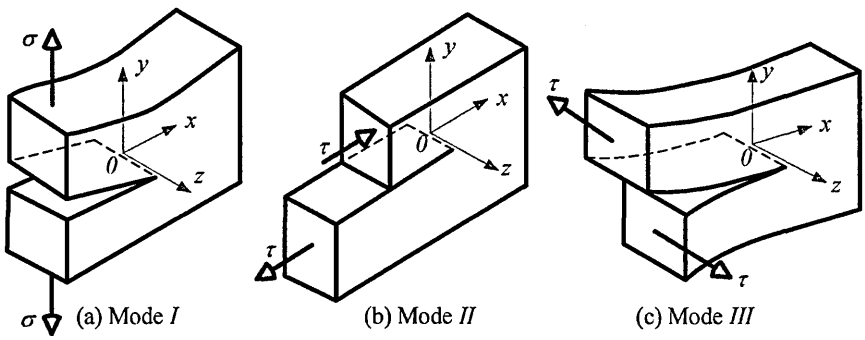

Figure 2.6.1 Three basic modes of continuum fracture (a) tensile opening (mode I); (b) in-plane sliding/shearing (mode II); (c) anti-plane shearing/tearing (mode III) [37]

2.6.2 Fracture mechanics approach

Two key methodologies are available to investigate the phenomena of crack growth, namely the energy criterion and the stress field approach [38]. The energy approach, initially proposed by Griffith [39] and later advanced by Irwin [40], defines the crack increment in terms of energy release rate. This approach considers that crack extension is only possible if the energy for crack growth is sufficient to overcome the resistance of the material. The material resistance may comprise the surface energy, plastic work, and dissipated energy during crack propagation. On the other hand, the stress field approach relies upon the analysis of stress behaviour near to a crack tip. These two methodologies are unified and comparable in many ways, and have their own advantages and inadequacies depending on the fracture conditions under consideration.

The present work focuses on the fundamental theory of the stress field approach, and in particular the application of linear elastic fracture mechanics (LEFM). For completeness, a brief account of elastic-plastic fracture mechanics (EPFM) is also included.

2.6.3 Linear elastic fracture mechanics

LEFM generally considers a cracked continuum is characterised by homogeneous, isotropic, linear elastic material [41], but some of its applications have also been extended

to problems of crack interfaces in dissimilar materials [42], thermo-elastic, anisotropic and non-homogeneous cases [35].

Assuming a through-thickness crack exists in a linear isotropic material of infinite plane with external boundaries subjected to arbitrary mode I loading (Figure 2.6.2(a)), the local stress field near the crack tip, as firstly derived by Westergaard [43], Irwin [44], Sneddon [45] and Williams [46] can be jointly expressed in a compact expression as follows [38]:

$$\sigma_{ij}(r,\theta)=\frac{K}{\sqrt{2\pi r}}f_{ij}(\theta)+\underbrace{\sum_{m=0}^{\infty}A_m r^{\frac{m}{2}}g_{ij}{}^{m}(\theta)}_{\text{Higher order terms}} \tag{2.6.1}$$

where σ_{ij} is the stress tensor; K represents a variable called the stress intensity factor; f_{ij} is a dimensionless function of θ; r and θ are the polar coordinates in relation to the crack tip. The higher order series are geometry-dependent, but the leading term is always proportional to $1/\sqrt{r}$. At the crack tip i.e. $r \rightarrow 0$, the leading term tends to infinity; whereas the higher order terms remain finite or approach zero and hence can be disregarded. Such simplification allows the stress σ_{ij} adjacent to the crack tip to vary with only $1/\sqrt{r}$ regardless of the crack configuration. A condition of stress singularity is then attained exactly at the crack tip for $r \rightarrow 0$.

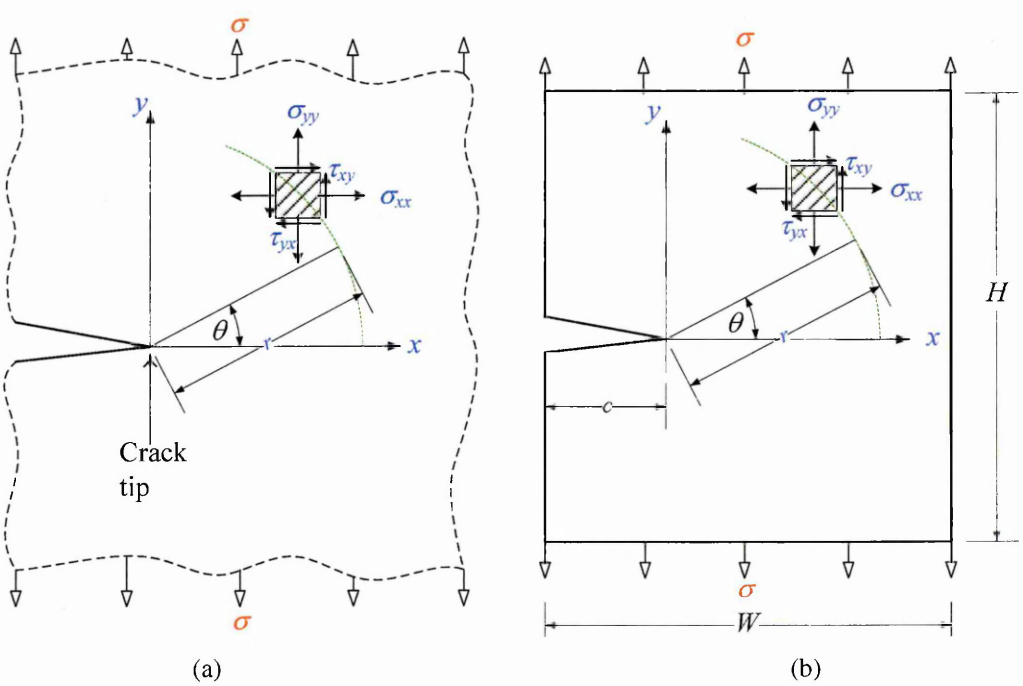

Figure 2.6.2 Cartesian coordinate system used to describe stresses in the vicinity of a crack. The z-axis is normal to the page.

In Figure 2.6.2(a), under the action of pure mode *I* loading, the Cartesian stress field within the singularity zone very near to the crack tip may be expanded from (2.6.1) as follows:

$$\sigma_{xx}(r,\theta)=\frac{K}{\sqrt{2\pi r}}\cos\left(\frac{\theta}{2}\right)\left[1-\sin\left(\frac{\theta}{2}\right)\sin\left(\frac{3\theta}{2}\right)\right] \tag{2.6.2}$$

$$\sigma_{yy}(r,\theta)=\frac{K}{\sqrt{2\pi r}}\cos\left(\frac{\theta}{2}\right)\left[1+\sin\left(\frac{\theta}{2}\right)\sin\left(\frac{3\theta}{2}\right)\right] \tag{2.6.3}$$

$$\sigma_{zz}(r,\theta)=\begin{cases}0, & \text{plane stress}\\ \nu\left(\sigma_{xx}+\sigma_{yy}\right), & \text{plain strain}\end{cases} \tag{2.6.4}$$

$$\tau_{xy}(r,\theta)=\frac{K}{\sqrt{2\pi r}}\cos\left(\frac{\theta}{2}\right)\left[1+\sin\left(\frac{\theta}{2}\right)\sin\left(\frac{3\theta}{2}\right)\right] \tag{2.6.5}$$

$$\tau_{xz}(r,\theta)=\tau_{yz}(r,\theta)=0 \tag{2.6.6}$$

$$\tag{2.6.7}$$

At $\theta = 0$, the shear stress $\tau_{xy} = 0$ and this defines the crack line to be the principal plane for mode *I* loading. Also, within this singularity dominated zone ($r \to 0$),

$$\sigma_{xx}=\sigma_{yy}=\frac{K_I}{\sqrt{2\pi r}} \tag{2.6.8}$$

In (2.6.8) the stress intensity factor, K_I determines the magnitude of the crack tip singularity and is directly proportional to the local crack tip stresses. Likewise, the SIF for mode *II* and *III* can be denoted as K_{II} and K_{III}, respectively. Detailed derivation of other equations pertinent to the stress/strain field for mode *I*, *II* and *III* can be found in [34, 38].

In practical applications, cracks normally propagate from components of finite boundaries under the action of remote external loading σ (see Figure 2.6.2(b)). Without loss of generality, the SIF can be expressed as

$$K_{I,II,III}=\beta\sigma\sqrt{2\pi c} \tag{2.6.9}$$

Where σ is the remotely applied stress; c denotes the crack size; β represents the compliance function that takes account of the effects of geometry such as width *W*, height *H*, hole radius *R*, etc, in relation to the crack size, *c*. The re-configuration of the local stress field (2.6.8) to global external applied loading (2.6.9) permits expedient calculation of SIF

for known c and σ; this is in addition to the fact that the exact stress field in the singularity dominated region is difficult to determine.

2.6.4 Determination of stress intensity factor

Within the concept of LEFM, the single K-parameter is widely used to correlate crack growth in materials. References [34-36, 47] provide some excellent compilations of K-solutions under various crack configurations for linear elastic bodies. Despite these existing solutions, new K-solutions are continuously being solved to deal with unforeseen complexities of both the crack geometries and loading, especially for cracks at structural discontinuities, self-balanced residual/thermal stress field, and in new materials with different reinforcing mechanisms introduced for reducing the effective K [42, 48].

Sih [35] and Sanford [49] independently summarised some of the well-known techniques used to determine K-solutions, based on analytical, numerical, and experimental approaches. The analytical tools, such as integral transform, complex variables, conformal mapping and dislocations, generally produce exact solutions but the treatments are mathematically demanding and only suitable for simple geometries. Numerical methods such as finite element, boundary element, and boundary collocation are normally employed to address complex geometries and loading but are high cost in terms of both specialized skills and computational resources. Experimental techniques, for instance interference pattern, Moiŕe pattern and photo-elasticity, are attractive and cost effective alternatives to analytical and numerical methods for verification and solving K-solutions for complex problems. Moreover, some problems can only be addressed by experimental measurement such as those found in dynamic crack propagation and arrest, and in-situ monitoring of flawed structures.

Amongst the analytical techniques, the Green's function, better known as the weight function or influence function, is an adaptable tool for calculating SIF. For particular crack

geometries, the weight functions are principally devised to provide *K*-solutions for arbitrary complex crack loading with remarkable computational efficiency and solution accuracy [42, 48]. The weight function approach has originally been used for two-dimensional elastic crack analysis [48], but recent interest has been shown in three-dimensional cracked bodies [50, 51]. In the work reported here, Green's functions were developed to calculate the residual SIF for various fatigue crack sizes in cold-worked holes.

2.6.5 Crack tip plastic zone in monotonic loading

The stress singularity zone around the crack tip is merely a consequence of the mathematical idealisation that the crack tip is infinitely sharp and the material is always elastic. In real materials, the crack tip radius is finite, and in addition plastic flow at a highly strained crack tip partially relaxes the crack tip stresses. The extent of the crack tip plastic zone under monotonic loading may be estimated from analytical models or experimental measurements [37]. On the premises of (1) elastic perfectly-plastic behaviour of the material, (2) the von Mises stress being equal to the material yield stress σ_Y, (3) equilibrium consideration of stress field, Irwin [52] postulated that the mode *I* crack tip plastic zone, $r_p = 2\ r_y$ at $\theta = 0$ to be (Figure 2.6.3) [41]:

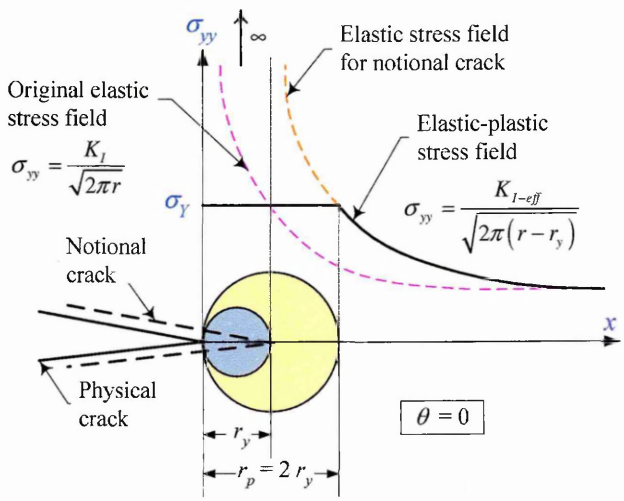

Figure 2.6.3 Irwin's plastic zone correction under monotonic loading. The approximated elastic-plastic stress field for mode I loading is constructed using stress equilibrium and notional crack argument. The increase in LEFM effective stress intensity is taken into account by assuming the crack length is longer by r_y.

$$\text{Plane Stress}: r_p = \frac{1}{\pi}\left(\frac{K_I}{\sigma_Y}\right)^2 \quad \text{and} \quad \text{Plane Strain}: r_p = \frac{1}{3\pi}\left(\frac{K_I}{\sigma_Y}\right)^2 \tag{2.6.10}$$

Irwin argued that in plane strain, due to the higher constraint and associated triaxial stress state, the crack tip yielding is raised by a factor of $\sqrt{3}$. Consequently, the approximated plastic zone for plane strain is smaller that that of plane stress by a factor of three [53].

Referring to Figure 2.6.3, for the same x-position ($x > r_y$) the elastic stress field after redistribution is higher than those predicted by (2.6.8), implying a higher effective stress intensity. Irwin observed that this increase in K can be solved by defining an effective crack length c_{eff} that is slightly longer that the physical crack length by r_y i.e. $c_{eff} = c + r_y$.

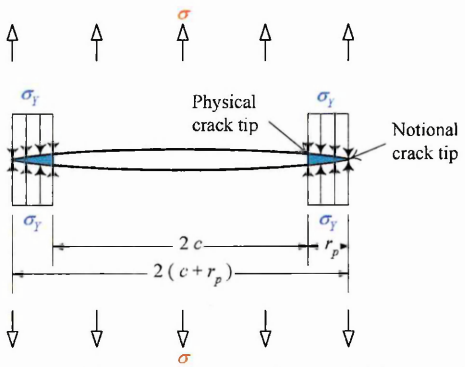

Figure 2.6.4 The strip yield model approximates crack tip yielding by superposition of two elastic fields: a Griffith's crack of $2c$ whose extension under remote tensile load is opposed by closure compressive yield stress acting at both ends of the crack tips.

The strip yield model proposed by Dugdale [54] and Barenblatt [55] is an alternative means to evaluate the plastic zone size of a mode I crack in an infinitely thin plate made of elastic perfectly-plastic material. The plastic regions r_y are assumed to be confined by slender strips extending ahead of the crack tips, with closure stress σ_Y applied at both crack tips (Figure 2.6.4). Given c >> r_y and $\sigma << \sigma_Y$, the Dugdale-Barenblatt model predicts

$$\text{Plane Stress} : r_p = \frac{1}{8\pi}\left(\frac{K_I}{\sigma_Y}\right)^2 \tag{2.6.11}$$

which is about 23% larger than Irwin's plastic zone for the case of plane stress.

2.6.6 Crack tip plastic zone in cyclic loading

During fatigue loading, a secondary reversed yield region called the cyclic plastic zone r_c exists when the crack is partially unloaded from far-field tension. In Figure 2.6.5(b), the maximum load in a fatigue cycle (point A in Figure 2.6.5(a)) produces a monotonic plastic zone and stress distribution. When the loading is reduced by $\Delta\sigma$ to point B in Figure 2.6.5(a), and due to the previous plastic tensile flow, a compressive reversed stress is induced locally with a smaller plastic zone size, r_c as shown in Figure 2.6.5(c). The amount of local stress change is between σ_Y and 2 σ_Y depending on the hardening behaviour of the material. When there is no crack face closure, the resultant stress distribution (Figure 2.6.5(d)) can be achieved simply by superimposing the stress field of the fully loaded state

with that of the partially unloaded state, with the smaller plastic zone size, r_c embedded within the monotonic plastic region.

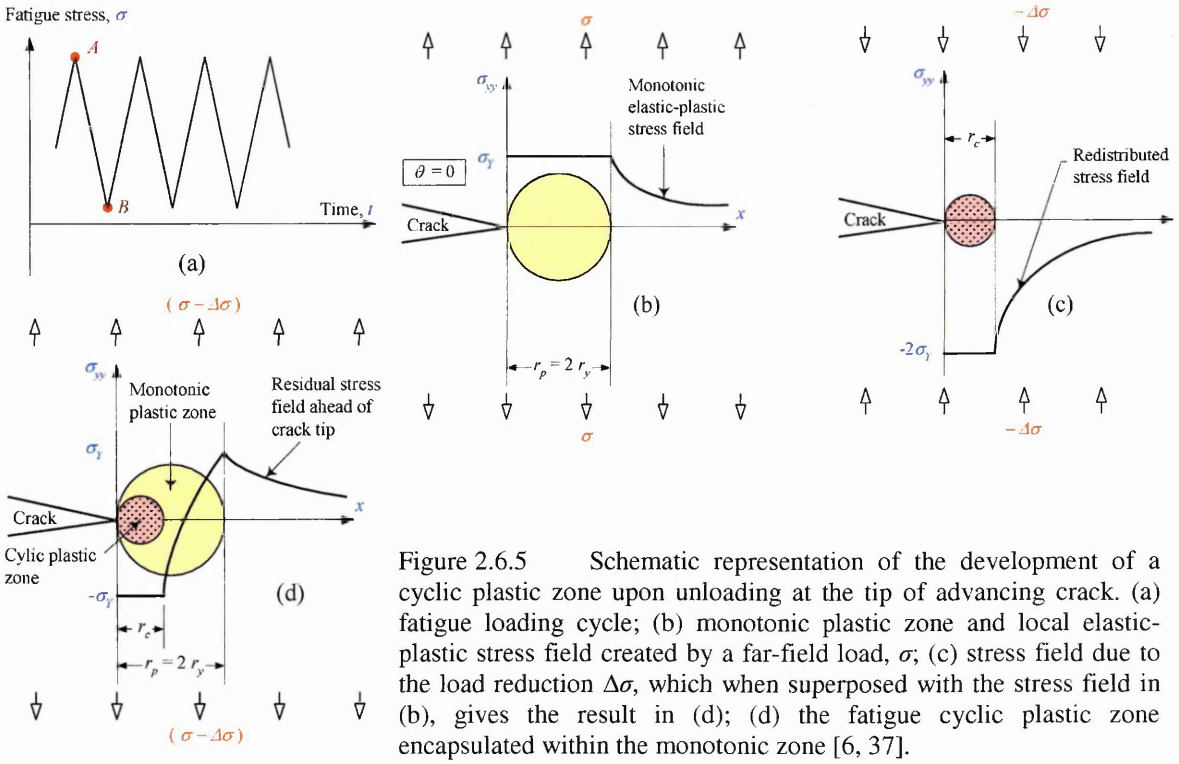

Figure 2.6.5 Schematic representation of the development of a cyclic plastic zone upon unloading at the tip of advancing crack. (a) fatigue loading cycle; (b) monotonic plastic zone and local elastic-plastic stress field created by a far-field load, σ; (c) stress field due to the load reduction $\Delta\sigma$, which when superposed with the stress field in (b), gives the result in (d); (d) the fatigue cyclic plastic zone encapsulated within the monotonic zone [6, 37].

According to Rice [56], from equation (2.6.10) by isotropic hardening rule replacing σ_Y by $2\sigma_Y$, and K_I by ΔK_I, and for stress ratio $R > 0$, the cyclic plastic zones may be expressed as

$$\text{Plane Stress}: r_c = \frac{1}{4\pi}\left(\frac{\Delta K_I}{\sigma_Y}\right)^2 \quad \text{and} \quad \text{Plane Strain}: r_c = \frac{1}{12\pi}\left(\frac{\Delta K_I}{\sigma_Y}\right)^2 \tag{2.6.12}$$

For $R = 0$, i.e. zero-tension-zero cyclic loading, $K_{max} = \Delta K$

$$\text{Plane Stress}: r_c = \frac{1}{4} r_p \tag{2.6.13}$$

For $R < 0$, the cyclic plastic zone size is even smaller when compared to its monotonic value [41]. The cyclic compressive residual stress field near the crack tip plays a crucial role in the behaviour of transient crack growth under many physical observations, e.g. the R-ratio effect due to crack closure [57] and fatigue life prediction under variable amplitude loading [6].

Within the concept of LEFM, the discussion so far is valid if the plastic zone size is negligible compared to the crack length and other characteristic dimensions. As a result,

small scale plastic deformation still validates the characterisation of the stress field near to the plastically deformed crack tip region by SIF. Otherwise, the applicability of LEFM is violated when the history of crack growth is dominated by large scale plasticity and elastic-plastic fracture mechanics should be used instead.

2.6.7 Elastic-plastic fracture mechanics

In elastic-plastic fracture mechanics (EPFM), the treatment of large scale yielding of time-independent crack growth commonly uses energy-based (e.g. *J*-integral) [58] or deformation-based (e.g. CTOD) methods [41]. The energy-based approaches normally involve the calculation of the change of potential energy per unit thickness associated with an increment of crack extension, while the deformation-based method uses the change of crack tip profile as a measure of the crack resistance of materials.

Notably, Rice [59, 60] formulated an established energy-based EPFM crack tip driving force parameter, termed the *J*-integral, for nonlinear elastic materials; but the *J*-integral has also found extensive application in elastic-plastic materials as long as the loading is in one direction as prescribed in the deformation plasticity theory. However, the *J*-integral loses its unique path-independency and hence potential energy interpretation when non-proportional loading of elastic-plastic materials occurs due to a change in the loading system or crack boundaries. The path-dependence problems of the *J*-integral are commonly encountered in elastic-plastic cracked bodies subjected to combined thermal–mechanical load or combined residual stress–mechanical load [61-63], and some significant progress has been accomplished recently to re-formulate Rice's *J*-integral to partially resolve some of the aforementioned problems [64-66].

Another EPFM parameter widely used to measure the crack tip plastic strain is the crack tip opening displacement (CTOD). Wells [67] argued that a sharp crack tip becomes blunt and shows finite displacement at the original tip when subjected to significant amounts of

plastic deformation. Consequently, the stresses induced near the blunted crack tip must reach a limiting value, in contrast to the LEFM stress singularity at an acute crack tip. For that reason, it is ultimately the further increase of plastic strain in response to external loading that is responsible for the final fracture of structures [41].

2.7 Fatigue of Materials

2.7.1 Introduction

Fatigue causes damage and gradual reduction of strength in materials due to repeated fluctuation of cyclic loading (e.g. mechanical, thermal, contact, etc.), even at stress/strain levels lower than the characteristic strength of the material. For mechanical fatigue, the service life of components depends on the maximum applied stress, stress amplitude, size effects, loading effects, surface finish and treatment, temperature, environment, etc [6, 68]. To assist our understanding, the sequence of fatigue damage of materials can be broadly classified into several stages [37]:

(1) Sub- and microstructural changes lead to permanent nucleation of a damage site.

(2) Formation of microscopic cracks.

(3) Growth and coalescence of microscopic flaws to form a macroscopic crack.

(4) Stable propagation of the dominant macroscopic crack.

(5) Unstable crack growth causing structural instability or complete fracture.

From the engineering practical point of view, the first three stages of crack development may be deemed as the initiation stage of a macroscopic crack. The remaining two stages define how the increase in size of a detectable macroscopic crack finally threatens the structural integrity of components. Therefore, the fatigue life of a component N_f, is made up of initiation N_i and propagation stages N_p of the crack [68].

2.7.2 Different approaches to fatigue design

Two main design philosophies have been adapted in the fatigue design of components. The classical total life methodology considers the fatigue life-to-failure in terms of cyclic stress range (*S–N* curve approach) or the plastic/total strain-life approach. This total life approach is normally used to design against crack initiation because at low strain amplitudes, up to 90% of the fatigue life may be consumed for the initiation of macroscopic cracks. The S-N curve approach is traditionally connected to high-cycle fatigue in terms of stress range because materials deform primarily elastically under these conditions. However, in the strain-life approach the low-cycle fatigue stresses encountered generally cause significant plastic deformation prior to failure, and therefore the fatigue life is defined as a function of strain range. In contrast, the damage tolerant approach evaluates the fatigue crack life starting from some definite flaw size based on the fracture mechanics methodology. The ultimate concern of the damage tolerant approach is to ensure structural safety within a specified period before the flawed items are repaired or replaced [37].

2.7.3 Fatigue crack initiation

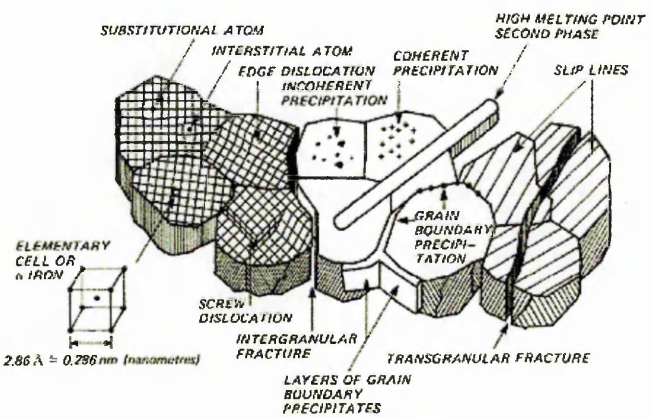

Figure 2.7.1 Schematic of microstructural features in metallic materials [41].

Figure 2.7.1 illustrates the complexity of microstructures of brittle and ductile polycrystalline materials along with two major fracture paths i.e. transgranular and intergranular fracture. Numerous models have been developed to explain how these features can give rise to microscopic flaws that eventually grow into macrocracks upon the continuous interaction with external loading. However, for the present fatigue study of aluminium alloy only the aspects of transgranular fracture by fatigue for ductile material are discussed here: on the free surface of ductile metals, irreversible shear movement

between planes within the grains relative to each other may take place, either under monotonic or cyclic loading. Monotonic loading promotes coarse slip bands; however, the surface of material which is fatigued tends to deform by cyclic slip accumulating at persistent slip bands (PSB). The PSB consist of very fine and irregular notched profiles of extrusions and intrusions (Figure 2.7.2). These effects cause localization of plastic strain by the formation of surface stress raisers.

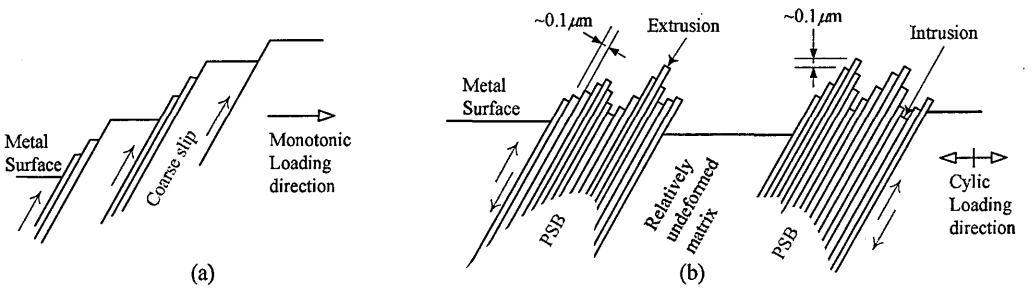

Figure 2.7.2 Surface slip phenomena. (a) A series of steps resembling a staircase pattern produced by a monotonic plastic strain; (b) A rough surface consisting of hills and valleys produced by cyclic plastic strain [37, 41].

Continuing cyclic slip further deepens the scale of intrusions and eventually leads to the formation of microscopic cracks along these slip planes. The slip plane cracking may extend a few grain-diameters before transforming to macrocrack propagation that operates on a continuum mechanism [6, 37, 41].

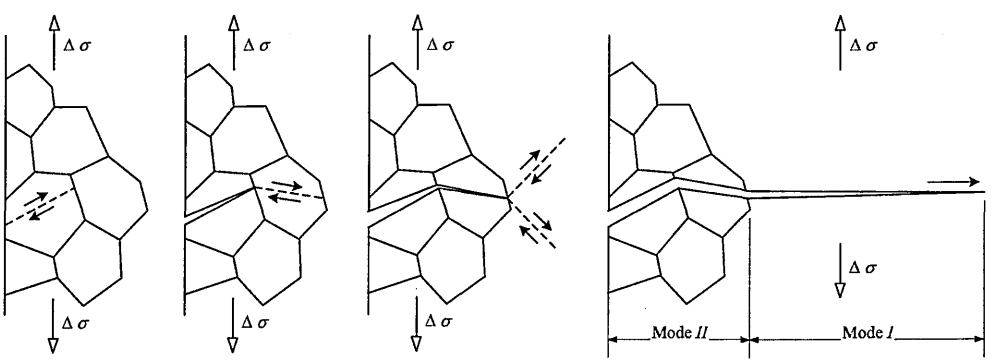

Figure 2.7.3 Schematic of trans-crystalline fatigue crack growth transition from mode II (shear) crack initiation to mode I (tensile) crack propagation [37, 41].

As shown in Figure 2.7.3, fatigue cracks nucleate locally from the PSB and tend to grow in the plane of maximum shear (mode II) on the order of several grain sizes. The active shear planes occur at ~45° in suitably orientated grains with respect to the applied stress. Once the microcracks are present, fatigue cracks tend to coalesce and grow in a zigzag manner

essentially perpendicular to, and governed primarily by, the maximum tensile stress range (mode I). At this stage, the growth of the crack proceeds by the repetitive plastic blunting and sharpening processes at the crack tip that register striations along the crack faces. However, microcracks may also nucleate and grow along the boundaries of grains (intercrystalline), depending on the material type, load, and environmental conditions.

2.7.4 Fatigue crack propagation

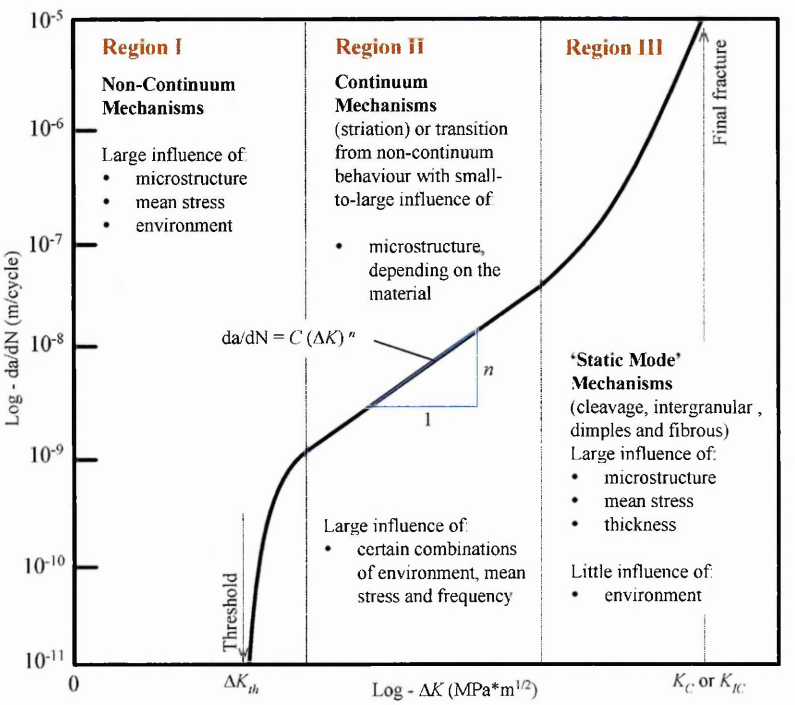

Figure 2.7.4 Typical variation of the fatigue crack growth rate as a function of stress intensity factor range.

In design, the damage tolerant approach allows the estimation of fatigue life by relating crack extension rate, da/dN with the applied range of a facture parameter, e.g. SIF in LEFM. For most metals, the logarithmic plot of da/dN–ΔK tends to follow a sigmoidal shape with three distinct regions (Figure 2.7.4). In region I, the da/dN decreases rapidly with decreasing ΔK until a threshold limit ΔK_{th} is reached; no crack propagation is possible if $\Delta K < \Delta K_{th}$. The crack growth rate in Region II is linear and is defined by the Paris law. Region III describes a rapid acceleration of crack propagation when the maximum SIF, K_{max} approaches the material fracture toughness, K_C or K_{IC}. In most metallic materials, a significant amount of fatigue life is spent during the threshold period (Region I) and followed by stable crack growth (Region II) before final fracture (Region III) is reached. The fatigue crack propagation rate da/dN, where N is the number of load cycles, has been found to be affected by (1) SIF range, ΔK (= K_{max}-K_{min}); (2) stress ratio, R (= $\sigma_{max}/\sigma_{min}$),

related to the cyclic variation of load; (3) material properties and environmental effect. However, in the simplest form only the first two factors are normally accounted for in fatigue life assessment:

$$\frac{da}{dN} = f\left(\Delta K, R\right) \tag{2.7.1}$$

For fatigue life modelling, various equations can be used to fit the experimental da/dN–ΔK data, and amongst them the Paris equation has been frequently used for Region II:

$$\frac{da}{dN} = C\left(\Delta K\right)^n \tag{2.7.2}$$

where C and n are fitting constants for a particular material and may vary for da/dN–ΔK data under different R-ratios. Afterwards, more involved fatigue life models have been proposed to capture the segmental or full characteristic of da/dN–ΔK curves incorporating various fracture elements (e.g. R-ratios, K_{th}, K_C, etc). Amongst those equations the models of NASGRO, Forman, Harter-T and Walker have been extensively implemented in fracture control analysis schemes of aero-structures [69] .

2.7.5 Fatigue crack closure

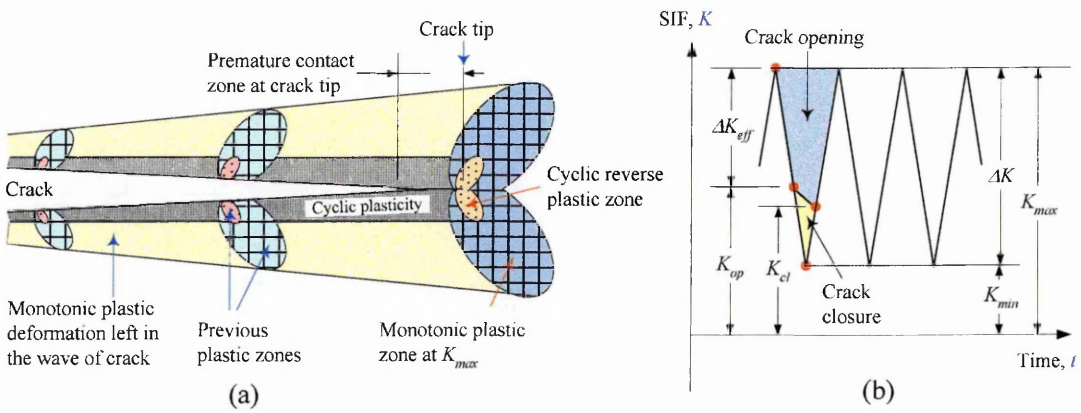

Figure 2.7.5 Plasticity-induced crack closure effect. (a) Schematic view of plastic wake along the crack flanks behind the crack tip causing premature contact at the crack tip, and (b) definition of opening and effective stress intensity factor range for fatigue life modelling [6, 37].

Elber [57, 70] experimentally confirmed that delay in variable amplitude fatigue crack growth, even under a tensile fatigue loading, is attributed to the premature contact of crack flanks near to the crack tip. Elber proposed that the decline in the crack tip driving force is a consequence of residual tensile deformation remaining in the wake of the fatigue crack

tip, as the crack grows inside the crack tip compressive stress region (Figure 2.7.5(a)). The residual tensile deformation promotes the crack flanks to come into contact prematurely before the minimum load is reached i.e. plasticity induced crack closure (Figure 2.7.5(b)). Additionally, numerous crack closure mechanisms (e.g. oxide film, fracture surface asperities, viscous fluid, crack deflection, etc.) have been successively identified to provide a more complete portrayal of crack growth retardation phenomena under constant amplitude loading [37]. As shown in Figure 2.7.5(b), the definition of SIF variation in a load cycle suggests that the crack tip might delay its opening to K_{op} or close prematurely at K_{cl} ; the condition being either $K_{op} = K_{cl}$ or $K_{op} > K_{cl}$. Here, K_{op} is used as the controlling parameter, and the crack growth rate da/dN should be correlated to the effective SIF range ΔK_{eff} (= $K_{max} - K_{op}$) in place of ΔK in the fatigue life models. For instance, the Paris law should now be modified as:

$$\frac{da}{dN} = C\left(\Delta K_{eff}\right)^n \tag{2.7.3}$$

In fact, crack closure typically occurs synergistically under two or more mechanisms, and helps the elucidation of various fatigue crack growth phenomena i.e. consistent shift of da/dN–ΔK under different R-ratios, residual stress effects, overload and underload in variable amplitude loading, etc. Prediction of the life of fatigue cracks for region II can be carried out by recasting (2.7.3) into the following form:

$$N_f = \int_0^{N_f} dN = \int_{a_0}^{a_c} \frac{da}{C\left(\Delta K_{eff}\right)^n} \tag{2.7.4}$$

where N_f is the total life estimated that allows the starting crack length a_0 to reach its critical crack length, a_c.

2.8 References

1. Hutchings, M.T., Withers, P.J., Holden, T.M., and Lorentzen, T., Introduction to the Characterization of Residual Stress by Neutron Diffraction. 2005: CRC Press.

2. Withers, P.J. and Bhadeshia, H.K.D.H., Residual stress Part 1 - Measurement techniques. Materials Science & Technology, 2001. 17(4): p. 355-365.
3. Withers, P.J. and Bhadeshia, H.K.D.H., Residual stress. Part 2 – Nature and origins. Materials Science& Technology, 2001. 17(4): p. 366-375.
4. Lodini, A., The recent development of neutronic techniques for determination of residual stresses. Radiation Physics and Chemistry, 2001. 61(3-6): p. 227-233.
5. Residual Stress Measurement by X-Ray Diffraction: HS-748. 2003: Society of Automotive Engineers, SAE International.
6. Stephens, R.I., Fatemi, A., Stephens, R.R., Fuchs, H.O., Stephens, R.I., Stephens, R.R., and Fuchs, H.O., Metal Fatigue in Engineering. 2nd ed. 2000: Wiley-Interscience.
7. Dutta, M., Residual stress measurement in engineering materials and structures using neutron diffraction, in Department of Materials Engineering. 1999, The Open University: Milton Keynes.
8. Fitzpatrick, M.E., A study of the effects of a quench residual stress field on fatigue in an AI/SiCP metal matrix composite, PhD Thesis, in Department of Materials Science and Metallurgy. 1995, University of Cambridge.
9. Krell, A., Teresiak, A., and Schlafer, D., Grain size dependent residual microstresses in submicron A12O3 and ZrO2. Journal of the European Ceramic Society, 1996. 16(8): p. 803-811.
10. Zhang, H., Minnetyan, L., Chamis, C.C., and Abdi, F. Microstress Level Damage Evolution in Composite Structures. in SAMPE 2001. 2001. Long Beach, CA: The Society for the Advancement of Material and Process Engineering.
11. Tryon, R.G., Dey, A., Krishnan, G., Chandran, K.S.R., and Oja, M. Identifying Sensitive Parameters at Fatigue Crack Nucleation Sites Using Microstructual Simulation Models. in Materials Science and Technology 2004. 2004.
12. Vasudevan, A.K. and Sadananda, K., Analysis of fatigue crack growth under compression-compression loading. International Journal of Fatigue, 2001. 23(Supplement 1): p. 365-374.
13. Vasudevan, A.K., Sadananda, K., and Glinka, G., Critical parameters for fatigue damage. International Journal of Fatigue, 2001. 23(Supplement 1): p. 39-53.
14. Almer, J.D., Cohen, J.B., and Winholtz, R.A., Effects of residual macrostresses and microstresses on fatigue crack propagation. Metallurgical & Materials Transactions A: Physical Metallurgy & Materials Science, 1998. 29A(8): p. p 2127-2136.

15. Almer, J.D., Cohen, J.B., and Moran, B., The effects of residual macrostresses and microstresses on fatigue crack initiation. Materials Science & Engineering A, 2000. 284(1-2): p. 268-279.
16. Nye, J.F., Physical Properties of Crystals: Their Representation by Tensors & Matrices. Reprint 2003, New York: Oxford University Press.
17. Hauk, V., Behnken, H., Genzel, C., Pfeiffer, W., Pintschovius, L., Reimers, W., Schneider, E., Scholtes, B., and Theiner, W.A., Structural & Residual Stress Analysis by Nondestructive Methods. 1997: Elsevier Science Pub. Co. 654.
18. Fitzpatrick, M.E. and Lodini, A., eds. Analysis of Residual Stress by Diffraction using Neutron & Synchrotron Radiation. 2003, CRC Press. 312.
19. Fitzpatrick, M., Fry, A., Holdway, P., Kandil, F., Shackleton, J., and Suominen, L., Measurement Good Practice Guide, GPG(052): Determination of Residual Stresses by X-ray Diffraction. 2002: National Physical Laboratory, U.K. 59.
20. Lu, J., ed. Handbook of Measurement of Residual Stresses. 1996, Fairmont Press. 253.
21. Noyan, I.C. and Cohen, J.B., Residual Stress: Measurement by Diffraction & Interpretation (Materials Research and Engineering). 1987: Springer-Verlag. 276.
22. Timoshenko, S. and Goodier, J.N., Theory of Elasticity. 1970, New York: McGraw-Hill Education.
23. Krawitz, A.D., Introduction to Diffraction in Materials Science & Engineering. 2001: Wiley-Interscience. 424.
24. Wang, D.Q.D., Strain measurement using neutron diffraction, PhD Thesis, in Department of Materials Engineering. 1996, The Open University: Milton Keynes.
25. Dutta, M., Residual stress measurement in engineering materials and structures using neutron diffraction, PhD Thesis, in Department of Materials Engineering. 1999, The Open University: Milton Keynes.
26. ISIS 2004 Annual Report. 2004, ISIS Facility, CCLRC, Rutherford Appleton Laboratory, Oxfordshire, UK.
27. Dann, J.A., Daymond, M.R., Edwards, L., James, J.A., and Santisteban, J.R., A comparison between Engin and Engin-X, a new diffractometer optimized for stress measurement. Physica B: Condensed Matter, 2004. 350(1-3, Supplement 1): p. E511-E514.
28. Johnson, M.W. and Daymond, M.R., An optimum design for a neutron diffractometer for measuring engineering stresses. Journal of Applied Crystallography, 2002. 35(49): p. 65-71.

29. Pawley, G.S., Unit-cell refinement from powder diffraction scans. Journal of Applied Crystallography, 1981. 14(6): p. 357-361.
30. Akeroyd, F.A., Ashworth, R.L., Johnston, S.D., Martin, J.M., Moreton-Smith, C.M., and Sivia, D.S., Open GENIE User Manual. 2005, IData Analysis and Computing Groups, ISIS Science Division , Rutherford Appleton Laboratory, Oxfordshire, UK.
31. Larson, A.C. and Dreele, R.B.V., General Structure Analysis System (GSAS), Los Alamos National Laboratory Report LAUR 86-748. 2000. 230.
32. Rietveld, H.M., A profile refinement method for nuclear and magnetic structures. Journal of Applied Crystallography, 1969. 2(2): p. 65-71.
33. Daymond, M.R., Bourke, M.A.M., Dreele, R.B.V., Clausen, B., and Lorentzen, T., Use of Rietveld refinement for elastic macrostrain determination and for evaluation of plastic strain history from diffraction spectra. Journal of Applied Physics, 1997. 82(4): p. 1554-1562.
34. Tada, H., Paris, P.C., and Irwin, G.R., eds. The Stress Analysis of Cracks Handbook. 3rd ed. 2000, American Society of Mechanical Engineers.
35. Sih, G.C., ed. Handbook of stress-intensity factors: Stress-intensity factor solutions and formulas for reference. 1973, Institute of Fracture and Solid Mechanics, Lehigh University: Bethlehem, PA.
36. Murakami, Y., ed. Stress Intensity Factors Handbook. 1987, Committee on Fracture Mechanics of the Society of Materials Science, Japan; Pergamon Press: New York.
37. Suresh, S., Fatigue of Materials (Cambridge Solid State Science Series). 1998: Cambridge University Press.
38. Anderson, T.L., Fracture Mechanics: Fundamentals and Applications. 1994: CRC Press.
39. Griffith, A.A., The phenomena of rupture and flow in solids. Philosophical Transactions of the Royal Society of London, 1920. A-221: p. 163-198.
40. Irwin, G.R. Onset of fast crack propagation in high strength steel and aluminum alloys. in 2nd Sagamore Sagamore Research Conference Ordnance Materials. 1956. Syracuse, New York: Syracuse University Press.
41. Janssen, M., Zuidema, J., and Wanhill, R.J.H., Fracture Mechanics. 2002: Delft University Press.
42. Munz, D. and Fett, T., Stress Intensity Factors and Weight Functions (Advances in Fracture Series). 1997, Southampton, UK: Computational Mechanics Publications, WIT Press.
43. Westergaard, H.M., Bearing pressures and cracks. Journal of Applied Mechanics, 1939. 6: p. 49-53.

44. Irwin, G.R., Analysis of stresses and strains near the end of a crack traversing a plate. Journal of Applied Mechanics, 1957. 24: p. 361-364.
45. Sneddon, I.N., The distribution of stress in the neighbourhood of a crack in an elastic solid. Proceedings of the Royal Society of London, 1946. A-187: p. 229-260.
46. Williams, M.L., On the stress distribution at the base of a stationary crack. Journal of Applied Mechanics, 1957. 24: p. 109-114.
47. Rooke, D.P. and Cartwright, D.J., Compendium of stress intensity factors. 1976, London: Her Majesty's Stationary Office.
48. Wu, X.-R. and Carlsson, A.J., Weight Functions and Stress Intensity Factor Solutions. 1991: Pergamon.
49. Sanford, R.J., Principles of Fracture Mechanics. 2003: Prentice Hall.
50. Rice, J.R., Weight Function Theory for Three-Dimensional Elastic Crack Analysis, in Twentieth Symposium of Fracture Mechanics: Perspectives and Directions, ASTM Special Technical Publication 1020, R.P. Wei and R.P. Gangloff, Editors. 1989, American Society for Testing and Materials: Philadelphia. p. 29-57.
51. Gao, H. and Rice., J.R., Application of 3D Weight Functions - II. The Stress Field and Energy of a Shear Dislocation Loop at a Crack Tip. Journal of the Mechanics and Physics of Solids, 1989. 37: p. 155-174.
52. Irwin, G.R. Plastic Zone Near a Crack and Fracture Toughness. in Proceedings of the Seventh Sagamore Ordonance Materials Conference. 1960. New York, USA: Syracuse University.
53. Gdoutos, E.E., Fracture Mechanics: An Introduction (Solid Mechanics and Its Applications). 2005: Kluwer Academic Publishers.
54. Dugdale, D., S., Yielding of steel sheets containing slits. Journal of the Mechanics and Physics of Solids, 1960. 8: p. 100-104.
55. Barenblatt, G.I., The mathematical theory of equilibrium cracks in brittle fracture, in Advances in Applied Mechanics, H.L. Dryden and T.v. Karman, Editors. 1962, Academic Press: New York. p. 55-129.
56. Rice, J.R., Mechanics of crack tip deformation and extension by fatigue, in Fatigue crack propagation, ASTM STP 415. 1967, American Society for Testing and Materials: Philadelphia. p. 247-309.
57. Elber, W., The significance of fatigue crack closure, in Damage Tolerance in Aircraft Structures, ASTM STP 486. 1971, American Society for Testing and Materials: Philadelphia. p. 230-242.
58. Saxena, A., Nonlinear Fracture Mechanics for Engineers. 1998: CRC Press.

59. Rice, J.R., A path independent integral and the approximate analysis of strain concentration by notches and cracks. Journal of Applied Mechanics, Transactions of ASME, 1968. 35: p. 379-386.
60. Rice, J.R., Mathematical Analysis in the Mechanics of Fracture, in Fracture: An Advanced Treatise, H. Liebowitz, Editor. 1968, Academic Press: New York. p. 191-311.
61. Pavier, M.J., Poussard, C.G.C., and Smith, D.J., Effect of residual stress around cold worked holes on fracture under superimposed mechanical load. Engineering Fracture Mechanics, 1999. 63(6): p. 751-773.
62. Smith, M.C. and Goldthorpe, M.R., The treatment of combined residual and thermal stresses in defect assessments—Part 1 zero primary load. ASME PVP, 2000. 412: p. 197–204.
63. Smith, M.C. and Goldthorpe, M.R., The treatment of combined residual and thermal stresses in defect assessments—Part 2, with additional primary load. ASME PVP, 2000. 412: p. 205–215.
64. Meith, W.A. and Hill, M.R., Domain-independent values of the J-integral for cracks in three-dimensional residual stress bearing bodies. Engineering Fracture Mechanics, 2002. 69(12): p. 1301-1314.
65. Lei, Y., O'Dowd, N.P., and Webster, G.A., Fracture mechanics analysis of a crack in a residual stress field. International Journal of Fracture, 2000. 106(3): p. 195-216.
66. Lei, Y., J-integral evaluation for cases involving non-proportional stressing. Engineering Fracture Mechanics, 2005. 72(4): p. 577-596.
67. Wells, A.A. Unstable Crack Propagation in Metals: Cleavage and Fast Fracture. in Proceedings of the Crack Propagation Symposium. 1962. Cranfield, UK: College of Aeronautics, Cranfield Institute of Technology.
68. Bannantine, J.A., Comer, J.J., and Handrock, J.L., Fundamentals of Metal Fatigue Analysis. 1997: Prentice Hall.
69. Harter, J.A., AFGROW Users Guide and Technical Manual. AFRL-VA-WP-TR-2004. 2004.
70. Elber, W., Fatigue crack closure under cyclic tension. Engineering Fracture Mechanics, 1970. 2(1): p. 37-45.

CHAPTER 3: THREE-DIMENSIONAL RESIDUAL STRAINS & STRESSES IN STRESSWAVE COLD-WORKED HOLES BY DIFFRACTION METHODS

This chapter concerns an experimental study of the characteristics of the three-dimensional residual stress distribution in 6.35 mm thick aerospace 2024-T351 aluminium alloy plate treated with the StressWave cold-working process. The residual strain/stress fields inside the material were quantified using the time-of-flight neutron diffraction technique and complemented with surface stress data from X-ray diffraction analysis. The measurements reveal that StressWave specimens experience a highly compressive residual hoop stress around the hole region. Two- and three-dimensional hoop stress mapping reveals that the StressWave technique generates a symmetric stress distribution in the material, and produces a higher magnitude and larger zone of compressive hoop stress field when compared to that produced by the traditional split-sleeve mandrelising method.

3.1. Introduction

The traditional FTI split-sleeve cold hole expansion method involves drawing an oversized mandrel through a hole interfaced with a lubricating split-sleeve to cause yield and subsequently introduce a beneficial compressive residual stress [1]. The method is widely practised to improve the fatigue properties fastener holes in aerospace structures. Previous work has shown this conventional cold-working technique induces rather complex three-dimensional residual stress distributions [2, 3]. This consequently causes complex cracks to propagate at dissimilar rates around the treated hole [4], and hence introduces uncertainties in modelling fatigue life.

Recently, in it has been shown that the novel StressWave (SW) cold-working method substantially improves crack symmetry and produces a higher fatigue life compared to the

conventional practice [5, 6] (see also Chapter 1). The observations suggest that more reliable fatigue crack growth prediction can be anticipated as the complexity of crack shape and residual stress required for modelling is reduced. As it is the nature of the plastic deformation, and the resulting residual stress that is responsible for such fatigue behaviour, for detailed analysis full information of the residual stress field is required. The neutron scattering technique was used to probe the residual stress field deep within the material whilst surface stress data was measured by the laboratory X-ray diffraction method.

3.2 Specimen Preparation

3.2.1 Plate material & geometry

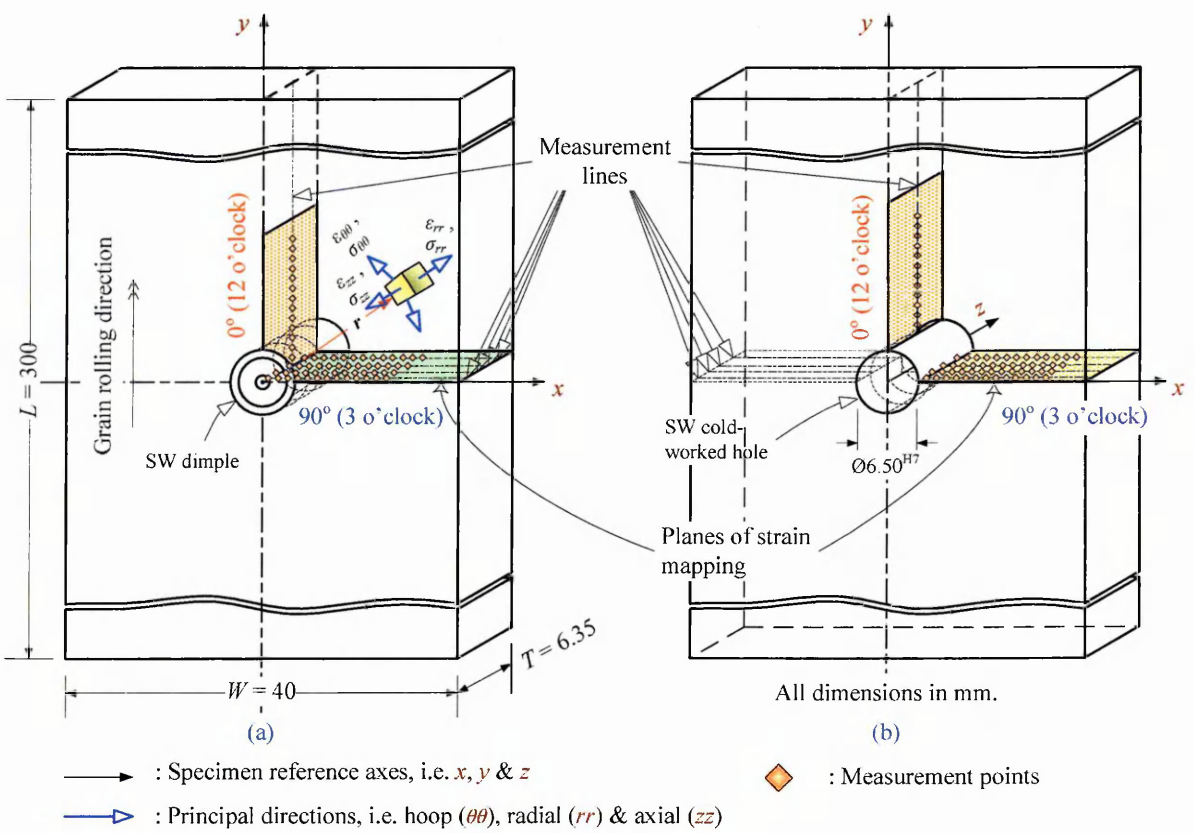

Figure 3.2.1 Schematic of samples treated using StressWave process: (a) with permanent indention or dimple (pre-reamed), and (b) cold-worked hole (post-reamed); both showing the principal directions and locations of neutron measurement.

The material used in the present investigation is aerospace grade 2024-T351 aluminium alloy plate. Two types of SW sample of dimensions 6.35 × 40 × 300 mm^3 (i.e. thickness × width × total length) were measured: a pre-reamed specimen contains a pair of concentric

dimples after cold-worked by SW indentation process (Figure 3.2.1(a)) but without a hole ; a post-reamed specimen contains a central Ø6.50 mm SW cold-worked fastener hole (Figure 3.2.1(b)) after drilling and reaming a hole on a pre-reamed specimen.

3.2.2 StressWave cold-indentation

The material used is supplied by the Department of Materials Engineering, The Open University. The plates were extracted from a larger sheet, and semi-machined to the specifications given in Figure 3.2.1 but without cold-working and reaming. The cold-working process was prepared by StressWave, Inc, USA using specially designed indenters [5]. Final holes were also drilled and reamed immediately after the cold-working. The 0.635 mm applied indentation used here was calibrated from finite element (FE) analysis by the manufacturer. The amount of indentation depth was optimised from several SW computer simulations by studying the possible magnitude and pattern of residual stress across the specimen width and thickness.

According to FE results, a more compressive residual stress field can be induced around the hole bore by deeper indentation, which is beneficial to raise the degree of fatigue life enhancement further in SW holes. However, bearing in mind that the width of the present specimen, W is fairly narrow, greater indentation also inevitably generates a higher balancing tensile residual stress at the outer edge of the specimens. When sufficiently high, the total effective stress resulted from the superimposed tensile residual and applied stresses can cause premature failure of the specimen edge under tensile fatigue loading [7].

3.3 Neutron Diffraction Experiment

3.3.1 Time-of-flight (TOF) neutron diffraction

The neutron diffraction measurements were carried out at the ENGIN-X engineering instrument at the ISIS spallation pulsed-neutron source, Rutherford Appleton Laboratory

near Didcot. ENGIN-X has two multi-detector banks which set the angle 2θ between the incident and diffracted beams at ± 90°. Operating on the time-of-flight (TOF) principle employing a white neutron beam, ENGIN-X records time-resolved spectra.

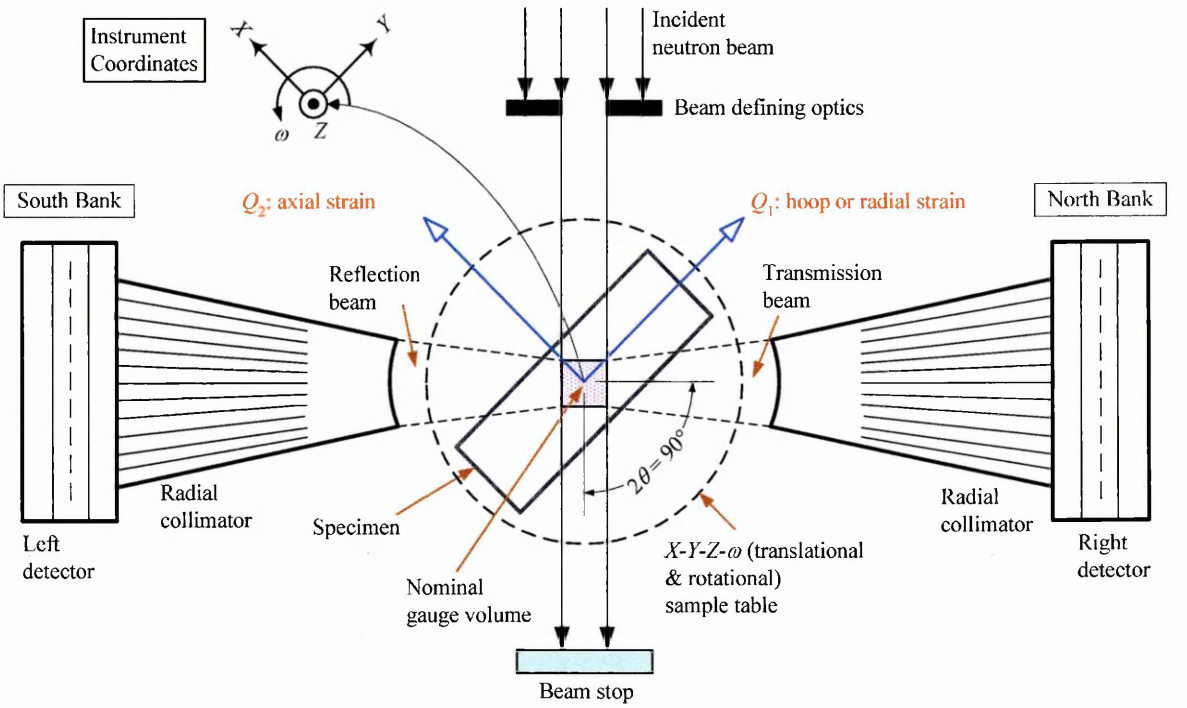

Figure 3.3.1 Bird's-eye schematic of the experimental setup at the ENGIN-X instrument in ISIS. The two detectors measure strain components in perpendicular directions, each at ± 45° to the incident neutron beam.

In Figure 3.3.1, the scattering vectors Q_1 & Q_2, are positioned either parallel or perpendicular to the specimen axis, i.e. at ± 45° to the incident beam. The orientation of the two detector banks each at ± 90°, making it possible to measure the strain components in two perpendicular axes simultaneously. (A typical diffraction spectrum obtained from Al 2024-T351 is shown in Figure 3.3.4). Full details on the neutron diffraction technique for residual strain/stress characterisation in materials are described elsewhere [8-10].

3.3.2 Experimental design & set-up

The three-dimensional residual stress field was determined at the two planes along (i.e. 0° / 12 o'clock position) and perpendicular (i.e. ± 90° / 3 or 9 o'clock position) to the grain flow direction of the plate, as indicated in Figure 3.2.1. Detailed scanning was also performed to map the three-dimensional residual strain/stress field created around the SW dimple (pre-reamed) and SW hole (post-reamed), and these results are compared to those

of split-sleeve cold-expanded holes measured earlier [3]. The mapping points on these planes are schematised in Figure 3.2.1 and detailed in Figure 3.3.2. For all three principal directions, four lines (13 ~ 15 points per line) corresponding to 1/9, ¼, ½ and ¾ of the specimen thickness were measured. However, for the 12 o'clock orientation, only the mid-thickness line was investigated.

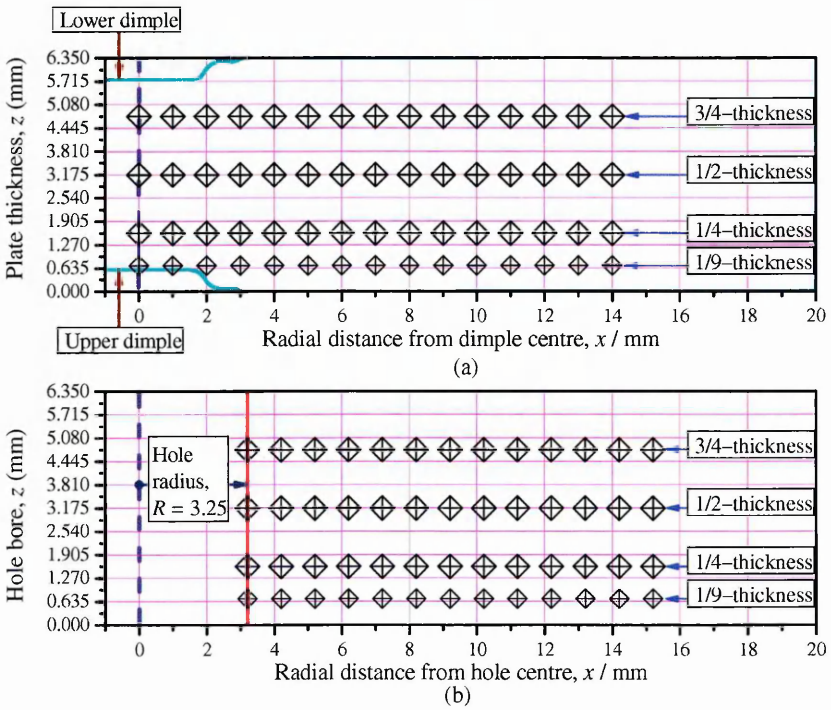

Figure 3.3.2 Measurement points on the mapping planes of SW samples: (a) with permanent indentation or dimple (pre-reamed), and (b) cold-worked hole (post-reamed) at the ±90° / 3 or 9 o'clock orientations.

The neutron diffraction experiment was conducted by measuring orthogonal strains on the assumed principal axes along the hoop, radial and axial orientations, starting from the SW dimple centre (Figure 3.2.1(a)), or from the transverse edge of the SW hole corresponding to the minimum cross-section of the plate (Figure 3.2.1(b)).

Accurate and reliable residual stress measurement requires the precise knowledge of the locations of gauge volumes with respect to the specimen surfaces, before the spatial positions of desired measurement points of Figure 3.3.2 can be established inside the material [8, 11]. This is achieved by a rapid wall-scanning technique at multiple discrete points, firstly performed across the specimen thickness, T, and followed by scanning from the hole boundary, R, to the outer edge of the specimen, $W / 2$ (Figure 3.2.1). The collected

diffraction intensity data were fitted into a Sigmoidal or Gaussian model to depict the integrated neutron intensity profile, I, as a function of the gauge volume locations passing into and out of the specimen. The location of specimen surfaces, and hence the gauge volume position were then determined to ± 0.1 mm precision, and optically confirmed by the use of alignment theodolites.

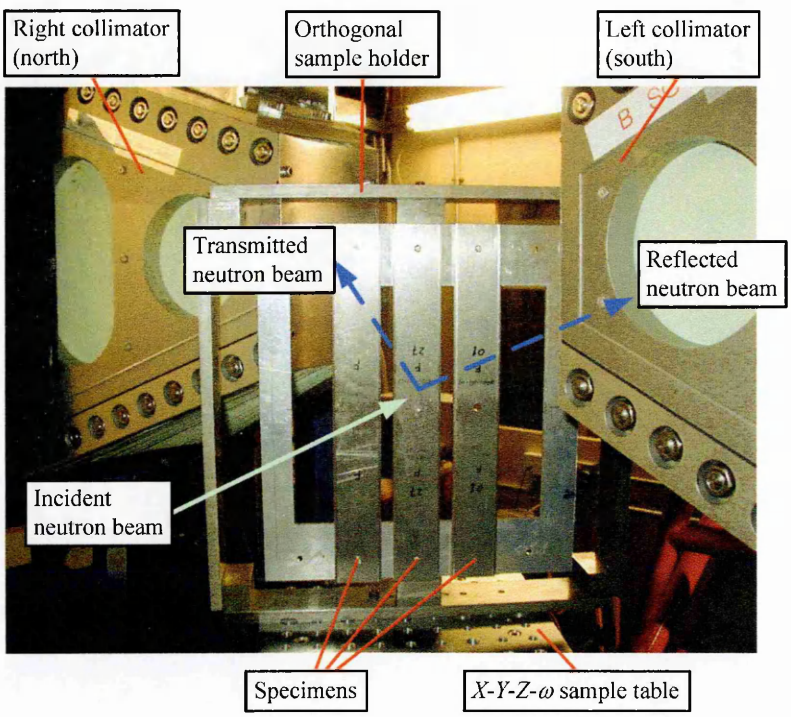

Figure 3.3.3 Experimental set-up for residual strain measurement surrounds StressWave cold-worked specimens on ENGIN-X. Left: as-received material for d_o calibration; middle: pre-reamed SW specimen with dimple; right: post-reamed SW specimen with Ø 6.50mm hole.

Considering the symmetry of the specimen geometry and SW cold-working technique, the principal strains/stresses in the hoop, radial and axial directions (σ_{ij} or ε_{ij} ; $ij = \theta\theta$, rr and zz) were assumed to align along the specimen major x-y-z axes (Figure 3.2.1). Consequently, the stress tensor can be determined from just the three principal strain components [12]. This was achieved by fixing the specimens on a square prismatic orthogonal frame (Figure 3.3.3). A precision ground stainless steel frame was specially fabricated, so that a reference point equidistant from the two most orthogonal faces of the frame was identified. Using a high resolution metrology table a known specimen reference point was marked and the specimen was later fixed with respect to the frame reference point. Previous research using an identical arrangement was reported to have achieved an orthogonality within 1° tilt for

scanning made in three orthogonal directions [9, 13]. The frame enables quick re-alignment of the specimen for subsequent orthogonal measurements.

To obtain the hoop or axial component, the long-axes (L) (in Figure 3.2.1) of the specimens were orientated horizontally. A cubic gauge volume of nominal dimensions $2 \times 2 \times 2$ mm^3 was selected: the incident slit used was 2 mm wide × 2 mm high, combined with a 2 mm radial collimator (viz. effective spatial resolution FWHM = 2 mm). For the radial and other axial component the specimen L-axes were positioned vertically and a $2 \times 4 \times 2$ mm^3 gauge volume was used. An exception is the lines at 1/9 specimen thickness (Figure 3.3.2): when a finer $1 \times 2 \times 1$ mm^3 gauge volume was employed to capture the high stress gradient near to the specimen surface. Diffraction spectra were acquired using exposure times of approximately 30 ~ 90 minutes per point at a beam current of 150 mV per hour and this varied depending on the gauge volume and statistical errors computed from the spectrum fitting routines.

3.3.3 Material stress-free lattice parameter, a_0

For strain determination, the reference stress-free lattice parameter of the plate material, a_0 was measured using the same gauge volumes at several pre-determined locations in a separate virgin Al 2024-T351 specimen similar to some locations in Figure 3.3.2 but without SW treatment. Several a_0 values extracted from the mid-thickness region of the as-received plate were averaged, and then used as the representative a_0 value for neutron strain/stress calculations outlined in Section 3.3.6. For consistency, separate a_0 values were used for each detector. Independently, a stress-free a_0 for a pure Al-powder contained in a vanadium tube was also measured as part of the experiment calibration procedure. The a_0–value of pure Al-powder was used to verify the repeatability of ENGIN-X measurement with respect to the previous calibrated spectrum for a similar substance.

3.3.4 Pseudo-strain & scattering gravity corrections for near surface effects

To quantify the strain/stress very close to the hole boundary (Figure 3.2.1 (b)), these locations inevitably give rise to the instrument gauge volume being only partially-immersed within the material. Under this condition, the centroids of the partially-filled (sampling) gauge volumes no longer represent the centre of the regular instrumental gauge volume, and only a fraction of the multi-collimated radial detectors see the sample. This situation leads to both geometric and scattering attenuation of neutron beam that causes a spurious pseudo strain to be measured. Pseudo-strains misrepresent the true strain state at the surface, and that can further introduce anomalous effect on the resultant stress components [10, 14]. The magnitude of the pseudo strain is dependent on the experimental configurations used and is instrument-specific.

As may be seen from the instrument coordinates in Figure 3.3.1 along with the specimen geometry in Figure 3.2.1, only the *X*- or *Y*-scanning mode performed at the hole edge is susceptible to irregular surface effects. For the *Z*-scanning mode no pseudo-strains are generated as the gauge volume moves out of the surface [15]. As a result, only the radial (*rr*) and axial (*zz*) components probed with partially-filled gauge volumes under the *X*- or *Y*-translation mode needed to be corrected.

Numerous methods to implement surface pseudo-strain corrections have been proposed [10, 14]. In this text, we considered the empirical-instrumental correction of Wang & Edwards [13] developed specifically for TOF instruments such as ENGIN-X (Figure 3.3.1). The approach was concocted based on the stress state equilibrium in thick-walled tube [16], or circular hole in infinite thin plate undergone elastic-plastic deformation by radial expansion [17]. Upon the removal of applied internal pressure or radial traction, the radial residual stress, σ_{rr} must be zero right at the hole bore. Therefore, in the neutron data

any strong deviations from zero stress condition in the unrevised radial residual stress at the hole edge manifests the presence of significant pseudo-strain due to the surface effects.

The Wang & Edwards approach only considers the strain/stress information slightly away from the hole edge [13]. Here, by extending the original idea in reference [13] the residual strain/stress values at the hole bore exactly have been estimated. This piece of information is critical for accurate computation of stress intensity factor for small cracks of 0.1 ~ 2.5 mm size under the influence of residual stress. In fatigue crack modelling, as the majority of fatigue life is spent when the cracks are still short, the local behaviour of small crack growth in residual stress fields is decisive in the accuracy and reliability of estimation [18]. The extended procedure for pseudo-strain correction is given in Appendix 3–A.

In addition, at the hole boundary the partly-immersed gauge volume assumes an irregular profile, and causes the determination of the scattering centre to be more complicated than for regular cubic or diamond-shaped gauge volumes. For the affected gauge volumes, the location of the new diffraction centre must be identified to reflect the actual measurement positions. Thus, the scattering centres of the affected positions were calculated according to the partially-filled geometry of the affected gauge volume. In other words, the geometrical centroid of the straddled gauge volume is made identical to those of the diffracting volume assuming no beam attenuation. This simplification is justified because the neutron attenuation coefficient, μ_a for aluminium is fairly weak, i.e. 0.01 mm^{-1} [10, 19]. In this case, the maximum path length the neutron beam travelled in the specimen thickness, T, is 16.54 mm with approximately 84.8% of depleted beam intensity remaining throughout the measurement process. For validation, the diffraction centres for straddled gauge volumes were estimated separately using the strain scanning simulation software (SScanSS) [20] written to assist experiment planning in ENGIN-X.

3.3.5 Time-of-flight diffraction pattern analysis

In this investigation, the lattice parameters a, required for subsequent strain determination were extracted from simultaneous multi-peak fitting of the entire diffraction spectrum using the Pawley-Rietveld refinement technique [21, 22]. The fitting routine was incorporated into the General Structure Analysis System (GSAS) code [23], and was part of the Open GENIE software developed at the ISIS spallation neutron facility.

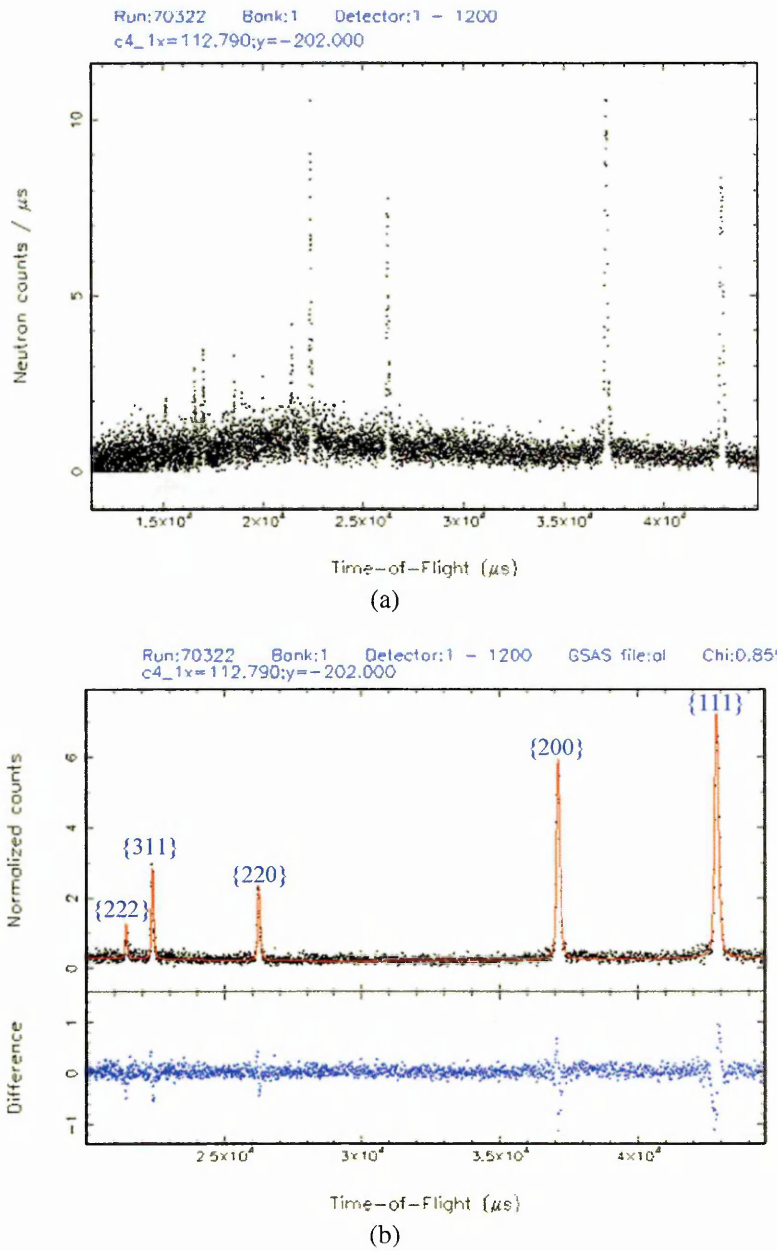

Figure 3.3.4 (a) A representative neutron diffraction spectrum of 2024-T351 aluminium alloy recorded on the ENGIN-X time-of-flight instrument. (b) Selected low order peaks have been labelled. These peaks relate to the lattice strain in crystallites of particular orientations with respect to the scattering vector and specimen direction.

Since the contributions from various {*hkl*} diffraction peaks appearing in the TOF spectrum are collectively weighted to establish the most representative lattice parameter, the result is generally less susceptible to elastic and plastic anisotropies [24]. Pawley refinement [21] is more advantageous for textured polycrystalline materials as the Rietveld procedure [22] is not flexible enough to treat the variation in intensities height due to material anisotropy. In the Pawley method, all the {*hkl*} peak positions are refined using the reference unit-cell parameters, while intensities are allowed to vary. Only the five most prominent peaks of (111), (200), (220), (311) and (222) reflections were analyzed to produce the lattice parameters, *a*.

3.3.6 Strain & stress determination from neutron diffraction

For a polychromatic beam, the volumetric lattice strain, ε is determined from the changes in the lattice spacing Δa (= $a - a_0$) with respect to their unstrained value d_0 in a stress-free state. At an arbitrary *ij*-direction, the elastic engineering strain may be expressed as [25]

$$\varepsilon_{ij} = \frac{a_{ij} - a_{0,ij}}{a_{0,ij}} \tag{3.3.1}$$

From the strain measured along different *ij*-directions, the corresponding stress is calculated using the generalised Hooke's Law equation [12]:

$$\sigma_{ij} = \frac{E}{1+\nu}\varepsilon_{ij} + \frac{\nu E}{(1+\nu)(1-2\nu)}\delta_{ij}\varepsilon_{kk} \tag{3.3.2}$$

where *k* is a dummy suffix summing over all *k*s, i.e. $\varepsilon_{kk} = \varepsilon_{11} + \varepsilon_{22} + \varepsilon_{33}$. δ_{ij} is Kronecker's delta function: $\delta_{ij} = \begin{cases} 1, \text{for } i = j \\ 0, \text{for } i \neq j \end{cases}$ The elastic constants were taken from the measured bulk values, namely Young's modulus $E = 71.9$ GPa and Poisson's ratio $\nu = 0.328$.

3.4 X-ray Diffraction Experiment

3.4.1 Experimental set-up

To complement the neutron data inside the plate, the laboratory X-ray diffraction technique was used to measure the surface residual stress induced around a SW hole. To reduce the experiment duration, only the hoop component was measured at the minimum transverse section of the specimen, starting from the hole edge (Figure 3.4.1). From the perspective of fracture mechanics, it is the hoop stress field along the crack path, rather than its radial or axial counterparts, which has direct effect on the entire crack face opening profile under superimposed loading [26]. Much attention has been paid to the hoop residual stress field in cold-worked holes for the purpose of fatigue crack growth modelling [27].

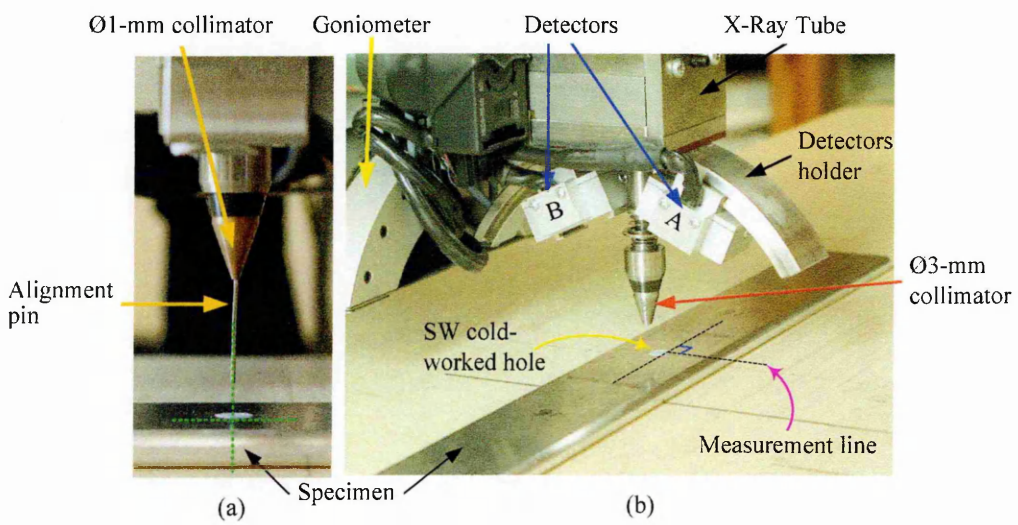

Figure 3.4.1 Experimental set-up of X-ray diffraction measurement in SW cold-worked hole.

The ψ–mode multi-exposure measurement was performed using the 'd versus $\sin^2\psi$' approach [25, 28] in a Stresstech X-STRESS 3000 X-ray diffractometer, and the experimental set-up is shown in Figure 3.3.1. The horizontality of the specimen table with respect to the X-ray measurement head unit was aligned to ± 0.1° using an electronic level. Careful position alignment of measurement lines with respect to the X-ray beam unit was conducted using a straight steel pin engaged in an Ø1-mm collimator, whose position was controlled precisely with a motorised X-Y-Z-ω translator (Figure 3.4.1 (a)). A circular Ø3-mm collimator was chosen for actual measurement. The SW hole was filled with plasticine

to eliminate possible diffraction contributed from the material inside the hole bore when surface measurement was made near to this region.

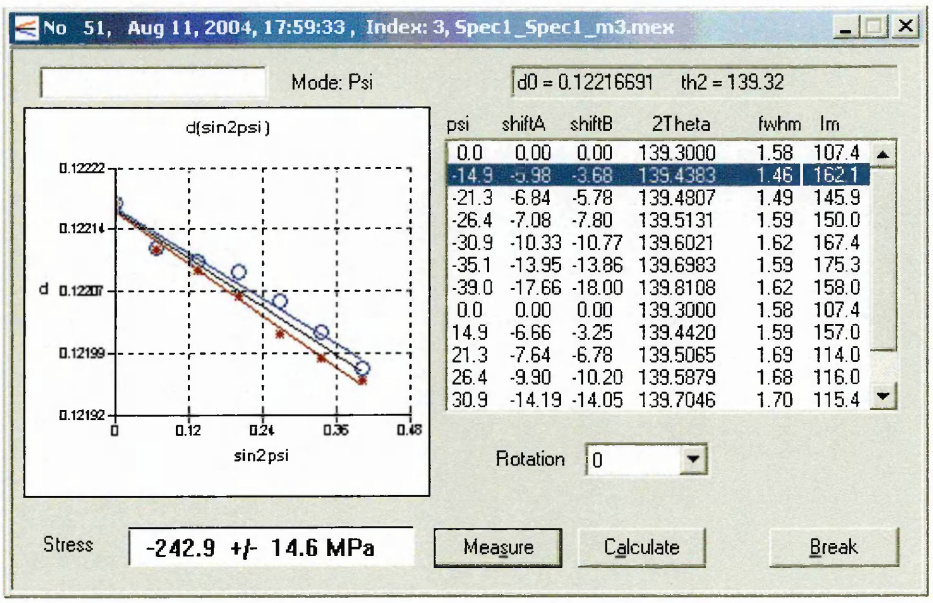

(a)

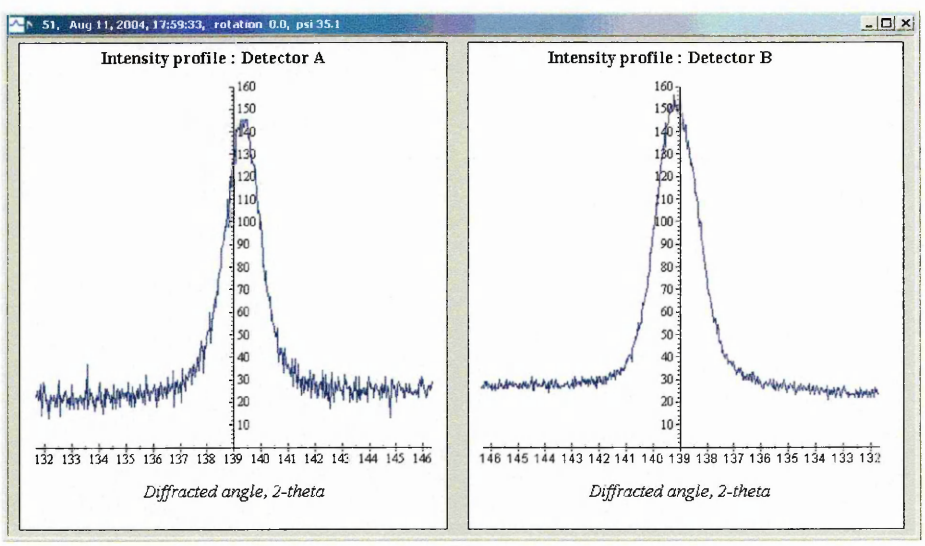

(b)

Figure 3.4.2 (a) Linear plot of 'd versus $\sin^2\psi$' plot. (b) Typical X-ray diffraction profiles recorded concurrently at the two detectors A and B.

The X-ray tube operates at voltage 30kV and a current of 6.7mA, emitting CrKα radiation of monochromatic wavelength λ_α ~2.291Å. Therefore, by selecting the aluminium (311)–reflection, a single diffraction peak of angle of $2\theta \approx 139°$ is produced [28]. A total of 27 hoop stress measurements were made along the predetermined line, each 0.5 mm distance apart starting from the hole edge. Each point was assigned 14 ψ-tilts spread evenly over ± 42° inclination range to establish a sufficiently linear trend as prescribed by the 'd versus

$\sin^2\psi$' plot (Figure 3.4.2(a)). A small amount of ± 3° ψ-oscillation, i.e. specific oscillation of the incident beam about each ψ-inclination angle, was also incorporated to improve accuracy due to the complications of large-grain size or texture in the material [28].

3.4.2 Data collection & analysis

For data acquisition, two position-sensitive MOS (metal oxide semiconductor) Linear Image Sensor detectors were positioned symmetrically at the desired 2θ–position along the arc-shaped holder (Figure 3.4.2 (b)). The angular resolution of the detectors is 0.029°/pixel with 512 pixels/ 12.8mm [28, 29]. Each ψ-tilt only required 10 ~ 20 seconds exposure time to produce two independent diffraction profiles (Figure 3.4.2(b)) from the two detectors A and B (Figure 3.4.1(a)). The individual angular peak shift of the intensity, $\Delta 2\theta$ was calculated using the global method of cross-correlation, in which the whole intensity distribution is utilised [25]. The default database values of Young's modulus, E_{311} = 70.6 GPa and Poisson's ratio, ν_{311} = 0.345 were used to define the elastic constants required in the stress calculation; these material parameters are comparable to Kröner theoretical modelling [30] and four-point bending tests for Al2024-T351 [31].

3.4.3 Residual stress calculation from X-ray diffraction

The attenuation length of Cr-Kα radiation for aluminium is rather low, namely about 0.0234mm, and therefore the measurement is only effective for a fairly thin surface layer. This permits us to use a bi-axial/plane stress analysis [25, 32] on the plane of measurement i.e. specimen surface. Only the salient features of the 'd versus $\sin^2\psi$' approach for practical application are described here. Knowing the constant wavelength λ_{311} and diffracted 2θ–angle from the detectors, the d_ψ–spacing can be calculated for any ψ-tilt using Bragg's law. These data of d_ψ-spacing are then fitted with linear regression scheme against the $\sin^2\psi$ component (Figure 3.4.2):

$$\frac{d_\psi - d_0}{d_0} \approx \frac{d_\psi - d_\perp}{d_\perp} = \left[\frac{(1+\nu_{hkl})}{E_{hkl}} \cdot \sigma\right] \cdot \sin^2\psi \qquad (3.4.1)$$

The unknown d_0 was approximated by the measurable $d_\perp$ (= $d_{\Psi=0}$) normal to the specimen surface with negligible error. The slope of the fitted curve given in the bracket, as related to equation (2.4.10), was then employed to infer the measured surface stress, σ (i.e. equation (2.4.11)) The method allows in-plane stress components to be measured expediently from a series of ψ-inclination without the prior knowledge of the stress free reference d_0 [28, 32].

3.5 Results and Discussion

SW specimens containing a permanent dimple and a cold-worked hole were successfully measured using neutron and laboratory X-ray diffraction. The typical neutron strain and stress errors estimated in the present measurement range between about ± 30 ~ 40 $\mu\varepsilon$ and ± 5 ~ 10 MPa respectively. For X-ray measurement the stress error was ± 10 ~ 20 MPa.

At locations measured with a small gauge volume, and especially near to the hole edge, although improvement may be attained from means of longer exposure, this was not practical within the time available on the instrument. Also, given the finer gauge volumes chosen and subsequently longer exposure time required, the measurement lines corresponding to 1/9–thickness of the plate were only partially completed and therefore subjected to higher statistical errors. However, for completeness all the measurement results are incorporated in the following sections.

3.5.1 StressWave indented specimen

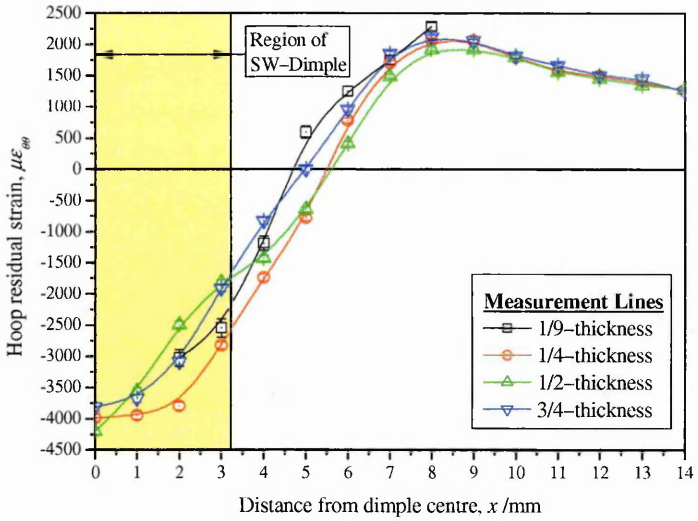

(a) Hoop strain

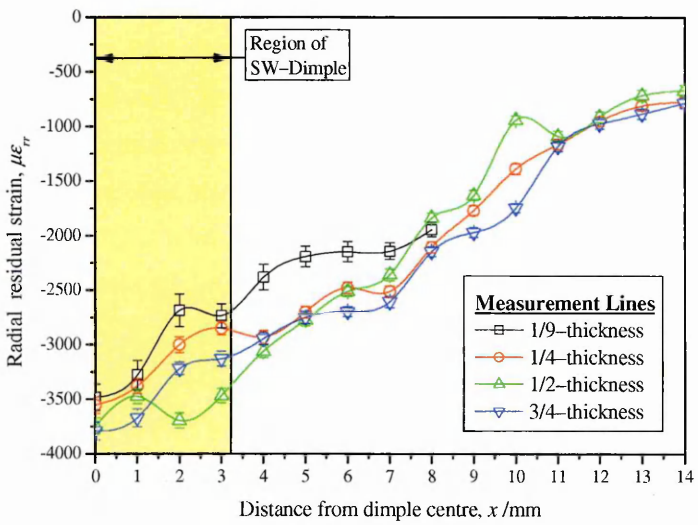

(b) Radial strain

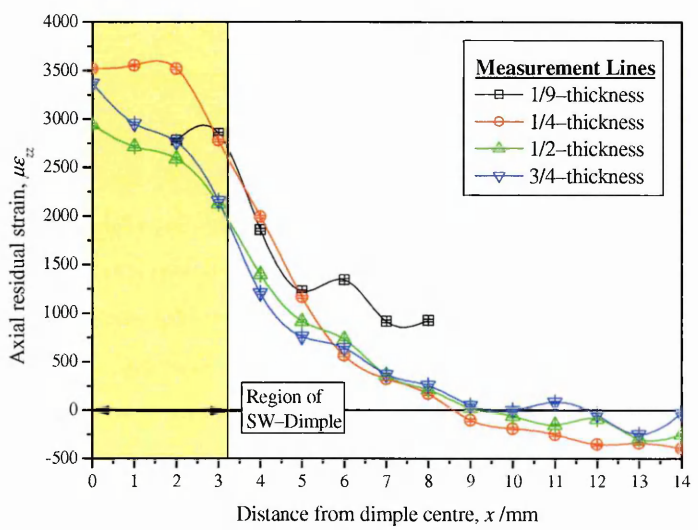

(c) Axial strain

Figure 3.5.1 Hoop, radial and axial residual strains measured along the lines corresponding to 1/9, ½, ¾ and ¼ thickness in a SW indented specimen; 3 o'clock direction.

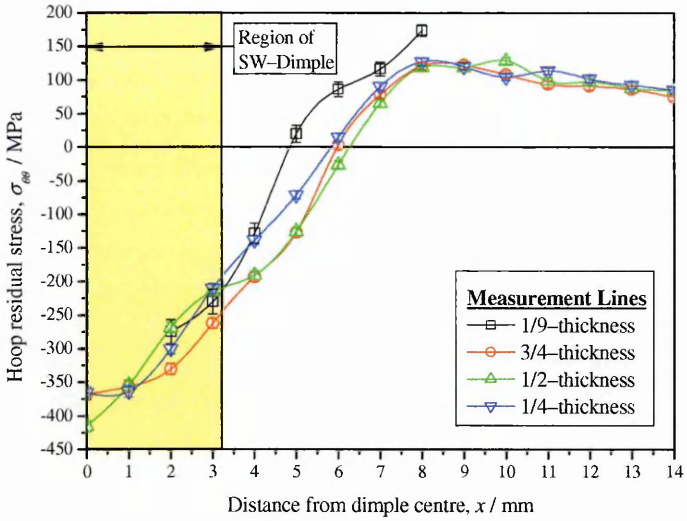

(a) Hoop stress

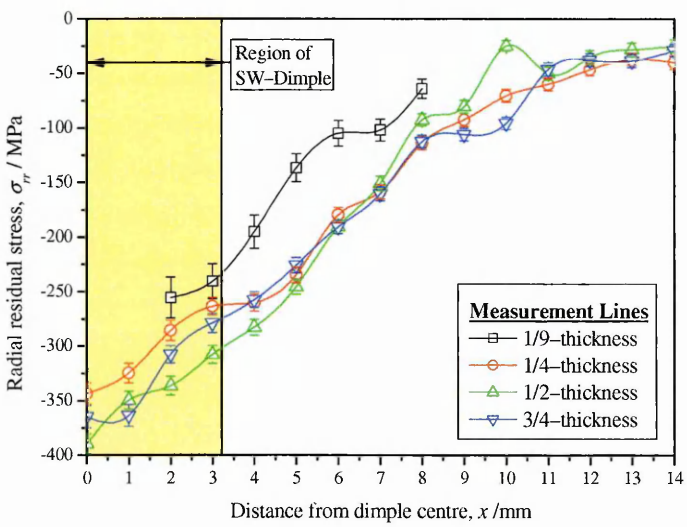

(b) Radial stress

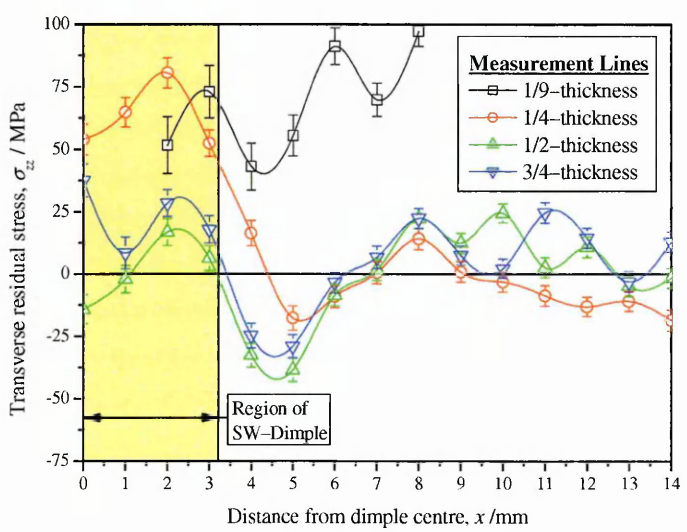

(d) Axial stress

Figure 3.5.2 Hoop, radial and axial residual stresses measured along the lines corresponding to 1/9, ½, ¾ and ¼ thickness in a SW indented specimen; 3 o'clock direction.

Figure 3.5.1 shows the principal residual strains around the permanent dimple introduced by SW cold-indentation as a function of position in the measurement planes (Figures 3.2.1

& 3.3.2), whilst the associated principal stresses are presented in Figure 3.4.2. The residual hoop ($\theta\theta$) strain/stress is compressive within approximately 4.5~5.5 mm and 4.75~6.25 mm radius, respectively, from the dimple centre. Further away from the hole, the hoop compressive zone is counterbalanced by an outer rim of material of tensile residual strain/stress.

The residual strain/stress in the radial (rr) orientation is entirely compressive in the specimen with SW dimple (Figures 3.5.1 & 3.5.2). In contrast, the axial (zz) component is mainly tensile starting from the dimple centre and gradually reduced to slightly compressive away from the indented region. The axial stress fluctuates from tension to compression from the centre of the dimple and its magnitude is lower compared to the other two principal counterparts. Overall, the 1/9-thickness data seems to replicate the strain/stress patterns of ¼, ½ and 3/4 -thickness locations. Since the gauge volume used to probe the 1/9-thickness lines were comparatively smaller, the measured data is vulnerable to a higher range of strain/stress error (Figures 3.5.1 & 3.5.2).

As can be seen from Figure 3.5.3, the principal strain/stress fields measured at 12 and 3 o'clock are very similar. Such behaviour suggests that the radial plastic deformation spread outward of the indentation site is fairly symmetric. Albeit with a slight discrepancy in Figure 3.5.3 for the SW dimple, it will be shown later (Figure 3.5.7) that upon the creation of the hole the difference of residual strain/stress field for 12 and 3 o'clock becomes more obvious. This effect is caused by dissimilar unloading pressures acting at different directions around the hole.

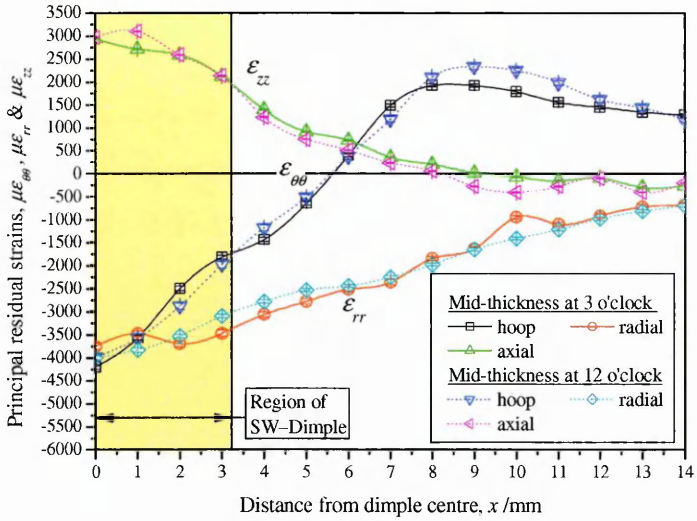

(a) Principal residual strains

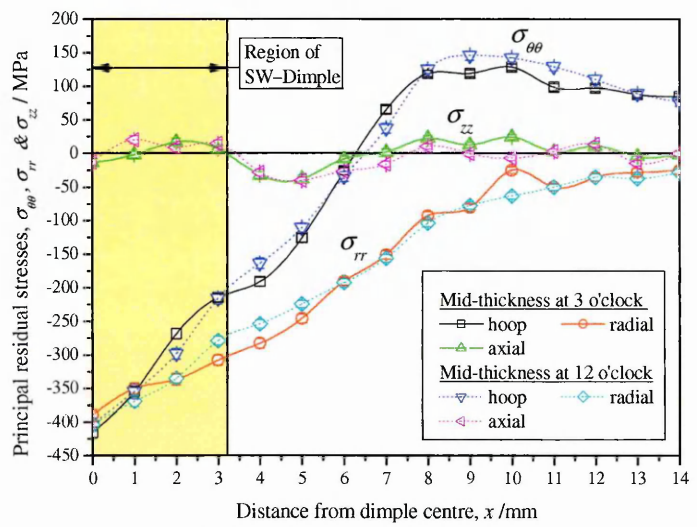

(b) Principal residual stresses

Figure 3.5.3 Comparison of mid–thickness principal residual strains/stresses at 3 and 12 o'clock orientations around a StressWave indented dimple.

3.5.2 StressWave hole data with & without pseudo-strain amendment

The principal strains/stress distribution along the mid-thickness line in the 3 o'clock direction, before and after pseudo-strain correction, is shown in Figure 3.5.4. For the first measurement point very close to the hole, the actual centre of the gauge volume is located at x = 3.72 mm as compared to the original value of x = 3.25 mm of a full cubical shape.

At x = 3.72 mm, it could be seen that the newly interpolated radial strain (ε_{rr} = 773 $\mu\varepsilon$) is approximately three times higher than the measured pseudo-strain (217.6 $\mu\varepsilon$). Evidently, the total difference $\Delta\varepsilon_{rr}$ = 555.4 $\mu\varepsilon$ is a direct consequence of the anomalous surface effect that misrepresents the strain state in the material. At the hole edge x = 3.25 mm, a 1887 $\mu\varepsilon$

radial strain is predicted from Equation (3.A2) (Figure 3.5.4(a)), which satisfies the compulsory condition of zero radial stress at the hole edge (Figure 3.4.4(b)). Of course, the hoop and axial residual strains at x = 3.72 mm remain unchanged under vertical Z-scanning mode. Accordingly, at the hole edge (x = 3.25 mm) by spline-extrapolating the unaffected dataset the hoop and axial strains are predicted to be –4714 $\mu\varepsilon$ and –138 $\mu\varepsilon$, respectively.

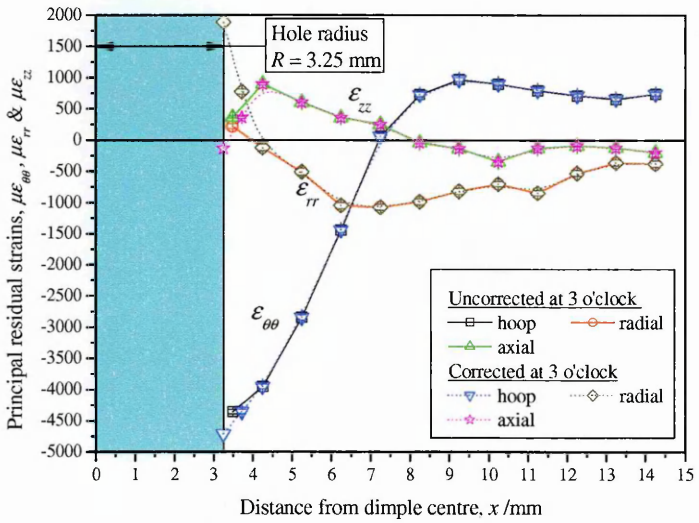

(a) Principal residual strains

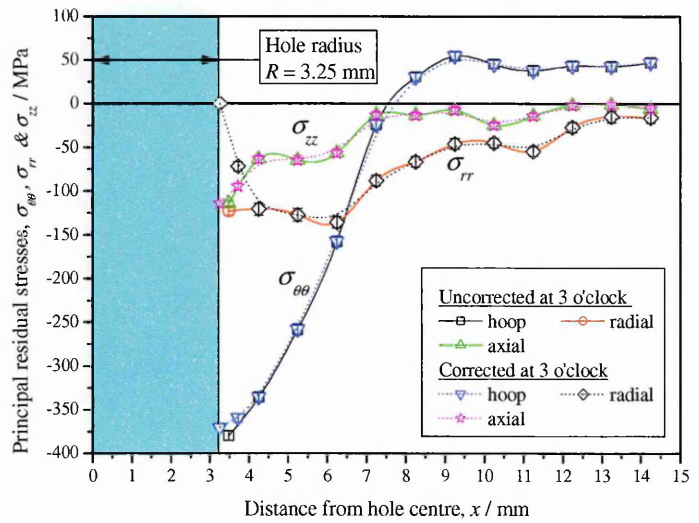

(b) Principal residual stresses

Figure 3.5.4 Principal residual strains/stresses measured along the lines corresponding to mid–thickness in a SW hole specimen; 3 o'clock direction (before and after pseudo-strain correction).

The overall trend of the residual strains/stresses at the SW hole shows excellent agreement with the literature of cold-expanded holes studied using various methods [2, 17, 27, 33-37]. However, a closer examination of Figure 3.5.4(b) reveals that the original principal stresses computed without the pseudo-strain amended result in more compressive behaviour near to the hole bore. When interpolated to the hole edge (x = 3.25 mm), the difference between

the revised and original data is about 51 MPa in radial stress and 20 MPa in hoop and axial stress. The corrected data indicate that there is some reduction of compressive hoop stress at the hole boundary. Previously, at the similar location in cold-expanded holes, pronounced residual stress relaxation was observed from destructive Sach's boring, and this pattern was also confirmed by separate neutron diffraction experiment adopting pseudo-strain correction [13, 33]. In contrast, the neutron result of Webster *et al.* has shown that neglecting the anomalous surface effect the uncorrected radial stress at the hole can reach as high as –150 MPa [38], rather than zero stress.

Stress relaxation within the region of reversed yielding is always accompanied by Bauschinger's behaviour in the Al 2024-T351 aluminium alloy [35, 37]. Coincidentally, this region starting from the hole edge is also the incipient sites of small cracks under fatigue load where the applied tensile hoop stress is a maximum [12]. Because a major fraction of the fatigue life is spent at the short crack stage, the accurate estimates of the residual stress field at these locations are critical for accurate fatigue life prediction.

3.5.3 StressWave hole specimen

Using the pseudo-strain corrections proposed in Appendix 3–A for an SW hole, the complete residual strain/stress fields along the measurement lines at several pre-determined locations of specimen thickness are presented in Figures 3.5.5 & 3.5.6. At the specimen mid-thickness adjacent to the hole bore, the magnitude of induced compressive hoop strains/stresses are the largest, and decrease gradually at ¼ or ¾ and then 1/9-thickness line approaching the specimen surfaces.

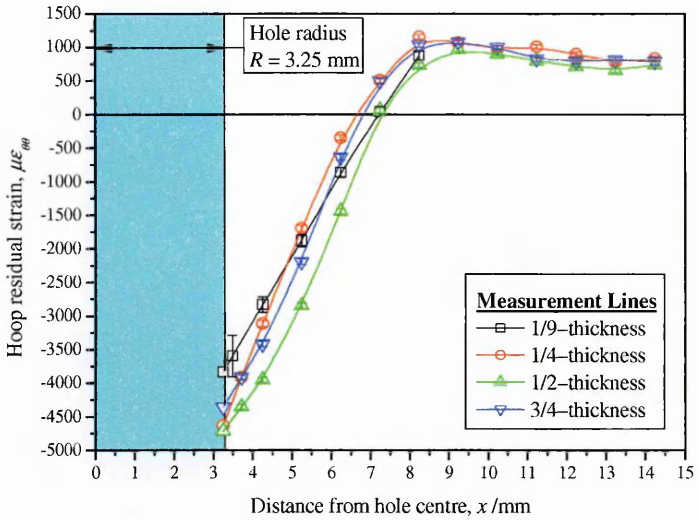

(a) Hoop strain

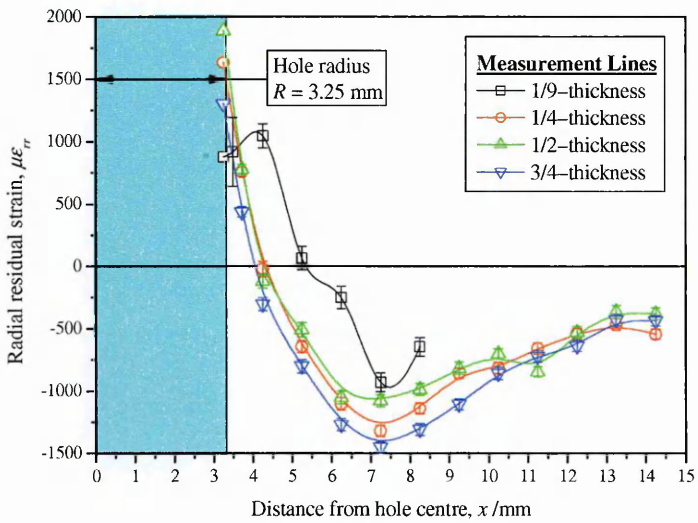

(b) Radial strain

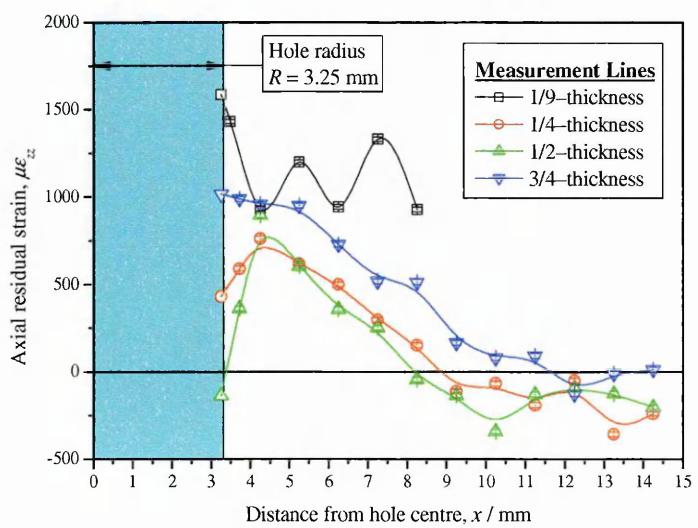

(c) Axial strain

Figure 3.5.5 Principal residual strains measured along the lines corresponding to 1/9, ½, ¾ and ¼ thickness in a SW hole specimen; 3 o'clock direction (with pseudo-strain correction)

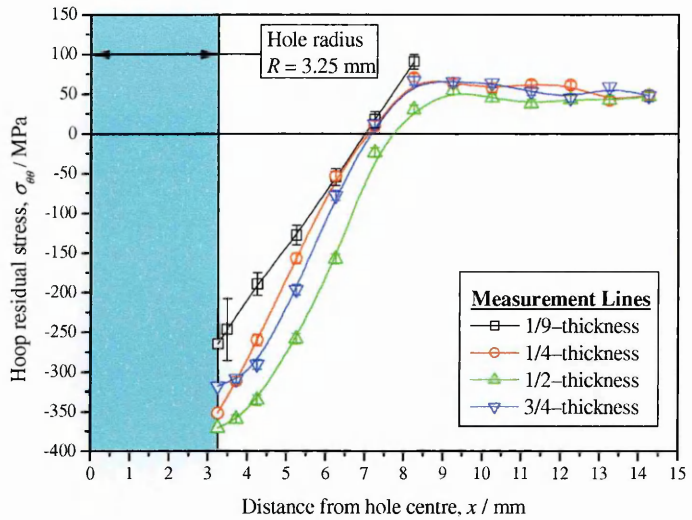

(a) Hoop stress

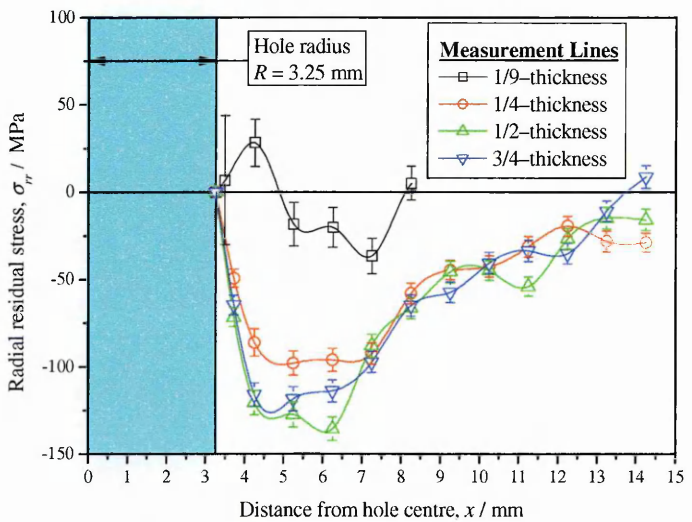

(b) Radial stress

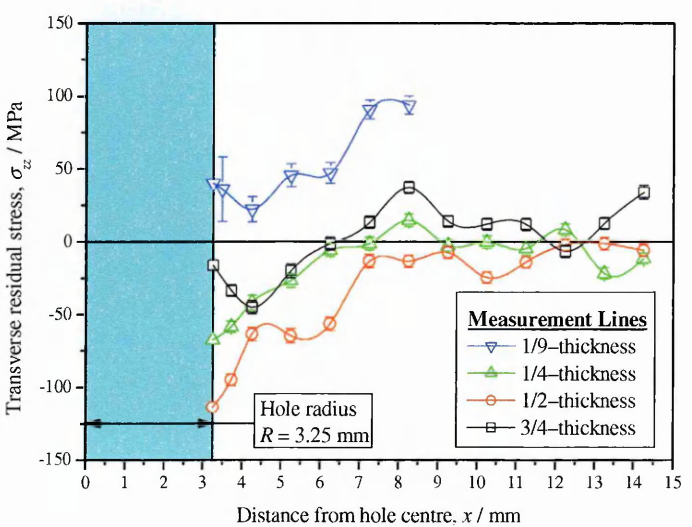

(c) Axial stress

Figure 3.5.6 Hoop, radial and axial residual stresses measured along the lines corresponding to 1/9, ½, ¾ and ¼ thickness in a SW hole specimen; 3 o'clock direction (with pseudo-strain correction)

Figure 3.5.7 plots the mid-thickness hoop strain/stress for the 12 o'clock direction to the plate rolling direction, which is slightly lower than its 3 o'clock counterpart. This confirms a similar stress behaviour reported in a 4.826 mm thick Al 7075-T651 plate containing a Ø6.35 mm SW hole obtained from a monochromatic neutron experiment [5], and also 2D in-plane strain mapping of a 5 mm thick 7075-T6 plate in FTI split-sleeved expanded hole using synchrotron X-ray diffraction [39].

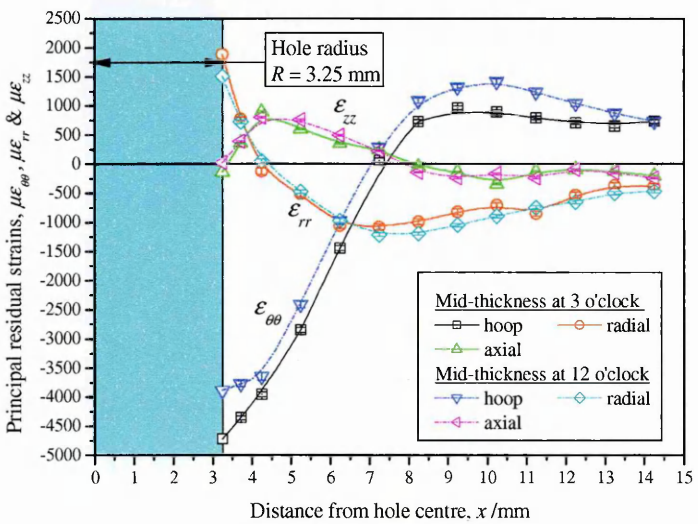

(a) Principal strains

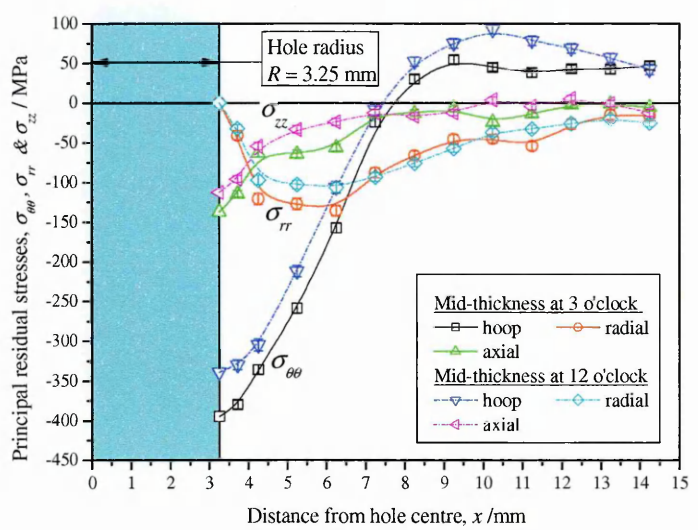

(b) Principal stresses

Figure 3.5.7 Principal residual stresses calculated along the mid-thickness lines in a SW hole specimen; 12 & 3 o'clock directions (with pseudo-strain correction)

This difference in the strain/stress field with orientation can be attributed to the specimen geometry. If a greater deformation constraint exists in the direction of specimen length, L, (in y-axis in Figure 3.2.1) during the SW indentation process the plastically deformed material will tend to flow more freely in the width direction, W, of the specimen (in x-axis

in Figure 3.2.1) where restriction on deformation is the less. Such an effect gives rise to a slightly greater permanent radial deformation or cold-working, and therefore more compressive hoop stress at the 9 o'clock orientations. A similar condition has also been observed in the FE simulation of the sleeveless cold hole expansion process in an isotropic material of similar plate dimensions [3].

3.5.4 Residual strain/stress redistribution due to hole drilling & reaming

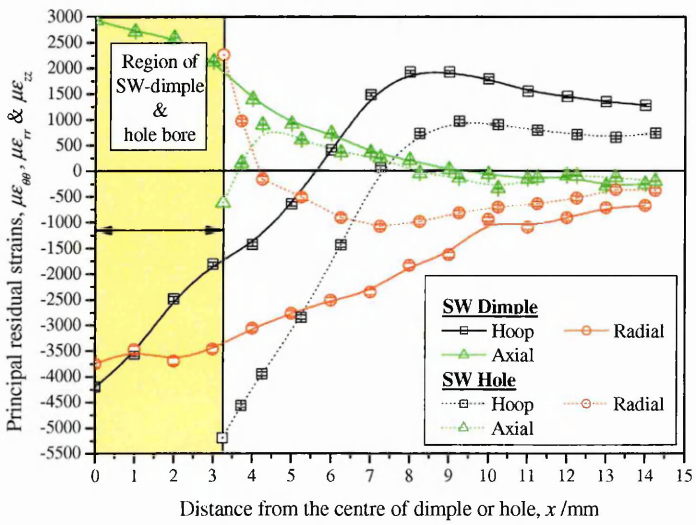

(a) Principal strain of mid-thickness of plate at 3 o'clock direction

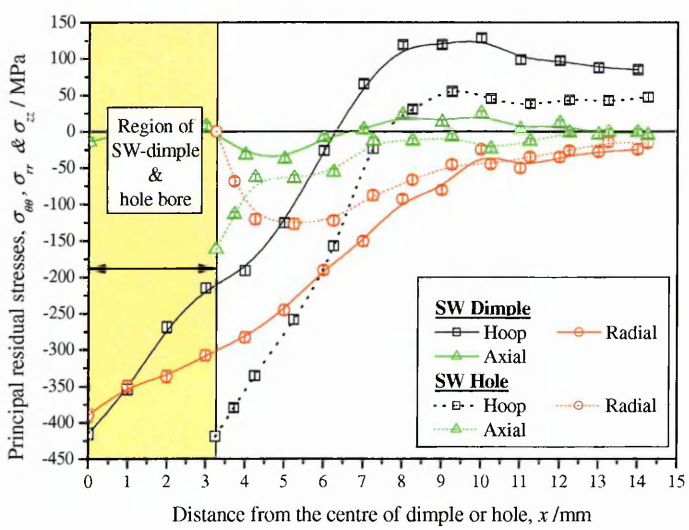

(b) Principal stresses at mid-thickness of plate at 3 o'clock direction

Figure 3.5.8 Initial and relaxed distribution of principal strains/stresses prior to and after hole production (at specimen mid-thickness and 3 o'clock direction).

Figure 3.5.8 features the distribution of principal residual strains/stresses at the mid-thickness of SW specimens before and after hole is introduced. As can be seen, the location

where the highest amount of residual strain/stress redistribution occurs is at the hole edge. At this location, the differences of strains before and after hole reaming are $\Delta\varepsilon_{\theta\theta}$ = 3480 $\mu\varepsilon$, $\Delta\varepsilon_{rr}$ = 5635 $\mu\varepsilon$ and $\Delta\varepsilon_{zz}$ = 2555 $\mu\varepsilon$, and the corresponding amounts of residual stress relaxation are $\Delta\sigma_{\theta\theta}$ = 208 MPa, $\Delta\sigma_{rr}$ = 300 MPa and $\Delta\sigma_{zz}$ =156 MPa, respectively. The greatest extent of strain/stress relaxation in the radial components ($\Delta\varepsilon_{rr}$, $\Delta\sigma_{rr}$) as a result of the removal of the hole material is analogous to the radial unloading of autofrettage pressure from the inner bore of a thick-walled tube. The observation agrees very well with the analytical prediction that the range of unloading state is the greatest for the radial component, followed by hoop and axial members in a radially cold-deformed hole [17, 37].

3.5.5 Three-dimensional neutron stress mapping in StressWave & FTI holes

Detailed X-ray and neutron residual stress data in the hoop direction measured around SW and FTI holes is compared in Figure 3.5.9. Using the neutron data of Nadri [3] treated with the pseudo-strain correction proposed in this text, the hoop stress is also produced for FTI split-sleeve 4% cold-expanded holes of similar plate material and geometry. The general trend of hoop stress for SW and FTI holes is very similar in Figures 3.4.9 (a) & 3.4.9(b), albeit with some distinct differences shown by the average through-thickness hoop stress (Figure 3.4.9(c)) obtained from X-ray and neutron data.

Away from the hole region, the X-ray data shows more fluctuation and is not as smooth as the neutron results as the cold-working effect diminishes gradually. This is possibly because the reflection obtained from low-penetrating X-ray radiation is susceptible to material texture and pre-existing residual stress before cold-working. Near to the hole edge, the X-ray hoop stress corresponding to the specimen surfaces is also lower that the neutron data. In general, the results of Figure 3.5.9 are a promising indication that the SW technique can possibly produce fatigue enhancement quality as least as good as the FTI method [5].

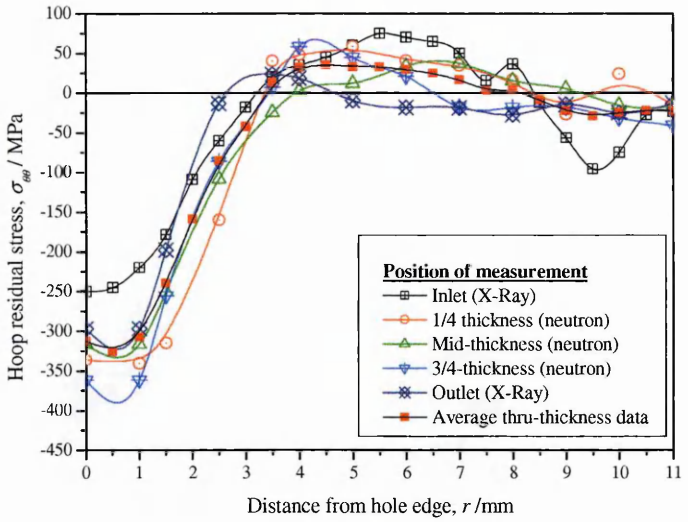

(a) FTI

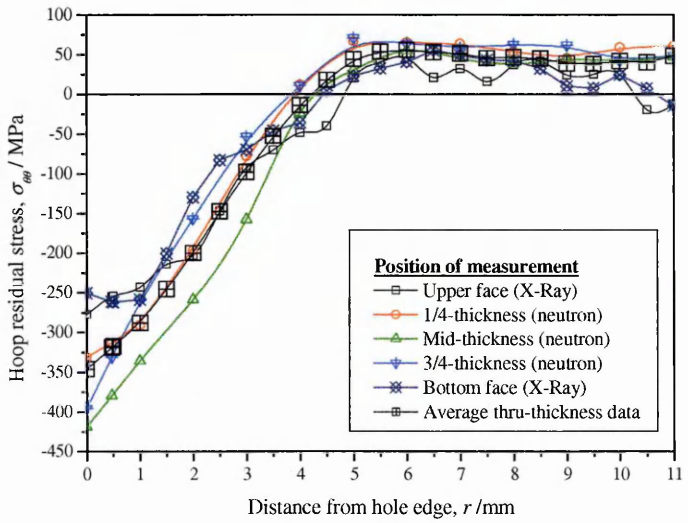

(b) StressWave

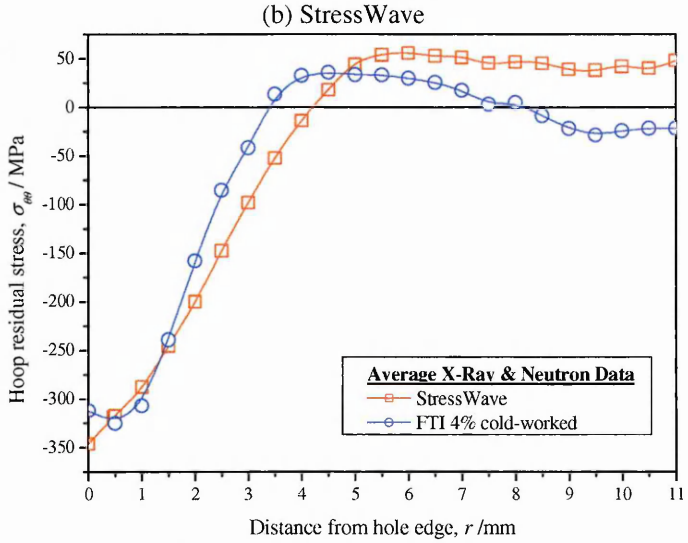

(c) FTI and StressWave specimens

Figure 3.5.9 A comparison of hoop residual stress at different thickness positions of StressWave and FTI specimens by X-ray and neutron hoop stress at specimen faces near to the hole (3 o'clock directions).

The through-thickness behaviour of the hoop component on the measurement planes is presented as full two- and three-dimensional (2D & 3D) residual stress maps in Figures

3.5.10 & 3.5.11. These maps were produced using the neutron stress data at the ¼, ½ and ¾-thickness of the SW specimen at 3 o'clock orientations from Figures 3.5.2 (a), 3.5.9 (a) & 3.5.9 (b). The partially-completed neutron data along 1/9-thickness lines is not included.

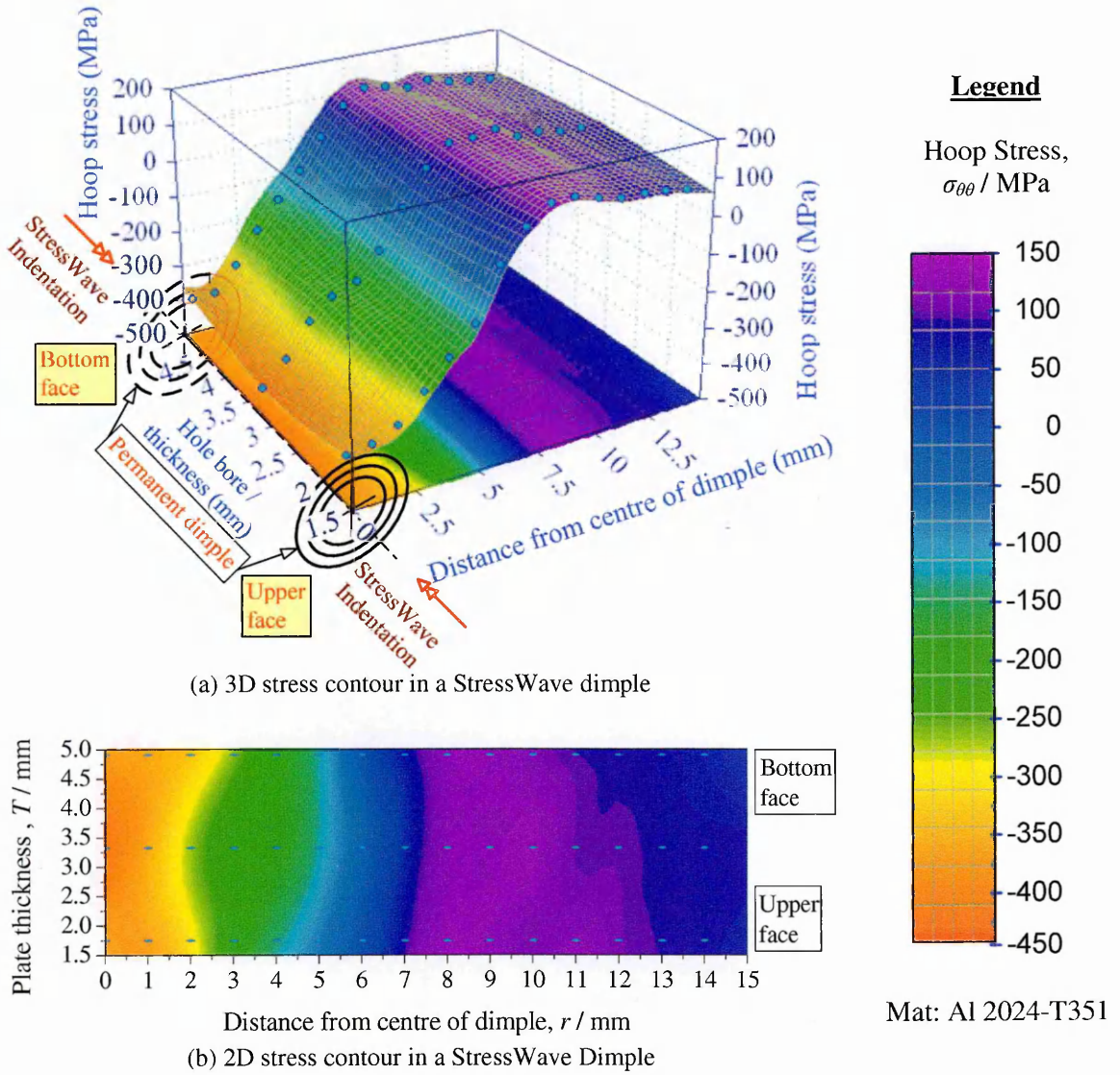

(a) 3D stress contour in a StressWave dimple

(b) 2D stress contour in a StressWave Dimple

Figure 3.5.10 Two- and three-dimensional hoop stress contour maps in a StressWave dimple (3 o'clock direction).

In Figure 3.5.10, the 2D and 3D contours indicate that the through-thickness hoop residual stress in a SW dimple is fairly symmetric about the plate mid-thickness. After the hole drilling and reaming procedure, a uniform distribution of hoop residual stress is seen at the SW hole, as exhibited in Figures 3.5.11 (a) & 3.5.12 (b).

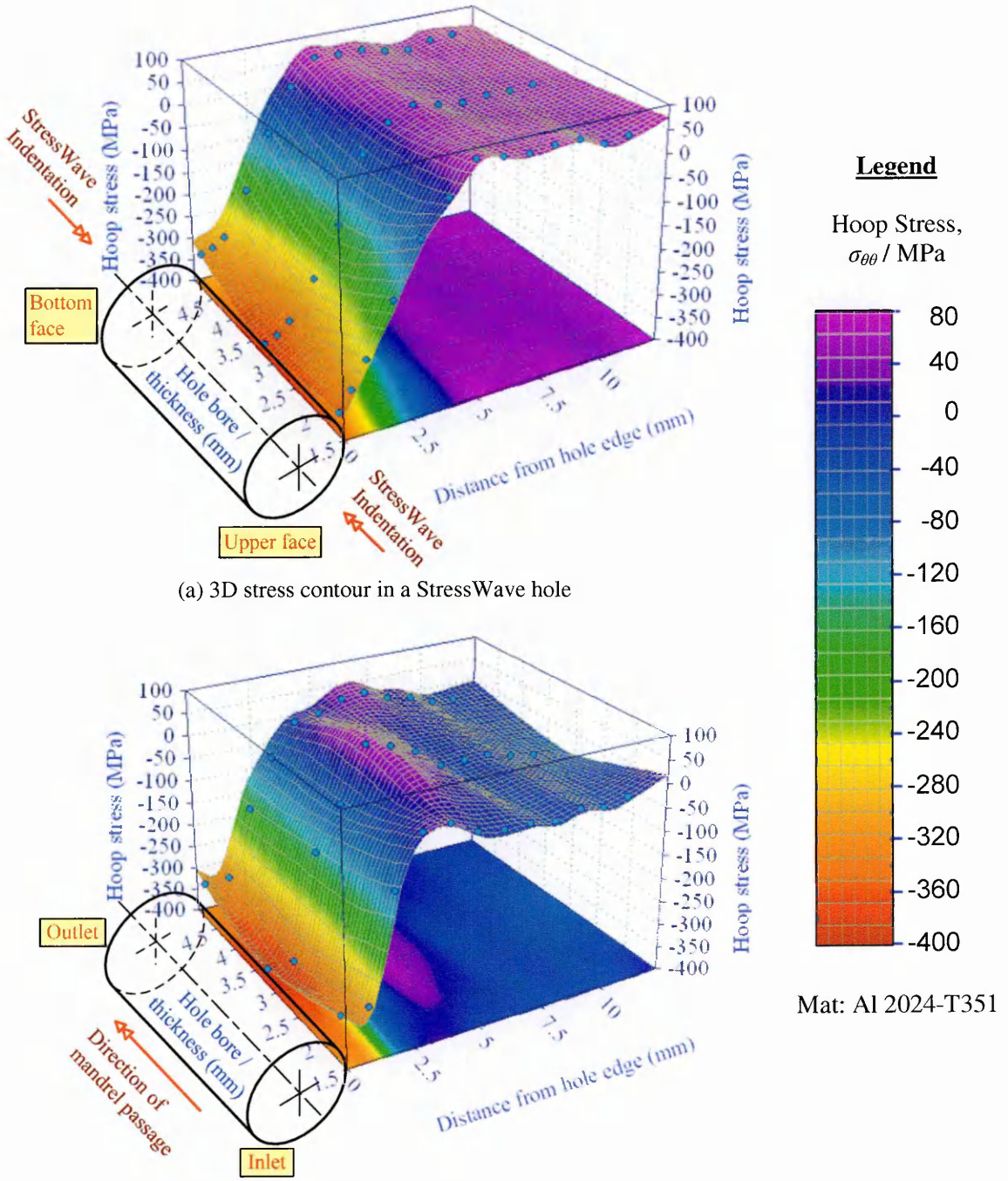

(a) 3D stress contour in a StressWave hole

(b) 3D stress contour in FTI hole

Figure 3.5.11 Comparison of three-dimensional hoop stress maps around (a) StressWave and (b) FTI cold-worked hole. (3 o'clock direction).

The FTI stress contour plots in Figures 3.5.11 (b) & 3.5.12 (b) imply that the residual stress field is uneven throughout the specimen thickness. The regions of mid-plane and mandrel-outlet typically experience more compressive residual stress than the region near to the mandrel-entrance face, and this is also well-supported by the X-ray data given in Figure 3.5.9 (a). In the SW hole the most compressive stress region occurs right at the hole bore; in the FTI specimen such a condition only occurs at approximately 0.5 mm from the hole

and that implies a greater zone of reversed yielding (Figures 3.5.9, 3.5.11 & 3.5.12). It is also apparent that the compressive residual stress zone generated around the SW hole is higher than the FTI hole, and this is always counterbalanced by higher tensile stresses formed about 4 mm away from the hole bore (Figure 3.5.12).

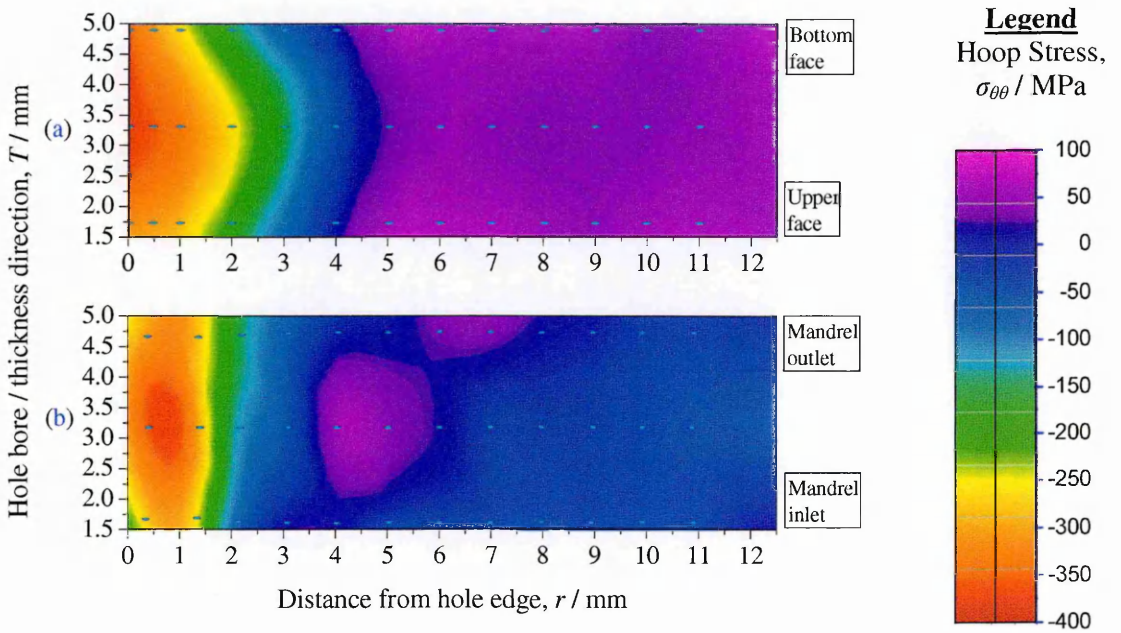

Figure 3.5.12 Comparison of three-dimensional hoop stress contour maps around (a) StressWave and (b) FTI cold-worked holes. (3 o'clock direction).

The differences in 2D and 3D hoop stress contour between the SW and FTI holes is the direct consequences of the different cold-working mechanisms. For the SW process, the indentation process in the z-direction of the specimen ensures that plastic material spreads symmetrically in all directions from the dimple concurrently (Figure 3.5.10). Interestingly, the SW process shares some similarities with the well-known problem of compression testing between two co-axial dies [17]. However, the process of drawing the mandrel in the FTI method is more akin to the one-side operation of a cold-extrusion process [16, 17]. Travelling from the specimen entry face to the outlet face, the oversized and tapered mandrel cold-works the hole bore material gradually through the plate thickness. The nature of the mandrel passage is believed to cause a significant amount of material to be extruded in thickness direction (z-axis) while the intended radial cold-expansion take place at the hole bore.

3.6 Conclusions

The present work reports successful measurements of the spatial residual strains in SW specimens in Al 2024–T351 aluminium alloy plate utilising both neutron and X-ray diffraction. Using practical sizes of sampling volumes accompanied with a pseudo-strain correction that eliminates the surface effect near to the hole boundary, it is illustrated that the two measurement techniques can resolve steep strain gradients around the SW cold-worked region of dimple and hole.

The coupling effect of the gauge volume used and highly steep strain gradients implies that the actual residual strain/stress measured here might be different from the exact values [13]. In the absence of an averaging effect of a finite sampling volume, it is anticipated that the actual magnitude of hoop stress is even more compressive at the hole edge. At present, it is difficult to obtain the exact strain/stress the averaged neutron data simply by de-convoluting the time-of-flight spectra measured in defined gauge volume. However, data refinement can be gained using a smaller gauge volume e.g. 0.5 or 0.2 mm dimensions normally, and would be helpful to characterise the pronounced stress relaxation in the reversed yield zone more precisely. Nevertheless, as a matter of practicality this requirement should be weighed with other limiting factors, such as intensity of neutron current, neutron flight path inside the specimens, and strain error, etc. Recently, as a complement to the neutron technique these limitations can be partially alleviated by the synchrotron X-ray diffraction reported in reference [39].

The material removal process from hole drilling and final-reaming of the SW dimple has been shown to cause a substantial amount of the original residual strain/stress in SW dimple to relax, particularly in material at the hole edge. Notably, the principal residual stress fields at the SW hole become compressive within about the first 5 mm from the hole bore (Figure 3.5.8). As the main interest is fatigue life enhancement study of fastener holes, the magnitude of the hoop stress gained at the hole bore on average increased by

approximately 200% upon hole production, associated with an 30% expansion of the compressive zone measured from the hole boundary.

The 2D and 3D hoop stress contours from neutron data have proven to be a useful tool to provide insight to the mechanism of plastic deformation worked in the material. From the stress contours of the SW dimple, it is shown that the novel SW cold-working technique is capable of inducing symmetric plastic material flowing from the indented locations on the upper and lower face of the specimen simultaneously, and this symmetric stress behaviour is closely echoed in the SW hole. In contrast, the FTI method generates an asymmetric residual stress distribution around the hole, especially in the through-thickness direction of the plate. It is also observed that the cold-working history of material around FTI hole is more complex in comparison to SW hole.

In summary, the residual stress data quantified in SW hole has been characterised with a high degree of confidence, and is reckoned to be accurate enough for damage tolerance research for components of similar materials containing SW cold-worked holes.

3.7 References

1. Fatigue Technology Inc, FTI Process Specification 8101C Cold Expansion of Holes Using the Standard Split Sleeve System and Countersink Cold Expansion™ (CsCx™). 1994: 401 Andover Park East, Seattle, WA 98188-7605 USA.
2. Ozdemir, A.T. and Edwards, L., Measurement of the three-dimensional residual stress distribution around split-sleeve cold-expanded holes. Journal of Strain Analysis for Engineering Design, 1996. 31(6): p. 413-421.
3. Nadri, B., Diffraction studies & finite element analysis of cold expanded holes, PhD Thesis, in Department of Materials Engineering. 2005, The Open University: Milton Keynes, U.K.
4. Stefanescu, D., Edwards, L., and Fitzpatrick, M.E., Stress intensity factor correction for asymmetric through-thickness fatigue cracks at holes. International Journal of Fatigue, 2003. 25(7): p. 569-576.

5. Easterbrook, E.T., Flinn, B.D., Meyer, C., and Juhlin, N. The StressWave™ Fatigue life Enhancement Process. in SAE Aerospace Automated Fastening Conference and Exhibition, Proceedings of 2001 Aerospace Congress, Paper No. 2001-01-2578. 2001. Seattle, USA: Society of Automotive Engineers.
6. StressWave Inc, Technical Report AL-02 Fatigue Testing of 2024 Low Load Transfer Aluminum Specimens (Nov. 1, 2001). 2001: 6644 South 196th Street, Suite T-106, Kent, WA 98032. p. 8.
7. Pilkey, W.D., Peterson's Stress Concentration Factors. 2nd ed. 1997, New York: Wiley-Interscience. 544.
8. Fitzpatrick, M.E. and Lodini, A., eds. Analysis of Residual Stress by Diffraction using Neutron and Synchrotron Radiation. 2003, CRC Press. 312.
9. Wang, D.Q.D., Strain measurement using neutron diffraction, PhD Thesis, in Department of Materials Engineering. 1996, The Open University: Milton Keynes, U.K.
10. Hutchings, M.T., Withers, P.J., Holden, T.M., and Lorentzen, T., Introduction To The Characterization Of Residual Stress By Neutron Diffraction. 2005: CRC Press.
11. Wang, D.Q. and Edwards, L. Precise determination of specimen surface position during near-surface strain scanning by neutron diffraction. in Proceedings of the 4th European Conference on Residual Stresses (ECRS4). 1998. Cluny en Bourgogne, France: Nancy J de Physique.
12. Timoshenko, S. and Goodier, J.N., Theory of Elasticity. 1970, New York: McGraw-Hill Education.
13. Wang, D.Q. and Edwards, L. Neutron diffraction determination of the complete 3D residual stress distribution surrounding a cold expanded hole. in Proceedings of the 4th European Conference on Residual Stresses (ECRS4). 1998. Cluny en Bourgogne, France: Nancy J de Physique.
14. Edwards, L., Near-surface stress measurement using neutron diffraction, in Analysis of Residual Stress by Diffraction using Neutron and Synchrotron Radiation, M.E. Fitzpatrick and A. Lodini, Editors. 2003, Taylor & Francis and CRC Press: London. p. 233-248.
15. Wang, D.Q., Harris, I.B., Withers, P.J., and Edwards, L. Sub-surface strain measurement by means of neutron diffraction. in Proceedings of the 4th European Conference on Residual Stresses (ECRS4). 1998. Cluny en Bourgogne, France: Nancy J de Physique.
16. Hoffman, O. and Sachs, G., Introduction to the Theory of Plasticity for Engineers. 1953, New York: McGraw-Hill Book Co, Inc.

17. Chakrabarty, J., Theory of Plasticity. 3rd ed. 2006: Butterworth-Heinemann. 832.
18. Tan, J.M.L., Fitzpatrick, M.E., and Edwards, L. Fatigue Crack Growth Prediction At StressWave Cold Worked Holes. in The 29th International Committee on Aeronautical Fatigue 2005: Structural Integrity of Advanced Aircraft and Life Extension for Current Fleets- Lessons Learned in 50 Years after the Comet Accidents. 2005. Hamburg, Germany: Engineering Materials Advisory Services Ltd (EMAS), Cradley Heath, West Midlands.
19. Webster, P.J., Strain mapping, in Analysis of Residual Stress by Diffraction using Neutron and Synchrotron Radiation, M.E. Fitzpatrick and A. Lodini, Editors. 2003, Taylor & Francis and CRC Press: London. p. 209-218.
20. James, J., Santisteban, J., Daymond, M., and Edwards, L., SScanSS (Strain Scanning Simulation Software) User Manual Version 2.0.1. 2005: Materials Engineering Department, The Open University and ISIS, UK.
21. Pawley, G.S., Unit-cell refinement from powder diffraction scans. Journal of Applied Crystallography, 1981. 14(6): p. 357-361.
22. Rietveld, H.M., A profile refinement method for nuclear and magnetic structures. Journal of Applied Crystallography, 1969. 2(2): p. 65-71.
23. Larson, A.C. and Dreele, R.B.V., General Structure Analysis System (GSAS), Los Alamos National Laboratory Report LAUR 86-748. 2000. 230.
24. Daymond, M.R., Bourke, M.A.M., Dreele, R.B.V., Clausen, B., and Lorentzen, T., Use of Rietveld refinement for elastic macrostrain determination and for evaluation of plastic strain history from diffraction spectra. Journal of Applied Physics, 1997. 82(4): p. 1554-1562.
25. Noyan, I.C. and Cohen, J.B., Residual Stress: Measurement by Diffraction and Interpretation (Materials Research and Engineering). 1987: Springer-Verlag. 276.
26. Grandt, A.F.J., Stress intensity factors for some through-cracked fastener holes. International Journal of Fracture, 1975. 11(2): p. 283-294.
27. Cathey, W.H. and Grandt, A.F.J., Fracture mechanics consideration of residual stresses introduced by coldworking fastener holes. Journal of Engineering Materials and Technology, Transactions of the ASME, 1980. 102(1): p. 85-91.
28. Stresstech Group, X3000 Software User's Guide Version 1.14, XSTRESS 3000 X-Ray Stress Analyzer. 2004, Vaajakoski, Finland.
29. Stresstech Group, X3000 Technical Manual Version 1.0o, XSTRESS 3000 X-Ray Stress Analyzer. 2004, Vaajakoski, Finland.

30. Lorentzen, T., Anisotropy of lattice strain response, in Analysis of Residual Stress by Diffraction using Neutron and Synchrotron Radiation, M.E. Fitzpatrick and A. Lodini, Editors. 2003, Taylor & Francis and CRC Press: London. p. 114-130.
31. Prevéy, P.S., X-ray diffraction residual stress techniques, in Metals Handbook®, K. Mills, Editor. 1986, American Society for Metals: Metals Park, OH. p. 380-392.
32. Residual Stress Measurement by X-Ray Diffraction: HS-748. 2003: Society of Automotive Engineers, SAE International.
33. Ozdemir, A.T., Wang, D.Q., and Edwards, L. Measurement of the 3D Residual Stress Distribution at Split Sleeve Cold Expanded Holes. in Proceedings of the Fourth International Conference on Residual Stresses. 1994. Baltimore, MD, USA: Society for Experimental Mechanics.
34. Özdemir, A.T. and Edwards, L., 3-D residual stress distributions around split-sleeve cold-expanded fastener holes. Journal of Strain Analysis for Engineering Design, 1996. 31: p. 701-709.
35. Poussard, C., Pavier, M.J., and Smith, D.J., Analytical and finite element predictions of residual stresses in cold worked fastener holes. Journal of Strain Analysis for Engineering Design, 1995. 30(4): p. 291–304.
36. Smith, D.J., Poussard, C.G.C., and Pavier, M.J., An assessment of the Sachs method for measuring residual stresses in cold worked fastener holes. Journal of Strain Analysis for Engineering Design, 1998. 33(4): p. 263-274.
37. Zhang, Y., Fitzpatrick, M.E., and Edwards, L., Analysis of the Residual Stress around a Cold-expanded Fastener Hole in a Finite Plate. Strain, 2005. 41(2): p. 59-70.
38. Webster, P.J., Mills, G., Browne, P.A., Hughes, D.J., and Holden, T.M. Residual stress around a cold expanded hole. in Proceedings of the Sixth International Conference on Residual Stresses (ICRS6). 2000. Oxford, UK: IoM Communications Ltd.
39. Stefanescu, D., Steuwer, A., Wen, R.A.O., Nadri, B., Edwards, L., Fitzpatrick, M.E., and Withers, P.J., Elastic strains around cracked cold-expanded fastener holes measured using the synchrotron X-ray diffraction technique. Journal of Strain Analysis for Engineering Design, 2004. 39(5): p. 459-469.
40. OriginLab Corporation. ORIGIN Version 6.1 - Scientific Graphing & Analysis Software. 1999.

APPENDIX 3–A

This section outlines the complete procedures involves in the pseudo-strain correction in SW hole using the extended empirical-instrumental method:

Step 1: We ignored the strain values at the position where the radial pseudo-strains ε_{rr}, were measured. However, the corresponding hoop, $\varepsilon_{\theta\theta}$ and axial, ε_{zz} strains remain unchanged at these locations under Z-scan approach.

Step 2: According to the generalised Hooke's law, the radial stress is computed from:

$$\sigma_{rr} = \frac{E}{(1+\nu)(1-2\nu)}\left[(1-\nu)\varepsilon_{rr} + \nu(\varepsilon_{\theta\theta} + \varepsilon_{zz})\right] \tag{3.A1}$$

At the surface of the hole bore, the radial stress $\sigma_{rr} = 0$. From relation (3.2.1), the associated radial strain can be inferred from

$$\varepsilon_{rr}\big|_{\text{hole edge}} = \frac{\nu}{(\nu-1)}(\varepsilon_{\theta\theta} + \varepsilon_{zz}) \tag{3.A2}$$

Using the two-dimensional cubic spline fitting scheme [40], we may extrapolate the hoop, $\varepsilon_{\theta\theta}$ and axial, ε_{zz} strain components at the hole edge to estimate the radial strain in (3.2.2). Up to this point, a complete set of three principal strains that correctly yields a zero radial stress condition at the hole edge is obtained.

Step 3: Afterwards, we may produce a new dataset of radial strain combining the ε_{rr} value of (3.2.2) with other correct values at the unaffected positions. Using this dataset, we can now replace the previously omitted radial pseudo-strains in Step 1 by interpolation of the new dataset at the appropriate locations.

The inter-extrapolation method used in present investigation shows reasonable estimation of residual strains around SW hole when other means of pseudo-strain correction are not readily accessible. This method is especially useful to supplement results at the surface because measuring residual strains at the hole surface exactly by neutron diffraction is

impossible due to the finite-size and averaging effects of gauge volumes. Nevertheless, predicting surface residual strains using present method must be treated with great precautions if the prediction is to be made out of only very limited data points measured near to the surface. Moreover, empirical correction based on prior knowledge of stress behaviour is essential to ensure the correctness of predicted data.

CHAPTER 4: FINITE ELEMENT SIMULATIONS OF STRESSWAVE & SPLIT-SLEEVE MANDREL COLD-WORKING PROCESSES FOR FASTENER HOLES IN AL 2024-T351 ALLOY PLATE

Employing the finite element method, the present chapter describes the comprehensive prediction of the residual stress field generated at fastener holes cold-worked by StressWave and the split-sleeve mandrelising techniques. The simulations were designed to reflect the actual hole production scenarios in an aluminium 2024-T351 plate. Various aspects in the modelling were taken into account, including material properties, tool geometries and contact conditions. An estimation of the StressWave cold-working equivalent to those used for split-sleeve mandrelising process is also proposed. The numerical analysis reveals that the split-sleeve mandrelising technique induced an irregular amount of cold-working and therefore an asymmetric stress field; whereas the StressWave technique imparts a uniform deformation and stress distribution around the hole. The numerical simulations were validated by neutron and X-ray diffraction data. The findings of this work indicate that simulation must closely model the actual material behaviour and cold-working process to produce reliable numerical predictions.

4.1. Introduction

Traditionally, various closed-form or analytical solutions have been proposed to describe the residual stress field created around cold-worked holes. The development of closed-form models are motivated by their adaptability to very broad range of problems, and hence enable parametric studies to be carried out. In closed-form solutions, the cold-expansion is modelled as the radial enlargement problem of a hole in an infinite plate [1, 2], or the autofrettage of a thick-walled disk or tube by internal pressure [3-6].

Comprehensive summaries of the analytical models available for cold-worked holes including the role of yield criterion, stress-state, along with mechanical response in the tension and compression regimes, have been described in [4, 7, 8]. Despite robustness in rapid generation of results, closed-form solutions suffer from various simplifying process assumptions. Notably, the process can be only described in two-dimensional (2D) plane stress or plane strain problems. Physically, the actual interactions of cold-working tools with a work-piece of finite thickness and geometry, together with the supporting conditions are all ignored.

In contrast to analytical approaches, previous experiments [9-13] and numerical investigations [8, 14-24] have unequivocally revealed that hole cold-working is inherently three-dimensional (3D) in nature. The spatial residual strain or stress field induced adjacent to the hole has a high gradient and is difficult to assess precisely. For experimental measurements such as the Sachs boring [13] and diffraction techniques [10, 11], data averaging effects from a small definite gauge volume of materials is inevitable. As an alternative, this chapter aims to study the entire cold-working process by finite element (FE) method using an axisymmetric assumption. It has been shown earlier that either the axisymmetric or full 3D FE simulations enable us to capture the complexity of residual stress field imparted in the specimens expediently [8, 16-19, 21-25]. Nevertheless, the computed results are highly dependent on how precisely the operational details are modelled. To increase the prediction accuracy, considerable efforts were devoted here to materials behaviour, tool dimensions and contact conditions.

The ABAQUS code [26] was chosen for present analysis and small strain behaviour along with the von Mises yield criterion were assumed throughout this FE work. The first FE analysis reported the simulations of the elastic-plastic indentation and hole machining process involved in the StressWave (SW) cold-working method [27]. This was followed by

the simulation of the split-sleeve mandrel (SSM) process [28, 29]. The FE model consists of drawing a mandrel through a hole interfaced by a split-sleeve, which operation is engaged with a supporting nosecap. The lubricated sleeve functions to reduce the mandrel pulling force dramatically and the mandrel can be easily removed without sticking to the hole. It also helps to mitigate the formation of axial shear or extrusion along the hole wall and ensures that hole expansion is principally radial.

As an overview, this chapter is arranged as follows: Section 4.2 describes the mechanical properties of Al 2024-T351, sleeve, mandrel and SW indenter. The FE model definitions of SW and SSM procedures are discussed in Section 4.3. This is followed by studies of manufacturing index regarding the amount of cold-deformation introduced into the sample in Section 4.4. A detailed evaluation of the history of deformation, strain and stress evolved at successive stages of cold-working is also analysed. Next, Section 4.5 describes the validation of the present FE results using experimental diffraction data.

4.2 Properties of Materials

4.2.1 Materials Models of plate

References [23, 30] reported dissimilarities of stress-strain curves in Al 2024 obtained from tension and compression testing at different orientations to the plate rolling directions – a direct indication of material anisotropy. However, for simplicity in this numerical work the Al 2024-T351 plate is assumed to be initially isotropic, using the data from the plate rolling direction.

The mechanical response of materials has a strong influence on the characteristics of residual stress field introduced in cold-worked holes. This study considered three distinct material hardening models to describe the constitutive behaviour of Al 2024-T351 alloy in

response to plastic deformation, namely nonlinear isotropic (IH), kinematic (KH) and combined hardening (CH).

The nonlinear IH curve is simply defined by using a set of 27 data points of true stress σ_{true} versus true plastic strain ε^{p}_{true} (Appendix 4-A) taken from the experimental unidirectional stress-strain curve (Figure 4.2.1). Considerable data points were concentrated in the highly non-linear region, especially for the small strain range $0.005 < \varepsilon < 0.02$. This ensures a smooth transition in the piecewise multi-linear representation and also accurate interpolation of the discrete data during numerical computations [26].

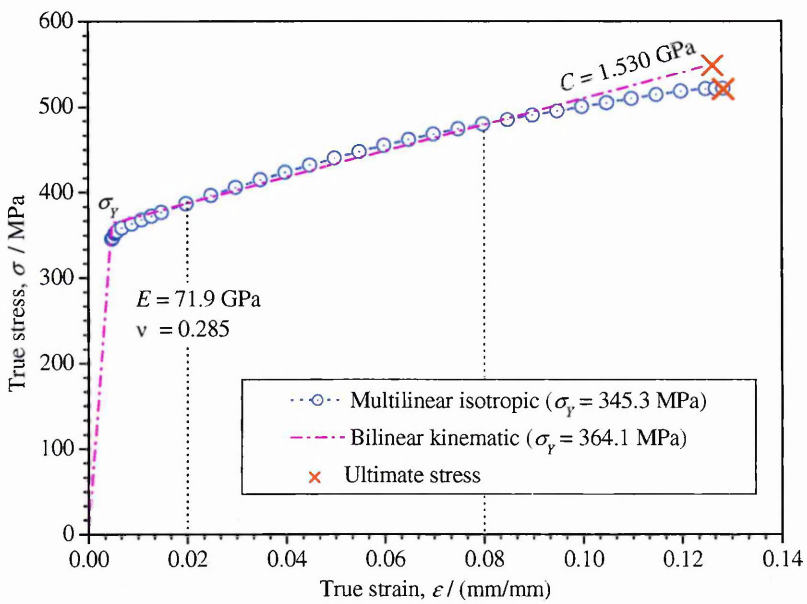

Figure 4.2.1 Tensile stress-strain data points for Al 2024-T351 aluminium alloy used to define isotropic and kinematic hardening.

The KH model requires the experimental curve in Figure 4.2.1 to be linearised into a bilinear curve [26]. The linear regression procedure on the inelastic region of the original curve was optimised to closely captured the stress-strain response for $0.02 < \varepsilon < 0.08$. The yield stress σ_Y was subsequently raised to about 5.4% higher that the actual value, with the linear KH modulus, C calculated to be 1.530 GPa (Appendix 4-A). It is observed that this provision gives physically reasonable results comparable to the overall behaviour of the experimental curve.

In ABAQUS [26], the CH model is a hybrid of a nonlinear KH with the IH formulated by Lemaitre & Chaboche [31, 32]. The CH model allows the evolution of nonlinear cyclic plasticity of materials to be simulated more closely to replicate the actual observation. Complete cyclic stress-strain data for Al 2024-T351 under various cyclic strain ranges is still meagre in the literature [23, 33, 34], especially at strain regimes exceeding ± 4%. In this text, distinctively for Al 2024-T351 we used the CH parameters calibrated and validated numerically by Bao & Treitler [34]. The experimental data were individually obtained from 1%, 2%, 3%, 3.5% and 5% pre-compression of circular bars followed by tension until specimen failure. The common CH parameters to these ranges of cyclic strain for Al 2024-T351 are given in Appendix 4-A(c).

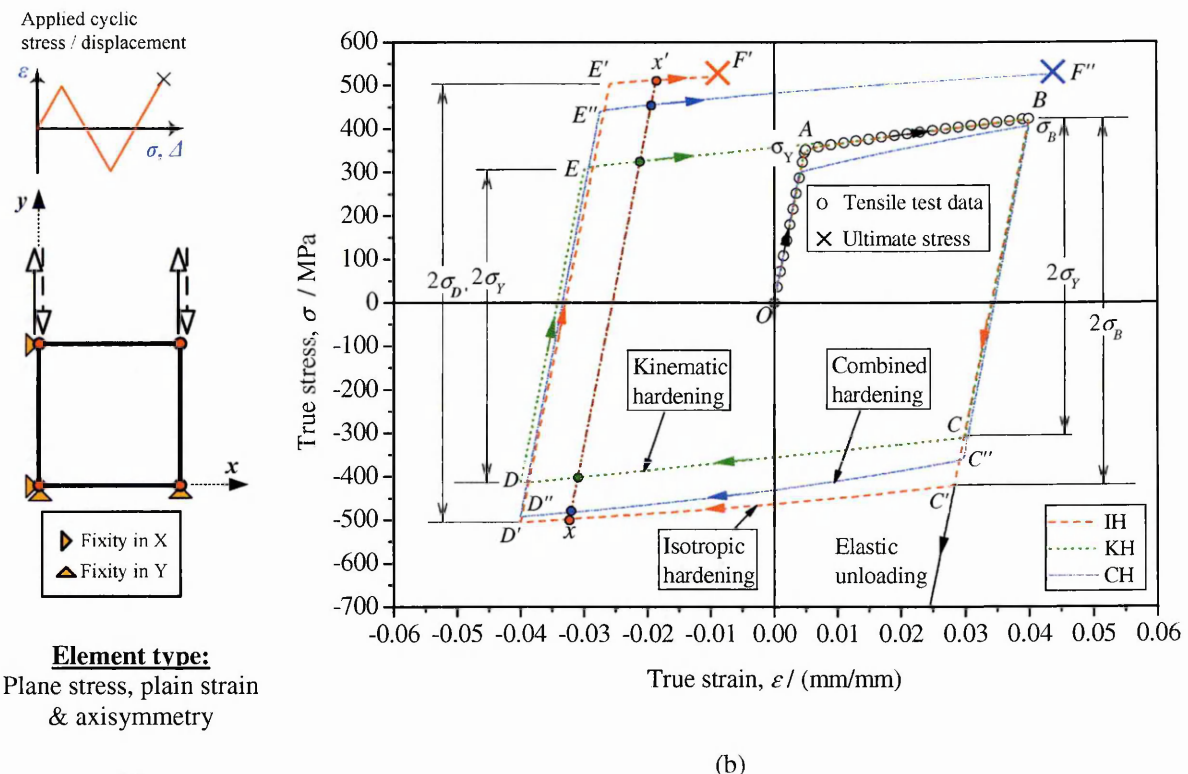

Figure 4.2.2 (a) Single element test in FE code. (b) Simulation of isotropic, linear kinematic and combined hardening response for 2024-T351 aluminium alloy at ±4% cyclic tension-compression strain-controlled conditions

As a precursor to the actual simulations, a preliminary analysis was used to validate the IH, KH and CH models of the material in response to subsequent cyclic yielding. A four-noded "single element" test for plane stress, plane strain and axisymmetric conditions was used. The models were assigned with proper boundary constraints, with the intended alternating

stress or displacement applied at the free nodes, as shown in Figure 4.2.2 (a). Three independent tension-compression cyclic strain-controlled simulations of ±2%, ±4% and ±6% were performed to obtain complete first cycle data.

Regardless of the element type subjected to the cyclic plasticity, induced either under displacement or stress mode, similar outcomes were individually produced for all cases. For simplicity, only the result of ±4% cyclic strain is discussed here. Figure 4.2.2 (b) shows the initial curve *OAB* that represents monotonic tensile testing is accurately reproduced by both IH and KH. A lower yield strength and hardening curve is given by CH, which after progressive tension straining until the stress σ_B at ε = +4% eventually approaches the experimental value.

A multi-linear (*B C'D'E'F'*) and bilinear (*BCDEF*) stress-strain path was assumed by the IH and KH, respectively, for the load reversal and stress recovery behaviour in compression. For linear elastic stress recovery, unloading must occur between the lines *B'C'* and *BC* at $\varepsilon = 4\%$, and this behaviour changes steadily to *DE* and *D'E'* along the compression to $\varepsilon = -4\%$. Therefore, given arbitrary in-between straining at $-4\% < \varepsilon < 4\%$, the intermediate elastic load-path, designated by two connecting points on the general line *xx'* intersecting the curves, is parallel to lines *OA*, *B'C'*, *BC*, *DE* and *D'E'*. However, the permissible stress range over which the elastic unloading $\Delta\sigma$ can occur, as dictated by the hardening models, is a dependent of the strain history, and this is enumerated by the absolute values of *OA*, *B'C'*, *BC*, *DE* and *D'E'*.

Compression along the path *BC* or *B C'* will bring the material into the region of inelastic stress recovery. The effective compressive yield stress occurs at point *C* or *C'* prior to entering the reversed hardening curve *CD* or *C'D'*. The remaining stress-strain cycles

D'E'F' or *DEA* associated with IH and KH are completed by reverse tension at the point *D'* or *D* (i.e. $\varepsilon = -4\%$), with the succeeding yielding at point *E'* or *E*.

For IH a complete closed loop of the cyclic stress-strain curve is not achieved, and the curve fails at point *F'* corresponding to the experimental ultimate true strength of the material (i.e. σ_f = 521.3 MPa). The absolute magnitude of the IH reverse yield stress (point *C'*) is always equal to that of preceding maximum tensile stress σ_B (point *B*), and similar phenomena were observed for point *D'* and *E'* for σ_D. As a result, the IH scheme does not realistically correlate with experimental data that shows a Bauschinger's effect [5, 32]. This is a consequence of the fact that IH assumes an infinite expansion of the yield surface at constant shape, until a failure criteria (i.e. maximum effective stress or strain) is reached.

On the contrary, the KH model proposed by Prager & Ziegler [5, 32] allows simple Bauschinger's and anisotropy effects to be introduced. The formation of a closed cyclic stress-strain loop *OABCDEA* designates a stable cyclic state in the material. The magnitude difference between the first yield stress (*B* or *D*) and the next one on reversal (*C* or *E*) remains constant, i.e. two times the initial yield stress, σ_Y. As a first approximation, linear KH is suitable to study the residual stress around cold-worked holes, particularly to estimate the influence of Bauschinger's effect on the secondary yielding region corresponding to path *CD*.

In Figure 4.2.2, the simulated CH curve is found sandwiched between the stress-strain loops of IH and KH. The CH reversed yield stress at *C''* is approximately in between *C* and *C'*; nonetheless the subsequent values at *D''* or *E''* are predicted more closely towards the values at *D'* or *E'* on the IH curve. Upon final tension till failure at point *F''* the CH open loop curve displays the behaviour of transient cyclic hardening, which is consistent with the experiment results in [34]. This phenomenon suggests that the current CH

parameters are only appropriate to simulate first-cycle elastic-plastic deformation. In contrast to several experimental findings [23, 33, 34], the nonlinearity in the transition region of reversed yielding at point *C''*, *D''* and *E''* is not very pronounced in the numerical curves shown in Figure 4.2.2.

4.2.2 Materials properties of sleeve, mandrel & StressWave indenter

The mandrel material is proprietary, and is not publicly available. Briefly, the mandrel is fabricated from high quality vacuum-melted tool steel which is double tempered and precision ground [28], and is subsequently hardened to HRC 60-62 to increase its wear-ability when subject to continuous cold-working. In general, mandrel service life depends variably on the dimension and material mechanical properties of component to be cold-worked, degree of mandrel–hole interference, mandrel surface wear, and the extent of abrasiveness of the solid lubricant on the sleeve. In the absence of exact information, the mandrel properties were assumed to be similar to that of AerMet® high-strength tool steel [30] often used in the aerospace industry. As a comparison, the elastic constants for AerMet® given in Appendix 4–B (a) are close to those used previously in cold-expansion simulations [2, 8].

The split-sleeve is manufactured from full hard Type 301 stainless steel (Appendix 4–B (b)), which acquires HRC 41 after heat treatment [30, 35]. Dry-film lubricant is used on the internal bore of the sleeve to prevent the mandrel from sticking to the hole during the cold-working process [28]. After use, a sleeve is always permanently deformed due to severe cold-working, and therefore must be discarded. The stiffness ratios of mandrel and sleeve to Al 2024–T351, i.e. $E_{mandrel}/E_{plate} = 2.65$ and $E_{sleeve}/E_{plate} = 2.50$, are reckoned effective to retain about 90% of the intended cold-expansion for a wide range of interference ratios [2].

The SW indenter is also made of a proprietary ultra-hard tool material of cemented carbide type, with mechanical properties equal to or better than those used for the mandrel. However, by representing the geometry of SW indenter using a rigid surface [26], the need for knowledge of mechanical properties of indenter can be eliminated (see Section 4.3.1). The SW indenter is less susceptible to surface wear problems, but requires a high rigidity to preserve its shape under repetitive indentation. For the SW process, even though the indenter material may deform slightly due to high axial compressive force, the specific depth of indentation can always be attained.

4.3 Finite element definitions

4.3.1 StressWave technique

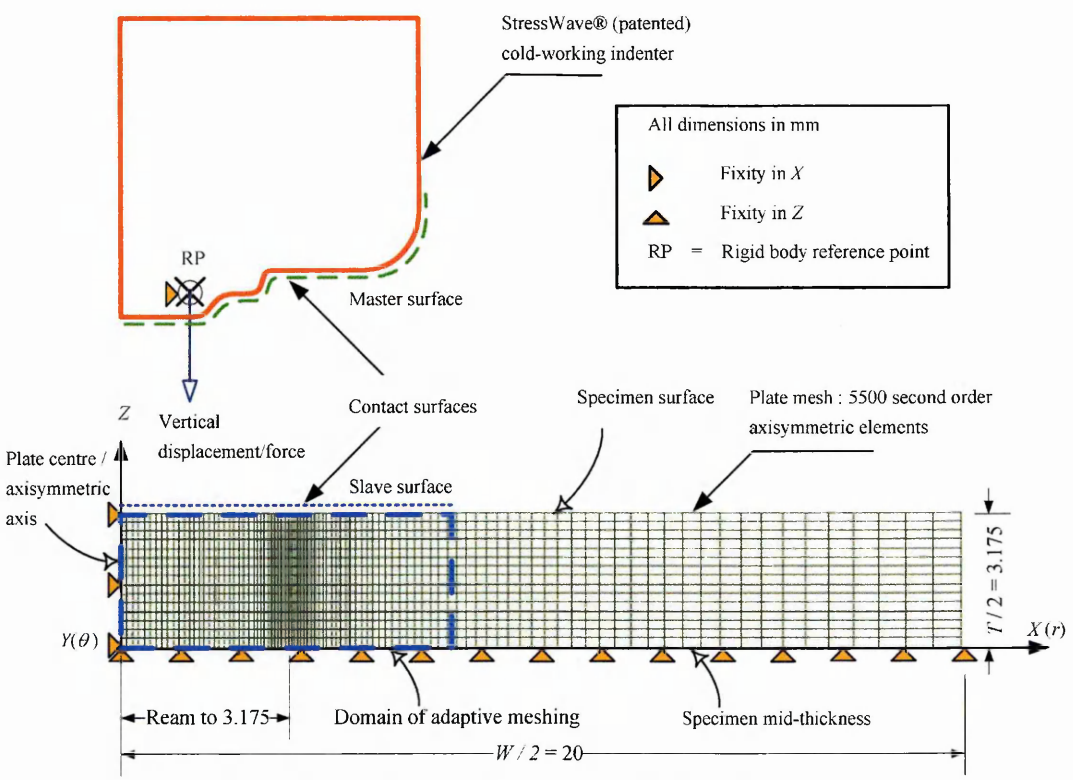

Figure 4.3.1 Axisymmetric FE model of the StressWave cold-working process in Al 2024-T351 plate.

An axisymmetric FE model was constructed to simulate the SW cold-indentation process. The actual SW indentation is coaxial on the upper and lower faces of the plate and essentially symmetric about the specimen mid-thickness, and hence allows simplification in modelling. Consequently, only a model of half–plate of thickness 3.175 mm with 20 mm

outer radial boundary along with the upper indenter was used. Nodes along the mid-thickness and symmetric axes of the plate were thus constrained in both X and Z directions. The complete SW model as depicted in Figure 4.3.1 consists of a set of elements for the plate, and a rigid surface for the indenter.

The geometry of the SW indenter was provided by StressWave, Inc.; however, the details cannot be disclosed owing to proprietary right. The indenter is assumed to undergo negligible deformation because it is 4 ~ 10 times stiffer than the Al–plate [36-38]. It was therefore considered justifiable to model the indenter as analytical rigid part with a smooth outer profile (Figure 4.3.1). The indentation displacement or force acting on the rigid-body indenter was assigned via a reference point (RP). The indenter X-axis freedom was also fixed at RP to ensure the process is always perpendicular with respect to the plate surface.

Surface-based contact was defined for the interaction between the indenter and the plate top face. As shown in Figure 4.3.1, at the contact interface the harder indenter was made the 'master surface' and matched with the 'slave surface' on the softer plate to form a contact pair. Since substantial deformation was expected throughout the analysis, a finite-sliding condition was used to allow the plate elements on the slave surface to slip freely. For the surface normal interaction, a hard-contact scheme was selected to prevent over-closure/ penetration at the contact interface, and simultaneously permit complete separation of the indenter from plate after cold-working. Hard-contact assumes the contact pressure is only transmitted provided the nodes of the slave surface contact the master surface (i.e. cohesion), and therefore the transfer of tensile stress across the interface is not permissible. Also, the magnitude of contact pressure transmitted is not limited at contact. Separately, an isotropic Coulomb coefficient of friction, $\mu = 0.1$ was used to describe the contact property tangential to the interacting interface. Both the normal and tangential contact interactions were evaluated using the classical Lagrange multiplier method.

The plate is modelled as 5500 4-noded linear elements (CAX4) analysed with a standard scheme of 2 × 2 Gauss integration points. Substantial mesh refinement using an element aspect ratio of 1.0 ~ 1.1 is concentrated around the contact zone to resolve the very sharp stress gradient. For the region away from the indented site, a mesh density of element aspect ratio of 1.1 ~ 4.0 was found to provide accurate results. Adaptive meshing was also employed to smooth element distortion in the contact domain. In this way, the original shape of the elements can be closely maintained, which in turn increases the overall reliability of the modelling. In the absence of the adaptive mesh algorithm, it was found that if the mesh was adequately dense, the average time required to produce comparable data can be 1.5 ~ 2 times faster. In both cases, excellent dimple profiles were obtained (Figure 4.3.2(b) & 4.3.2(c)) in spite of extreme elastic-plastic deformation.

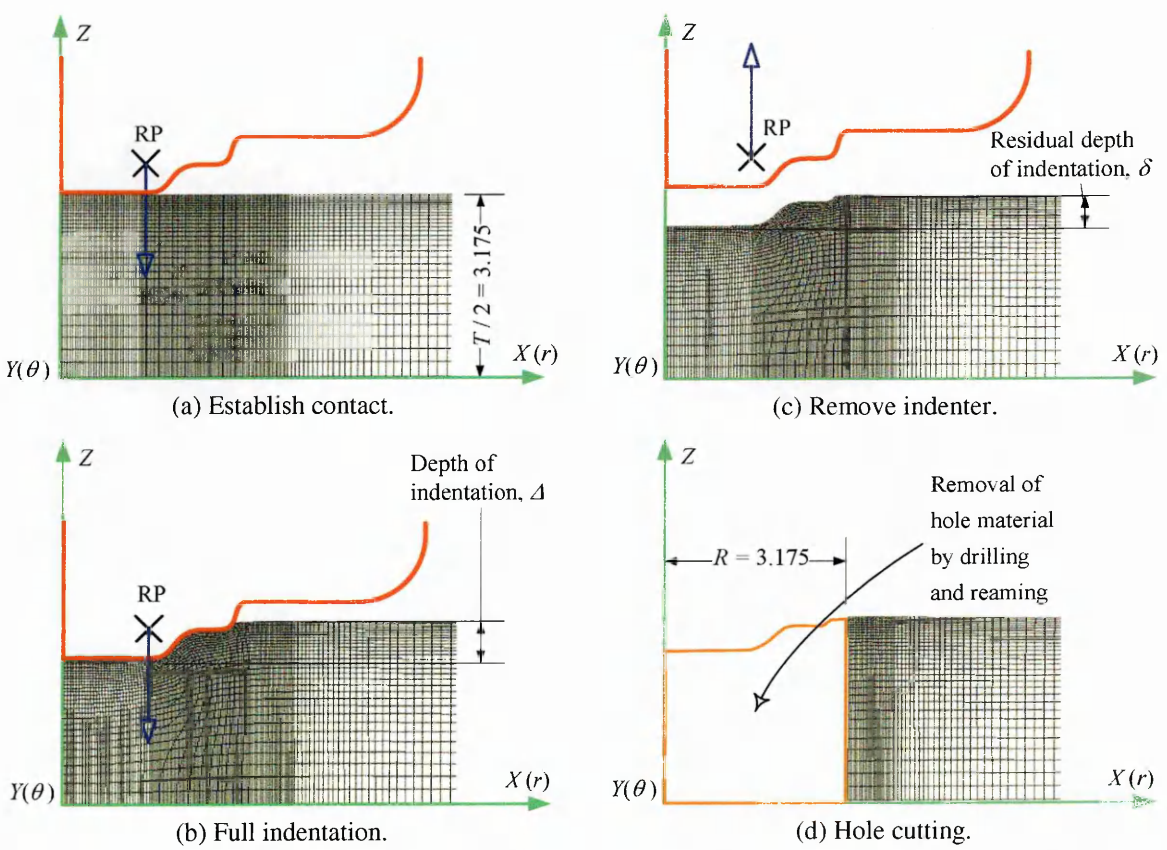

Figure 4.3.2 Close-up views of FE simulations of StressWave indentation technique and subsequent fastener hole cutting procedure.

Figure 4.3.2 summaries four essential steps to model the SW process. The indentation procedures simply involve the prescribed movement of the indenter in the *Z*-axis. Initially,

the indenter was pinched slightly (i.e. 0.01mm) on the plate to establish an equilibrium elastic state (Figure 4.3.2 (a)). Then, the indenter was further pressed into the material to arrive at a full indentation depth, Δ of 0.635 mm (Figure 4.3.2 (b)). Upon withdrawal of indenter, the plate resumes a new equilibrium condition, and a first residual stress field is formed around the permanent dimple of depth, δ (Figure 4.3.2 (c)). Then, a set of elements corresponding to the prospective hole radius, R = 3.175 mm was removed concurrently from the FE mesh to represent the combined steps of pilot drilling and final reaming (Figure 4.3.2 (d)). Numerically, the element deactivation ramps the selected nodal forces to zero and then allow stress redistribution to take place steadily. The material removal generates a second state of residual stress field similar to those found in split-sleeve hole. A total of 250 iterations was required to accomplish the automatic load increment scheme in the analysis.

4.3.2 Split-sleeve mandrel technique

Compared to the novel SW process, abundant 2D and 3D FE analyses concerning the conventional cold expansion process in metallic plate are widely accessible in the literature [8, 16-19, 21-25]. Besides the material mechanical properties, many different assumptions concerning mandrel, sleeve, specimen supports and interface friction have been incorporated, which are summarised in Table 4.3.1.

In some cases, an elastic mandrel [8, 14, 15, 21-24, 39] and sleeve [8, 17, 20, 23] was assumed to take account of the contribution of component deformation in cold-working. Others used a rigid body representation, assuming that the mandrel was much stiffer than the target hole material, or when the associated mechanical properties were not available [16, 18, 20, 40]. Simplification was also accomplished by increasing the dimensions of a rigid [16-18, 21, 22, 24, 39, 40] or elastic mandrel [8, 14, 15, 21-24] to incorporate the sleeve thickness, treating both the sleeve and mandrel materials as identical. Idealisation

was also made in [8, 19, 25] to substitute the physical role of the mandrel in cold-working by an equivalent uniform radial displacement or pressure imposed along the hole bore.

Reference	Mandrel	Sleeve	Plate Support	Friction
Forgues *et. al* (1993) [18]	Rigid	Sleeveless	At outer boundary along the plate thickness.	-
Bernard *et. al* (1995) [16]	Rigid	Sleeveless	At outer boundary along the plate thickness.	-
Pavier *et. al* (1997) [8]	Elastic	Elastic	At outer boundary along the plate thickness.	Mandrel–sleeve: frictionless Sleeve–plate: frictionless
Papanikos & Meguid (1998, 1999) [21, 22]	Elastic	Sleeveless	Variable distance from hole edge at plate bottom along $X(r)$ axis & at outer boundaries along the plate thickness.	Mandrel–plate: elastic Coulomb's friction, μ = 0.1~0.4
O'Brien (2000) [20]	Rigid	Elastic	-	-
Arora *et al.* (2001) [14, 15]	Elastic	Sleeveless	Variable distance from hole edge at plate bottom along $X(r)$ axis & at outer boundaries along the plate thickness.	Mandrel–plate: frictionless
Garcia-Granada *et. al* (2001) [40]	Rigid	Sleeveless	Used spring elements to simulate nosecap support.	Mandrel–plate: frictionless
Zhang *et al.* (2002) [24]	Elastic	Sleeveless	Variable distance from hole edge at plate bottom along $X(r)$ axis & at outer boundaries along the plate thickness.	Mandrel–plate: frictionless
Kang *et. al* (2002) [19]	Uniform radial displacement	Sleeveless	-	N/A
Chakherlou & Vogwell (2004) [39]	Elastic	Sleeveless	Partial support away from the hole at plate bottom along $X(r)$ axis.	Mandrel–plate: elastic Coulomb's friction, $\mu = 0.1$
de Matos *et. al* (2005) [17]	Elastic	Elastic	Variable distance from hole edge at plate bottom along $X(r)$ axis & at outer boundaries along the plate thickness.	Mandrel–sleeve: frictionless sleeve–plate: frictionless

Table 4.3.1 Summary of axisymmetric and three-dimensional model finite element modelling of fastener hole cold-working procedures using split-sleeve and mandrel.

It is also observed that boundary conditions assigned in the FE models dictate the deformation behaviour around the hole. Notably, amongst others Arora *et. al* [14, 15] and de Matos *et. al* [17] reported the occurrence of secondary bending affecting the resulting residual stress, as a result of different external support conditions on the plate. However, the numerical studies in [8, 14-18, 23, 24, 39] do not reflect the actual operation constraints

intrinsic to the actual FTI cold-working procedure [29]. In reality, the specimen is constrained by the complex interaction between sleeve, nosecap of the pulling gun and hole when the mandrel is drawn through the hole (Figure 4.3.3). An exception is the effort of Gracia-Granada *et. al* [40] which simplifies the nosecap–plate interaction using very stiff spring elements attached near to the hole edge at the mandrel exit face.

The precise contact condition between the plate, mandrel and sleeve is complicated, if not impossible to determine. Consequently, frictionless (viz. $\mu = 0$) interaction was repeatedly used in most FE analyses [8, 14, 15, 24, 40], although significant impact of μ on the residual stress created was observed [21, 22, 39]. The assumptions of frictionless sleeve–mandrel contact is usually justified by the use of lubrication [8, 17, 23], but this is not necessarily true for the sleeveless mandrelising technique.

In FE modelling, the use of the rigid mandrel, the elimination of the sleeve, and the assumption of zero friction undoubtedly minimise convergence difficulties in numerical calculations, which also increases the computational efficiency. Nevertheless, the wider implications of these simplifications can be complicated and are not yet thoroughly understood, and hence the results obtained often differ from measurements. To describe the process as faithfully as possible, the present SSM simulation incorporates the tool assembly comprising of mandrel, plate, sleeve and nosecap (Figure 4.3.3.). Material nonlinearities in the plate, sleeve and mandrel are considered along with complex boundary nonlinearity due to multi-body contact.

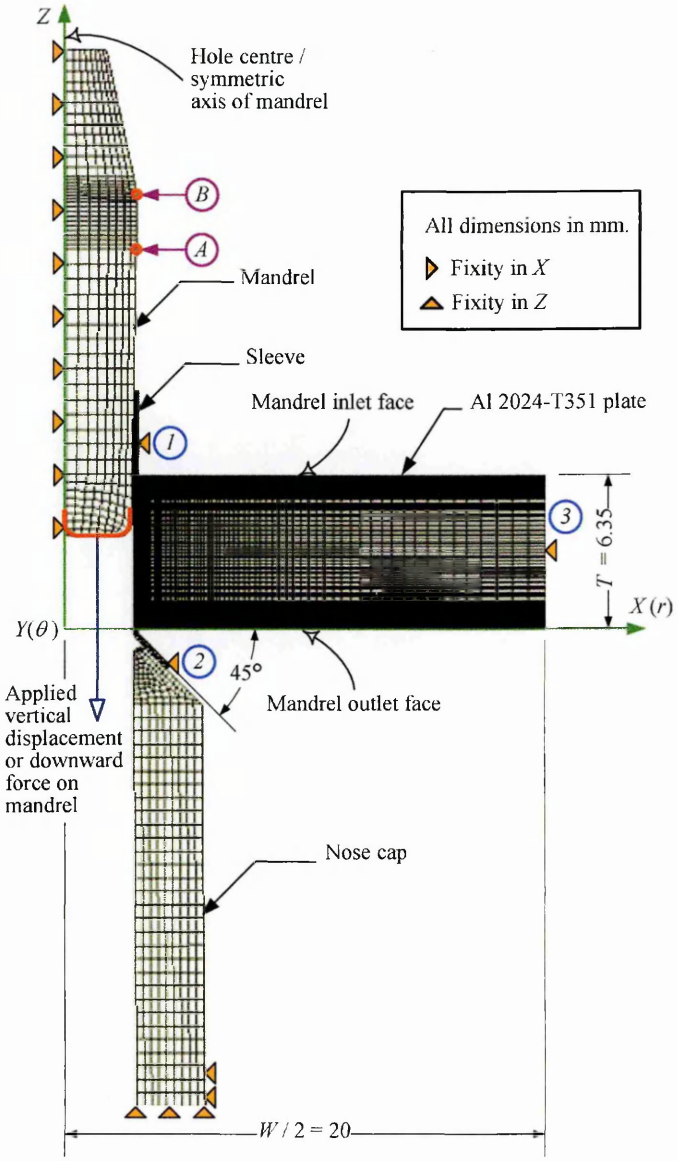

Figure 4.3.3 Finite element representation of FTI 4% cold-working set-up for Ø6 mm hole in an Al 2024-T351 plate.

In this study, to perform a 4% nominal expansion in Ø6 mm hole, the following hand-operated cold-working tools and consumables manufactured by FTI, Inc [29] were used: CBS–8–0–N–16F split-sleeve, CBM–8–0–N–1–40–V1 mandrel, and CBC-11-10F extension-nosecap assembly. Owing to the process symmetry, the complete FE set-up can be reduced to a half-model about the *Z*-axis, as shown in Figure 4.3.3. Geometrical details of each component, as physically measured in the laboratory, are provided in Figure 4.3.4.

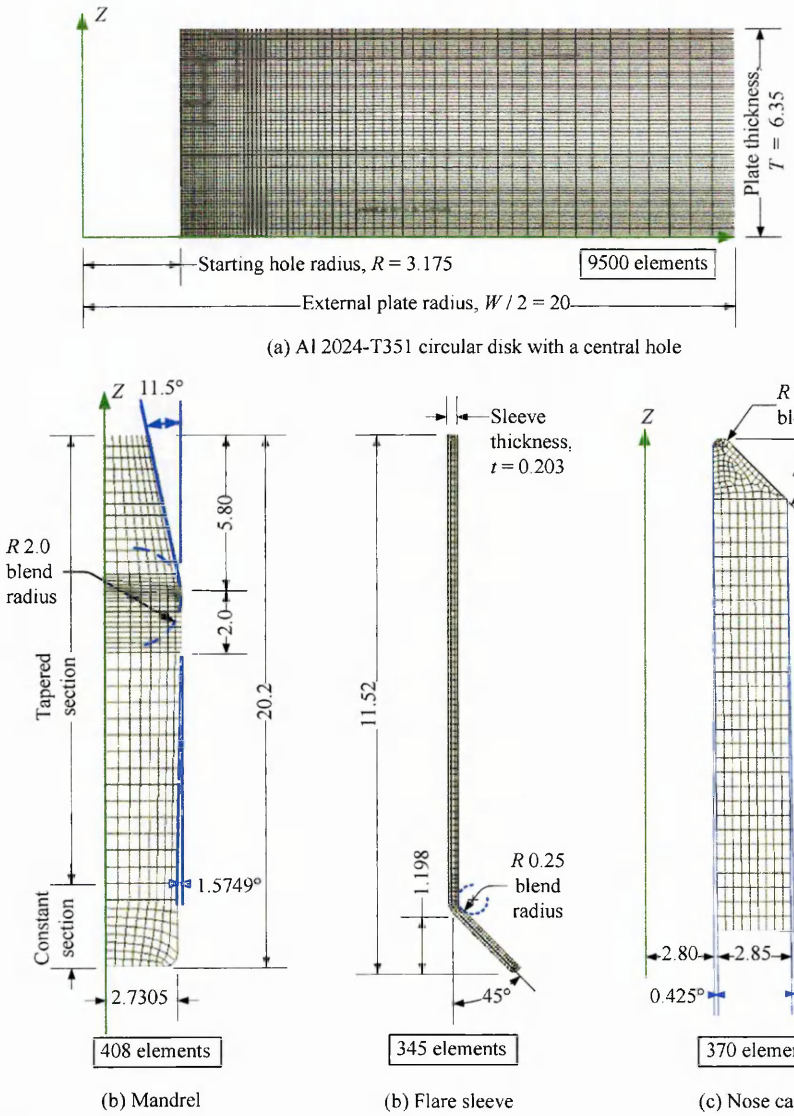

Figure 4.3.4 Physical dimensions and FE mesh of plate, mandrel, sleeve and nosecap.

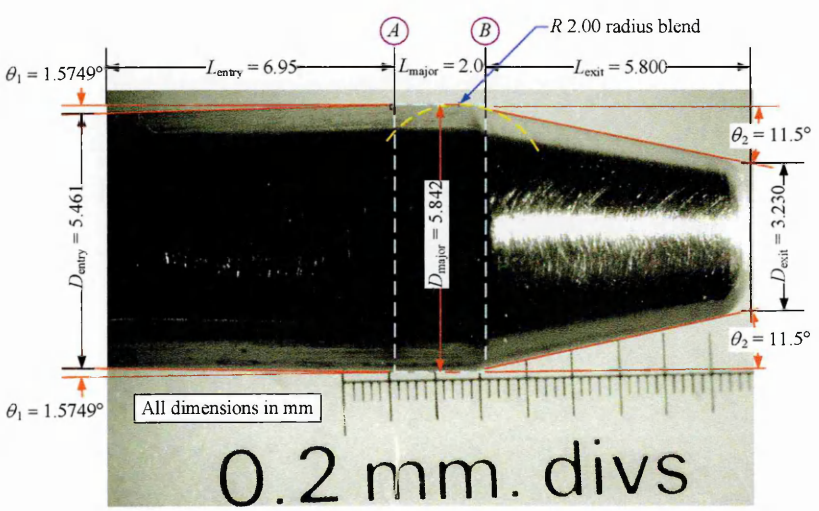

Figure 4.3.5 Physical dimensions of oversized section of cold-working mandrel.

Besides the sleeve (Figure 4.3.4), particular attention was paid to the mandrel as the geometrical influence of mandrel dimension is believed to be crucial. A literature survey

indicated that various mandrel dimensions and sizes, e.g. tapered angle on the entrance and exit face, θ_1, θ_2; constant width of oversized section, L_{major}; etc, have been used [8, 14-18, 20-22, 24, 39, 40]. The FE dimensions of the mandrel were inferred indirectly from a few sources [29, 41, 42] without actually being measured or validated. To remove any ambiguity, a digital micrometer and precisely calibrated photographs were used to quantify the mandrel dimensions. The dimensions θ_1, θ_2 and L_{major} in Figure 4.3.5 show some discrepancies compared to the values reported in literature, e.g. [8].

To avoid convergence problems in the numerical analysis, a radius blend was used to smooth the sharp corner in the mandrel, sleeve and nose-cap (Figure 4.3.4). Entire FE meshes for the individual components were constructed with 4-noded quadratic linear elements (CAX4) of 2 × 2 full integration scheme. The contact algorithm (Figure 4.3.3) was similar to that used for the SW simulation. A total of four sets of "master-slave" contact conditions, i.e. mandrel–sleeve, sleeve–plate, mandrel–capnose and nosecap-sleeve, were assigned with respective frictional coefficients of 0.10, 0.40, 0.10 and 0.10 [43]. The mechanical properties of plate, sleeve (i.e. full hard AISI 301), and mandrel (i.e. AerMet®) were described in Section 4.2. For the nosecap, presuming elastic behaviour we assigned E = 210 GPa and v = 0.30. The mandrel was fixed in X-axis and coincided with the mandrel and hole centre axes to permit downward Z-axis movement.

Initially, the plate and sleeve were temporarily fixed in the Z-axis at locations 1, 2 and 3 in Figure 4.3.3 to avoid unlimited rigid body motions (i.e. numerical singularity). The mandrel was positioned to establish an elastic contact condition with the sleeve interior. Second, the cold-working was simulated by incrementing the node position, or applied force on the mandrel lower face in 20 load steps. At the same time, the constraints 1, 2 and 3 were released during the 1st load step to allow uninterrupted repositioning of sleeve, plate and nosecap in response to the mandrel travel.

The constraints 1, 2 and 3 (Figure 4.3.3) were revived at the 20th load step just before the mandrel detached from the sleeve. Afterwards, the plastically deformed sleeve was found to adhere to the hole wall, which required its elements to be deactivated at subsequent steps before analysis was carried out. The complete SSM simulation required 716 iterations in response to the automatic load-increment procedure implemented in ABAQUS.

4.4 Finite Element Results

4.4.1 Cold expansion definitions

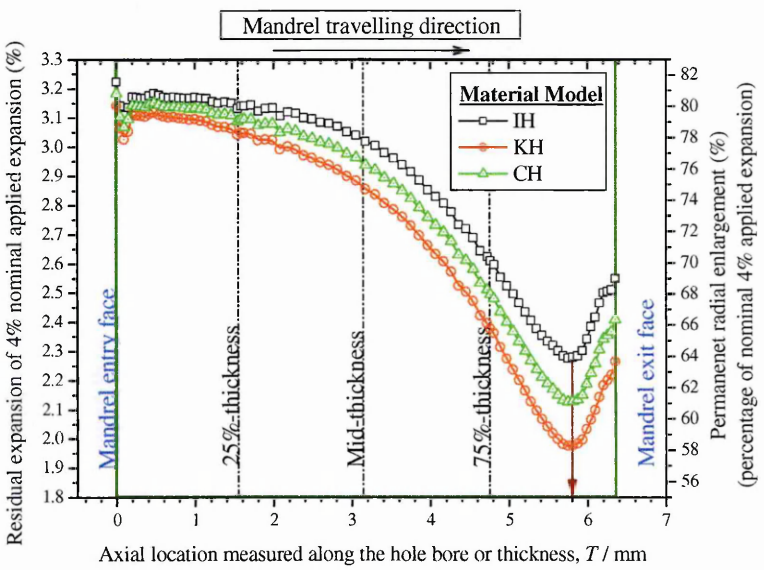

Figure 4.4.1 Definitions of amount of cold-working induced by SSM method.

Essentially, the amount of radial plastic expansion introduced in fastener holes must be controlled. For the SSM method, the nominal applied cold-expansion is expressed as a percentile of starting hole diameter *SHD*:

$$I_{a-FTI} = \frac{\left(D_{major} + 2 \cdot t\right) - SHD}{SHD} \times 100\% \tag{4.4.1}$$

where the mandrel major diameter D_{major}, combined with twice the sleeve thickness $2t$, is instrumental to achieve the required hole enlargement. For typical hole sizes in aluminium, the cold-working ranges from 3 ~ 6% according to the initial hole size and tooling tolerances. However, 4% cold-working is normally found to be the optimum value for a wide range of fatigue conditions [28, 29].

In Figure 4.4.1, the variations of permanent radial enlargement retained along the hole wall are presented as a fraction and percentage of nominal 4% expansion. It can be seen that high permanent expansion occurs at the first half of the plate thickness, and the trend decreases rapidly to the minimum at $T \sim 5.8$ mm before increasing near the outlet surface. This shows that the post-deformed hole wall is not perfectly straight, but in practice this is amended by reaming before fastener installation [28, 29]. Some previous studies [8, 17] predicted maximum retained expansion at the exit surface. This marked disagreement between present and previous studies is believed to be attributed to the difference in how the plate model is constrained or supported in the FE simulation.

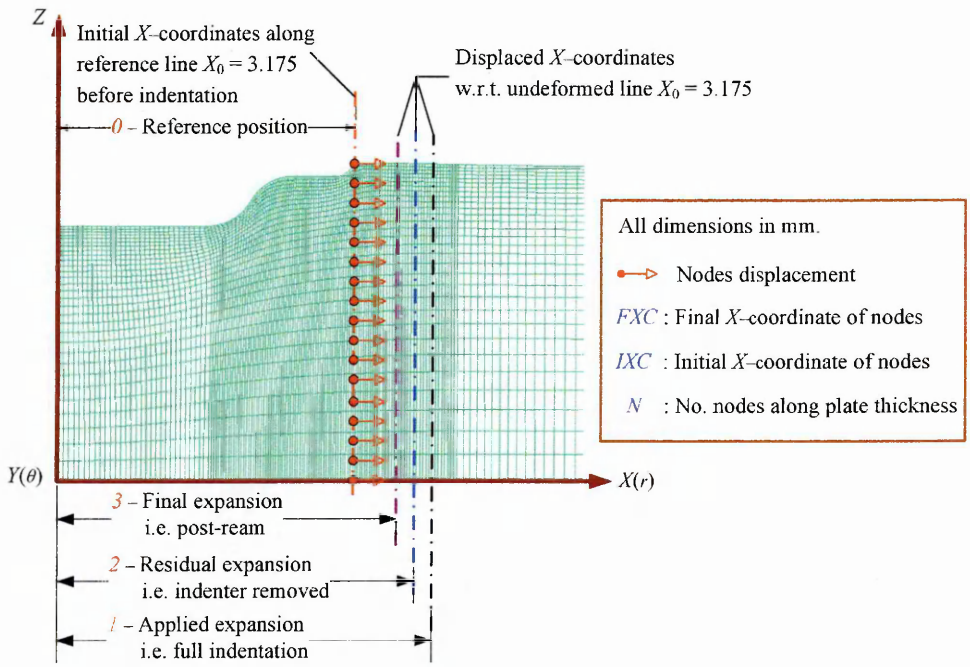

Figure 4.4.2 Definitions of amount of cold-working induced by StressWave method.

The amount of SW cold-working induced, when the indenter head is firmly pressed into the plate, is governed by the maximum depth of indentation Δ, (Figure 4.3.2 (b)). A simple way of deriving an equivalent SW radial expansion comparable to the SSM method is not obvious. However, based on a similar idea given by Equation (4.4.1), and in conjunction with the FE analysis in Figure 4.4.2, the level of SW cold-working can be computed as:

$$I_{a-SW} = \frac{\sum_{i=1}^{N}(FXC)_i - \sum_{i=1}^{N}(IXC)_i}{\sum_{i=1}^{N}(IXC)_i} \times 100\% \qquad (4.4.2)$$

where *FXC* is the final *X*-coordinate measured from the reference node; *IXC* represents the initial *X*-coordinate of the reference node, normally taken as the diameter of the post-ream hole; *N* designates the total number of nodes on the reference thickness line. Different stages of indentation were analysed (Figure 4.3.2) using the IH, KH and CH schemes. The expansion level based on the 35 discrete FE nodes displaced along the plate half-thickness in *X*-axis, as a percentage of Ø 6.35 mm reamed-hole, is calculated in Figure 4.4.3.

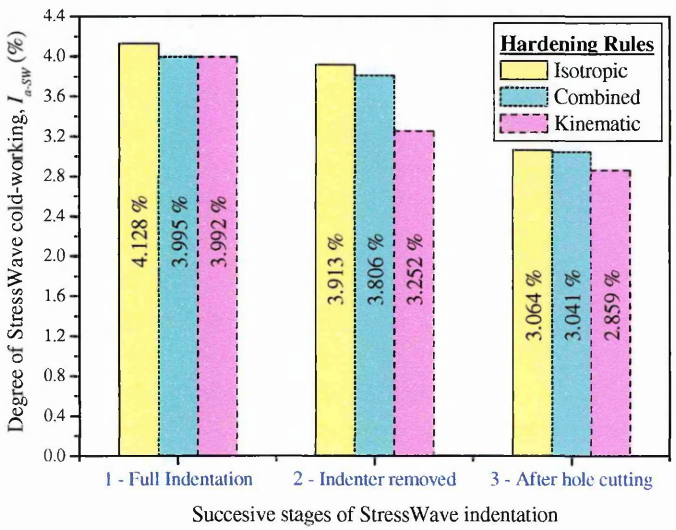

Figure 4.4.3 Average through-thickness radial expansion (%) derived from FE simulations of SW technique.

It is evident that the maximum radial expansion, I_{a-SW} was achieved when the indenter was fully engaged at its maximum depth, Δ. The equivalent applied SW cold-working, I_{a-SW} is close to the optimum value of the SSM method, i.e. I_{a-SW} = 4 % [28, 29]. Some relaxation in radial expansion took place upon indenter withdrawal, and further relaxation was observed after the final hole machining. In any stage of the SW indentation, IH and KH predicted the highest and lowest cold-working, respectively; the amount of radial expansion estimated by CH was persistently bound between the two hardening rules.

Using a total of 12 post-reamed SW specimens, the average hole diameter was determined to be 6.501 mm to 3 decimal places. The individual hole diameters were precisely measured at several diametric distances across the hole centres under a microscope with a

travelling *X*–*Y* stage. In Table 4.4.1, the numerically estimated diameters agree very well with the measured mean value, with relative errors of 0.169 ~ 0.677 %.

Final reamed hole diameter, Ø / mm	Hardening rules in FE model			Experiment
	Isotropic	Combined	Kinematic	
	6.545	6.543	6.512	6.501

Table 4.4.1 Comparison of the average through-thickness hole diameter by finite element analysis and laboratory measurements.

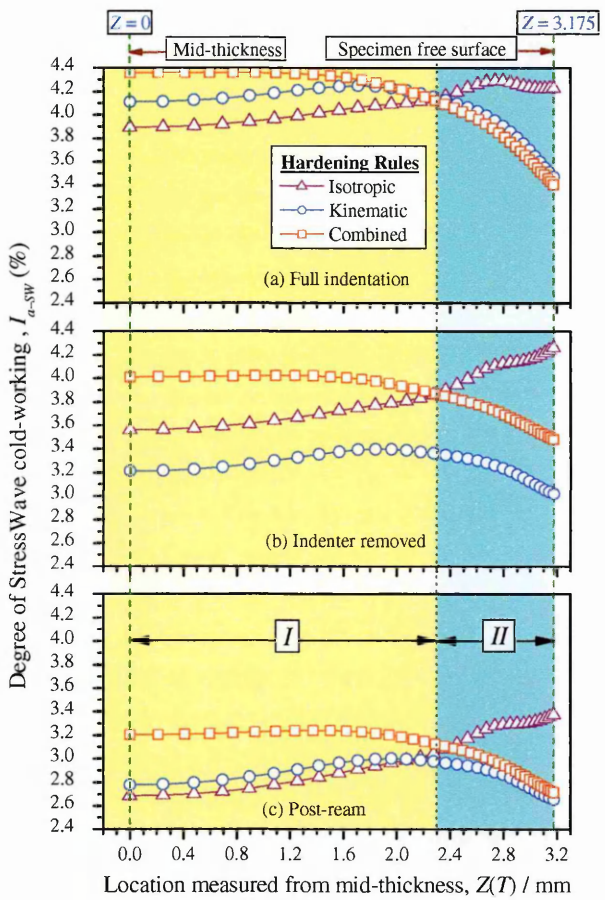

Figure 4.4.4 Local radial cold-expansion of specimen at various stages of the StressWave process as a function of depth measured from the specimen mid-thickness.

Figure 4.4.4 shows the history of local radial deformation occurring from the mid-plane to the surface of the SW specimen. The general patterns of the curves associated with KH and CH are fairly close, showing a high degree of radial expansion in region–*I* located approximately $0 < Z < 2.30$ mm, and a rapid decrease for $2.30 < Z < 3.175$ mm in region–*II*. In contrast, the IH curve retains a majority of high cold-working near to the surface (region–*II*) compared to the location near to the mid-plane (region–*I*).

4.4.2 Permanent axial & surface plastic deformation

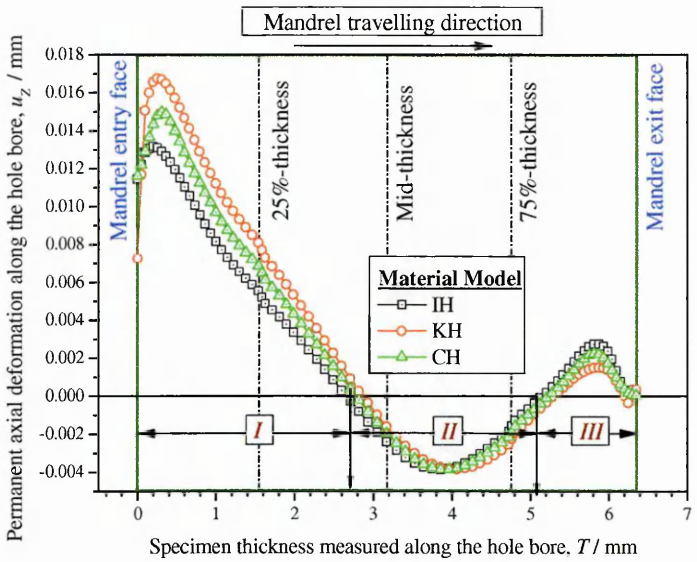

(a) u_Z along hole bore

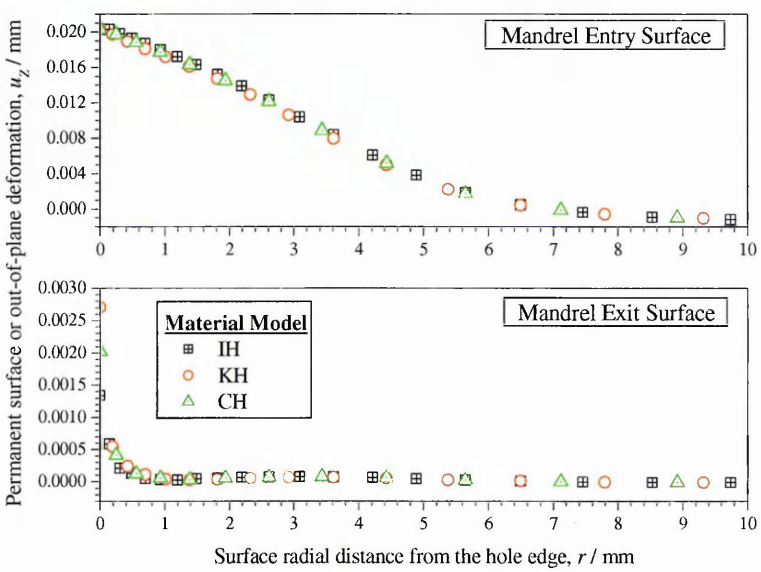

(b) u_Z on surfaces near to the hole

Figure 4.4.5 Local radial cold-expansion of specimen at various stages of the SSM process as a function of depth measured from specimen mid-thickness.

The dimensional instability or distortion related to cold-working is one of the critical issues in the parts assembly phase of manufacturing, and sometimes causes unexpected fatigue-cracking problems surrounding mechanical joints [44, 45]. It was reported that out-of-plane deformation, u_Z, can initiate cracks several millimetres away from the cold-worked holes in bolted joints via a fretting mechanism [46]. Also the full potential of cold-working cannot be fully realised, since the crack shape formed in these sample is very complex, and this makes life prediction even more complicated.

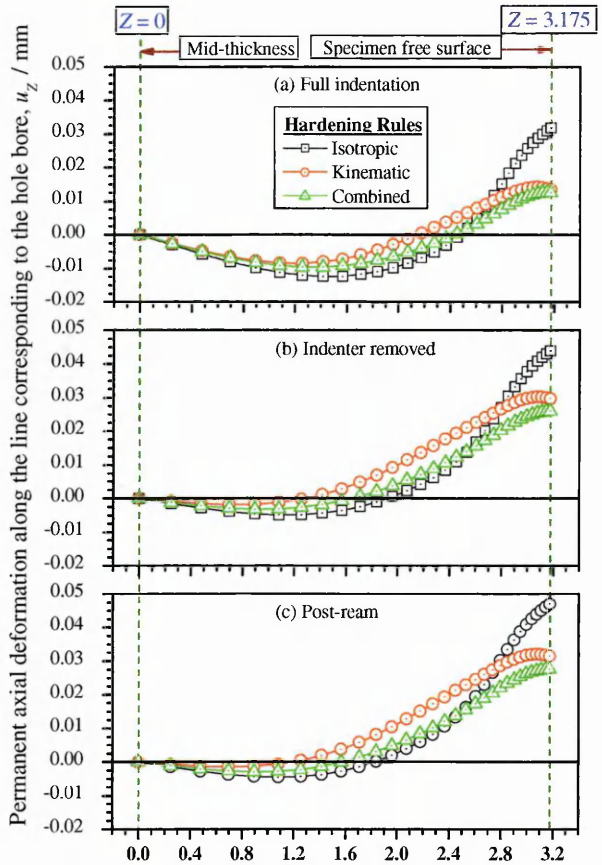

(a) u_Z along hole bore

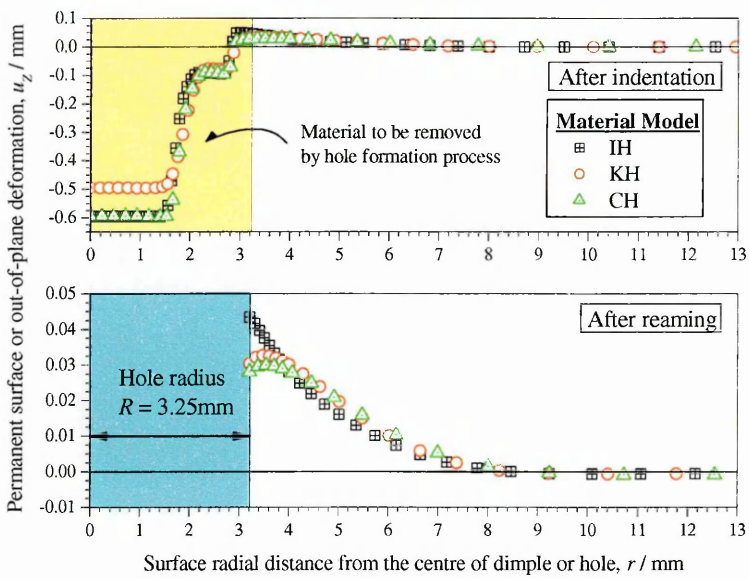

(b) u_Z on surfaces near to the hole

Figure 4.4.6 Local radial cold-expansion of specimen at various stages of the StressWave process as a function of depth measured from specimen mid-thickness.

The permanent axial u_Z–deformation as a function of axial position (Figures 4.4.5 & 4.4.6) reflects the increase in thickness at the cold-worked region. In a SSM hole, regions–*I*, *II* and *III* corresponds to the axial material flow of the hole wall after mandrelising (Figure 4.4.5 (a)). Judging from Figures 4.4.5 (a), Region–*I* is more prone to dimensional growth

than region–*III*. In other words, the formation of a permanent set, sometimes termed the 'volcano effect' [28, 29], on the surface around the hole at the mandrel inlet face was simulated to be greater at the mandrel exit face (Figure 4.4.5 (b)). For the SW hole, most of the contribution in thickness growth is expected to be associated with the near-surface region (Figure 4.4.6 (a)). The dimple profile after indentation is shown in Figure 4.4.6 (a) and the trend and magnitude of the SW surface permanent set is similar to that of SSM in Figure 4.4.5 (b). Minimisation of part distortion in cold-worked holes would require parametric studies involving several factors, e.g. tool dimensions and contact conditions.

4.4.3 Development of residual stress field

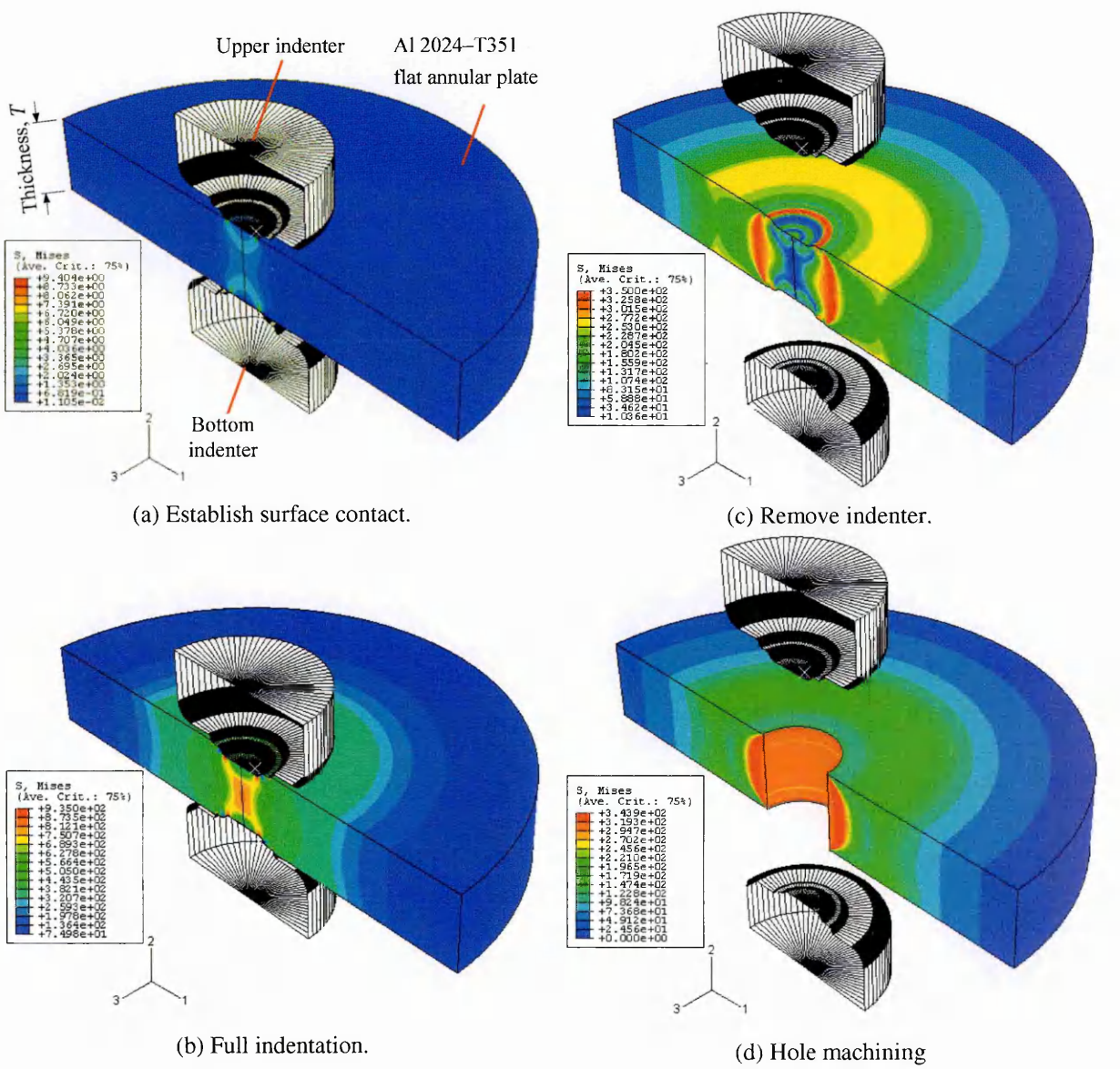

(a) Establish surface contact.

(c) Remove indenter.

(b) Full indentation.

(d) Hole machining

Figure 4.4.7 Successive evolution of von Mises stress field in FE simulations of StressWave® indentation and subsequent fastener hole cutting.

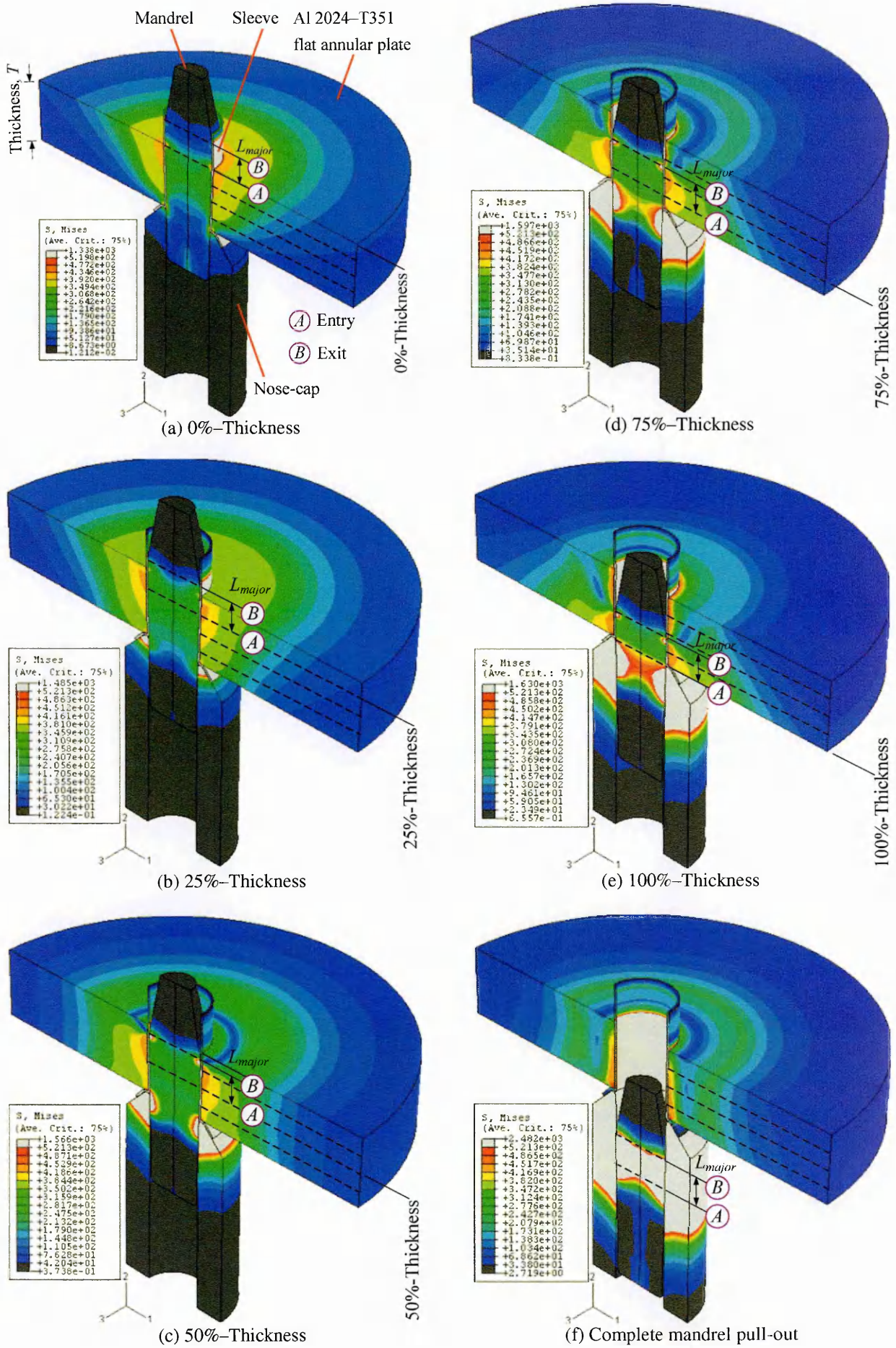

Figure 4.4.8 Successive evolution of von Mises stress field in FE simulations of mandrel drawing in SSM hole cold-working.

Figure 4.4.7 illustrates the 3D evolution of the von Mises effective stress for consecutive stages of the SW process (Figure 4.3.2.). Using the "Sweep & Extrude" display functionality in ABAQUS, the actual production scenario can be visualised. The axisymmetric FE simulation is rendered into cross-sectional views of a flat annular disk cold-worked with a pair of co-axial rigid indenters. In Figure 4.4.7 (b), the characteristic 45° X–shape bands are a consequence of the maximum plastic shear stress flow directions under simple compression [47], and persist in Figure 4.4.7 (c) even after unloading.

For an SSM hole, the evolution of the von Mises stress is related by the relative position of the mandrel oversized section (L_{major}, represented by points A & B), with respect to the hole bore (Figures 4.3.3, 4.3.5 & 4.4.8). For clarity, the legend at different stages was adjusted to scale the stress in the specimens. The stress field spreads unevenly in the through-thickness direction and the highest stressed zone always corresponds to the location of the mandrel major (oversized) section.

4.4.4 Hoop residual stress mappings

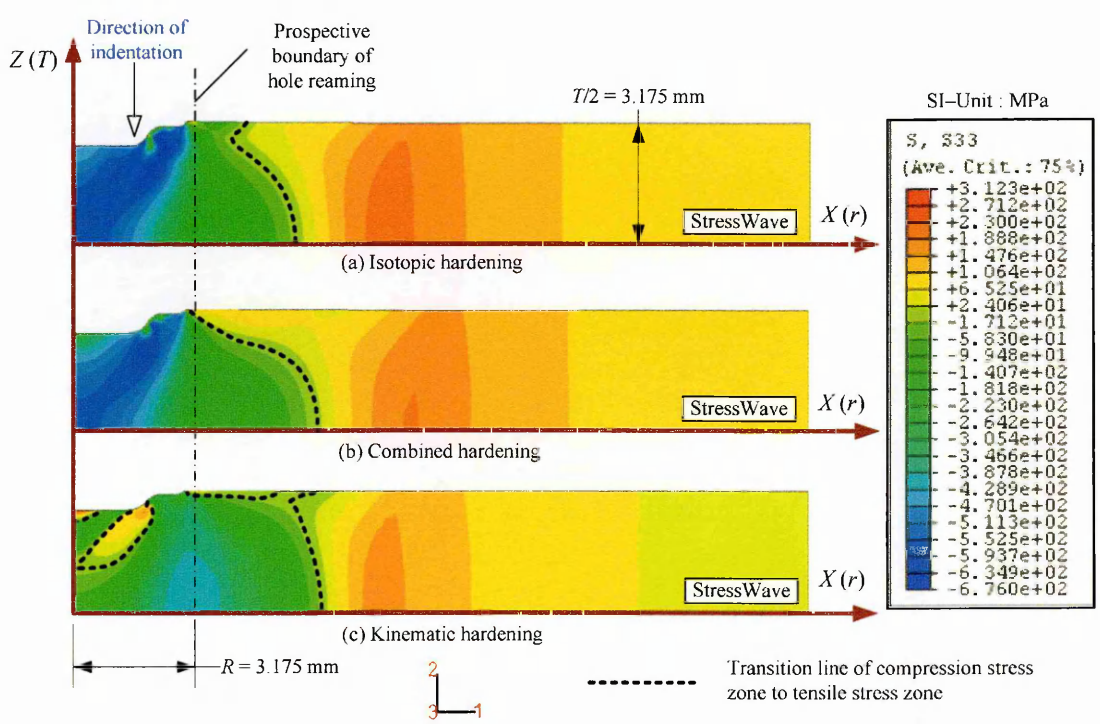

Figure 4.4.9 Comparison of FE prediction of hoop residual stress, $\sigma_{\theta\theta}$ / MPa, distributions in SW dimple for three distinct material hardening models.

In most cases, crack growth operates under a Mode-I loading condition. Corresponding to this in-plane fatigue loading, the hoop stress component has a direct effect on in crack growth retardation at a cold-worked hole. This section will provide further information about the hoop residual stress field.

The FE hoop stress contours for the half-thickness SW dimple models, after unloading of the indenter, are illustrated in Figure 4.4.9. Regardless of the material hardening rules employed, the hoop stress is predominantly compressive around the dimple and is balanced by an outer tensile stress region, as indicated by the transition lines. For the IH and CH contours, the domains of intense compressive stress are located very near to the surface where the contact between the indenter and plate takes place. However, for the KH model the high compressive stress zone spreads closer to the plate mid-plane and possesses the largest compressive domain of all three.

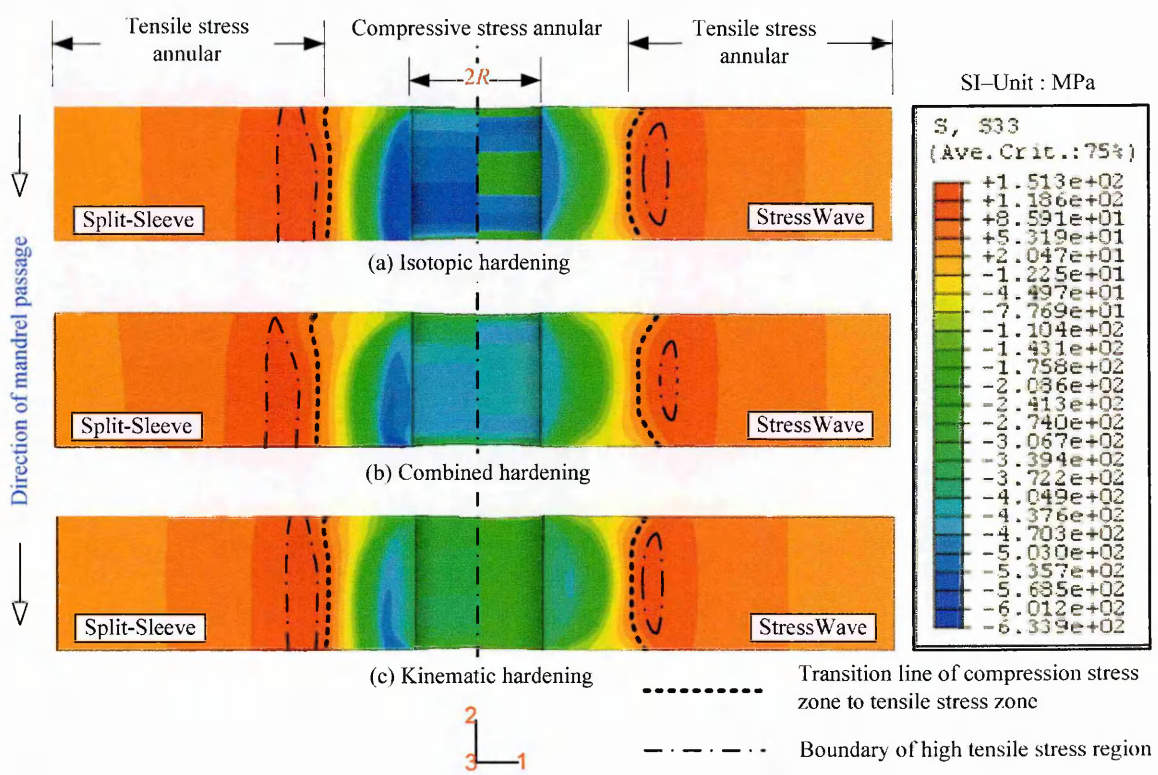

Figure 4.4.10 Comparison of FE prediction of hoop residual stress, $\sigma_{\theta\theta}$ / MPa, distribution in split-sleeve and SW cold-worked hole for three distinct material hardening models.

Six independent FE maps of hoop residual stress are jointly presented in Figure 4.4.10, which correspond to the different material hardening models. The SSM contours generally

indicate an uneven asymmetric hoop stress around the hole, especially in the thickness direction (Z-axis). The SSM stress characteristic is found to be responsible for the formation of a complicated 3D fatigue crack [48], and existing stress intensity factor solutions are still inadequate to account for such complexity [49, 50].

Near to the hole bore, envelopes of localised peak stress spreading from the mid-thickness to the mandrel exit face are also observed. The relatively low permanent radial expansion from 75 % to 100 % thickness may be because that material flow is highly constrained, similar to a plane strain condition (Figure 4.4.2). It has been revealed by analytical solutions that plane strain models inevitably predict a higher magnitude of residual stress in cold-worked holes than plane stress models [51].

However, it is possible that contact conditions between the nosecap, sleeve and plate contribute to the pseudo-plane strain condition near the mandrel outlet face. The contact pressure is intensified in a small area, which is the only critical means to provide the necessary spatial constraints for sleeve and plate while the mandrel was steadily pulled through the hole. Nonetheless, the presence of the sleeve flare section (Figure 4.3.3) between the plate and nosecap is capable of protecting the material at the mandrel exit face from severe surface deformation (Figure 4.4.5 (b)).

It is postulated that in the SSM technique a small fraction of material in the affected region is damaged, but the impaired location is normally removed by subsequent final reaming step [28, 29]. Also, the precise effect of the gap in the split-sleeve on the hole cannot be incorporated in the axisymmetric model. Rather, in this attempt the sleeve is simplified as a seamless thin-walled tube. The absence of the split feature in the sleeve certainly covers a higher mandrel drawing force and hence counteracting force of the nosecap. A 3D FE model may be necessary to replicate the split sleeve function in the SSM process.

In contrast, a balanced hoop stress field mirrored about the plate mid-plane exits in SW holes. The stress field was found to be effective to grow simple through-thickness cracks of equal surface lengths in fatigue crack growth experiments [52]. As outlined in Figure 4.4.10, though the magnitude of the compressive stress is not as high as SSM holes, SW holes possess a wider compressive zone. Also, the SSM method induces a larger region of high tensile residual stress. The areas of high tensile stress away from SSW holes that equilibrate the compressive domain are about 2 ~ 5 times greater than those observed in SW holes. For example, in Figure 4.4.5 this is demonstrated by the boundaries for hoop stress region, $\sigma_{\theta\theta} > 118$ MPa. For both SSM and SW, the through-thickness stress fields are not constant near to the hole. However, away from the holes for the SW case the through-thickness hoop stress field gradually becomes more constant in contrast to SSM holes.

For the three hardening models used, IH generally tends to overestimate the magnitude and distribution of compressive and tensile hoop stress in cold-worked holes. Conversely, KH predicts the smallest residual stress field due to stress reduction related to the idealised Bauschinger's effect. Consistent with the fact that Al 2024-T351 exhibits pronounced compressive strain hardening and Bauschinger's behaviour, the CH scheme is more realistic to represent the actual material deformation. CH results are bound between the extremes cases of IH and KH. The reliability of the FE predictions for given material hardening models will be assessed in the light of experimental data in the next section.

4.5 Validation of Finite Element Modelling

4.5.1 StressWave dimple

Neutron data at the mid-thickness plane of the specimen was used to validate FE predictions applying the IH, KH and CH models. The principal residual strains ($\varepsilon_{\theta\theta}$, ε_{rr}, ε_{zz}) and stresses ($\sigma_{\theta\theta}$, σ_{rr}, σ_{zz}) from FE computations and experiment are shown separately in Figures 4.5.1 & 4.5.2. In general, the FE results are in excellent agreement with the neutron

data where elastic deformation prevails i.e. material away from the dimple. Marked differences are noticed near the dimple due to the severe deformation close to this area.

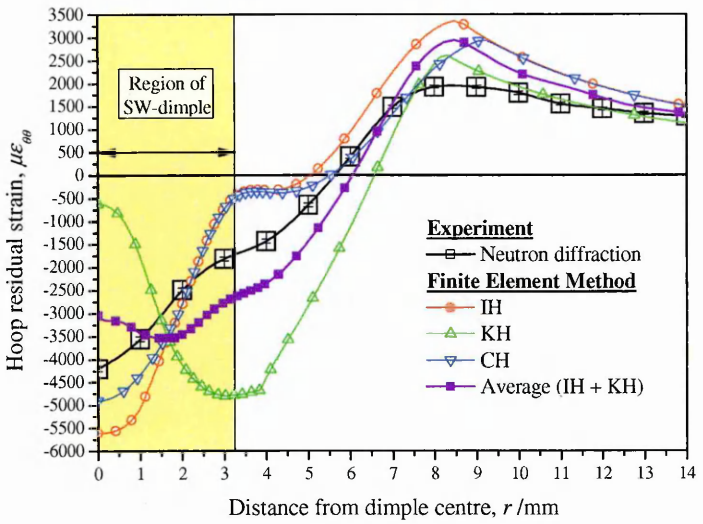

(a) Hoop residual strain

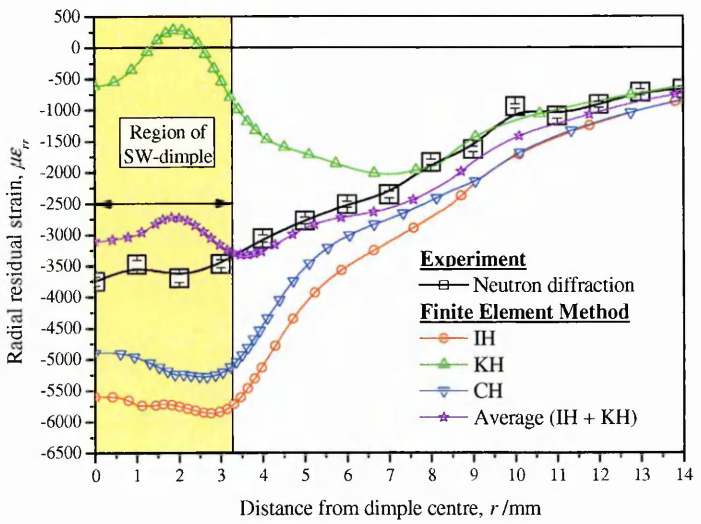

(b) Radial residual strain

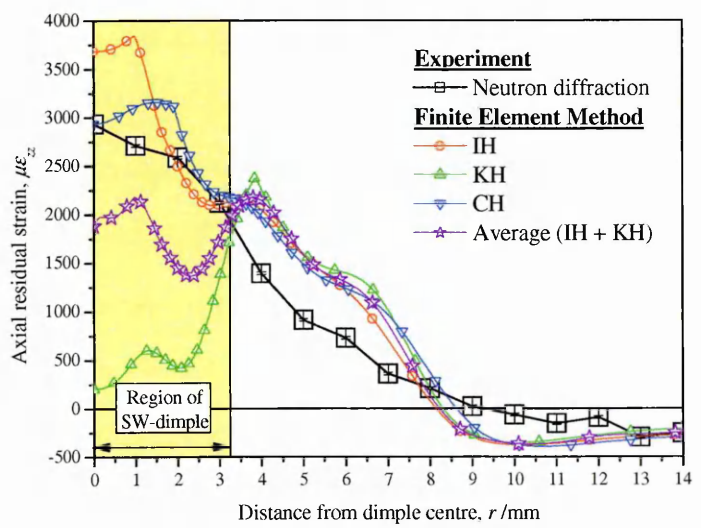

(c) Axial residual strain

Abbreviations

IH: Isotropic hardening

KH: Kinematic hardening

CH: Combined hardening

Figure 4.5.1 Experimental validation of FE principal residual strain fields, $\varepsilon_{\theta\theta}$, ε_{rr}, and ε_{zz} in SW dimple using neutron diffraction measurement. Location: specimen mid-thickness.

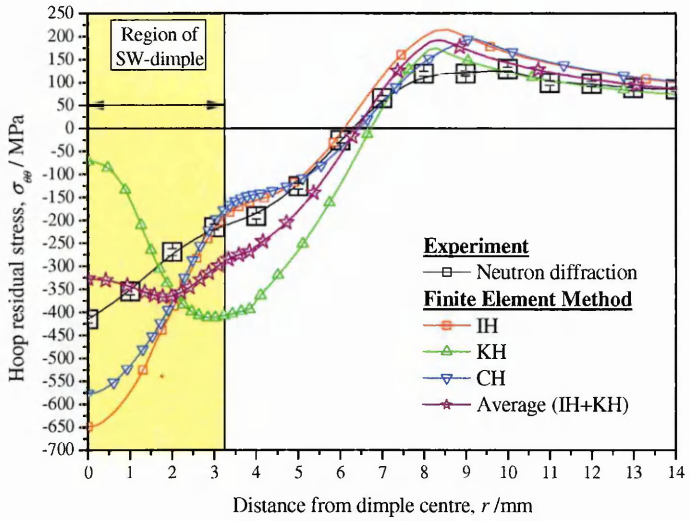

(a) Hoop residual stress

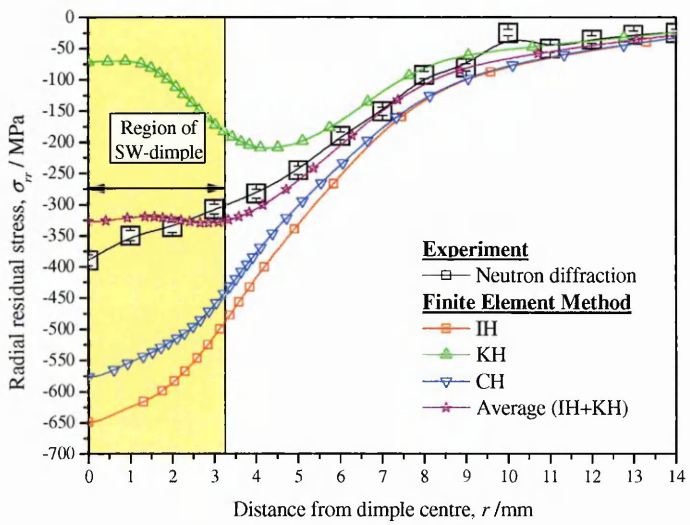

(b) Radial residual stress

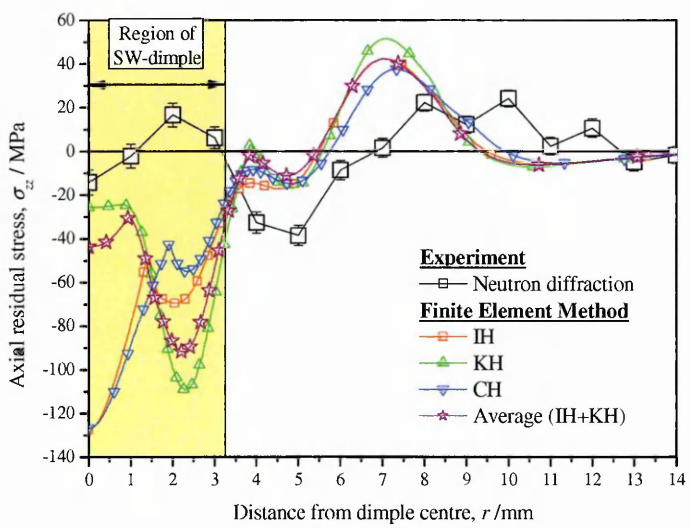

(c) Axial residual stress

Figure 4.5.2 Experimental validation of FE principal residual strain fields, $\sigma_{\theta\theta}$, σ_{rr}, and σ_{zz} in SW dimple using neutron diffraction measurement. Location: specimen mid-thickness.

In all cases, the FE simulation of IH and KH formulations respectively over- or under-predict the residual strains/stresses in the indented zone. Despite the provision of a Bauschinger's effect, the KH model is found to be less reliable under the large strain conditions involved in the SW process. The CH scheme seems to alleviate the problem, but the prediction is inherently close to the IH results (see also Figure 4.2.2). Mathematically, there are parametric restrictions to the CH model incorporating large straining more than 5% effective strain (Section 4.2.1).

An alternative to improve the limitations of the hardening models in replicating excessive elastic-plastic deformation at the indented region is the averaging procedure (Figure 4.5.1 & 4.5.2). The strain and stress data averaged from individual IH and KH simulations shows dramatic improvement, which matches the experimental data very well. Though it is an estimate, the simplicity of the averaging procedure satisfies the conditions that the experimental cyclic stress-strain curves of Al 2024–T351 always falls in between the IH and KH extremes loop [23]. The CH shows the dominant effect of parameters associated with IH especially at larger strain (Figures 4.2.2, 4.5.1 & 4.5.2). Conversely, the averaging procedure adopted here assumes equal contribution of IH and KH components in describing the material constitutive behaviour.

4.5.2 StressWave hole

Figures 4.5.3 & 4.5.4 show the second equilibrated state of residual strain and stress around SW hole after the hole forming process. The results of neutron measurement and FE predictions for the SW hole agree very well. In the FE simulation, the hole machining involves mainly the deformed region subjected to considerable elastic-plastic material flow. The disappearance of inner material or constraints via hole cutting enables the outer rim of elastic material to exert pressure onto the inner zone of plastic material adjacent to the hole. The entire process requires a new residual state to be established.

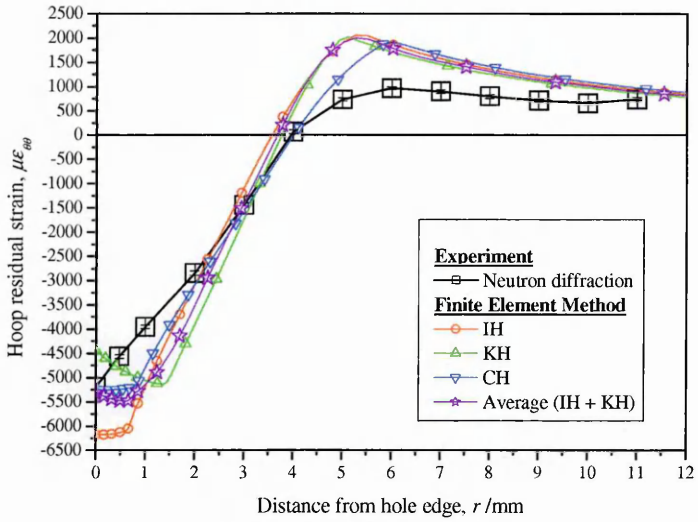

(a) Hoop residual strain

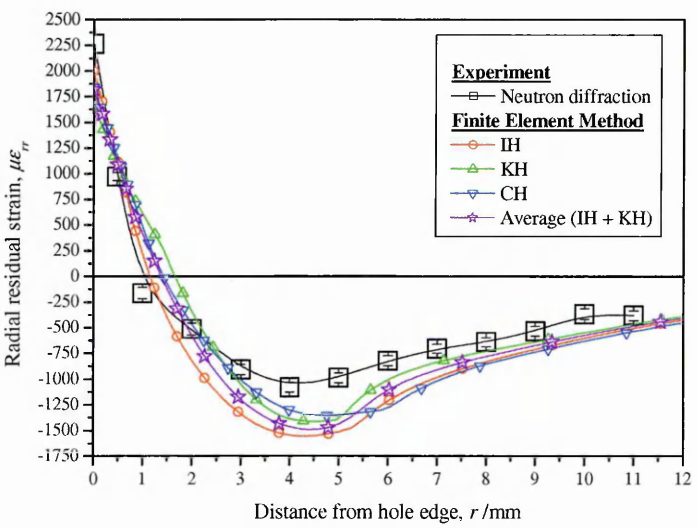

(b) Radial residual strain

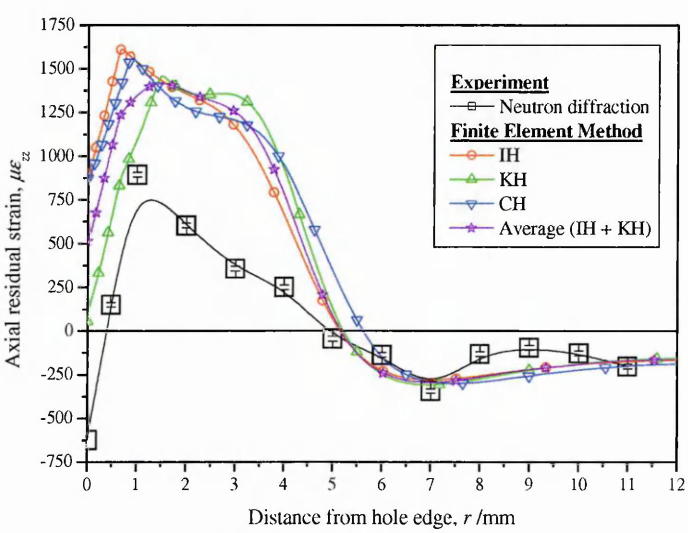

(c) Axial residual strain

Figure 4.5.3 Experimental validation of FE principal residual strain fields, $\varepsilon_{\theta\theta}$, ε_{rr}, and ε_{zz} in SW hole using neutron diffraction measurement. Location: specimen mid-thickness.

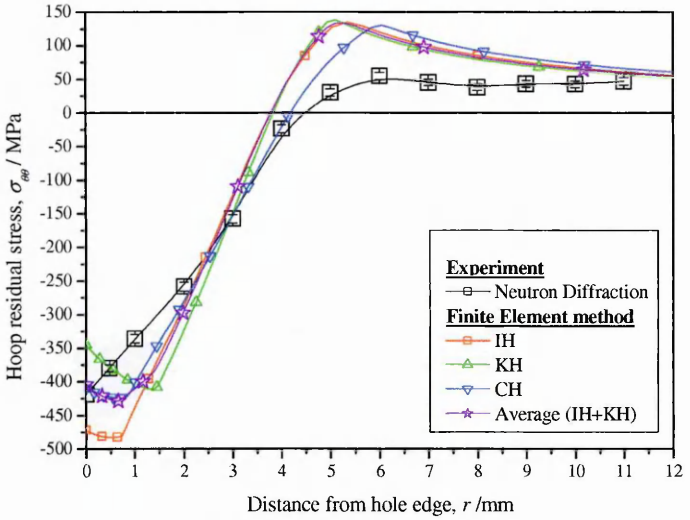

(a) Hoop residual stress

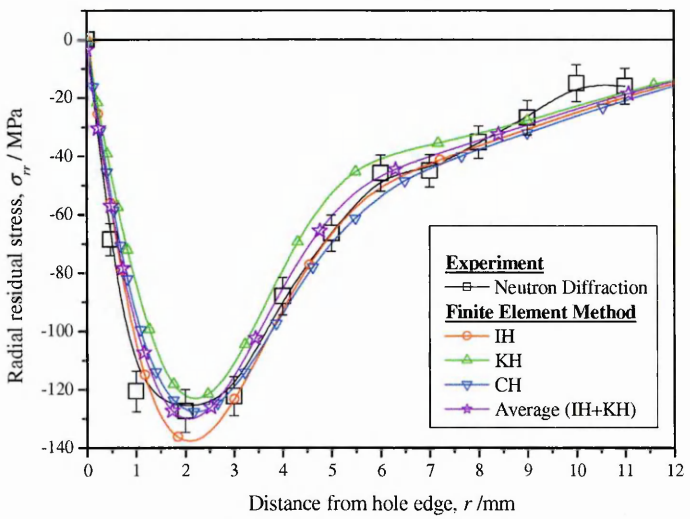

(b) Radial residual stress

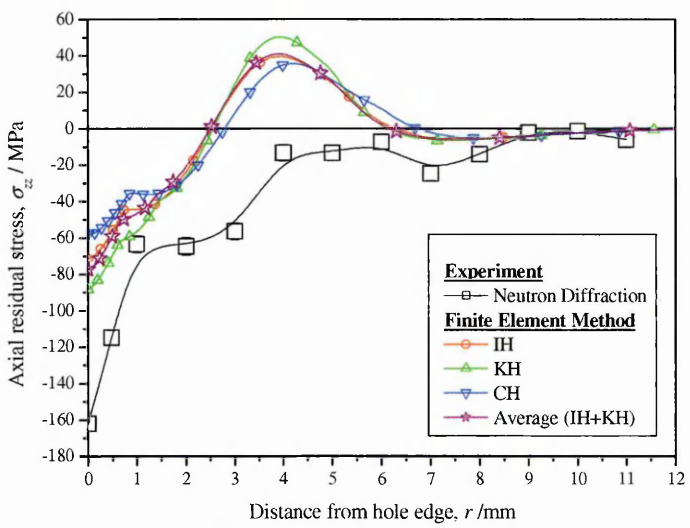

(c) Axial residual stress

Figure 4.5.4 Experimental validation of FE principal residual stress fields, $\sigma_{\theta\theta}$, σ_{rr}, and σ_{zz} in SW hole using neutron diffraction measurement. Location: specimen mid-thickness.

The reaming process is also accompanied by secondary plastic deformation as manifested by the reverse yield region in the hoop strain and stress fields (Figures 4.5.3 & 4.5.4). The

reversed yield boundary occurs at about 0.5 ~ 1.5 mm from the hole bore (Figures 4.5.3 (a) & 4.5.4 (a)). However, the primary elastic-plastic boundary both in the SW dimple and hole remains undisturbed; depending on the FE hardening models, they are predicted to be in the range of 7.5 ~ 9.5 mm from the dimple or hole centre (Figures 4.5.3 (a) & 4.5.4 (a)), and are estimated from the position of peak tensile hoop stress /strain.

Considerable improvement between the FE results was achieved for the SW hole in comparison to the SW dimple. The discrepancy observed earlier in the numerical and experimental data (Figures 4.5.1 & 4.5.2) is confined only to the highly strained region at the dimple. However, away from the dimple this localised effect fades gradually with the steady decrease of plastic deformation, and good agreement between the predicted and measured data in this region can be seen. This implies that the FE hardening models may still provide satisfactory prediction for moderately deformed material, and the subtraction of highly deformed material will not jeopardise the reliability of the subsequent FE analysis. In fact, this hole machining simulation has further contributed to the agreement between the predictions by various hardening models and experiment (Figures 4.5.3 & 4.5.4). The FE analysis predicted an average of 5 ~ 7 % effective plastic strain induced at the hole edge.

In the light of the experimental outcomes, the averaging procedure using the IH and KH data (Figures 4.5.1, 4.5.2, 4.5.3 & 4.5.4) may be valuable for SW manufacturing simulations, since precise material data are frequently not readily available for accurate estimation of residual stress fields. The method can also be a vital tool for identifying optimum SW tool designs and indentation, so that the generation of realistic residual stress fields can be maximised. Nonetheless, the averaging technique proposed here is merely restricted to Al 2024-T351, and is not necessarily applicable to other materials without further experimental validations.

4.5.3 Split-sleeve mandrelised hole

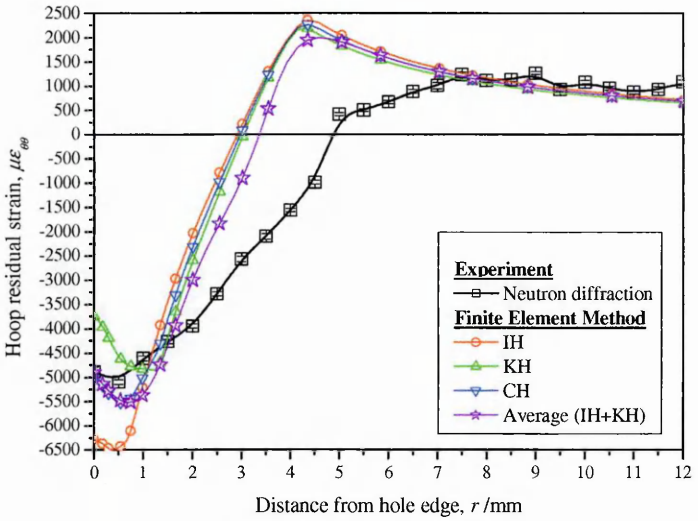

(a) SSM hole: Hoop strain

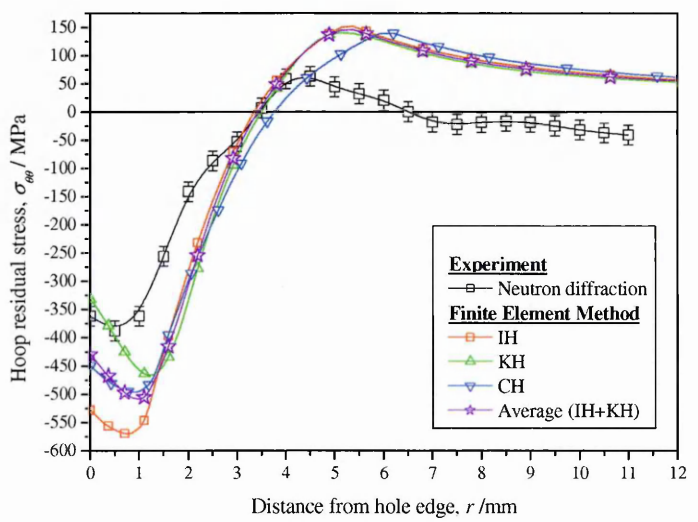

(b) SSM hole: Hoop stress

Figure 4.5.5 Experimental validation of FE hoop residual strain and stress fields, $\varepsilon_{\theta\theta}$ & $\sigma_{\theta\theta}$ in SSM hole using neutron diffraction measurement. Location: specimen mid-thickness.

Comparison of numerical and experimental hoop strain and stress for a SSM hole is given in Figures 4.5.5. The qualitative trend between the FE prediction and the neutron results are reasonable. However, quantitatively the neutron strain data, $\varepsilon_{\theta\theta}$ shows excellent agreement for distance near to (i.e. $0 < r < 2$ mm) and far from the hole edge (i.e. $r > 7$ mm) with a larger distribution of the compressive zone than the FE predictions. In terms of hoop stress, $\sigma_{\theta\theta}$, the magnitude of the FE compressive and tensile stresses in SSM hole are generally higher than the neutron measurement. Nonetheless, the measured and numerically predicted sizes of the compressive stress zones are similar.

4.5.4 Surface X-ray

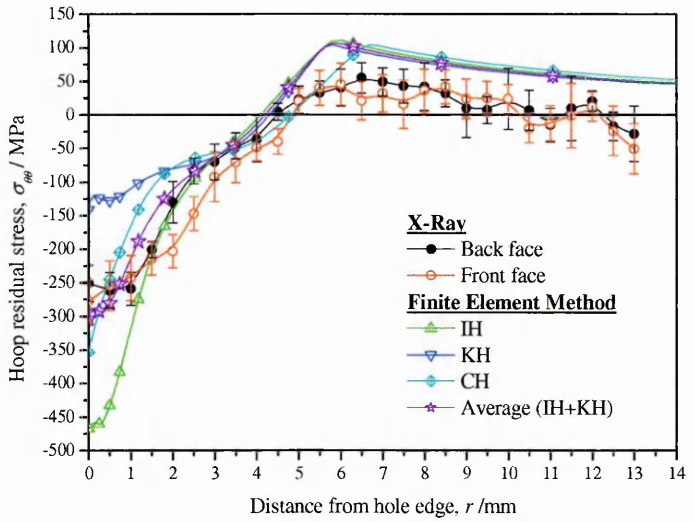

(a) SW hole

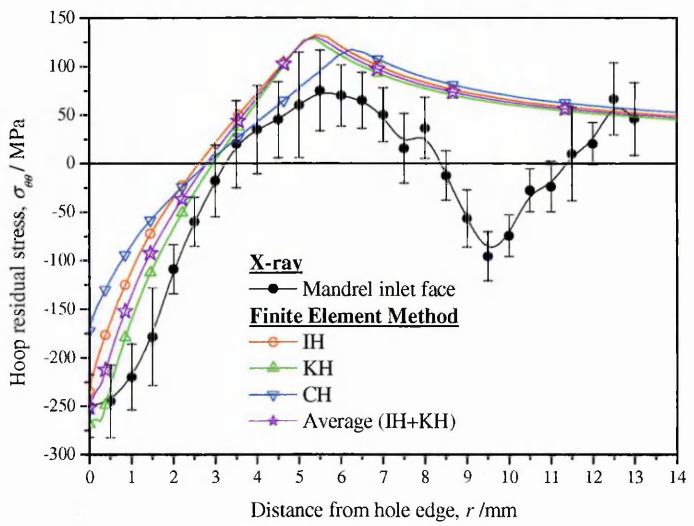

(b) SSM hole: mandrel inlet face

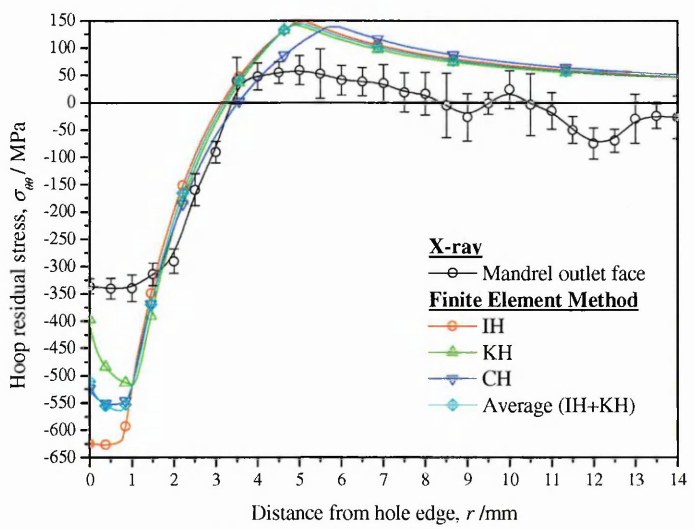

(c) SSM hole: mandrel outlet face

Figure 4.5.6 Experimental validation of surface FE hoop residual stress fields, $\sigma_{\theta\theta}$ in SW and SSM holes using laboratory X-Ray measurement. Location: specimen surfaces.

Laboratory X-ray diffraction studies were also carried out to furnish additional information of hoop residual stress induced on the specimen surfaces by different cold-working techniques. For the SW sample, Figure 4.5.6 (a) features encouraging agreement between the X-ray and numerical data of CH and averaging procedure. The measured hoop stress at both faces in the SW sample is virtually symmetric.

Separately, in Figure 4.5.6 (b) the measured hoop stress data at the mandrel inlet face of the SSM hole is slightly more compressive than the FE predictions. For the mandrel exit face, the FE data predict higher compressive hoop stress between about $0 < r < 1.5$ mm. In general, the measurement away from the hole reveals a strong attenuation tendency of tensile stress with gradual transition into compressive nature. This phenomenon is possibly due to initial rolling-induced residual stress pre-existing in the plate before cold-working.

4.5.5 Average through-thickness stress

Cracks emanating from non-cold expanded fastener holes are commonly of semi-elliptical or quarter-elliptical shape. Depending on the specimen and fatigue configurations, the presence of a residual stress field can further influence the complexities of crack shapes. Pell *et al.* [48] and Su *et al.* [53] observed bulbous-shape cracks formed in fatigued SSM holes. Recent studies by Stefanescu [54] and Nadri [11] advocated that double cold-working the fastener hole by SSM technique in reversed directions can improve the regularity of the crack shape substantially. However, in practice, the cost per hole for double cold-working is more expensive due to the consumption of extra split-sleeves and mandrel wear. Moreover, this technique may not be feasible if fastener holes can be accessed from one side only.

Despite the complication of crack shape, as a first approximation a straight crack profile is traditionally assumed for cold-worked holes in fatigue crack growth life prediction [51].

This requires a simplification of the stress field. For the FE analysis and measurements, 3D hoop stress data taken from the both surfaces, 25%, 50% and 75% of specimen thickness were averaged, and are presented in Figure 4.5.7. Except for the CH result, no significant influence of secondary reversed yielding is seen in the SW hole, which is validated by the measurement. The SSM results reveal considerable reversed plasticity of ~1 mm radius around the hole causing some reduction of stress at the hole wall. The compressive zone of hoop stress (i.e. 3.85 ~ 4.30 mm) of the SW hole is slightly larger than that of the SSM hole stress (i.e. 3.3 ~ 3.70 mm). The stress results in Figure 4.5.7 can be used to explain the extra benefits of increased the fatigue life in SW samples [52].

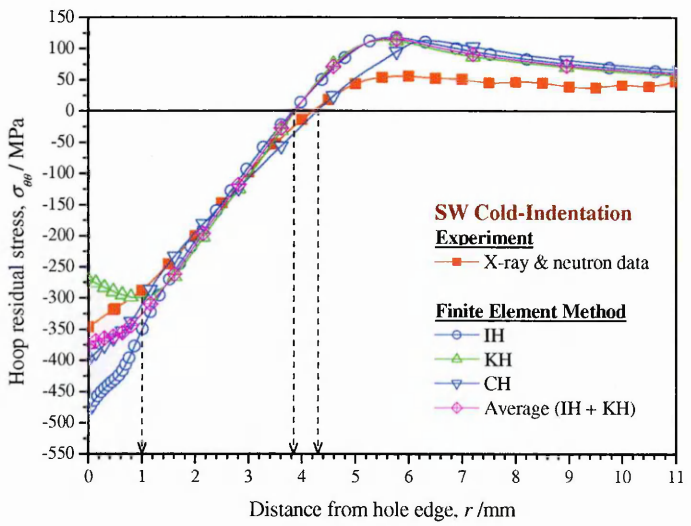

(a) SW hole

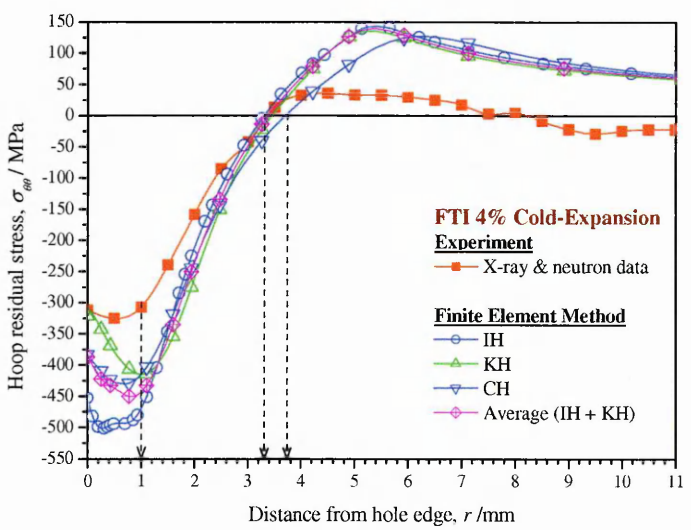

(b) SSM hole

Figure 4.5.7 Average through-thickness hoop residual stress in cold-worked hole.

4.6 Conclusions

(a) Finite element simulations of StressWave and split-sleeve cold-working techniques were carried out using axisymmetric models to study the residual stress field generated in a nominal Ø6 mm hole in a 6.35mm thick 2024-T351 aluminium plate. Compressive residual stress that is favourable to improve fatigue durability was observed around the hole edge after cold-working.

(b) Hardening models that include the material response to cyclic plasticity are essential to predict the residual stress field correctly. Simple validation implies the stress magnitude estimated by combined hardening is always bounded in between the isotropic and kinematic hardening predictions. Similar observations were found in subsequent stress-based or deformation-based analyses. In general, the data trend of combined hardening is closer to kinematic hardening simulation in strain-based analysis. In contrast, the stress-based analysis indicates that the combined hardening results are usually closer to an isotropic hardening prediction. The largest stress differences for different hardening rules occur in the area of reversed yield.

(c) FE analysis using isotropic, kinematic and combined hardening formulations fail to provide reasonable predictions at the StressWave dimple which material subjected to extreme plastic deformation. However, good agreement with the experimental results can still be achieved by averaging the strain or stress data obtained from isotropic and kinematic hardening simulations. Upon hole machining, the removal of severely indented material has allowed further improvement in the numerical and measured results.

(d) The evolution of residual stress contours at consecutive phases of the StressWave and split-sleeve mandrel process suggests different mechanisms are involved. In the

StressWave hole, the primary working mechanics is the outward radial flow of compressed material related to the depth of indentation. For the split-sleeve mandrel hole, the primary mechanism is dictated by the oversize dimensions of the mandrel, in combination with the axial deformation of material along the hole bore throughout the mandrel passage. This secondary mechanism can be attributed to the geometry of mandrel tapered sections.

(e) Good agreement between the simulated and measured residual stress data were obtained in the present analysis. Good conformity in StressWave results implies that the numerical analysis is reliable enough for future fatigue crack growth studies. Due to the complexity considered, it is thought that further improvement can be gained in split-sleeve mandrel simulation, but this entails a comprehensive parametric investigation.

4.7 References

1. Hsu, Y.C. and Forman, R.G., Elastic-plastic analysis of an infinite sheet having a circular hole under pressure. J Appl Mech Trans ASME, 1975. 42 Series E(2): p. 347-352.
2. Ball, D.L., Elastic-plastic stress-analysis of cold expanded fastener holes. Fatigue & Fracture Of Engineering Materials & Structures, 1995. 18(1): p. 47-63.
3. Chen, P.C.T., Bauschinger and hardening effect on residual stresses in an autofrettaged thick-walled cylinder. Journal of Pressure Vessel Technology, Transactions of the ASME, 1986. 108(1): p. 108-112.
4. Zhang, Y., Fitzpatrick, M.E., and Edwards, L., Analysis of the Residual Stress around a Cold-expanded Fastener Hole in a Finite Plate. Strain, 2005. 41(2): p. 59-70.
5. Lubliner, J., Plasticity Theory. 1998, New York: MacMillan Publishing Company. 495.
6. Hoffman, O. and Sachs, G., Introduction to the Theory of Plasticity for Engineers. 1953, New York: McGraw-Hill Book Co, Inc.
7. Mann, J.Y. and Jost, G.S., Stress fields associated with interference fitted and cold-expanded holes. Metals Forum, 1983. 6: p. 43–53.

8. Pavier, M.J., Poussard, C., and Smith, D.J., A finite element simulation of the cold working process for fastener holes. The Journal of Strain Analysis for Engineering Design, 1997. 32(4): p. 287-300.
9. Webster, P.J., Mills, G., Browne, P.A., Hughes, D.J., and Holden, T.M. Residual stress around a cold expanded hole. in Proceedings of the Sixth International Conference on Residual Stresses (ICRS6). 2000. Oxford, UK: IoM Communications Ltd.
10. Wang, D.Q. and Edwards, L. Neutron diffraction determination of the complete 3D residual stress distribution surrounding a cold expanded hole. in Proceedings of the 4th European Conference on Residual Stresses (ECRS4). 1998. Cluny en Bourgogne, France: Nancy J de Physique.
11. Nadri, B., Diffraction studies & finite element analysis of cold expanded holes, PhD Thesis, in Department of Materials Engineering. 2005, The Open University: Milton Keynes, U.K.
12. Priest, M., Poussard, C.G., Pavier, M.J., and Smith, D.J., Assessment of residual-stress measurements around cold-worked holes. Experimental Mechanics, 1995. 35(4): p. 361-366.
13. Ozdemir, A.T. and Edwards, L., Measurement of the three-dimensional residual stress distribution around split-sleeve cold-expanded holes. Journal of Strain Analysis for Engineering Design, 1996. 31(6): p. 413-421.
14. Arora, P.R., Rashdi, A.A.A., Hamouda, A.M., and Sahari, B., Coldworking process: A parametric finite element study. Journal of Malaysia Institute of Engineers, 2001. 62(4): p. 37-50.
15. Arora, P.R., Rashdi, A.A.A., and Hamouda, A.M., Residual stresses around cold worked holes in 2024-T351 aluminum alloy plate specimen. Journal Mekanikal, 2001. 12(December 2001): p. 11-22.
16. Bernard, M., Bui-Quoc, T., and Burlat, M., Effect of re-coldworking on fatigue life enhancement of a fastener hole. Fatigue & Fracture of Engineering Materials & Structures, 1995. 18(7-8): p. 765-775.
17. de Matos, P.F.P., Moreira, P.M.G.P., Camanho, P.P., and de Castro, P.M.S.T., Numerical simulation of cold working of rivet holes. Finite Elements in Analysis and Design, 2005. 41(9-10): p. 989-1007.
18. Forgues, S.A., Bernard, M., and Bui-Quoc, T., 3-D axisymmetric numerical analysis and experimental study of the fastener hole cold working process, in Computer Methods & Experimental Measurements for Surface Treatment Effects, M.H.

Aliabadi and C.A. Brebbia, Editors. 1993, Computational Mechanics Publications. p. 61–70.

19. Kang, J., Steven Johnson, W., and Clark, D.A., Three-dimensional finite element analysis of the cold expansion of fastener holes in two aluminium alloys. Journal of Engineering Materials & Technology, Transactions of the ASME, 2002. 124(2): p. 140-145.
20. O'Brien, E.W., Beneficial residual stress from the cold expansion of large holes in thick light alloy plate. Journal of Strain Analysis for Engineering Design, 2000. 35(4): p. 261-276.
21. Papanikos, P. and Meguid, S.A., Three-dimensional finite element analysis of cold expansion of adjacent holes. International Journal of Mechanical Sciences, 1998. 40(10): p. 1019-1028.
22. Papanikos, P. and Meguid, S.A., Elasto-plastic finite-element analysis of the cold expansion of adjacent fastener holes. Journal of Materials Processing Technology, 1999. 92-93: p. 424-428.
23. Poussard, C., Pavier, M.J., and Smith, D.J., Analytical and finite element predictions of residual stresses in cold worked fastener holes. Journal of Strain Analysis for Engineering Design, 1995. 30(4): p. 291–304.
24. Zhang, Y., Edwards, L., and Fitzpatrick, M.E. Finite element simulation of hole cold expansion process in EN8 steel plates. in Proceedings of the Sixteenth ABAQUS UK User Group Conference. 2002. Warrington, UK.
25. Kim, C., Kim, D.-J., Seok, C.-S., and Yang, W.-H., Finite element analysis of the residual stress by cold expansion method under the influence of adjacent holes. Journal of Materials Processing Technology

Proceedings of the International Conference in Advances in Materials and Processing Technologies, 2004. 153-154: p. 986-991.

26. ABAQUS/Standard User's Manual Version 6.5., Hibbit, Karlsson & Sorensen, Inc., Providence, R.I. 2004.
27. Easterbrook, E.T., Flinn, B.D., Meyer, C., and Juhlin, N. The StressWave™ Fatigue life Enhancement Process. in SAE Aerospace Automated Fastening Conference and Exhibition, Proceedings of 2001 Aerospace Congress, Paper No. 2001-01-2578. 2001. Seattle, USA: Society of Automotive Engineers.
28. West Coast Industries, Expendable Tooling Section, WCI Coldwork Tooling Catalog. 1996, Seattle, Washington.

29. Fatigue Technology Inc, FTI Process Specification 8101C Cold Expansion of Holes Using the Standard Split Sleeve System and Countersink Cold Expansion™ (CsCx™). 1994: 401 Andover Park East, Seattle, WA 98188-7605 USA.
30. Military Handbook MIL-HDBK-5H, Metallic Materials and Elements for Aerospace Vehicle Structures, MIL-HDBK-5H. 1998: US Department of Defence.
31. Chaboche, J.L., Time-independent constitutive theories for cyclic plasticity. International Journal of Plasticity, 1986. 2(2): p. 149-188.
32. Lemaitre, J. and Chaboche, J.-L., Mechanics of Solid Materials (English Translation). 1994: Cambridge University Press. 582.
33. Caulk, D.A. and Naghdi, P.M., On the Hardening Response in Small Deformation of Metals. Journal of Applied Mechanics, Transactions of ASME-Series E, 1978. 45: p. 755.
34. Bao, Y. and Treitler, R., Ductile crack formation on notched Al2024-T351 bars under compression-tension loading. Materials Science and Engineering A, 2004. 384(1-2): p. 385-394.
35. Source Book on Stainless Steels. ASM Periodical Publication Department, 1976, Metals Park, Ohio: American Society for Metals.
36. ASM Metals Handbook®. 10th ed. Vol. 2: Properties & Selection - Nonferrous Alloys and Special-Purpose Materials. 1990, Metals Park, OH: American Society for Metals.
37. Pierson, H.O., Handbook of Refractory Carbides & Nitrides : Properties, Characteristics, Processing & Applications. 1996, Westwood, New Jersey: Noyes Publications. 340.
38. Upadhyaya, G.S., Cemented Tungsten Carbides: Production, Properties, and Testing. 1998, Westwood, New Jersey: Noyes Publications. 403.
39. Chakherlou, T.N. and Vogwell, J., A novel method of cold expansion which creates near-uniform compressive tangential residual stress around a fastener hole. Fatigue & Fracture of Engineering Materials & Structures, 2004. 27(5): p. 343-351.
40. Garcia-Granada, A.A., Lacarac, V.D., Holdway, P., Smith, D.J., and Pavier, M.J., Creep relaxation of residual stresses around cold expanded holes. Journal of Engineering Materials and Technology, Transactions of the ASME, 2001. 123(1): p. 125-131.
41. Phillips, J.L., Sleeve coldworking fastener holes, Technical Report AFML-TR-74-10, Volume 1. 1974, Air Force Materials Laboratory, Wright-Patterson Air Force Base: Ohio.

42. Phillips, J.L. Fatigue improvement by sleeve coldworking. in National Aerospace Engineering & Manufacturing Meeting. 1973. Los Angeles, CA: Society of Automotive Engineers.
43. Nam, T., Private communications, StressWave, Inc. 2005.
44. Forsyth, P.J.E., Occurence of fretting fatigue failures in practice, in Fretting Fatigue, R.B. Waterhouse, Editor. 1981, Applied Science Publishers Ltd.: London.
45. Fujimoto, W.T. Analytic Testing of Joints with Cold Worked Holes. in Fifth Joint NASA/FAA/DoD Aging Aircraft Conference. 2001. Kissimme, Florida, USA: The Joint Council on Aging Aircraft (JCAA).
46. Mann, J.Y., Sparrow, J.G., and Beaver, P.W., Fatigue characteristics of joints with holes cold-expanded in a multi-layer stack. International Journal of Fatigue, 1989. 11(4): p. 214-220.
47. Rowe, G.W., An Introduction to the Principles of Metalworking. 1965: Edward Arnold Ltd. 306.
48. Pell, R.A., Beaver, P.W., Mann, J.Y., and Sparrow, J.G., Fatigue of thick-section cold-expanded holes with and without cracks. Fatigue and Fracture of Engineering Materials & Structures, 1989. 12(6): p. 553-567.
49. Harter, J.A., AFGROW: Users Guide and Technical Manual. AFRL-VA-WP-TR-2004 (Version 4.0009e.12). 2004: Air Vehicles Directorate, 2790 D Street, Ste 504, Air Force Research Laboratory, WPAFB OH 45433-7542.
50. Forman, R.G., Shivakumar, V., Mettu, S., and Newman, J.C., NASGRO Version 3.00 Reference Manual : Fatigue crack growth computer program, NASA Document JSC-22267B. December 2000.
51. Wang, Z. and Zhang, X., Predicting fatigue crack growth life for cold-worked holes based on existing closed-form residual stress models. International Journal of Fatigue, 2003. 25(9-11): p. 1285-1291.
52. Lamb, G.J., Jr., A.F.G., and Easterbrook, E.T. Fatigue Performance of an Advanced Hole Cold Working Method. in 2001 USAF Aircraft Structural Integrity Program Conference. 2001. Williamsburg, VA.
53. Su, X., Gu, M., and Yan, M., Simplified residual stress model for predicting fatigue crack growth behavior at coldworked fastener holes. Fatigue & Fracture of Engineering Materials & Structures, 1986. 9(1): p. 57-64.
54. Stefanescu, D., Experimental study of double cold expansion of holes. The Journal of Strain Analysis for Engineering Design, 2003. 38(4): p. 339-347.

55. Peckner, D. and Bernstein, I.M., Handbook of Stainless Steels. 1977: Mcgraw-Hill. 800.

APPENDIX 4–A

(a) Multi-linear isotropic hardening

E = 71900 MPa, ν = 0.328					
True Plastic Strain, ε^p_{true} (mm/mm)	True Stress, σ_{true} (MPa)	(Continued)		(Continued)	
0.0000	345.3000	0.01	376.4258	0.100	504.4999
0.0003	348.8366	0.02	396.2592	0.105	509.4131
0.0006	351.5975	0.03	414.3955	0.110	514.0700
0.0009	353.7196	0.04	431.4034	0.115	518.0663
0.0010	354.3138	0.05	447.1532	0.120	520.7490
0.0020	358.3270	0.06	461.328	0.121	521.0492
0.0040	363.1832	0.07	473.8021	0.122	521.2500
0.0060	367.7686	0.08	484.8073	0.123	521.3415
0.0080	371.9046	0.09	494.8867	0.1235	521.3429

(b) Linear kinematic hardening

E = 71900 MPa, ν = 0.328, C = 1.530 GPa	
True Plastic Strain, ε^p_{true} (mm/mm)	True Stress, σ_{true} (MPa)
0.0	364.073
0.12	547.694

(c) Combined hardening [26, 31, 32, 34]

E	ν	$\sigma\|_o$	C	γ	Q_∞	b
74633 MPa	0.30	300 MPa	750 MPa	10	220 MPa	14

Table 4-A Information of materials models of Al 2024-T351 alloy used as an input in the ABAQUS finite element code.

APPENDIX 4–B

(a) Basic mechanical properties of AerMet® 100 for Tooling Tool Steel with AMS 6532 specifications assumed for mandrel [30].

E	ν	σ_Y	ε_Y	σ_{utl}	ε_f
193 GPa	0.30	1620 MPa	0.839 %	1930 MPa	10 %

(b) Basic mechanical properties of full-harden AISI 301 full hard stainless steel assumed for split-sleeve [30, 35, 55].

E	ν	σ_Y	ε_Y	σ_{utl}	ε_f
180 GPa	0.27	965 MPa	0.536 %	1275 MPa	8 %

CHAPTER 5: GREEN'S FUNCTION FOR DOUBLE CRACKS GROWING FROM A HOLE

This chapter aims to provide a general stress intensity factor solution for two symmetric cracks emanating from a circular hole in an infinite plate. A Green's function method is developed to overcome the limitation of existing weight function solutions in the literature particularly in terms of crack sizes, applicable crack ranges and accuracy. The present method can be directly used to compute stress intensity factors for cold-worked holes, interference-fitted holes and composite-patched holes.

Several universal Green's functions based on the point-load acting on a Griffith crack in an infinite sheet elucidated earlier [1] have been employed here. The universal Green's functions were initially used to solve the stress intensity factors for an arbitrary crack face pressure loading acting on a central crack. In this text, this kernel solution is subsequently expanded for double symmetric cracks growing from a hole. Validations using the data from existing literature have been performed to confirm the accuracy and applicability of the Green's function. Furthermore, the development procedure ensures that the method is computationally efficient and can be easily subjected to future modification for other cases.

Also, the procedures of this chapter will be extended in next Chapter 6 to solve stress intensity factor of single crack in a StressWave cold-worked hole.

5.1 Introduction

Weight functions (WF) and Green's functions (GF) are two of the most common analytical methods employed to compute the stress intensity factors (SIF) for flawed components under the influence of residual stress and external loading.

5.1.1 Weight function

One of the main prerequisites of the WF technique, as discovered by Bueckner [2] and Rice [3], entails that the crack opening profile $u_r(x, a)$, along with the related SIF of a reference load solution, be explicitly defined (Figure 5.1.1). Based on the WF approach, many SIF solutions for a large plate with single or double through-thickness cracks emanating from a hole subjected to arbitrary crack face traction have been developed [4-8].

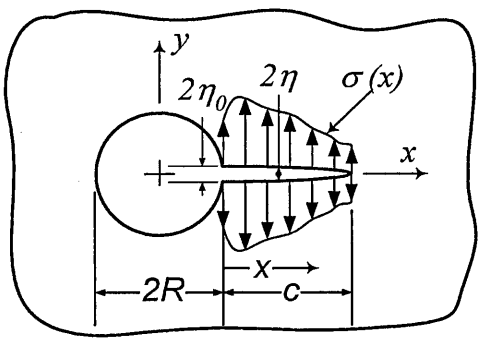

Figure 5.1.1 Open hole containing a radial crack subjects to arbitrary pressure/normal stress $\sigma(x)$ and the associated crack mouth, η_0 and crack shape profile, η along the crack flanks.

To date, because there is no exact crack opening profile yet available for cracked holes, the existing crack profile models have been widely obtained from finite element (FE) analysis [6], analytical treatment [5] or a simple crack profile coupled with a geometry correction function [4], and therefore these models are approximate in nature. Furthermore, as the crack profiles for an infinite crack lengths are generally lacking, most approximated crack profiles can be only sensibly derived for limited crack ranges, e.g. $0 < c/R < 3.0$ in [4], $0 < c/R < 2.5$ in [6] and $0 < c/R < 2.0$ in [5].

The accuracy of WF models depends highly upon the crack profile representation, crack size limitations, and the correct reference load cases. Indeed, Hsu and Rudd [9] argued that the WF accuracy may not be warranted upon differentiation of the approximated crack profile. Despite its usefulness, the WF method is often mathematically and computationally demanding, e.g. [5].

5.1.2 Green's function

Historically, as the derivation of GF necessitates only minimal computational resources the emergence of GF as preferred SIF solutions naturally preceded the development of WF. In

the early study of fracture mechanics, GFs were normally expressible in simple analytical manner to ease calculations. The mathematical tools for developing GF were primarily considering for through-thickness crack in two-dimensional plane problems, especially using the Muskhelishvili complex-variable approach [10] or Westergaard stress functions [11]. A general overview of relevant information concerning the derivation and application of various GFs is given in [11, 12].

While WF and GF methods are strongly linked, from the application standpoint both the methods are conceptually distinct [13]. The GF, $G(x, c)$, or unit-point-load function, describes the crack tip reaction in terms of K_I, when given a pair of opposing unit point loads P acting normal to the crack flanks of length, c, at a distance x from the crack reference point, O . For example, see Figure 5.3.1 for central crack geometry.

$$K_I = P \cdot G(x,c) \tag{5.1.1}$$

In this treatise, the proposed GF method and alike [14, 15] eliminate the need for prior knowledge of the crack opening profile, and generally retains the capability of covering an infinite range of crack size. In the cases in which a closed-form GF are not available, geometry correction functions or weighting functions can be simply generated from basic and reference solutions that still provide highly accurate results.

Abundant GFs exist in the literature, and of particular interest to the present study are GFs for cracks growing from a circular hole in a plate. Shah [15] used the GF for a Griffith crack with a hole free surface correction factor to account for short crack lengths for double-symmetric through-thickness cracks. Hsu and Rudd [9, 16] proposed a GF developed from a finite element (FE) model for limited double radial cracks that resembles the GF for a Griffith crack for $x/c < 0.9$. Due to FE limitation, another limiting expression was devised to resolve the singularity domain for $x/c < 0.9$ around the crack tips. Later, a more elegant methodology using the series approach and Muskhelishvili formulation [10]

in two-dimensional elasticity wasadopted by Shivakumar and Forman [14] to derive the GF for a single through-thickness crack at a circular hole in an infinite plane. The numerical coefficients were provided as functions of two independent normalised parameters, c/R and x/c.

In the present study, a SIF solution is developed for arbitrary crack face pressure for a pair of through-thickness cracks of equal length growing from a hole in an infinite plate. The main impetuses of the this work are (1) to develop a closed-form solution that enables rapid generation of SIF without recourse to laborious computation, (2) to derive GFs that omit the possible sources of error propagation that have been traditionally associated with WF via complex mathematical manipulation and numerical methods.

The arrangement of this chapter is outlined as follows. In Section 5.2, the structural features governing the SIF in a plate containing cracked holes are discussed and specified into several influential functions of geometric entities. A brief account of the possible construction of these geometric functions is also given. Section 5.3 demonstrates how the special case of GF by Sih–Paris–Erdogan [1], has been subsequently expanded in this work. In Section 5.4, the results from numerical integration of non-linear crack face pressure with the kernel GF, and its closed-form counterpart are compared. The aspects of profiling of stress data and the effect of biaxial loading are also assessed. This is followed by the derivation of geometry correction functions that augment the true effect of a hole on the SIF. Next, the present formulation is used to calculate the mode-I SIF of a known stress field, either induced by remote loading, or local plastic deformation around the hole by cold-working, as described in Section 5.5. Finally, the idea of SIF magnification factors for rapid calculation of SIF is introduced and the discrepancy between results obtained using different reference SIF solutions is examined.

5.2 Universal Green's Function for Cracked Hole

From a practical point of view, Figure 5.2.1 illustrates one of the most commonly encountered flawed hole problems in engineering components subjected to fatigue loading [6, 17]. Figure 5.2.1(a) illustrated a fatigue sample with a central hole of the type commonly used in laboratory work; whereas, Figure 5.2.1(b) is a universal representation of a cracked hole that encloses all the main features defining the present solution. The outer boundary acted upon by external loadings in Figure 5.2.1(b) can be arbitrary in shape and size as long as the hole and crack boundaries are contained. In fact, Figure 5.2.1(a) can be perceived as a special case of Figure 5.2.1(b) in which an external periphery has been explicitly defined.

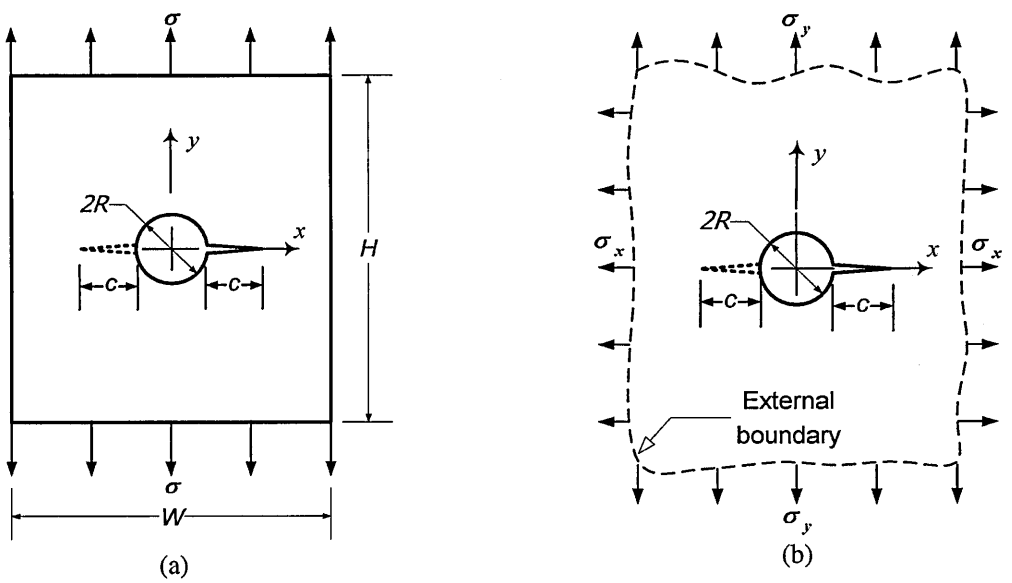

Figure 5.2.1 Single or double cracks emanating from a circular hole in (a) a rectangular plate of finite width and height subjected to uniaxial loading; (b) a plane domain of arbitrary external boundary subjected to biaxial loading.

5.2.1 Formulation of Green's function

Without loss of generality, taking account of the interacting effects of the various specimen geometries and loadings, it can be assumed that the complete GF for cracks emanating from circular holes is:

$$G_I(\xi,\lambda,B,\zeta)=F_\phi(\xi,\lambda)\cdot F_B(B_1,B_2,...,B_m)\cdot G(\zeta) \tag{5.2.1}$$

where $\xi = c/R$ and $\zeta = x/c$; $F_{\emptyset}(\xi, \lambda)$ introduces the effects of hole curvature, ξ and biaxial load, λ; F_B accounts for the interplay between m-number of external boundaries, B_1, B_2, ..., B_m and the flawed hole, e.g. finite width, w, or height of plate, H, or eccentricity of hole from the edges, e, etc; $G(\zeta)$ is the essential GF of the central crack, as discussed in detail in Section 5.3. For the current problem, the cracked hole lies in an infinitely large plate without any external boundary effect, i.e. $F_B(B_1, B_2, \ldots, B_m) = 1$.

5.2.2 Universal stress intensity factor model

Making use of the GF proposed by Equation (5.2.1) and coupling with the originally un-cracked stress distribution $\sigma_{\theta\theta}(x)$ acting perpendicularly to the prospective crack line, the SIF model for hole with cracks can be written as

$$\begin{aligned} K_I &= \int_{-c}^{c} \sigma_{\theta\theta}(x) \cdot G_I(\xi, \lambda, B, \zeta)\, dx \\ &= \int_{-c}^{c} \sigma_{\theta\theta}(x) \cdot F_{\phi}(\xi, \lambda) \cdot F_B(B_1, B_2, \ldots, B_m) \cdot G(\zeta)\, dx \\ &= F_{\phi}(\xi, \lambda) \cdot F_B(B_1, B_2, \ldots, B_m) \cdot \int_{-c}^{c} \sigma_{\theta\theta}(x) \cdot G(\zeta)\, dx \end{aligned} \tag{5.2.2}$$

The procedures to arrive at Equation (5.2.2), i.e. a mode-I SIF model for a double cracked hole, are accomplished as follows. Firstly, in the next section the appropriate kernel GF, $G(\zeta)$ founded on the unit point-load idea, was identified from the work of Sih–Paris–Erdogan [1]. Then, the derivation of the hole boundary correction function $F_{\emptyset}(\xi, \lambda)$, consisting of two components $F_{KGF}(\xi, \lambda)$ and $F_S(\xi, \lambda)$, is explained in Sections 5.3 & 5.4.

5.3 Kernel Green's Function G(x, c) or G(x/c)

The kernel GF employed is attributed to Sih, Paris and Erdogan [1] using the complex stress function approach of Muskhelishvili [10]. The kernel GF adopted here offers several advantages over WF; namely it eradicates the necessity of knowing the crack opening profile, and accounts exactly for any crack size in an infinite plane with minimal computational effort.

5.3.1 Mathematical expressions of kernel Green's function

Reference [1] derived the original GF which consists of an internal through-thickness central crack of size, $2c$, located in an infinite sheet i.e. Griffith's crack. The upper and lower crack faces are acted on by a pair of eccentric point loads P, at an arbitrary distance, x, from the crack origin. Accordingly, several point-load GFs for eccentric or symmetric situations were formulated and simultaneously extended to consider the complex stress field encountered in practical situations [12].

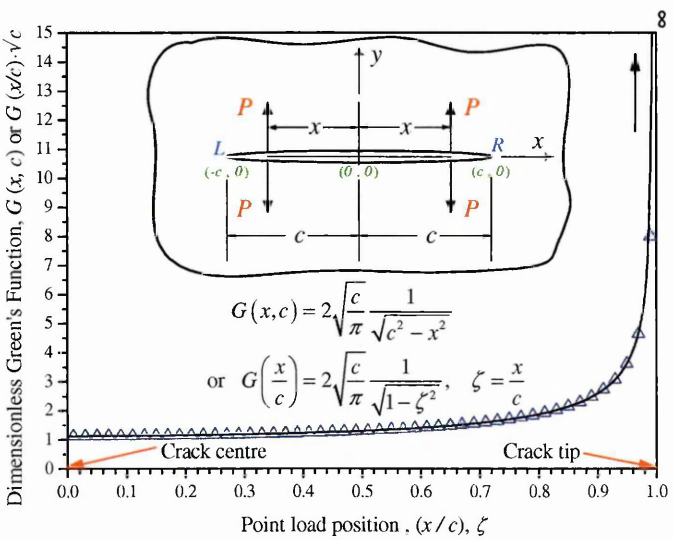

Figure 5.3.1 Green's function for Griffith's crack subjected to two pairs of equidistant splitting point loads at a distance x, from the crack centre; Equations (5.3.1 (a)) & (5.3.1 (b)).

Investigation of the crack configuration of Figure 5.2.1 reveals that under the action of remote mode-I loading, the locally induced hoop stress field, $\sigma_{\theta\theta}$ (x, R), is inherently symmetric about the hole centre (Figure 5.3.2(c)). Correspondingly, the GF for a symmetric stress about the crack centre (0, 0) is considered to be suitable to take account of this symmetric load effect. The mode-I SIF of the left (L) or right (R) crack tip is equal (Figure 5.3.1), and the kernel GF is simply expressed as [1, 12]:

$$K_I = K_I\big|_L = K_I\big|_R \qquad \therefore K_I = \int_0^c \sigma_{\theta\theta}(x) \cdot \left[2\sqrt{\frac{c}{\pi}} \frac{1}{\sqrt{c^2 - x^2}} \right] dx \qquad (5.3.1(a))$$

Normalising the variable x with respect to the crack size, c, simplifies (5.3.1(a)) to

$$K_I = \int_0^1 \sigma_{\theta\theta}(\zeta c) \cdot \left[2\sqrt{\frac{c}{\pi}} \frac{1}{\sqrt{1-\zeta^2}} \right] d\zeta, \quad \zeta = \frac{x}{c} \qquad (5.3.1(b))$$

Both terms in the brackets of integrals 5.3.1(a) & 5.3.1(b) are the kernel GF, $G(x, c)$ and $G(\zeta)$, respectively, in which the former caries the unit $\sqrt{m}$, while the latter is dimensionless. Expressions 5.3.1(a) & 5.3.1(b) produce identical results, and thus can be used interchangeably. Also, Figure 5.3.1 shows the response of the GF with respect to the location of a constant point load P travelling from the crack centre to the crack tip. It is clearly seen that as the load position x approaches the crack tip, c, the curve tends to infinity. Consequently, the stress field near the crack tip has the greatest effect on the SIF.

5.3.2 Effect of biaxial loading on stress intensity factor

It should be remembered that Equations 5.3.1(a) & 5.3.1(b) are merely appropriate for Griffith cracks without the feature of a circular hole. In order to incorporate the hole effect in the present model, a basic review is firstly essential to understand the interaction between a hole and a Griffith crack.

Based on the framework of linear elastic fracture mechanics, and consistent with several independent findings, the mode-I SIF for a Griffith crack is independent of the biaxial load factor, λ [18, 19]. In such cases, only the axial loading, ($\sigma_y = \sigma$) acting normal to the crack faces has a direct effect on the SIF, regardless of the level of transverse load ($\sigma_x = \lambda\sigma$) imposed.

On the contrary, when crack(s) propagate from the edge of stress concentrators, such as a hole or edge notch, a significant influence of biaxial loading on the SIF is inevitable [12, 20]. With regard to the present geometry, as shown in Figure 5.3.2(a), let us consider the locally induced hoop stress field at the angular locations $\theta = \pi/2; 3\pi/2$ of the hole [21]. For $\lambda \leq 0$ (or $\sigma_x \leq 0$), the hole region experiences compression in the x-direction and this

consequently contributes to the opening mode-I effect. Conversely, for $\lambda > 0$ the compressive effect is extenuated by the superimposed transverse tension σ_x (> 0) that subsequently minimises the extension of crack opening i.e. a reduction in the SIF.

5.3.3 Exact integral of kernel Green's function, K_{KGF}

An approximate closed-form SIF solution for the crack geometry in Figure 5.3.3, termed the exact kernel SIF, is formulated in this section. The solution is essentially the integral of Equation 5.3.1 using the local stress field around a hole due to remote loading, and is very useful because it provides fast and accurate results as compared to numerical integration.

The derivation of the kernel SIF, K_{KGF} is carried out by firstly considering two symmetric through-thickness cracks of equal radial length, c, emanating from a hole of radius, R, in an infinite sheet and subjected to remote biaxial tension (Figure 5.3.2(a)). Linear elastic superposition allows the equilibrated stress system to be resolved as shown in Figures 5.3.2(b) & 5.3.2(c).

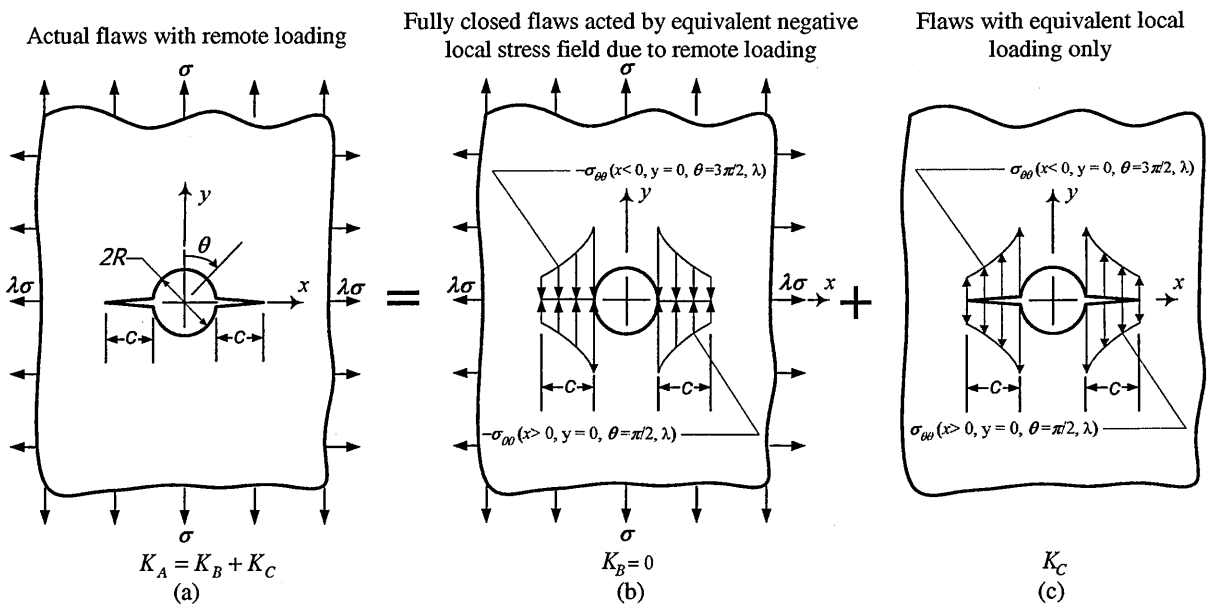

Figure 5.3.2 Stress intensity factor model for two symmetric radial cracks at hole by superposition method.

Figure 5.3.2(c) depicts the resultant hoop stress acting locally on the crack flanks at a circular hole for given biaxial loading in Figure 5.3.2(a). Mathematically, for an infinite plate this hoop stress is given by Kirsch's formula [21]:

$$\sigma_{\theta\theta}(x,R,\lambda,\theta)=\frac{\sigma}{2}\left[1+\frac{(1+\lambda)R^2}{(x+R)^2}\right]-\frac{\sigma}{2}\left[1+3\frac{(1+\lambda)R^4}{(x+R)^4}\right]\cos(2\theta) \qquad (5.3.2)$$

where σ is the loading at the remote boundaries; R denotes the hole radius; λ is termed the biaxial load factor; x represents the radial distance from the hole centre (0, 0); θ is the angular position about the hole centre (0, 0). The equivalent action of this resulting hoop stress can then be reversed and transferred locally to pressurise the crack faces for $-c < 0 < c$ as shown in Figure 5.3.2(b). Since the upper and lower crack faces are entirely closed in full contact, this implies that the effects of crack opening vanish in Figure 5.3.2(b), and hence the SIF, K_B can be set to zero. The remaining task is to establish K_A through K_C.

At this stage, the correct SIF solution K_A or K_C matching the Figure 5.3.2(a) or (c) could not yet be realized. However, producing a geometrically approximated SIF i.e. the kernel SIF, K_{KGF}, as an analytical solution, is feasible. The approximation, utilising the Griffith crack configuration, is tackled by visualizing that Figure 5.3.3 can be almost mimicked by Figure 5.3.3(b) otherwise Figure 5.3.3(c). Two slightly different approaches are presented next to offer possible alternative available for the integration procedures of the kernel GF.

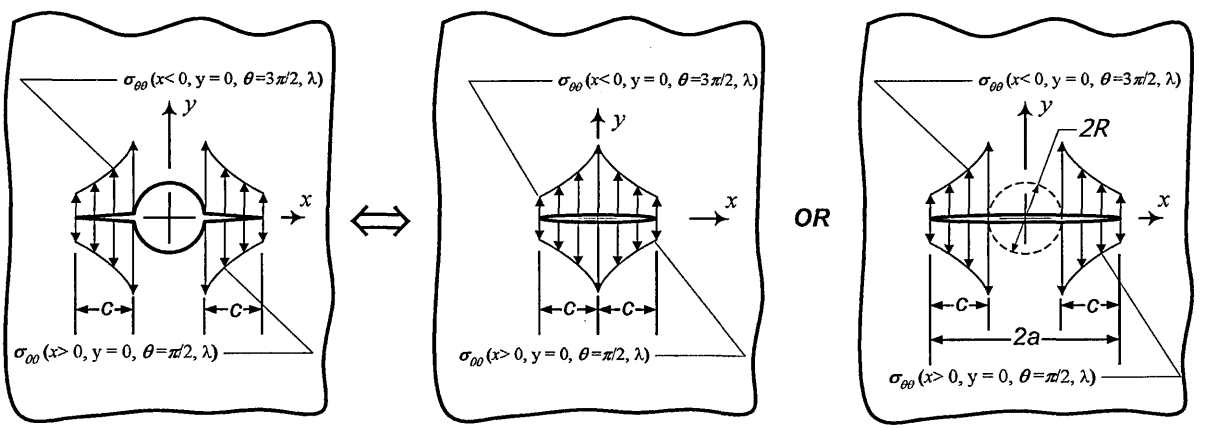

(a) (b) (c)

Figure 5.3.3 Two alternative stress intensity factor solutions of (b) & (c) for approximating double symmetric radial cracks at hole in (a) or Figure 5.3.2(c).

1st Approach: In Figure 5.3.3(b), although the hole radius, R, appears in Equation (5.3.2), the effect of the hole geometry is implicitly included as an arbitrary radius. The computations were carried out starting from the crack centre, i.e. $x = 0$ to the crack tips $x = \pm c$. In other words, this procedure is mathematically equivalent to integrating a central

crack with identical pressure loading (Figure 5.3.3(b)), without taking account of the hole geometry directly. As explained later in Section 5.4, using the findings of Figure 5.3.3(b) here, accurate representation of Figure 5.3.3(a) can be achieved via the hole geometry correction function $F_{\emptyset}(\xi, \lambda)$.

2nd Approach: An alternative approach is to deem the hole diameter, $2R$, as part of the entire crack length itself, $2a$ (Figure 5.3.3(c)). Therefore, the integration procedure must be carried out from the hole edge, i.e. $x = \pm R$ to the crack tip $x = \pm c$, which is akin to a pair of symmetric stress segments acting on both ends of the crack flank. In this case, Equations (5.3.1) & (5.3.2) can still be used with appropriate modification, namely treating the half crack length $a = c + R$ instead of c. Nevertheless, this approach still does not fully depict a true influence of the hole geometry. Clearly, adhering to the schematic representation of Figure 5.3.3(c) will require a different hole geometry correction function compared to that of Figure 5.3.3(b).

The first approach, founded on several premises, was adopted here. Firstly, the idea illustrated in (Figure 5.3.3(a)) creates a simpler version of the analytical solution. Second, given the integration limits involve lesser variables, this requires less computational resource. Also the closed-form integral of both Equations (5.3.1)& (5.3.2) could be achieved easily [22, 23]. In contrast, the second approach yields a higher relative error (> 10 %) when checked with the standard solution because of the longer crack length, $2a$.

Substituting Equation (5.3.2) into (5.3.1) along with mathematical manipulations in closed form [22, 23], we can arrive at a similar expression as derived by Shah [15]. However, in the original work of Shah, the closed form solution, K_{KGF}, is incomplete and has a few typographic errors, and hence the correct set of solutions is reported here:

$$K_{KGF} = \sigma\sqrt{\pi c}\left\{1+\frac{(1+\lambda)R^2I_2+3(1-\lambda)R^4I_4}{\pi}\right\} \tag{5.3.3}$$

Where R^2I_2 and R^4I_4 are given by Equations 5.3.4(a–c)

$$\left.\begin{aligned} R^2I_2 &= \frac{1}{1-\xi^2}\left[-\xi+RI_1\right] && (5.3.4(a)) \\ R^4I_4 &= \frac{1}{3\left(1-\xi^2\right)}\left[-\xi+\frac{\xi\left(\xi^2-16\right)}{2\left(1-\xi^2\right)^2}+\frac{\left(6+9\xi^2\right)}{2\left(1-\xi^2\right)^2}RI_1\right] && (5.3.4(b)) \end{aligned}\right\} \text{for } \xi \neq 1$$

$$\left.\begin{aligned} R^2I_2 &= 2/3 \\ R^4I_4 &= 12/35 \end{aligned}\right\} \textit{for } \xi = 1 \tag{5.3.4(c)}$$

ξ and RI_1 are given by the following equations

$$\xi = c/R \geq 0 \tag{5.3.5(a)}$$

$$RI_1 = \frac{2}{\sqrt{1-\xi^2}}\arctan\sqrt{\frac{1-\xi}{1+\xi}} \quad \text{for } 0 \leq \xi < 1 \tag{5.3.5(b)}$$

$$RI_1 = \frac{1}{\xi} = 1 \quad \text{for } \xi = 1 \tag{5.3.5(c)}$$

$$RI_1 = \frac{1}{\sqrt{\xi^2-1}}\ln\left[\frac{\sqrt{\xi+1}+\sqrt{\xi-1}}{\sqrt{\xi+1}-\sqrt{\xi-1}}\right] \quad \text{for } \xi > 1 \tag{5.3.5(d)}$$

5.3.4 Numerical validation of analytical kernel stress intensity factor, K_{KGF}

In this section, the closed-form kernel SIF, K_{KGF} (Equation (5.3.3–5)) derived in the last section is compared with counterpart results from numerical schemes [24, 25]. To obtain a reliable numerical outcome, two important considerations are required, namely a numerical strategy suitable for improper integrals with a singularity, and a method of stress profiling. Numerical integration of a modified Romberg algorithm is considered to take account of the precise nature of the singularity at the crack tips, as observed in Figure 5.3.1. Several data profiling methods were also used to characterize the stress distribution acting along the crack flanks. Curve fitting using a polynomial stress function appears to be attractive due to its robustness:

$$\sigma(x/R) = \sum_{i=1}^{n} \sigma_n (x/R)^n = \sigma_0 + \sigma_1 (x/R) + \sigma_2 (x/R)^2 + \ldots + \sigma_n (x/R)^n \quad ; \quad n \geq 0 \qquad (5.3.6)$$

Besides that, interpolation between the data points is capable of capturing the local stress perturbations more realistically. Amongst the interpolation methods tested, the cubic-spline interpolation with cubic endpoints was found to be most suitable.

In order to study the effect of stress profiling on the accuracy of numerical integration, the stress field is represented by Kirsch's formula (Equation (5.3.2)), by polynomial curve-fitted expression (Equation (5.3.6)) and by cubic-spline interpolation, independently. Kirsch's formula serves as a reference hoop stress and therefore its exact SIF data can be used to analyse the numerical accuracy of the polynomial functions for $3 \leq n \leq 20$, and also the cubic-spline interpolation. The validation procedures were carried out for the conditions: $\sigma = R = 1$, $0 \leq \xi \leq 10000$, $-2 \leq \lambda \leq 2$.

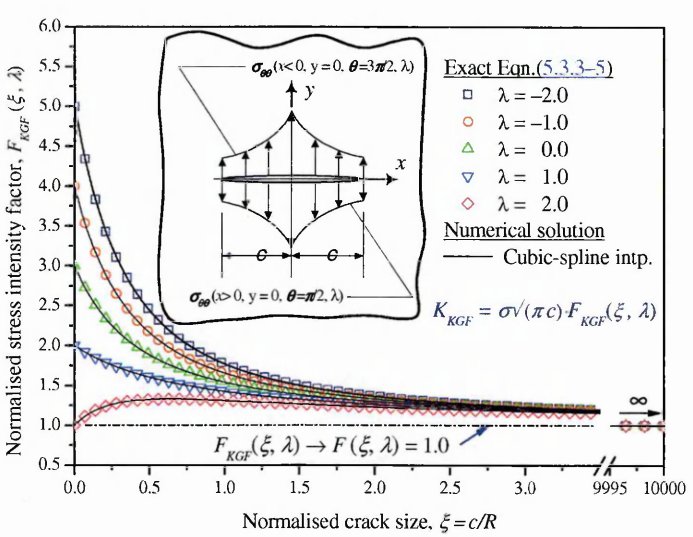

Figure 5.3.4 Approximated stress intensity factors for symmetric load for through-thickness cracks derived from kernel Green's function for Figure 5.3.3(b).

This numerical scheme using the Kirsch expression and cubic-spline interpolation shows excellent agreement with the analytical solution of the kernel SIF, K_{KGF} (Equation (5.3.3–5)) for $-2 \leq \lambda \leq 2$ (Figure 5.3.4). It is found that the curves representing various biaxial loads converge to a common single value i.e. $F_{KGF}(\xi, \lambda) \rightarrow F(\xi, \lambda) = 1.0$ for $\xi > 20$, indicating that the effect of the hole geometry fades gradually for increasing crack length.

Sometimes $F(\xi, \lambda)$ is also known as the unitary geometry correction factor given a unit of constant pressure applied at the Griffith's cracks (Figure 5.3.1 & Equation (5.3.2)).

The polynomial curve-fitting approach in general shows accuracy improvement, in accord with the analytical solution, only with increasing of powers of n. In most cases, the curve-fitting procedure provides satisfactory results for a wide range of crack sizes if $n \geq 10$.

5.4 Hole Surface Correction Factor, $F_{\emptyset}(\xi, \lambda)$

This section examines the SIF derived previously from the kernel GF (Figure 5.3.4) and the standard SIF of cracked holes (Figure 5.4.1), with particular attention to the hole effect. Then, it is shown how the geometry influence function, $F_{\emptyset}(\xi, \lambda)$ can be developed to amend the consequence of this local structural detail.

5.4.1 Comparison of approximate & standard stress intensity factor solutions

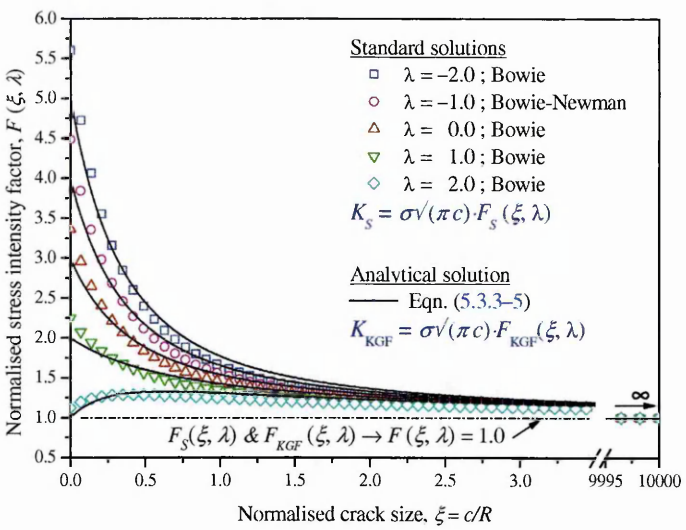

Figure 5.4.1 Stress intensity factors by kernel Green's function, K_{KGF}, and Bowie standard solutions. [19, 26]

As explained earlier in Section 5.3.2, the closed-form kernel SIF is an approximate solution for a hole with two radial cracks based solely on the GF for a Griffith crack in Figure 5.3.1. To comprehend the degree of approximation and the behaviour of the kernel SIF with respect to the actual SIF, some qualitative and quantitative comparison is carried out next.

To benchmark K_{KGF}, the SIF data of symmetric double cracks extending from a hole edge which was firstly solved by Bowie [26] using the complex mapping technique is used. Figure 5.4.1 illustrates that the exact K_{KGF} matches Bowie's solution [19, 26] fairly well for limited cases of biaxial loadings. If the hole is small with respect to the crack lengths, the exact/numerical solution of K_{KGF} can be used with caution depending on the accuracy required.

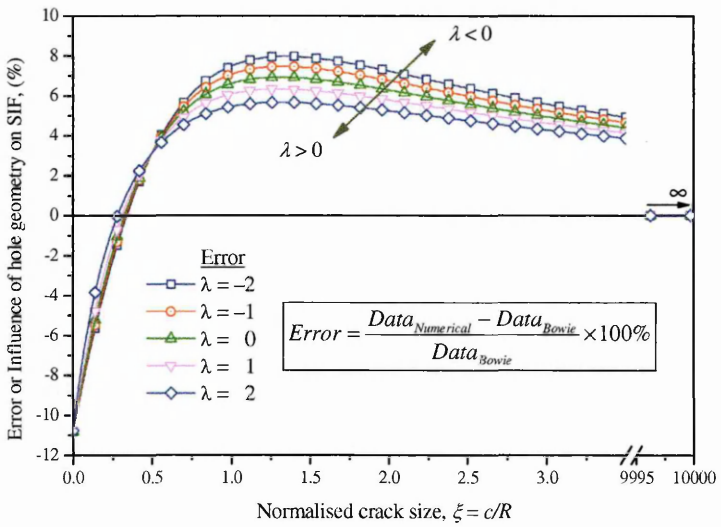

Figure 5.4.2 Accuracy study of present numerical data compared to standard solution.

Figure 5.4.2 provides detailed analysis of the accuracy study for limited cases of biaxial loading with respect to Bowie's result; and it is, in general, not applicable to other λ values. The influence of the hole on the SIF accuracy is considerable: only in the crack regime ($0.28 < \xi < 0.35$) is the error ranges below ±1 %; otherwise, the error variation in the SIF can be as high as −10.8 % to 7.96% depending on the crack size. Interestingly, the general trend indicates some improvement in error for $\lambda > 0$, but deterioration when $\lambda < 0$. As $\xi \rightarrow \infty$, the effect of the hole geometry gradually disappears, and both the kernel GF and Bowie's solutions converge to $F(\xi, \lambda) = 1.0$.

5.4.2 Approximate hole curvature correction factors, $F_{\emptyset}(\xi)$

The approximate nature of the kernel SIF, K_{KGF} is susceptible to a certain degree of error because the free surface effect of the hole is not taken in consideration. In the following

text, two geometry functions, proposed by earlier researchers to improve SIF for a hole with cracks, are assessed in detail. For the case of uniaxial loading, Shah [15] suggested that the highest discrepancy in the ratio of his analytical K_{KGF} solution to Bowie's data is less than 7 % for $0.05 \leq \xi \leq \infty$ (Figure 5.4.3).

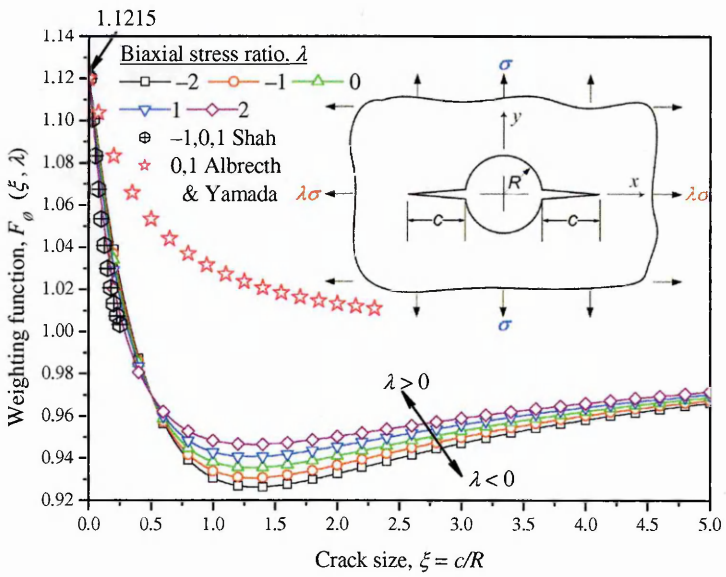

Figure 5.4.3 Weighting function for compensating hole surface effect for two through-thickness cracks emanating from a hole in an infinite plate subjected to biaxial stress field.

However, the present assessment shows more precisely that the underestimation of this ratio can be as high as 12%, especially in the short crack regime $\xi \leq 0.1$. Shah [15] also introduced a correction factor, $F_{\emptyset}(\xi)$ to compensate for the hole free surface effect, considering only a small crack range, ξ, for limited number of biaxial stress ratios, $\lambda = -1$, 0 and 1:

$$F_{\phi}(\xi) = 1.0 + 0.12\left[1 - \xi/0.3\right]^2 \quad \text{for } 0 \leq \xi < 0.3 \tag{5.4.1}$$

Later, Albrecth and Yamada [27] formulated a slightly different form of the correction factor, $F_{\emptyset}(\xi)$ for the biaxial stress ratio, $\lambda = 0$, 1:

$$F_{\phi}(\xi) = 1.0 + 0.12/\left[1 + \xi\right]^2 \quad \text{for } 0 \leq \xi < 2.5 \tag{5.4.2}$$

As shown earlier in Figure 5.4.3, even for crack size $\xi > 0.3$ the discrepancy in SIF ratio can be still significant, which is overlooked by Shah's correction factor, $F_{\emptyset}(\xi)$ of (Equation (5.4.1)). Closer inspection shows that Shah's correction is generally not

applicable to wide range of biaxial stress ratio, λ. Also, the correction function of Albrecth & Yamada (Equation (5.4.2)) introduces an unacceptably high error, and therefore is not useful in most applications.

5.4.3 Exact hole curvature correction factor, $F_{\phi}(\xi, \lambda)$

Consequently, to improve the above situation desirably a universal compensation factor must be devised to cover both the infinite crack domain and biaxial ratio. This is achieved by firstly allowing the SIF results from the superposition of local crack faces (Figure 5.3.3) to match the standard SIF solution around the cracked hole (Figure 5.4.1). The integration of Kirsch's formula (5.3.2) with the proposed kernel GF in expression (5.2.2) leads us to (5.4.3(a)) that is made equivalent to the standard solution (5.4.3(b)):

$$K_I = F_{\phi}(\xi,\lambda)\cdot\int_0^c \sigma_{\theta\theta}(x,R)\cdot G(x,c)\,dx \tag{5.4.3(a)}$$

$$= F_{\phi}(\xi,\lambda)\cdot F_{KFG}(\zeta,\lambda)\cdot\sigma\sqrt{\pi c}$$

$$= F_S(\xi,\lambda)\sigma\sqrt{\pi c} \tag{5.4.3(b)}$$

$$\therefore \underbrace{F_{\phi}(\xi,\lambda)\cdot F_{KFG}(\zeta,\lambda)\cdot\sigma\sqrt{\pi c}}_{\substack{\textit{local crack face loading;}\\ \textit{kernel Green's Function}}} \equiv \underbrace{F_S(\xi,\lambda)\cdot\sigma\sqrt{\pi c}}_{\substack{\textit{remote loading;}\\ \textit{standard solution}}} \tag{5.4.3(c)}$$

Equation (5.4.3(c)) is interrelated as

$$F_{\phi}(\xi,\lambda) = \frac{F_S(\xi,\lambda)}{F_{KFG}(\xi,\lambda)} \tag{5.4.4}$$

Earlier, from Equation (5.3.3–5), it is proven that the related exact influence function, F_{KGF} (ξ, λ), due to the kernel GF is

$$F_{KFG}(\zeta,\lambda) = \left\{1+\frac{(1+\lambda)R^2I_2 + 3(1-\lambda)R^4I_4}{\pi}\right\} \tag{5.4.5}$$

The remaining task is to obtain a standard SIF function F_S (ξ, λ) appropriate for present crack geometry, as described in the following section.

5.4.4 Standard reference solution, $F_S(\xi, \lambda)$

Several standard SIF functions $F_S(\xi, \lambda)$ for a hole containing double-symmetric cracks ($N = 2$) either published in the literature, or implemented in fracture mechanics codes, are presented in this section. This comparison is not intended to identify the best solution, but examines the effect of different $F_S(\xi, \lambda)$ on the problem investigated. Table 5.1 shows the six most prominent $F_S(\xi, \lambda)$ functions. $F_0(\xi, \lambda)$ and $F_1(\xi, \lambda)$ are component functions related to the uniaxial ($\lambda = 0$) and equal-biaxial tension ($\lambda = 1$) cases; $F_5(\xi, \lambda)$ is the component function related to uniaxial tension applied parallel to the crack plane i.e. $\sigma_y = 0$. The variables, s and t, used in Table 5.1 can be reworked in terms of the normalised crack $\xi = c/R$:

$$s = \frac{c}{R+c} = \frac{\xi}{1+\xi} \qquad (5.4.6(a))$$

$$t = \frac{R}{R+c} = \frac{1}{1+\xi} \qquad (5.4.6(b))$$

Thus far, there is still no comprehensive assessment on, or unequivocal consensus about, the most precise SIF solution for this type of cracked geometry. In the absence of an exact solution, the SIF accuracy for a flawed hole relies on the type of methods employed to reach the final numerical outcome. For instance, Tweed & Rooke [28] commented that Bowie's complex mapping technique is not accurate enough to produce a reliable SIF. Schijve [29] also observed that Bowie's data [26], as cited from [11], shows a lack of systematic data trends that can be accurately expressed in mathematical form. On the contrary, Newman's data from the boundary collocation method [30] with high degree of accuracy should be used instead.

All these $F_S(\xi, \lambda)$ expressions, such as those formulated independently by Tada et al. [12], Liu [19], Schijve [29] and Grandt [29], are the products of regression of well-known discrete data by Bowie [26] or Newman [30]. Several of these functions in Table 5.1 allow biaxial loading, while for others only the uniaxial loading is accounted for. Reference [19]

provides a clear explanation how to develop $F_S(\xi, \lambda)$ for arbitrary load biaxiality, λ using the discrete data taken from other sources.

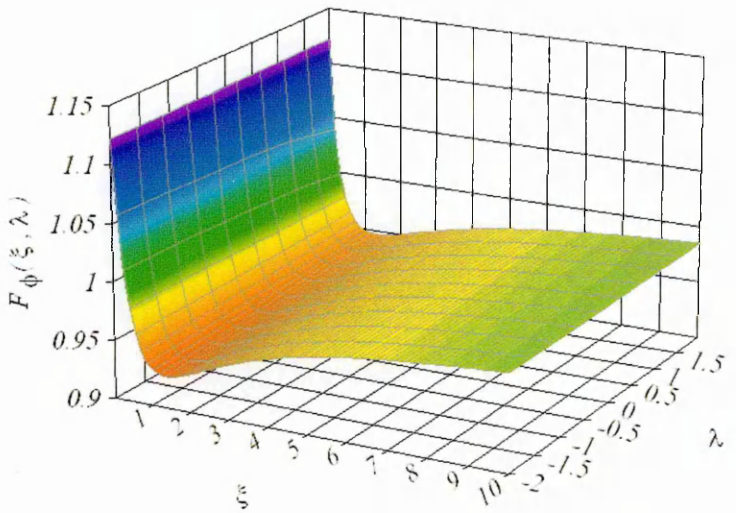

Figure 5.4.4 Three-dimensional distribution of hole surface correction or weighting function, $F_\phi(\xi, \lambda)$.

Figure 5.4.4 exemplifies the three-dimensional relationship of $F_\phi(\xi, \lambda)$ (Equation (5.4.4)) plotted according to the $F_S(\xi, \lambda)$ expression of Tada-Paris-Irwin [12], and is given in Table 5.1 along with the influence function F_{KGF} (Equation (5.4.5)). As a simple validation of self-consistency, the SIF computed by Equation (5.4.3) according to the local crack face stress approach matches favourably with the equivalent remote stress solution by Bowie (Figure 5.4.5).

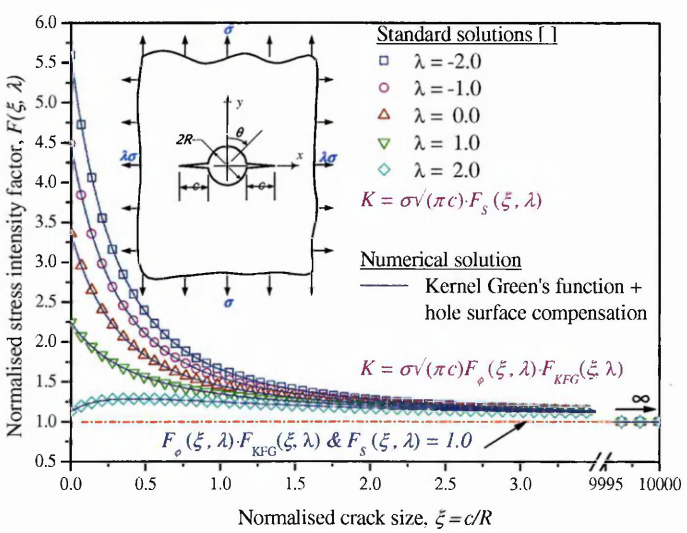

Figure 5.4.5 Stress intensity factor of standard solutions and kernel Green's function corrected with hole surface weighting function.

Reference	Reference Stress Intensity Factor Functions, $F_S(\xi, \lambda)$	Origin of Data	Crack Size Limit	Accuracy†
Tada-Paris-Irwin [12] (2000)	Solution : Biaxial loading, λ $F_S(s,\lambda)\big\|_{N=2} = (1-\lambda)F_0(s,\lambda) + \lambda F_1(s,\lambda)$; $F_0(s,\lambda=0)\big\|_{N=2} = 0.5(3-s)\left[1+1.243(1-s)^3\right]$ $F_1(s,\lambda=1)\big\|_{N=2} = 1+(1-s)\left[0.5+0.743(1-s)^2\right]$ where $s = \frac{c}{R+c} = \frac{\xi}{1+\xi}$	Bowie [26]. Newman [30]	$0 \le \xi \le \infty$	1%
A. F. Liu [19] (1988)	Solution : Biaxial loading, λ $F_S(t,\lambda)\big\|_{N=2} = (1-\lambda)F_0(t,\lambda) + \lambda F_1(t,\lambda)$; $F_0(t,\lambda=0)\big\|_{N=2} = 1-0.15\,t+3.46\,t^2-4.47\,t^3+3.52\,t^4$ $F_1(t,\lambda=1)\big\|_{N=2} = 1-0.0436\,t+3.1256\,t^2-4.46077\,t^3+2.6281\,t^4$ where $t = \frac{R}{R+c} = \frac{1}{1+\xi}$	Bowie [26]	$0 \le \xi \le \infty$	0.8 %
Isida & Nemat-Nasser [31] (1987)	Solution : Biaxial loading, λ $F_S(t,\lambda)\big\|_{N=2} = F_0(t,\lambda) - \lambda F_X(t,\lambda)$ $F_0(t,\lambda=0)\big\|_{N=2} = 1.0377+0.0061\,t+2.5633\,t^2-3.0360\,t^3+2.78142\,t^4$ $F_X(t,\lambda=0)\big\|_{N=2} = 0.0177-0.2239\,t+1.0065\,t^2-1.0751\,t^3+1.40932\,t^4$ where $t = \frac{R}{R+c} = \frac{1}{1+\xi}$	Isida & Nemat-Nasser [31]	$0 \le \xi \le 7$	0.2 %
Schijve [29] (1983)	Solution : Uniaxial loading, $\lambda = 0$ $F_S(t,\lambda=0)\big\|_{N=2} = 1+\frac{1}{2\xi^2+1.93\xi+0.539}+\frac{1}{2(\xi+1)}$	Newman [30]	$0 \le \xi \le \infty$	0.2 %
AFGROW‡ [32] (2004)	Solution : Uniaxial loading, $\lambda = 0$ $F_S(\xi,\lambda=0)\big\|_{N=2} = \begin{cases} \frac{a+b\xi^{0.5}+c\xi+d\xi^{1.5}+e\xi^2}{1+f\xi^{0.5}+g\xi+h\xi^{1.5}+i\xi^2+j\xi^{2.5}}, & for\ 0 \le \xi \le 10 \\ \sqrt{1+1/\xi}, & for\ \xi > 10 \end{cases}$ The regression coefficients of the rational function are $a = 3.364976244$, $b = -23.6763023$, $c = 52.50653039$, $d = -40.5162804$, $e = 27.60984863$, $f = -6.68155935$, $g = 14.13763127$, $h = -13.5218534$, $i = 16.68405526$ and $j = 1.530329789$.	StressCheck® *p*-version FE modelling [33]	$0 \le \xi \le \infty$	0.05 %

Table 5.1 Stress intensity factor reference functions for two symmetry cracks emanating from a hole in an infinite plate.

† Accuracy of regression with respect to the original data, either mentioned in the original texts, or checked in present work.
‡ The functional equation is curve-fitted for AFGROW data by present author.

5.5 Application of Green's Function

This section demonstrates the application of the universal SIF of the kernel GF using the tabulated data organised in Appendix 5–A for cold-worked holes. Cold-working of holes has been widely used to combat fatigue cracks emanating from mechanical joints in metallic aero-structures, and knowing the SIF corresponding to the stress field at cold-worked holes is of paramount importance in damage tolerant analysis of cracked holes.

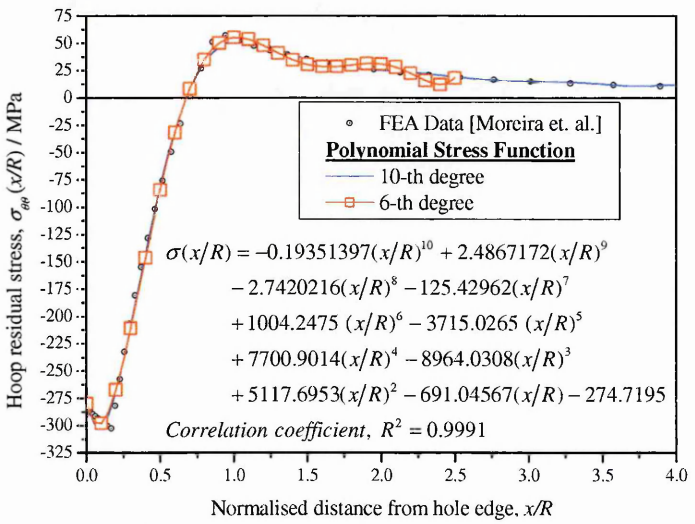

Figure 5.5.1 Typical hoop residual stress distribution around 4% cold expanded hole

5.5.1 Residual stress around cold-worked holes

Figure 5.5.1 depicts the hoop residual stress field around a 4% mandrelized Ø20 mm hole in a infinite plate of clad Al–2024 alloy, obtained from a two-dimensional FE simulation [34]. The hoop residual stress, $\sigma_{\theta\theta}$ is taken as equivalent to the crack face pressure acting in normal to the crack flanks. The SIF calculation is given step-by-step as follows:

Step–1: Using the least-square technique of data regression, a 10^{th} degree polynomial can be accurately used to represent the stress field as a function of x/R (Equation (5.3.6)). To ensure accuracy, the stress coefficients of regression σ_n (SI-unit: MPa) in Figure 5.5.1 are calculated to eight significant figures:

$$\sigma_0 = -274.7195;\ \sigma_1 = -691.04567;\ \sigma_2 = 5117.6953;\ \sigma_3 = -8964.0308;$$
$$\sigma_4 = 7700.9014;\ \sigma_5 = -3715.0265;\ \sigma_6 = 1.0042475 \times 10^3;\ \sigma_7 = -125.42962 \times 10^2; \qquad (5.5.1)$$
$$\sigma_8 = -2.7420216;\ \sigma_9 = 2.4867172;\ \sigma_{10} = -0.19351397$$

5.5.2 Stress intensity magnification factor, M_n

Since the numerical procedure to generate the SIF in Equation 5.4.3(a) is quite tedious, and in order to ease future application, the stress intensity magnification factors (SIMF), corresponding to the stress coefficients of Equation (5.3.6), are tabulated in Appendix 5–A. The SIMF operates on the principle of summation of a n-degree polynomial terms in arbitrary crack face loading [7]. The crack sizes considered typically range from $0 < c/R <$ 5. Using Equation (5.3.1), the SIMF can be calculated as

$$M_n(x/R) = \frac{K_n}{\sigma_n(x/R)\sqrt{\pi c}} \tag{5.5.2}$$

The data developed from Equation (5.5.2) must be further augmented by F_{ϕ} (ξ, λ), and hence are different to those of Grandt [7, 8]. According to Equation (5.4.4), uncoupling M_n with F_{ϕ} permits flexible use of different F_S (Appendix 5–A) in the calculations.

Step–2: To demonstrate the use of SIMF data in Appendix 5–A, given c = 5 mm, R = 10 mm and $\lambda = 0$, the SIMF for $c/R = 0.5$ taken from Tables 5.A1 & 5A2 are:

$$\begin{aligned}
&M_0 = 1.0\ ;\ M_1 = 0.3183099;\ M_2 = 0.125;\ M_3 = 5.305165 \times 10^{-2};\\
&M_4 = 2.34375 \times 10^{-2};\ M_5 = 1.061033 \times 10^{-2};\ M_6 = 4.882813 \times 10^{-3};\\
&M_7 = 2.273642 \times 10^{-3};\ M_8 = 1.068115 \times 10^{-3};\ M_9 = 5.052538 \times 10^{-4};\\
&M_{10} = 2.403259 \times 10^{-4}
\end{aligned} \tag{5.5.3}$$

Step–3: Correspondingly, from Table 5.1 we have F_S (ξ, λ) = 1.824395 employing Schijve expression, and following Equations (5.3.4–5) & (5.4.5) F_{KGF} (ξ, λ) =1.881363. Therefore, referring to Equation (5.4.4) the hole surface weighting factor F_{ϕ} (ξ, λ) = 0.969720. From the information obtained from the Step–1 to 3, the SIF may be evaluated as

$$\begin{aligned}
K_I &= F_{\phi}(\xi,\lambda)\sqrt{\pi c}\sum_{n=0}^{n=10}(\sigma_n \cdot M_n)\\
&= (0.969720)\sqrt{\pi \cdot 5}\left\{\begin{matrix}(-274.7195)(1.0)+(-691.04567)(0.3183099)+\ldots\\ +(-0.19351397)(2.403259\times10^{-4})\end{matrix}\right\}\\
&= (0.969720)\sqrt{\pi \cdot 5}\,(-184.8420189)\\
&= -22.46502\ MPa\sqrt{m}
\end{aligned} \tag{5.5.4}$$

Alternatively, a numerical integration gives $K_I = -22.3265$ MPa$\sqrt{m}$, so there is a negligible difference between the two methods. The parametric functions in Equations (5.3.3–5) and (5.4.4–5) calculated to obtain Figure 5.5.1, are given in Figure 5.5.2(a).

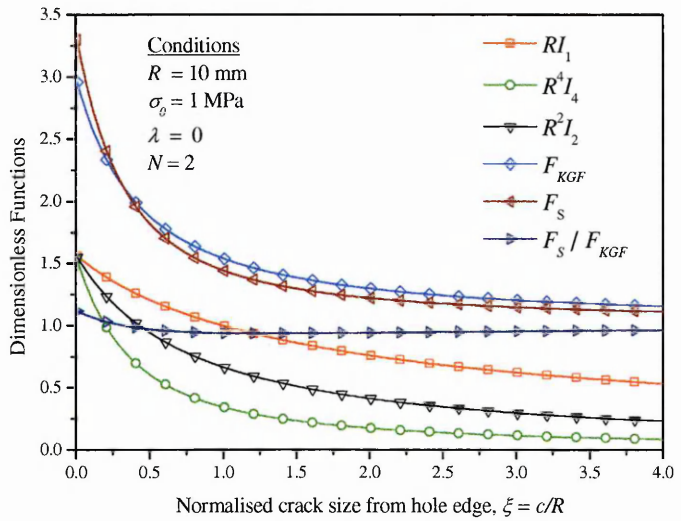

(a)

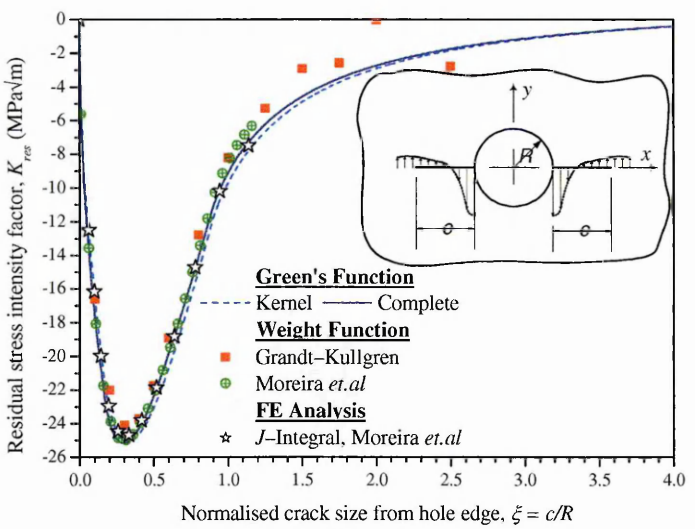

(b)

Figure 5.5.2 (a) Related parametric functions of Equation 5–13, and (b) comparison of residual SIF using different models.

The applicability of the present GF approach was further confirmed using the WF and FE methods (Figure 5.5.2(b)). Amongst them, the data from *J*-integral of FE simulation [34] matches the curve of Equation (5.4.3(a)) most favourably. The curve produced by the kernel model of Equation (5.3.1) overestimates the SIF for $c/R < 0.3$, underestimates SIF for for $c/R > 0.3$, and shows slow convergence compared to other results approximately for $c/R > 3$. The WF method of Grandt [7, 8] operates on polynomial stress field and magnification factors. Given the present stress field, Grandt's WF model covers only a

limited number of stress intensity magnification factors of discrete crack sizes that produces scattered SIF data points for 1.0 < *c/R* <2.5 in Figure 5.5.2(a) . The highest 6th degree polynomial stress function formulated in [7, 8] also fails to capture the data trend at this region, as indicated by the curve fluctuation in Figure 5.5.1. This problem can be improved if a higher e.g. 10th degree polynomial function is used.

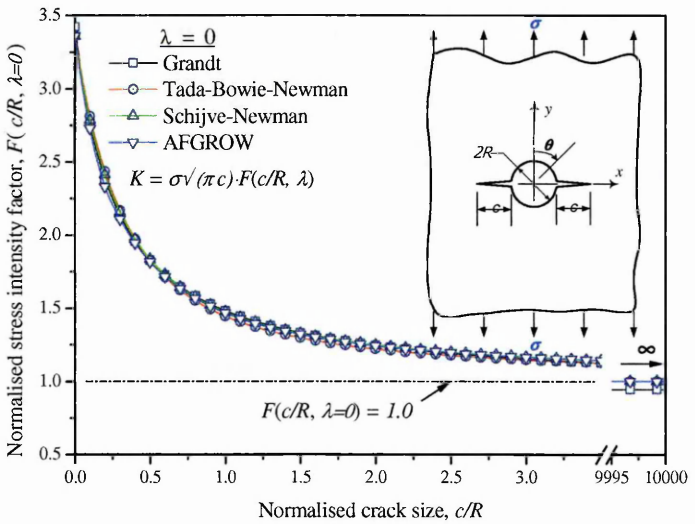

(a)

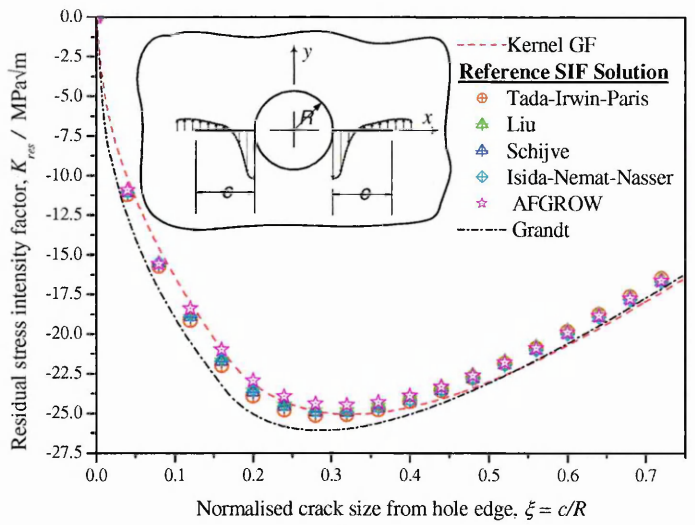

(b)

Figure 5.5.3 Comparison of (a) weighting functions for compensating hole surface effect under uniaxial tension, (b) resulting residual stress intensity factors in cold-worked hole.

5.5.3 Effect of standard reference solution, F_S (ξ, λ)

In view the fact that the majority of fatigue life studies of cold-worked holes have been carried out under uni-axial fatigue testing (λ = 0), it is worthwhile to consider the effect of different reference solutions under such loading conditions.

Figure 5.5.3(a) shows there are clear discrepancies between the correction functions F_S (c/R , $\lambda = 0$) related to the reference solutions, which in turn give rise to SIF differences as high as 2.0 MPa$\sqrt{m}$ at $c/R = 0.25$ in Figure 5.5.3(b). Nevertheless, some cursory judgment can be made about the reliability of these reference solutions by inspecting Figure 5.5.3(b). Both the data by Grandt [7, 8] and the kernel GF exhibit noticeable deviation from the majority of the curves, and should be avoided in application. The remaining models show reasonably good agreement for $c/R > 0.45$ except for some difference at $c/R < 0.45$. At this short crack regime, the AFGROW [32] and Tada-Irwin-Paris solutions [12] can be regarded as upper and lower bounds respectively, in which the data of Liu [19], Schijve [29] and Isida-Nemat-Nasser [31] lie within.

5.6 Discussions

It can be observed that the solution presented in Equation (5.4.3) satisfies all the pertinent requirements of accurate SIF models as suggested by Wu-Carlsson [5]. Firstly, the proportionality in the mathematically relationship between the applied load and GF model is well-defined, as fundamentally characterised in Equation (5.1.1). Secondly, the self-consistency is automatically satisfied, i.e. exact recovery of standard SIF reference, $K_S(\xi, \lambda)$ when the complete GF is fed back with the reference load case itself.

For an appropriate SIF model, an accurate SIF is achievable as long as the stress profiling method is precise enough to capture the complexity of the stress field given a sufficient number of data points. Despite the versatility of the polynomial approach widely adopted in defining the stress profile [5, 7, 35, 36], it is especially prone to overlook localised data trends; and hence the accurate derivation of SIF for the actual stress distribution is not always possible to obtain. Referring to Figure 5.5.1, the single-piece polynomial stress function does not fully represent the actual stress data at $0 < x/R < 0.25$ within the small crack regime. The knowledge of the SIF corresponding to the growth of short cracks is of

technological importance, since the majority of the fatigue life of a structure is spent while the cracks are small. In such cases, the "divide-and-rule" strategy using several polynomials to represent the entire stress data, along with the related analytical integrals of kernel GF may further improve the SIF results.

The GF solution devised in this chapter computes a reliable SIF for two through-thickness radial cracks in a relatively wide plate with a central hole. Nevertheless, when the crack dimension is large enough to interact with the finite boundary of the specimens (Figure 5.2.1(a)), the resulting SIF can be progressively amplified as a function of crack sizes to finite boundary ratios, $2R/W$ or H/W. Typically, a finite width correction is essential in SIF estimation when $2R/W \leq 6$ [32] and/or $H/W \leq 5$ and can be incorporated directly into the universal SIF model mentioned in Section 5.2.2. These correction data are available for finite width plate with central hole from several literature sources, such as Newman [30], Fuhring [37] and Kitagawa–Yuuki [38].

Besides the utility of the present GF model to predict SIF in cold-worked holes, as shown in Section 5.5, other important applications of present work are the estimation of SIF in overloaded or pre-yielded holes [39], interference-fitted holes with or without cold-working [6, 15, 40-42], riveted holes [40] and recently composite repairs to cracked holes under biaxial loading [43].

5.7 Summary & Conclusions

(a) Based on the earlier work of Sih–Paris–Erdogan [1], the GF for a through-thickness crack in an infinite plate suitable for a hole with two symmetric cracks has been identified in Section 5.3.1. This GF is the kernel component implemented in a universal SIF model that takes account of the nature of crack tip singularity.

(b) With prior knowledge of the hoop stress field around the hole, an exact integral of the kernel GF has been derived to calculate the SIF, K_{KGF}. The analytical form of the integral was validated by numerical integration of the hoop stress field with kernel GF in Section 5.3.1. The effect of different stress profiling methods on the accuracy of K_{KGF} has also been discussed. In general, the polynomial function is quite adaptable in representing the global trend of stress data, albeit with some limitations.

(c) Comparison with standard solutions and further error analysis implies that the SIF calculated by the kernel GF is an approximation, as the actual effect of the free hole on the cracks behaviour is neglected. Therefore, a correction factor, $F_{\emptyset}$ (ξ, λ) has been formulated to improve the accuracy of the SIF for a cracked hole.

(d) With the aid of the stress intensity magnification factors M_n (x/R) tabulated in Table 1, the proposed GF method permits the generation of a SIF for any crack sizes and biaxial loading with great accuracy and speed, and can be suitably implemented in a spreadsheet environment for routine calculations. The effect of function F_S (ξ, λ) put forward by different sources was also studied.

5.8 References

1. Sih, G.C., Paris, P.C., and Erdogan, F., Crack-tip stress-intensity factors for plane extension and plate bending problems. Journal of Applied Mechanics, Transactions of the ASME, 1962. 29: p. 306–312.
2. Bueckner, H.F., A novel principle for the computation of stress intensity factors. Zeitschrift für Angewandte Mathematik und Mechanik, 1970. 50(9): p. 529–548.
3. Rice, J.R., Some remarks on elastic crack-tip stress fields. International Journal of Solids and Structures, 1972. 8(6): p. 751-758.
4. Impellizzeri, L.F. and Rich, D.L., Spectrum Fatigue Crack Growth in Lugs, in Fatigue Crack Growth Under Spectrum Loads, ASTM STP 595. 1976, American Society for Testing and Materials: Philadelphia, PA. p. 320–336.

5. Wu, X.R. and Carlsson, A.J., Weight Functions and Stress Intensity Factor Solutions. 1991: Pergamon Press, Oxford.
6. Grandt, A.F.J., Stress intensity factors for some through-cracked fastener holes. International Journal of Fracture, 1975. 11(2): p. 283-294.
7. Grandt, A. and Kullgren, T., A compilation of stress intensity factor solutions for flawed fastener holes. 1981, Materials Laboratory, Air Force Wright Aeronautical Laboratories: Wright-Patterson Air Force Base, Ohio, USA.
8. Grandt, J., A. F. and Kullgren, T.E., Tabulated stress intensity factor solutions for flawed fastener holes. Engineering Fracture Mechanics, 1983. 18(2): p. 435-451.
9. Hsu, T.M. and Rudd, J.L. Green's function for thru-crack emanating from fastener holes. in Proceedings of 4th International Conference on Fracture. 1977. University of Waterloo, Canada.
10. Muskhelishvili, N.I., Some basic problems of the mathematical theory of elasticity. Fundamental Equations, a plane problem, torsion and bending (English translation of the 3rd Russian edition). 4th ed. ed. 1963: Noordhoff, The Netherlands.
11. Paris, P.S. and Sih, G.C., Stress analysis of cracks, in Fracture Toughness Testing and its Applications, ASTM STP 381. 1964, American Society for Testing and Materials: Philadelphia, PA, USA. p. 30–83.
12. Tada, H., Paris, P.C., and Irwin, G.R., The Stress Analysis of Cracks Handbook. 3rd ed. 2000, New York: The American Society of Mechanical Engineers.
13. Cartwright, D.J. and Rooke, D.P., Green's Functions in Fracture Mechanics, in Fracture Mechanics: Current Status, Future Prospects, R.A. Smith, Editor. 1979, Pergamon: Cambridge. p. 91-123.
14. Shivakumar, V. and Forman, R.G., Green's Function for a Crack Emanating From a Circular Hole in an Infinite Sheet. International Journal of Fracture, 1980. 16(4): p. 305-316.
15. Shah, R.C., Stress intensity factors for through and part through cracks originating at fastener holes, in Mechanics of Crack Growth ASTM STP 590. 1976, American Society for Testing and Materials. p. 429-459.
16. Hsu, T.M., McGee, W.M., and Aberson, J.A., Extended Study of Flaw Growth at Fastener Holes, AFFDL-TR-82-3073. 1978, Air Force Flight Dynamics Laboratory (AFFDL/FBE), Wright-Patterson AFB Ohio 45433.
17. Ozdemir, A.T., Cook, R., and Edwards., L. Residual Stress Distributions Around Cold Expanded Holes. in Durability and Structural Integrity of Airframes, Proc.

ICAF '93, (International Committee on Aircraft Fatigue). 1993. Stockholm, Sweden: EMAS, Cradley Heath, West Midlands.

18. Liebowitz, H., Lee, J.D., and Eftis, J., Biaxial load effects in fracture mechanics. Engineering Fracture Mechanics, 1978. 10(2): p. 315-335.
19. Liu, A.F., Structural Life Assessment Methods. 1998: ASM International. 419.
20. Yan, X., Analysis for a crack emanating from a corner of a square hole in an infinite plate using the hybrid displacement discontinuity method. Applied Mathematical Modelling, 2004. 28(9): p. 835-847.
21. Timoshenko, S.P. and Goodier, J.N., Theory of Elasticity. 3rd ed. 1970: McGraw-Hill, New York.
22. Gröbner, W. and Hofreiter, N., Integraltafel. Teil 2: Bestimmte Integrale (In German). 1973, Wien: Springer Verlag.
23. Gröbner, W. and Hofreiter, N., Integraltafel. Teil 1: Unbestimmte Integrale (In German). 1975, Wien: Springer Verlag.
24. Chapra, S.C. and Canale, R., Numerical Methods for Engineers: With Software and Programming Applications. 4th ed. July 16, 2001: McGraw-Hill Science/Engineering/Math. 944.
25. Press, W.H., Flannery, B.P., Teukolsky, S.A., and Vetterling, W.T., Numerical Recipes in Fortran. 2nd ed. 1992: Cambridge University Press. 992.
26. Bowie, O.L., Analysis of an infinite plate containing radial cracks originating at the boundary of an internal circular hole. Journal of Mathematics and Physics, 1956: p. 60-71.
27. Albrecht, P. and Yamada, K., Rapid calculation of stress intensity factors. Journal of the Strucutural Division, American Society of Civil Engineers, 1977. 103(ST2): p. 377-389.
28. Tweed, J. and Rooke, D.P., The distribution of stress near the tip of a radial crack at the edge of a circular hole. International Journal of Engineering Science, 1973. 11(11): p. 1185-1195.
29. Schijve, J., Stress Intensity Factors of Hole Edge Cracks-Comparison between One Crack and Two Symmetric Cracks. International Journal of Fracture, 1983. 23: p. R111-R115.
30. Newman, J.C.J., An improved method of collocation for the stress analysis of cracked plates with various shaped boundaries, NASA Technical Note D-6376. 1971, Langley Research Centre: Hampton, Va.

31. Isida, M. and Nemat-Nasser, S., A unified analysis of various problems relating to circular holes with edge cracks. Engineering Fracture Mechanics, 1987. 27(5): p. 571-591.
32. Harter, J.A., AFGROW: Users Guide and Technical Manual. AFRL-VA-WP-TR-2004-3016 (Version 4). 2004: Air Vehicles Directorate, 2790 D Street, Ste 504, Air Force Research Laboratory, WPAFB OH 45433-7542.
33. Engineering Software Research and Development, I.E., StressCheck ® : P-Version Finite Element code. 2000: St. Louis, Missouri.
34. Moreira, P.M.G.P., De Matos, P.F.P., Pinho, S.T., Pastram, D., Camanho, P.P., and De Castro, P.M.S.T., The residual stress intensity factors for cold-worked cracked holes: A technical note. Fatigue & Fracture of Engineering Materials & Structures, 2004. 27(9): p. 879-886.
35. Munz, D. and Fett, T., Stress Intensity Factors and Weight Functions (Advances in Fracture Series). 1997, Southampton, UK: Computational Mechanics Publications, WIT Press.
36. Grandt, J., A. F., Crack face pressure loading of semielliptical cracks located along the bore of a hole. Engineering Fracture Mechanics, 1981. 14(4): p. 843-852.
37. Fuhring, H., Approximation Functions for K-Factors of Cracks in Notches. International Journal of Fracture, 1973. 9: p. 328-331.
38. Kitagawa, H. and Yuuki, R., Analysis of arbitrarily shaped crack in a finite plate using conformal mapping: 1st Report-Construction of analysis procedure and its applicability. Transactions of the Japanese Society for Mechanical Engineering, 1977. 43(376): p. 4354–4362.
39. Liu, A.F., Effect of residual stresses on crack growth from a hole. AIAA Journal, 1984. 22(12): p. 1784-1785.
40. Lanciotti, A. and Polese, C., The effect of interference-fit fasteners on the fatigue life of central hole specimens. Fatigue and Fracture of Engineering Materials and Structures, 2005. 28(10): p. 1-11.
41. Zhang, Y., Fitzpatrick, M.E., and Edwards, L., Analysis of the Residual Stress around a Cold-expanded Fastener Hole in a Finite Plate. Strain, 2005. 41(2): p. 59-70.
42. Shah, S., Duffié, K., Ramachandran, S., and Lamb, T. Test And Analysis Based Stress Intensity Factors For Interference-Fit (Taper-Lok ®) Fasteners. in The 5th Joint FAA/DoD/NASA Conference on Aging Aircraft. 2001. Kissimmee, Florida, US.
43. Jones, R. and Peng, D., Composite repairs to cracked holes under bi-axial loading. Composite Structures, 2002. 57(1-4): p. 459-464.

Appendix 5–A

Note: The original data were computed to the accuracy of 15 decimal places. However, in the following tables only precisions up to 6 decimal places are presented. These discrete data are deemed sufficiently accurate for most engineering purposes. Tabulated SIF magnification factors: range of crack, 0 < c/R<5 and power of polynomial regression, n = 0 to 10.

c/R	Magnification Factor, $M_n(x/R) = K_n/\sigma_n(x/R)\sqrt{\pi c}$					
	Degree of polynomial expansion, n					
	0	1	2	3	4	5
0.0	0.0000E+00	0.000000E+00	0.000000E+00	0.000000E+00	0.000000E+00	0.000000E+00
0.1	1.0000E+00	6.366198E-02	5.000000E-03	4.244132E-04	3.750000E-05	3.395306E-06
0.2	1.0000E+00	1.273240E-01	2.000000E-02	3.395306E-03	6.000000E-04	1.086498E-04
0.3	1.0000E+00	1.909859E-01	4.500000E-02	1.145916E-02	3.037500E-03	8.250592E-04
0.4	1.0000E+00	2.546479E-01	8.000000E-02	2.716244E-02	9.600000E-03	3.476793E-03
0.5	1.0000E+00	3.183099E-01	1.250000E-01	5.305165E-02	2.343750E-02	1.061033E-02
0.6	1.0000E+00	3.819719E-01	1.800000E-01	9.167325E-02	4.860000E-02	2.640190E-02
0.7	1.0000E+00	4.456339E-01	2.450000E-01	1.455737E-01	9.003750E-02	5.706490E-02
0.8	1.0000E+00	5.092959E-01	3.200000E-01	2.172996E-01	1.536000E-01	1.112574E-01
0.9	1.0000E+00	5.729578E-01	4.050000E-01	3.093972E-01	2.460375E-01	2.004894E-01
1.0	1.0000E+00	6.366198E-01	5.000000E-01	4.244132E-01	3.750000E-01	3.395306E-01
1.1	1.0000E+00	7.002818E-01	6.050000E-01	5.648940E-01	5.490375E-01	5.468173E-01
1.2	1.0000E+00	7.639438E-01	7.200000E-01	7.333860E-01	7.776000E-01	8.448607E-01
1.3	1.0000E+00	8.276058E-01	8.450000E-01	9.324358E-01	1.071038E+00	1.260653E+00
1.4	1.0000E+00	8.912677E-01	9.800000E-01	1.164590E+00	1.440600E+00	1.826077E+00
1.5	1.0000E+00	9.549297E-01	1.125000E+00	1.432395E+00	1.898438E+00	2.578310E+00
1.6	1.0000E+00	1.018592E+00	1.280000E+00	1.738396E+00	2.457600E+00	3.560236E+00
1.7	1.0000E+00	1.082254E+00	1.445000E+00	2.085142E+00	3.132038E+00	4.820848E+00
1.8	1.0000E+00	1.145916E+00	1.620000E+00	2.475178E+00	3.936600E+00	6.415661E+00
1.9	1.0000E+00	1.209578E+00	1.805000E+00	2.911050E+00	4.887038E+00	8.407113E+00
2.0	1.0000E+00	1.273240E+00	2.000000E+00	3.395306E+00	6.000000E+00	1.086498E+01
2.5	1.0000E+00	1.591550E+00	3.125000E+00	6.631456E+00	1.464844E+01	3.315728E+01
3.0	1.0000E+00	1.909859E+00	4.500000E+00	1.145916E+01	3.037500E+01	8.250592E+01
3.5	1.0000E+00	2.228169E+00	6.125000E+00	1.819672E+01	5.627344E+01	1.783278E+02
4.0	1.0000E+00	2.546479E+00	8.000000E+00	2.716244E+01	9.600000E+01	3.476793E+02
4.5	1.0000E+00	2.864789E+00	1.012500E+01	3.867465E+01	1.537734E+02	6.265294E+02
5.0	1.0000E+00	3.183099E+00	1.250000E+01	5.305165E+01	2.343750E+02	1.061033E+03

Table 5–A1 Magnification factors for kernel Green's function with polynomial type crack face traction acting on a pair of symmetric radial cracks (N = 2).

c/R	Magnification Factor, $M_n(x/R) = K_n / \sigma_n(x/R)\sqrt{\pi c}$				
	Degree of polynomial expansion, n				
	6	**7**	**8**	**9**	**10**
0.0	0.000000E+00	0.000000E+00	0.000000E+00	0.000000E+00	0.000000E+00
0.1	3.125000E-07	2.910262E-08	2.734375E-09	2.586899E-10	2.460937E-11
0.2	2.000000E-05	3.725135E-06	7.000000E-07	1.324492E-07	2.520000E-08
0.3	2.278125E-04	6.364743E-05	1.794023E-05	5.091794E-06	1.453159E-06
0.4	1.280000E-03	4.768173E-04	1.792000E-04	6.781401E-05	2.580480E-05
0.5	4.882813E-03	2.273642E-03	1.068115E-03	5.052538E-04	2.403259E-04
0.6	1.458000E-02	8.146871E-03	4.592700E-03	2.606999E-03	1.488035E-03
0.7	3.676531E-02	2.396726E-02	1.576313E-02	1.043907E-02	6.951539E-03
0.8	8.192000E-02	6.103261E-02	4.587520E-02	3.472078E-02	2.642411E-02
0.9	1.660753E-01	1.391969E-01	1.177059E-01	1.002218E-01	8.580758E-02
1.0	3.125000E-01	2.910262E-01	2.734375E-01	2.586899E-01	2.460937E-01
1.1	5.536128E-01	5.671277E-01	5.861376E-01	6.099773E-01	6.383038E-01
1.2	9.331200E-01	1.042799E+00	1.175731E+00	1.334783E+00	1.523748E+00
1.3	1.508378E+00	1.826146E+00	2.230514E+00	2.743277E+00	3.392611E+00
1.4	2.352980E+00	3.067809E+00	4.035361E+00	5.344805E+00	7.118376E+00
1.5	3.559570E+00	4.972455E+00	7.007904E+00	9.944910E+00	1.419101E+01
1.6	5.242880E+00	7.812175E+00	1.174405E+01	1.777704E+01	2.705829E+01
1.7	7.542990E+00	1.194193E+01	1.907434E+01	3.067749E+01	4.961235E+01
1.8	1.062882E+01	1.781721E+01	3.013271E+01	5.131355E+01	8.786697E+01
1.9	1.470184E+01	2.601401E+01	4.643943E+01	8.347606E+01	1.508817E+02
2.0	2.000000E+01	3.725135E+01	7.000000E+01	1.324492E+02	2.520000E+02
2.5	7.629395E+01	1.776283E+02	4.172325E+02	9.868238E+02	2.346933E+03
3.0	2.278125E+02	6.364743E+02	1.794023E+03	5.091794E+03	1.453159E+04
3.5	5.744580E+02	1.872442E+03	6.157472E+03	2.038881E+04	6.788613E+04
4.0	1.280000E+03	4.768173E+03	1.792000E+04	6.781401E+04	2.580480E+05
4.5	2.594927E+03	1.087476E+04	4.597886E+04	1.957457E+05	8.379647E+05
5.0	4.882813E+03	2.273642E+04	1.068115E+05	5.052538E+05	2.403259E+06

Table 5–A2 Magnification factors for kernel Green's function with polynomial type crack face traction acting a pair of symmetric radial cracks (N = 2).

CHAPTER 6: THEORETICAL EVALUATION OF STRESS INTENSITY FACTORS IN CRACKED HOLES INCORPORATING THE INTERACTION OF EXTERNAL LOADING AND LOCAL RESIDUAL STRESS FIELD

This chapter describes the first part of the experimental and theoretical work undertaken to predict fatigue crack growth from StressWave cold-worked holes in aerospace aluminium alloys. The predictive technique is tailored for the damage tolerance analysis of fatigue-cracked holes in structures. The focus in this chapter is devoted primarily on the fracture mechanics study incorporating residual stress, along with the theoretical treatment of stress intensity factors in several loading scenarios. The surface residual stress data around a StressWave cold-worked hole determined from X-ray measurement was used. Incorporating the averaged surface stress field, the representative stress intensity factor is subsequently obtained from a Green's function model with a suitable amendment for specimen geometry effect. This is followed by a systematic assessment of the residual stress intensity factor during fatigue cycle, based on mean stress and crack closure criteria. The analytical framework provides a consistent and logical foundation to integrate residual stress effects in the fracture control programme of fatigue-aged structures.

6.1 Introduction

In this thesis, the study of fatigue-aging in StressWave (SW) cold-worked holes is motivated by several practical considerations. First, for both the structural design of aerospace structures as well as their inspection and repair schedules, it is of paramount importance to be able to predict the fatigue life of cold-worked holes in aero-components reliably. Second, there is, as yet, little published in the open literature on SW holes when

compared to other cold working processes such as split-sleeve mandrel technique. As discussed earlier in Chapter 1, although there is laboratory evidence that SW pre-stressed holes can achieve equivalent or even greater fatigue resistance compared to split-sleeve holes [1, 2], a description of the fatigue life estimation in SW holes has yet to be published. Third, to reap the benefits of accurate life modelling of SW holes, a systematic understanding of prediction methodology featuring residual stress effect is a prerequisite.

The chapter discussed about the inclusion of SW residual stress effect into fatigue crack growth (FCG) study. Here, we expand the application of linear elastic fracture mechanics (LEFM) expounded in Chapter 5 into the theoretical treatment of stress intensity factor (SIF), using the superposition principle. This chapter is arranged in the following manner. The residual stress data required for damage tolerance analysis is firstly taken from Chapter 3, and then expressed in terms of equivalent residual SIF. This involves the derivation of suitable SIF model for a single crack hole using the Green's function (GF) approach similar to the concept proposed in Chapter 5. Then, the residual SIF associated with the SW hole is integrated into an analytical framework to understand its crack tip interaction with fatigue loading. For this purpose, we have investigated two conventional LEFM methodologies currently co-executed in a life prediction code called AFGROW [3]. It is envisaged that this chapter will be a useful and insightful tool for designers and damage tolerance analysts dealing with durability of cold-worked holes. As extension, application of the knowledge in this chapter in predictive work is illustrated in Chapter 7.

6.2 Residual Stress Field at Cold-Worked Fastener Holes

In order to obtain accurate prediction of FCG, a detailed knowledge of the residual stress in the SW hole is firstly required. The geometry and cold-worked condition of Al 2024-T351 specimen (Figure 6.2.1 (a)) used to study the fatigue behaviour of SW hole is similar to that described earlier in Section 3.2 for stress measurement. However, in this chapter to

facilitate FCG work from a pre-determined location the hole edge was installed with a straight electro-discharge-machined (EDM) notch using a nominal 0.10 mm diameter wire. As detailed in Figure 6.2.1(b), high optical magnification of 20× to 50× was used for careful examination of the EDM notch geometry. Unfortunately, for the magnification used the material removed by countersinking prohibited a complete edge profile to be clearly seen in the microscope due to lost of depth contrast. However, for completeness the original hole boundary before countersinking is schematised in Figure 6.2.1(b) to aid visualisation.

This controlled artificial flaw entails only the progress of a single crack propagation to be monitored, without further complications of possible multiple crack lengths around the hole region. This condition also ensures that the life prediction model developed is accurate enough to represent the actual crack geometry.

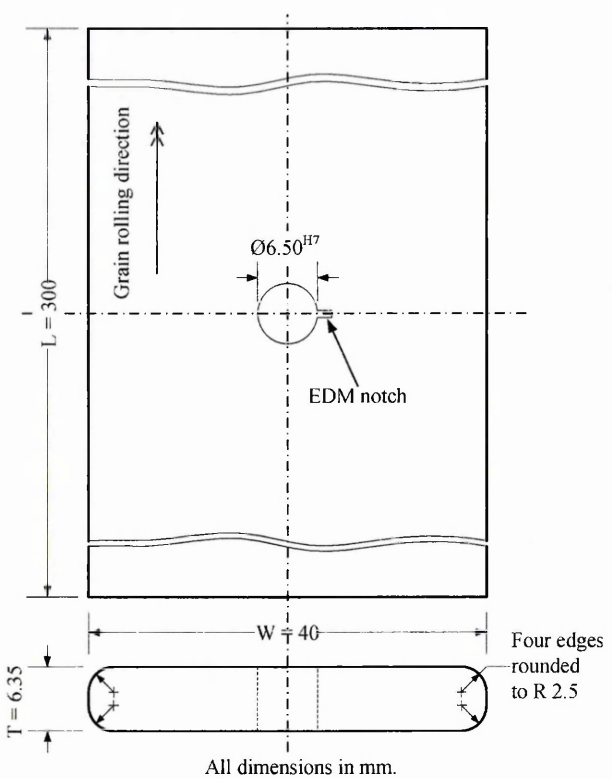

(a)

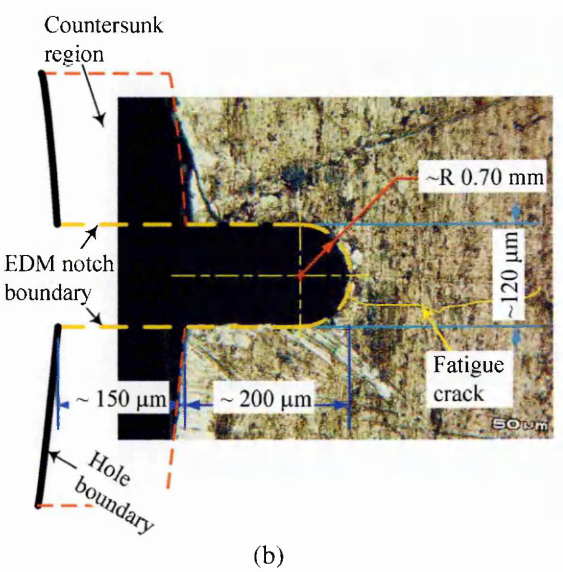

(b)

Figure 6.2.1 (a) Overall geometry of SW fatigue specimen and (b) detail view of single EDM notch introduced at the hole edge oriented perpendicular to the major loading axis (50×).

Material : Al 2024-T351

In Chapter 3 & 4, a complete assessment of the residual stress field induced around SW cold-worked hole has been carried out using diffraction measurement and numerical analysis. However, for brevity only the hoop stress component, $\sigma_{\theta\theta}$, is presented here for

subsequent analysis. We used the surface data measured from the X-ray diffraction technique (see Figure 3.5.9) to establish the residual hoop stresses accompanying the SW hole, as shown in Figure 6.2.2. The surface stress data of split-sleeve 4% mandrelised hole is also included for comparison.

In Figure 6.2.2 (also in Chapters 3 & 4), the hoop residual stress field around a SW hole is significantly more symmetric in the through-thickness direction than the split-sleeve mandrel hole. Following the previous discovery by Lamb *et al.* [4], the symmetric stress behaviour at the SW hole can be used to grow symmetric cracks from artificially produced through-thickness flaws, such as an EDM notch (Figure 6.2.1). This also provides some indication that a two-dimensional crack model giving one-dimensional SIF solution may be sufficient to analyse the FCG life. Thus, although a more complete analysis could be done using the full three-dimensional stress data from the neutron diffraction measurements, here, we consider only the average surface residual stress measured by the X-ray technique.

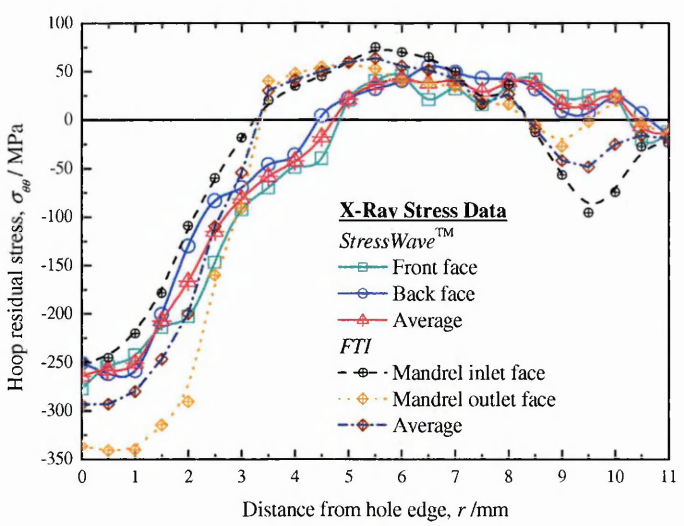

Figure 6.2.2 Surface hoop residual stress measured along the prospective crack line in a SW specimen using the X-ray diffraction technique.

A further justification for this simplified approach is that the crack growth measurement is made directly on the specimen surfaces where the residual stress field was quantified. Also, the measurement of near-surface residual stress in aerospace materials using laboratory X-ray facility is widely accessible compared to the neutron scattering method. Hence in many

cases, as a first estimate the X-ray stress data is commonly used in the preliminary phase of damage tolerance analysis [5, 6]. It is envisaged that the neutron diffraction data will provide a more physically-correct model in FCG prediction work. However, this will require the development of three-dimensional GF model to describe the SIF along the crack fronts.

6.3 Stress Intensity Factor Model

According to LEFM, the SIF, K, is a controlling parameter used to describe the state of crack tip in relation to applied loading. However, calculating the SIF under the influence of local residual stress field is not straightforward. Based on similar idea presented in Chapter 5, here, a GF approach using local crack face tractions has been adopted.

6.3.1 Green's function

The GF to represented the crack geometry described in Figure 6.2.1 is based on the central through-thickness crack solution in an infinite plate under biaxial loading [7]. The model is an extension of the double cracks case documented in Chapter 5. To calculate the SIF for a given local residual stress, the GF model associated with a single radial crack at a hole in an infinite plate (Figure 6.2.1) may be expressed as:

$$K_{res} = \frac{F_S}{F_{KGF}} \cdot \left[\frac{1}{\sqrt{\pi c}} \int_0^c \sigma_{res}(x) \cdot \sqrt{\frac{c+x}{c-x}} dx \right] \tag{6.3.1}$$

where F_s is the reference SIF solution; F_{KGF} is termed the kernel GF that represents the closed-form SIF incorporating the reference Kirsch stress solution (Equation (5.3.2)); c denotes the single crack length measured from the hole edge and x is an arbitrary location along the crack face, i.e. $0 \leq x \leq c$. As can be seen, the term (F_S/F_{KFG}) in Equation (6.3.1) is the hole curvature magnification factor, $F_{\emptyset}$, explained in Equation (5.4.4). Similar to the notion of Equation (5.3.6), in Equation (6.3.1) it is easier to integrate the discrete residual stress data by transforming the residual stress field, $\sigma_{res}(x)$, into an nth–degree polynomial,

$$\sigma_{res}(x/R)=\sum_{i=0}^{n}\sigma_n(x/R)^n=\sigma_0+\sigma_1(x/R)+\sigma_2(x/R)^2+...+\sigma_n(x/R)^n \quad ; \quad n\geq 0 \qquad (6.3.2)$$

Combining Equations (6.3.1) & (6.3.2), we have

$$\begin{aligned}
K_{res} &= \frac{F_S}{F_{KGF}}\left\{\frac{1}{\sqrt{\pi c}}\cdot\int_0^c \sigma_{res}(x)\cdot\sqrt{\frac{c+x}{c-x}}dx\right\} \\
&= \frac{F_S}{F_{KGF}}\sqrt{\pi c}\left\{\int_0^c \frac{\left[\sigma_0+\sigma_1(x/R)+\sigma_2(x/R)^2+...+\sigma_n(x/R)^n\right]}{\pi c}\sqrt{\frac{c+x}{c-x}}dx\right\} \\
&= \frac{F_S}{F_{KGF}}\sqrt{\pi c}\left\{\begin{array}{l}\sigma_0\cdot\left[\frac{1}{\pi c}\int_0^c\sqrt{\frac{c+x}{c-x}}dx\right]+\sigma_1\cdot\left[\frac{1}{\pi c}\int_0^c(x/R)\cdot\sqrt{\frac{c+x}{c-x}}dx\right]+ \\ ...+\sigma_n\cdot\left[\frac{1}{\pi c}\int_0^c(x/R)^n\cdot\sqrt{\frac{c+x}{c-x}}dx\right]\end{array}\right\} \\
&= \frac{F_S}{F_{KGF}}\sqrt{\pi c}\{\sigma_0H_0+\sigma_1H_1+...+\sigma_nH_n\} \\
&= \frac{F_S}{F_{KGF}}\sqrt{\pi c}\sum_{i=0}^{n}[\sigma_nH_n]
\end{aligned} \qquad (6.3.3)$$

where σ_n is the coefficient for polynomial stress function in (6.3.2), and H_n is related to the individual component of integral evaluated within the bracket in (6.3.3) called exact stress intensity magnification factor (SIMF). It has been shown by Isida [8] that the closed-form solution of SIMF is a convenient means to calculate SIF since it avoids the inherent complexities of numerical integration, and the numerical values of SIMF have been tabulated in Appendix 6–A, and their applications can be referred to the explanation given in Section 5.5. Given in exact form, the SIF computation for residual stress field in cold-worked holes can be implemented directly into a spreadsheet environment.

6.3.2 Exact closed-form expression, F_{KGF}

By integrating Kirsch's hoop stress solution (Equation (5.3.2)) with Equation (6.3.1), the outcome in the form of exact integral called the kernel GF, F_{KGF} is given by (6.3.4–6):

$$F_{KFG}=\left(\frac{1}{\pi}+\frac{1}{2}\right)+\frac{(1+\lambda)R^2I_2+3(1-\lambda)R^4I_4}{2\pi} \qquad (6.3.4)$$

where λ (= σ_x / σ_y) is the biaxial ratio of stress. The 2nd order and 4th order integrals, R^2I_2 and R^4I_4, are expressed respectively in Equation (6.3.5):

$$\left.\begin{aligned} R^2 I_2 &= [\alpha_3 + \ln(\xi + \alpha_3)] \;/\; [\alpha_1 \alpha_3] \qquad (6.3.5a) \\ R^4 I_4 &= \frac{\left\{\alpha_3 [\xi + \alpha_2]\left[\xi\alpha_1 - 1 - \frac{5}{\alpha_1}\right] + 3\left[\alpha_2 - 2 - \frac{5}{\alpha_1}\right]\ln(\xi + \alpha_3)\right\}}{6\alpha_3^5} \qquad (6.3.5b) \end{aligned}\right\} \text{for } \xi \neq 1$$

$$\left.\begin{aligned} R^2 I_2 &= 1 \\ R^4 I_4 &= 7/15 \end{aligned}\right\} \text{for } \xi = 1 \qquad (6.3.5c)$$

where ξ, α_1, α_2 and α_3 are the basic (dimensionless) geometry scaling terms defined by:

$$\xi = c/R \geq 0 \qquad (6.3.6a)$$

$$\alpha_1 = \xi + 1 \qquad (6.3.6b)$$

$$\alpha_2 = \xi - 1 \qquad (6.3.6c)$$

$$\alpha_3 = \sqrt{\xi^2 - 1} = \sqrt{\alpha_1 \alpha_2} \qquad (6.3.6d)$$

6.3.3 Standard reference solution, F_S

Many standard reference SIF solutions F_S are available in the open sources e.g. [8, 9]. The reference SIF is used to amended the effect of hole geometry during the computation of residual SIF, i.e. K_{res}. Corresponding to uni-axial loading used in the fatigue testing to grow crack in Figure 6.2.1, i.e. λ = 0, we used the Schijve's expression [10] for a single hole edge crack growing in an infinite plate:

$$F_S = \sqrt{\frac{2+\xi}{2(1+\xi)}} \cdot \left[1 + \frac{0.2\xi}{(1+\xi)^3}\right] \cdot \left[1 + \frac{1}{2\xi^2 + 1.93\xi + 0.539} + \frac{1}{2(\xi+1)}\right] \qquad (6.3.7)$$

This completes the description of the SIF model for a single crack emanating from a hole in an infinite sheet. The application of GF model prescribed in Equation (6.3.1) is similar to the description in Chapter 5 for a hole with double symmetric cracks. The model was validated by comparison with the solutions of Shivakumar & Forman [11] and Wu & Carlsson [12], however, with extra advantage of covering an infinite range of crack size.

6.3.4 Generic stress intensity factor model in AFGROW

AFGROW is a public domain fracture mechanics and FCG analysis code developed by United States Air Force (USAF) dedicated to the damage tolerance analysis of aero-structures. AFGROW covers extensive predictive capabilities for damage durability and fracture control of aero-structure elements such as crack initiation, FCG, fracture, and service-life assessment of metallic structures, which enable various possible scenarios of crack growth in materials to be analysed.

In particular related to this investigation, AFGROW is capable of including the residual stress effect in FCG analysis. It is therefore the interest of present study to investigate such capability of AFGROW in parallel to the author's model developed in Sections 6.3.1–6.3.3. In AFGROW version 4.0009e.12 [3], no specific solution is available for the present crack configuration to calculate the SIF of residual stress field given in Figure 6.2.1. Instead, as an approximation, AFGROW has implemented a generic point load SIF solution of a semi-infinite edge crack geometry from Sih & Hartranft [13]:

$$K_{res} = \frac{2}{\sqrt{\pi c}} \int_0^c \sigma_{res} \left[\frac{1.3 - 0.5(x/c) - 0.2(x/c)^2 - 0.3(x/c)^3 + 0.25(x/c)^4}{\sqrt{1-(x/c)^2}} \right] dx \qquad (6.3.8)$$

Equation (6.3.8) is a universal expression for any crack configuration should no suitable SIF model be provided in AFGROW. The residual SIF in Equation (6.3.8) is computed within AFGROW by a Gaussian integration routine, and coupled with a Newton interpolation scheme to resolve the Gaussian integration points between the tabulated residual stress data. Other variants of Equation (6.3.8) yielding identical results are also provided by references [9, 14].

6.3.5 Finite-width geometry correction factors, f_{FW}

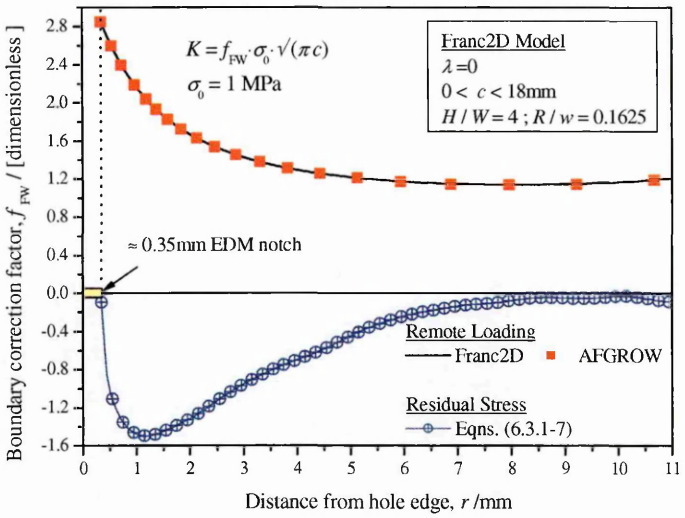

Figure 6.3.1 Crack geometry factor of plain hole and SW hole in finite-width plate.

The K_{res} in SW hole contained in an infinite sheet described in Sections 6.3.1–6.3.4 needs to be augmented to take account of the crack interaction with the finite width, W (= $2w$), of the plate. For this purpose, the SIF data obtained from the finite element crack growth simulator FRANC2D [15] was used to formulate a finite-width correction factor, f_{FW} (c, r). Figure 6.3.1 shows that, for hole with and without residual stress field, the derived geometry correction data, f_{FW} (c, r), for a single edge-crack hole in a finite-width plate matches the equivalent AFGROW β-solution very well [3].

6.3.6 Comparison of stress intensity factor results

Using the averaged X-ray surface stress data of SW hole given in Figure 6.2.3 along with the methodology outlined in Sections 6.3.1–6.3.5, the residual SIF, K_{res}, as a function of crack length, c, was calculated in Figure 6.3.2. Some differences in residual SIF also occurred due to the introduction of an EDM notch (Figure 6.3.2).

Figure 6.3.2 contrasts the K_{res} computed from the present and the AFGROW models at the hole edge with and without the EDM notch installed. According to the idea of crack face traction, only the SIF accounting for the presence of the notch is valid; the residual stress before the EDM notch is machined does not contribute to the total SIF for a given crack.

Therefore, the following discussion will concentrate on the residual SIF calculated from the notch tip as a function of total crack, c.

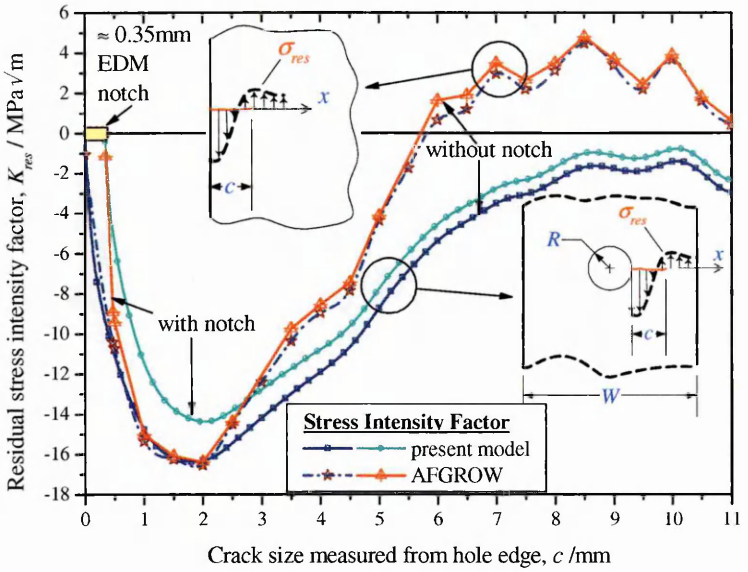

Figure 6.3.2 Residual stress intensity factors computed from Green's function and AFGROW models.

The AFGROW results show less reduction in SIF values except near the EDM notch as compared to those of the GF model. At short crack lengths of $0 < c < 2.5$mm of notch-free geometry, the SIF data of AFGROW and the present model match quite well; but both results show marked disagreement for larger crack size. The comparison suggests the GF and AFGROW model probably predict similar fatigue life at small crack length, but the application of the generic model in AFGROW might not be warranted for longer cracks.

Figure 6.3.2 shows that in the absence of external loading the SIF corresponding to the residual stress, K_{res}, as predicted by the GF is entirely negative. Conversely, the AFGROW generic SIF model calculates a transition of K_{res} from negative at $0 < c < 5.5$ mm to positive for $c > 5.5$mm. Physically, such a difference in K_{res} behaviour can be related to the geometrical influence of approximated (i.e. AFGROW) and exact (i.e. GF model) crack configurations on the crack tip, i.e. β-solution.

6.4 Characteristic of Stress Intensity Factors In Compounded Stress Field

Cracking in materials containing self-equilibrating residual or thermal stress fields are encountered regularly in engineering. The central notion of the principles of LEFM in these problems relies on the appropriate definition and derivation of a SIF that is directly correlated to fatigue crack growth. In a broader spectrum two LEFM methodologies have been adopted to integrate the effects of the self-equilibrating stress in fatigue life calculation, namely the superposition and crack face contact principles.

To date, the linear elastic superposition principle is undoubtedly the most well-received method to determine SIF in compound residual and applied stress fields [16]. For any crack size, the total SIF is merely considered as a linear summation of the contributions from the residual stress and applied stress. This constitutes a convenient means of calculating the SIF range for life modelling. Despite its simplicity the superposition method is not without shortcomings. The presence of net negative values of SIF by superposition, normally associated with a compressive stress field, indicates that there may be interpenetration of crack surfaces which is, in reality, not viable. However, a total negative SIF is frequently acknowledged as the consequence of crack closure, and hence is either disregarded in calculations or requires further manipulation.

An elegant approach to address the problems of crack face penetration is the crack face contact principle, which eliminates the appearance of negative SIF in computations. The contact behaviour between opposite crack faces due to compressive surface tractions is a nonlinearity problem that affects the crack tip condition. This necessitates that both the contact region and traction pressure between crack flanks be determined for a given combination of crack geometry and residual stress field, before the SIF can be readjusted for subsequent analysis. These pertinent information can be solved using the weight

function-based crack opening displacement either in exact form or by numerical estimation [17-19] for very simple geometry; or implemented in fracture mechanics-orientated finite element codes for realistic simulations of crack growth in complex geometry [20]. Another alternative is the equilibrated superposition of two elastic cases representing the remote uniform stress and traction along the crack surfaces, which preclude crack flank interference [21-23]. Nonetheless, these solutions are inherently time consuming and expensive both for modelling preparation and analysis, especially when plasticity and friction are included.

Due to its simplicity, the former principle of superposition is adopted here in line with the fatigue crack growth (FCG) prediction methodology widely used for cold-worked holes. In the following discussion, a comprehensive account of the superposition of SIF of cracks embedded in a compound stress field is presented, and a systematic and unified framework embodying the concepts of crack closure and mean stress criterion is suggested. This unified framework was devised to tackle the active SIF in response to the fatigue cycle with great clarity. Assessment and discussion along with the possible implementation of both concepts, based on the crack tip condition, are drawn in light of preceding fatigue studies by various researchers.

6.4.1 Analysis of the interaction of stress intensity factors from residual stress with fatigue loading

To estimate the FCG life of a cold-worked hole reliably, one must first establish the crack tip response of a given residual SIF, K_{res} in relation to the elastic SIF, K_{apply}, related to an external load. It has been argued that since the total local stress, σ_{tot} in materials can be inferred by superimposing the local residual stress, σ_{res} with local elastic stress induced by remote loading σ_{apply}, the principle is deemed equally valid to the calculation of total local SIF. This assumption remains legitimate as long as the imposing stress or crack boundary

does not drastically disturb the original stress state during crack growth. This consists of the summation of the two basic components (Figure 6.4.1(c), (f) & (i)):

$$K_{tot} = K_{apply} + K_{res} \tag{6.4.1}$$

Therefore, for a crack length, c, the total SIF corresponding to the peak and valley of the active/compounded stress cycles are

$$\begin{aligned} K_{tot-\max} &= K_{apply-\max} + K_{res} \\ K_{tot-\min} &= K_{apply-\min} + K_{res} \end{aligned} \tag{6.4.2}$$

This common conception of superposition has been widely adopted to study the influence of local residual stress on fatigue life of metallic components [22, 24-27]. However, there have been several ways to interpret how the total SIF range, ΔK_{tot} responsible for crack extension. These interpretations can be traced back to two central entities: the mean-stress and the crack closure approaches. As can be seen later, the selection of either methodology necessitates different sets of requirements for the FCG analysis of cold-worked holes.

Using the residual SIF (K_{res}) calculated earlier for SW hole in Figure 6.3.2, the superposition techniques shown in Figure 6.4.1 is then used to study the SIF response of the crack tip under compounded K_{res} and K_{apply}. Figure 6.4.1 will be discussed in the light of mean-stress approach in Section 6.4.2, and crack closure approach in Section 6.4.3.

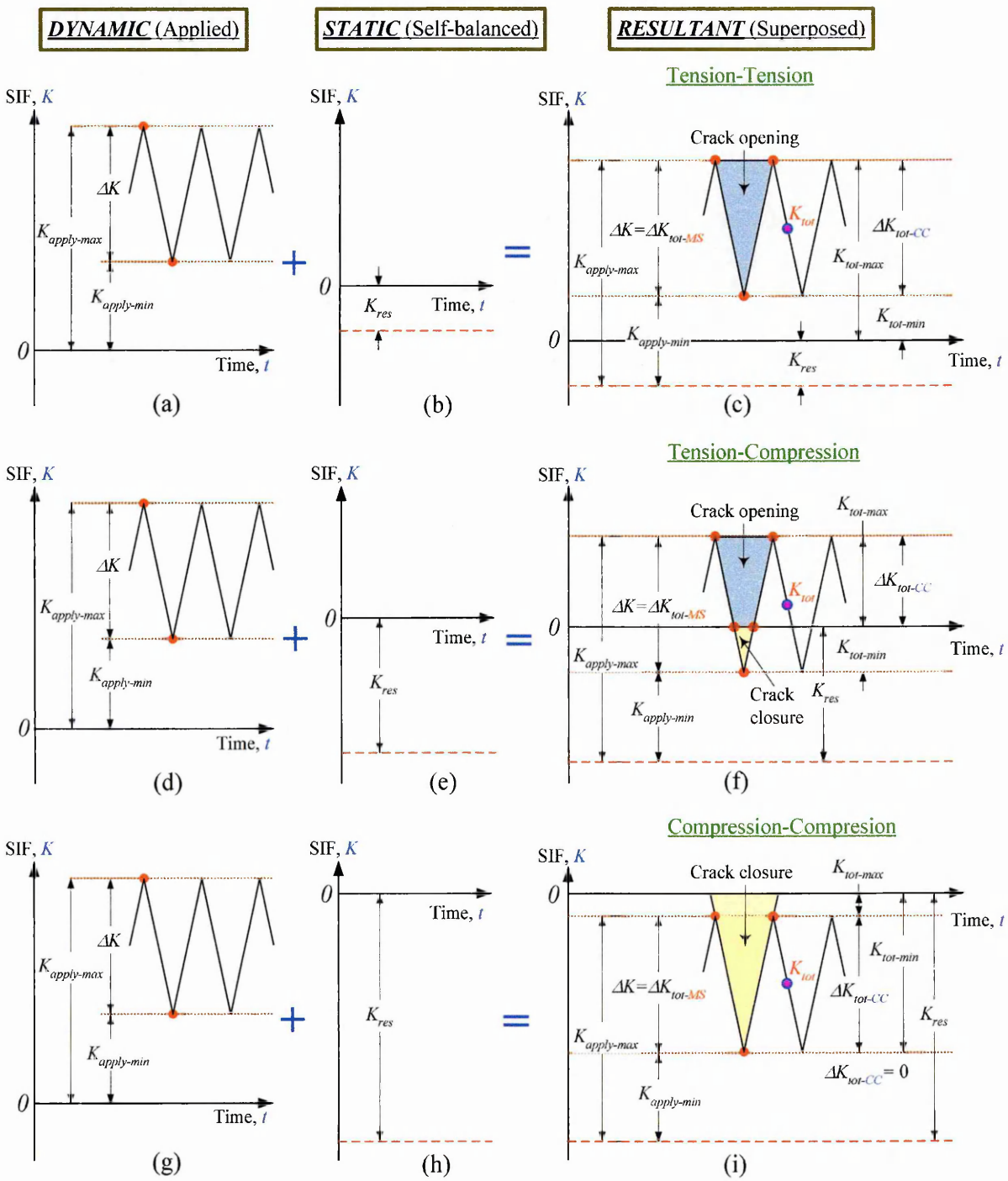

Figure 6.4.1 The opening and closure conditions of crack tip in the presence of compressive residual stress field. Stress intensity factors of applied tensile loading (a), (d) and (g) are superimposed with those of residual stress field (b), (e) and (h) to produce (c), (f) and (i). Mean stress : MS; crack closure: CC.

6.4.2 Mean stress approach

The mean stress (or *R*-ratio) methodology advocates that under constant amplitude loading, both the applied and local SIF range are equal, and independent of residual stress effects [27]. Invoking Equation (6.4.2),

$$\Delta K_{tot-CC} = K_{tot-\max} - K_{tot-\min} = K_{apply-\max} + K_{res} - \left(K_{apply-\min} + K_{res}\right)$$
$$\therefore \Delta K_{tot-CC} = K_{applied-\max} - K_{applied-\min} = \Delta K \tag{6.4.3}$$

Let us consider a local residual stress distribution that varies along the prospective crack path. During fatigue loading, as the crack propagates through the superimposed stress field, the local stress ratio R_{eff}, changes continually in spite of the constant applied R. The residual stress merely alters the local mean stress (or R-ratio) at the crack tip according to the variation of local K_{res} at different crack size, but not the SIF range as shown by Equation (6.4.3). The remote and local stress ratios, i.e. R and R_{eff}, written in term of SIF are, respectively

$$R = \frac{K_{apply-\min}}{K_{apply-\max}} \text{ and } R_{eff} = \frac{K_{tot-\min}}{K_{tot-\max}} = \frac{K_{apply-\min} + K_{res}}{K_{apply-\max} + K_{res}}$$
$$\therefore R \neq R_{eff} \tag{6.4.4}$$

6.4.3 Crack closure approach

The crack closure approach advocates that a crack can only propagate if the crack tip is tensioned in a mode I, i.e. $K > 0$, and therefore this condition is also true for ΔK_{tot} [28]. Physically, the crack tip must be sufficiently opened to induce local material damage leading to subsequent crack extension. From this viewpoint, the benefit of a cold-worked hole is seen to be governed purely by the behaviour of residual stress (i.e. compressive or tensile) that is mathematically correlated to the sign of K_{res} (i.e. positive = opened crack tip, or negative = closed crack tip). Considering Equation (6.4.2), we have

$$K_{tot} < K_{apply} \quad for \quad K_{res} < 0 \tag{6.4.5a}$$
$$K_{tot} \geq K_{apply} \quad for \quad K_{res} \geq 0 \tag{6.4.5b}$$

Equation (6.4.5) infers that the superposed residual SIF can either have a K-reduction or a K-increasing effect depending on the sign of K_{res} i.e amount of crack tip opening. Under an arbitrary R-ratio, the crack tip only opens for a fraction of the cycle if $K_{\text{tot}} > 0$. For the remainder of the cycle, the crack tip is closed i.e. $K_{\text{tot}} < 0$. Accordingly, the crack opening conditions defined by the active SIF range are:

$$\Delta K_{tot-CC} = \begin{cases} K_{tot-\max} - K_{tot-\min}; & R_{eff} = K_{tot-\min}/K_{tot-\max} \quad , \; K_{\min-tot} \geq 0 \\ K_{tot-\max}; & R_{eff} = 0 \quad , \; K_{\min-tot} < 0 \\ 0; & R_{eff} > 1 \; or \; R_{eff} = \infty \quad , \; K_{\max-tot} \,\&\, K_{\min-tot} \leq 0 \end{cases} \tag{6.4.6}$$

The qualitative interpretation of both the crack closure (CC) and mean stress (MS) mechanisms, in agreement with superposition, are established in Figure 6.4.1. The respective mathematical relations of ΔK_{tot} and R_{eff} are summarised in Table 6.4.1.

Approach / Condition	Mean Stress	Crack closure
Fig. 6.1(c) **Tension-Tension**	$\Delta K_{tot-MS} = \Delta K_{tot-CC} = \Delta K = K_{tot-\max} - K_{tot-\min} = K_{apply-\max} - K_{apply-\min}$; $0 \leq R_{eff} \left(= \frac{K_{tot-\min}}{K_{tot-\max}}\right) < 1$	
Fig. 6.1(f) **Tension -Compression**	$\Delta K_{tot-MS} = \Delta K = K_{tot-\max} - K_{tot-\min} = K_{apply-\max} - K_{apply-\min}$ and $-\infty \leq R_{eff} \left(= \frac{K_{tot-\min}}{K_{tot-\max}}\right) \leq 0$	$\Delta K_{tot-CC} = K_{tot-\max} - 0 = K_{apply-\max} - K_{res}$ and $R_{eff} = \frac{0}{K_{tot-\max}} = 0$
Fig. 6.1(i) **Compression-Compression**	$\Delta K_{tot-MS} = \Delta K_{tot-CC} = 0$; $R_{eff} = \frac{K_{tot-\min}}{K_{tot-\max}} > 1$ or $R_{eff} = \frac{K_{tot-\min}}{K_{tot-\max}} = \infty$ i.e. no crack propagation as the crack flanks are assumed to be fully intact.	

Table 6.4.1 Algebraic definitions of total stress intensity factor range, ΔK_{tot} and effective stress ratio, R_{eff} according to the mean stress (MS) and crack closure (CC) approaches.

The schematic in Figure 6.4.1 enables explicit correlation of the degree of influence of compressive residual stress on the SIF range and R-ratio for any compound stress field. For constant amplitude loading, the SIF of identical remote loading K_{apply}, in Figures 6.4.1(a), (d) & (g) superposed on different residual SIF, K_{res}, of Figures 6.4.1(b), (e) & (h) gives rise to three distinct scenarios of crack tip condition suggested by Figures 6.4.1(c), (f) & (i). These different scenarios of tension-tension, tension-compression and compression-compression loading in Figure 6.4.1 are equally relevant to characteristics of variable amplitude loading experienced in cracked components [3, 29]. Figure 6.4.1 is by no means limited to a compressive residual stress field as a similar assessment is also valid to tensile

residual stress. Notably, replacing the compressive residual stress in Figure 6.4.1 with tensile residual stress will produce different effects on crack propagation.

6.4.4 Discussion

In the following discussion, all the three loading scenarios of Figures 6.4.1(c), (f) & (i) are examined individually in detail. Firstly, for the tension-tension loading in Figure 6.4.1(c), Table 6.4.1 signifies that the same values of ΔK_{tot} and R_{eff} are obtained from the mean stress and crack closure approach as

$$\Delta K = \Delta K_{tot-MS} = \Delta K_{tot-CC} \tag{6.4.7a}$$

$$R_{eff-MS} = R_{eff-CC} \neq R \tag{6.4.7b}$$

Equation (6.4.7b) indicates that the crack closure condition in Figure 6.4.1(c) is also accompanied by an R-effect, and this can be seen as a special case of the mean stress approach according to Table 6.4.1.

Next, for tension-compression loading the presence of negative K_{res} can be related to the phenomenon of crack tip closure (Figure 6.4.1(f) & Section 6.4.3). A review of previous work has shown some inconsistency in the adoption of ΔK_{tot} and R_{eff} in fatigue assessment incorporating residual stress. The majority of the earlier FCG studies in cold-worked holes [26, 30-35] were founded on the crack closure criteria. Nevertheless, for both the conditions in Figure 6.4.1(c) & (f) references [26, 30-35] ignored the mean stress effect R_{eff}, (i.e. assuming $R_{eff} = 0$ throughout), and instead considered only the variation of ΔK_{tot} solely responsible for crack extension. In parallel, no conformity is observed for the material basic crack growth rate data used for FCG prediction [26, 30-35]. For instance, several researchers [26, 30, 32] extended the used of the single baseline data of Al 7075-T6 derived at $R_{apply} \approx 0$ to calculate for FCG data occur at other stress ratio, e.g. Hsu *et al.* [35] employed the reference data of Al 2219-T851, and Josefson [33] used those of Al 6061-T6, both derived from $R_{apply} = 0.1$, and Torpali *et al.* [34] calculated the material crack

propagation constants of low carbon steel of $R_{apply} = -1$. As expected, the majority of these analyses rely on a single curve of crack growth rate data and do not yield consistent correlation with fatigue crack data.

Later, a more sensible and consistent implementation of the crack closure principle, allowing appropriate use of ΔK_{tot} and R_{eff} (Figure 6.4.1(c) and (f)) in relation to the opening fatigue cycle of the crack tip, was summarised systematically by Parker [16]. Parker's crack closure approach, as exemplified by Impellezzeri & Rich in cold-worked lugs [25] and Stacey & Webster for autofrettaged tube [24], permits the positive variation of R_{eff} and $\Delta K_{tot} \geq 0.0$ in FCG prediction. The obvious advantage of this approach is that the baseline da/dN–ΔK curves correspond only to positive R-ratios (i.e. $0 \leq R < 1.0$), which can be readily generated in the laboratory.

In contrast, the mean stress effect (Figure 6.4.1(c) & (f)) that allows R_{eff} to assume both positive and negative values with $\Delta K_{tot} = \Delta K$, were also considered in many investigations [27, 36-41]. A common feature in these studies is the prerequisite of a wide spectrum of baseline crack growth rate curves, $da/dN = f(\Delta K_{tot}, R_{eff})$, often accomplished by the aid of empirical models e.g. Walker [36, 37, 40], Forman [25, 41, 42] or Bell-Creager expressions [43], or inter-/extrapolation scheme of multiple $da/dN = f(\Delta K_{tot}, R_{eff})$ curves [27, 38, 39]. The necessity of an extensive range of calibration curves, especially those associated with highly negative R_{eff} values (i.e. high compressive stress) causes some potential complications for the mean stress approach. However, as will be shown later simple judgement can often provide a suitable estimate of R_{eff} values that give reasonable FCG predictions.

Finally, the compression-compression response in Figure 6.4.1(i), theoretically should not induce crack extension because the crack faces are supposed to be remain entirely intact throughout the fatigue cycle. To date, however, still very little attention is paid to the effect

of crack extension under compression-compression loads. Notably, Vasudevan and Sadananda [44] argued that remote compression-compression fatigue cycles possibly promote crack activities if a localized tensile internal stress field is formed, particularly around stress raisers. Even for the pre-existing residual stress, excessive compressive load can be detrimental to the quality of fatigue durability in cold-worked holes [42, 45, 46], such that the residual stress near to the hole alters from compressive to tensile. Physically, the applied compressive load generates a shakedown in the residual stress associated with significant reversed cyclic plasticity. However, in the superposed Figure 6.4.1(i) it is unlikely that the crack will grow due to the tensile remote load of Figure 6.4.1(g); favourably, this precludes any change in pre-existing residual stress behaviour during the fatigue cycling that possibly causes subsequent gross yielding in the material.

6.4.5 Calculation of the ΔK_{tot} and R_{eff}

In the FCG prediction, various fracture components presented earlier in Section 6.3–4 are required, and this involves the computations of Equations (6.3.1–7), (6.4.1–7) and Table 6.4.1. The derivations of ΔK_{tot} and R_{eff} using both the mean stress and crack closure approaches correspond to the laboratory fatigue conditions of R = 0.1 and σ_{max} = 138.12 MPa. The resulting ΔK_{tot} and R_{eff} versus crack size, c are shown in Figures 6.4.2–3. Figure 6.4.2 (a) exhibits the complete definition of ΔK_{tot} as prescribed by the mean stress and crack closure methods. For crack closure criteria, region-*A* represents crack tip closure and region-*B* indicates that the crack tip is fully open. Figure 6.4.2 (b) provides a comparison of ΔK_{tot} definitions needed for numerical integration in the FCG algorithm. The crack length c $\approx$ 7.45 mm designates the transition point of ΔK from tension-compression to tension-tension loading at the crack tip.

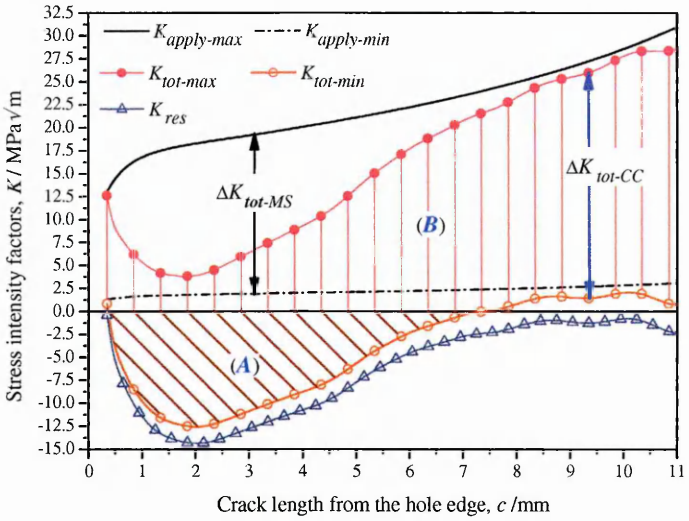

(a)

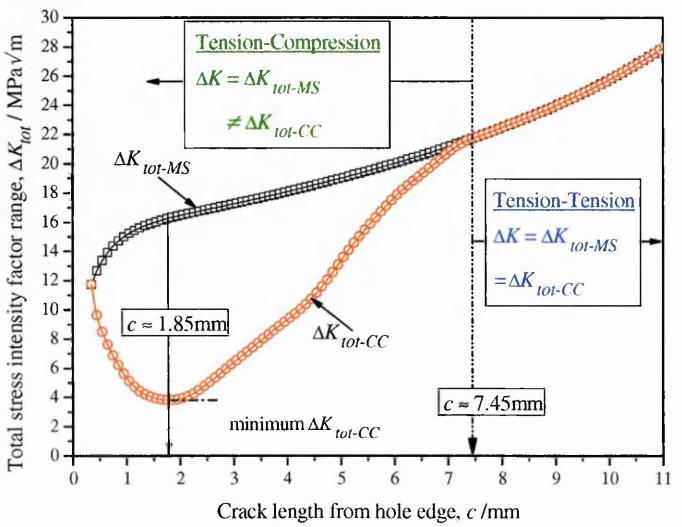

(b)

Figure 6.4.2 For constant amplitude of fatigue loading: $R = 0.1$ and $\sigma_{max} = 138.12$ MPa, (a) definitions of total SIF range, ΔK_{tot} and (b) summary of ΔK_{tot} according to mean stress or crack closure approach. CC = crack closure; MS = mean stress; A = closed crack tip; B = opened crack tip.

The change in R_{eff} along the prospective crack path length, c, is portrayed in Figure 6.4.3. As can be discerned, comparison with the results of AFGROW fracture mechanics code [3] substantiates the calculations based on the present analytical framework of superposition of SIF. The overall trend implies that near to the hole edge $c < 7.45$mm: (1) the crack closure calculations produced a reducing ΔK with constant R; and (2) the mean stress maintains a constant ΔK in response to the total SIF range of applied stress throughout, but experiencing a decreasing–increasing pattern of R_{eff}. For $c > 7.45$mm (tension-tension), the relation of Table 6.4.1 confirms the uniformity of the characteristic of ΔK and R_{eff} for the two methods. Close inspection of Figures 6.4.2(b) and 6.4.3 in the vicinity of crack length

c = 1.85 mm where is residual stress most compressive should correspond to the minimum FCG rate, dc/dN (viz. maximum retardation) in cold-worked holes. This condition is irrespective of whether the crack closure or mean stress model is used.

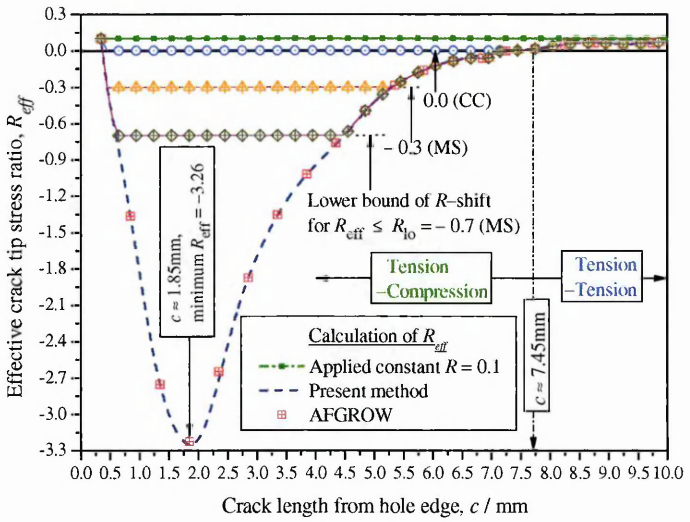

Figure 6.4.3 Comparison of effective R-ratio for mean stress and crack closure methodologies, and the actual R-ratio range used in AFGROW. CC = crack closure; MS = mean stress.

For the assigned loading and crack configuration, the computed minimal R_{eff} ratio accompanying mean stress model reaches around –3.26 in which the related da/dN = f (ΔK, R) is unlikely to be available for most cases. A practical option to overcome this problem is the introduction of a limiting R_{eff} invoked in the FCG calculation, as employed in AFGROW [3]. Related specifically to the situation in Figure 6.4.3, the parameter R_{lo} is the lower bound of R-shift in da/dN = f (ΔK, R) curves, and can be used to fine-tune the prediction in FCG life to experimental data. Three values of R_{lo} = 0.0, –0.3 and –0.7 were used to simulate the alternative R_{eff} –'routes' in the FCG calculation routine. Further details about the application R_{lo} are discussed in the next chapter.

6.5 Model of Crack Opening Stress & Effective Stress Intensity Factor Range in Compounded Stress Field

As discussed in the preceding section, the total SIF range of the remotely applied stress and local residual stress are determined purely from the LEFM perspective, and without taking the intrinsic effect of the successive plasticity associated with FCG into account. Elber in

his pioneering work [47, 48] discovered that, under constant or variable amplitude loading, for nominally elastic materials cracks can remain closed during part of the load cycle; and this will be equally applicable for the plastically-deformed cold-worked holes. The premature crack closure of a crack growing from a plain hole is related alone to the plastic wake along the crack faces, and in cold-worked holes this is subjected to the combinations of the primary due to residual stress with secondary Elber-type crack-induced plasticity. Earlier of this discussion, the primary effect of residual stress on R_{eff} and ΔK_{tot} has already been accounted for via the superposition of K_{apply} with K_{res}; whereas at this stage the issue of secondary crack closure on the crack opening behaviour is dealt with.

6.5.1 Crack opening stress function

It is unclear how the presence of cracks and the subsequent formation of secondary crack-induced plasticity affects the overall crack tip response in a residual stress field. Nevertheless, as a first estimate we assume the original residual stress, and therefore the residual SIF, remains unchanged throughout the course of crack propagation. The remaining task is to determine the effective SIF range, ΔK_{eff} from the total SIF range ΔK_{tot}, for any given effective stress ratio response R_{eff} at the crack tip.

The inclusion of ΔK_{eff} concept in life prediction of components containing residual stress was noted in the work of Buxbaum & Huth [41], Lam & Lian [49] and recently Ball & Doerfler [42]. In present investigation, we used the Newman plasticity-induced crack opening model, f [50] for constant amplitude loading, which application has been widely accepted in damage tolerance analysis of aero-structures [3, 21, 29]. The model was an adaptation of two-dimensional Dugdale-type strip-yield model [51] that leaves plastically-deformed material in the wake of propagating crack. The numerical result derived from the strip-yield model was then expressed as an analytical function of stress ratio R, maximum

remote stress level S_{max} (or K_{max}), and the specimen thickness effect governed by a three-dimensional constraint α, given as follows:

$$f = \frac{S_{op}}{S_{max}} = \frac{K_{op}}{K_{max}} = \begin{cases} \max\left(R, A_0 + A_1 R + A_2 R^2 + A_3 R^3\right) & \text{for} \quad 0 \le R \le 1.0 \quad (6.5.1a) \\ A_0 + A_1 R & \text{for} \quad -2 \le R < 0 \quad (6.5.1b) \end{cases}$$

The associated coefficients, A_0, A_1, A_2 and A_3 are defined by:

$$A_0 = \left(0.825 - 0.34\alpha + 0.05\alpha^2\right)\left\{\cos\left[(\pi/2) S_{max} / \sigma_0\right]\right\}^{1/\alpha} \quad (6.5.2a)$$

$$A_1 = \left(0.415 - 0.071\alpha\right) S_{max} / \sigma_0 \quad (6.5.2b)$$

$$A_2 = 1 - A_0 - A_1 - A_3 \quad (6.5.2c)$$

$$A_3 = 2A_0 + A_1 - 1 \quad (6.5.2d)$$

α is the constraint factor to include the three-dimensional crack tip yielding effect when simulated by two-dimensional closure model [51]. The local yield condition at the crack tip is controlled by $\alpha \cdot \sigma_0$ by varying α between plane stress (α = 1) or plain strain (α = 3). However, for compression yielding the crack tip stress state becomes – σ_0. S_{op} or K_{op} is the crack opening level; and S_{max} / σ_0 is the ratio of the maximum applied stress to the flow stress; and the flow stress σ_0 is assumed as the average of yield stress σ_Y, and ultimate strength, σ_u of the material. No further detail is provided here, but additional information of the Newman model can be found elsewhere [21, 50, 52-54].

6.5.2 Application of the Newman model

For illustration, the parameters derived from constant amplitude FCG experiments for Al 2024-T351 under several *R*-ratios in L-T grain orientation and room temperature were considered. The FCG specimens were also nominally free from initial residual stress or plastic deformation. The information, namely pseudo-plane stress constraint i.e. α = 1.5 and S_{max}/σ_o = 0.3, is taken from AFGROW materials database [3] derived specifically for a semi-analytical FCG rate expression called NASGRO equation [54].

The variation of the degree of crack closure f, as a function of R, α and S_{max}/σ_0 are depicted in Figure 6.5.1. In regime-I of positive R, the closure level f, is negligible for $0.7 \geq R \geq 1.0$ (i.e. $S_{op} = S_{min}$) and almost independent of α; and the FCG data affiliated to this closure-free condition is normally used as a reference state for model fitting purposes. The closure effect is more noteworthy for $0 < R < 0.7$.

In Figure 6.5.1(a), for a given σ_0 the remote stress S_{max} has strong influence on the local crack opening stress S_{op}. For the same R-ratio in Figure 6.5.1(b), the model also predicts lower closure stress f for pseudo-plane strain condition ($\alpha \rightarrow 3$) than plane stress state ($\alpha \rightarrow 1$). In regime-II of negative R, the closure factor f is linearly-dependent on R-ratios.

At regime-III of Figure 6.5.1(a), particularly at higher S_{max}/σ_0, near to the material yield limit, along with negative R-ratios, the model predicts crack opening at a sub-zero stress level. Crack opening at sub-zero stress is still a subject of debate; however, the abovementioned condition was experimentally observed by several researchers [55-57].

In Figure 6.5.1, the condition $\sigma_{max}/\sigma_0 = 0$ implies small-scale yielding around the crack tip i.e. the value of σ_{max} is small compared to the flow stress σ_0, with the global behaviour of the specimen is elastic. The ratio σ_{max}/σ_0 is an indication of the amount of remote applied maximum stress σ_{max}, with respect to the material flow stress σ_0. Remembering that due to the singularity, even at small applied (elastic) stress σ_{max} at remote boundary would still cause local plastic deformation at crack tip, and therefore the presence of crack closure behaviour around the crack region.

Also, from Figure 6.5.1 of Newman model for constant amplitude loading, there is tendency that a crack consistently loaded with high stress ($\sigma_{max}/\sigma_0 \rightarrow 1$) give arises to large-scale yielding has lower opening stress. There is more plastic deformation associated with greater crack opening displacement, which responsible for lower crack opening loads.

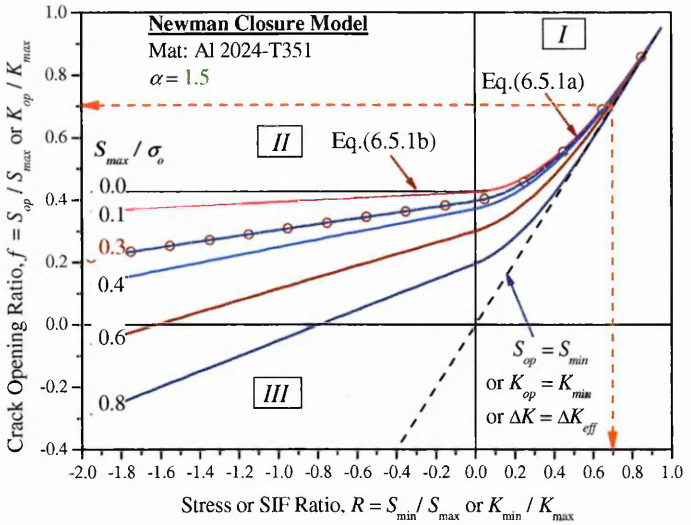

(a)

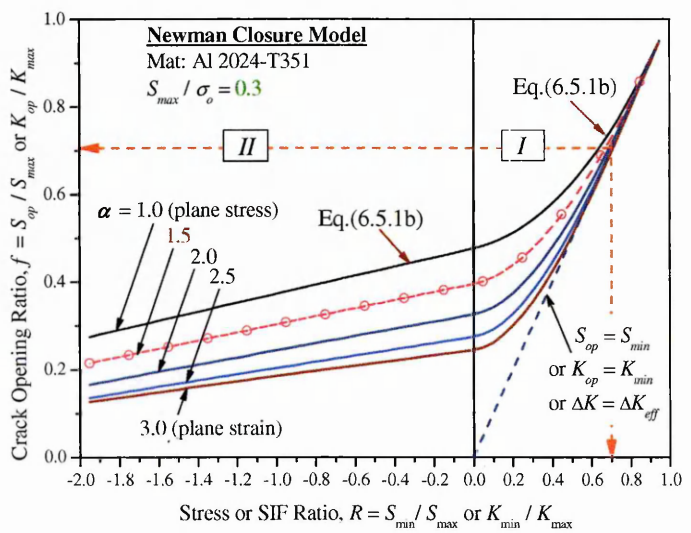

(b)

Figure 6.5.1 Newman model of crack opening stress or SIF. The fitting parameters of A1 2024-T351, α = 0.15 and S_{max} / σ_{op} = 0.3 is taken from NASGRO 3.0 equation. (a) Fixed α = 1.5, and varying S_{max}/σ_o and (b) fixed S_{max}/σ_o = 1.5, and varying α.

Silva [55, 56] argued that crack opening values for compression-tension loadings can be determined reliably only if both the extrinsic properties of materials e.g. da/dN–ΔK curves and the intrinsic properties e.g. cyclic plasticity or internal stress are considered simultaneously. In principle, Silva's conclusion was in line with the unified fatigue damage approach of Vasudevan & Sadananda [44, 58]; nevertheless, Vasudevan & Sadananda addressed the contribution of internal stress by using two independent crack driving forces, ΔK and K_{max} with respect to R-ratio [59]. Also, Silva concluded that the Newman model is not sufficiently reliable to predict crack opening stress when compared to his laboratory measurements. In short, the complications in Regime-III require more in-depth studies to

produce a better crack opening stress model in the future. The limitations in the Newman model to address crack opening for large negative R_{eff} as observed in Figure 6.4.3 will be addressed in the next section.

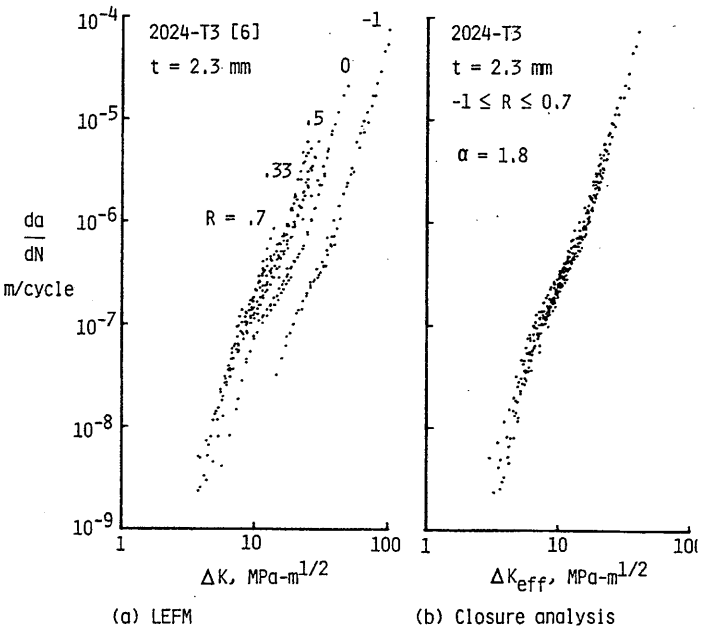

Figure 6.5.2 Correlation of crack growth rates using LEFM and crack closure ($\alpha = 1.8$) analysis [50].

For many materials, the presence of plasticity-induced crack closure tends to cause a systematic rightward spread of da/dN vs. ΔK curves a function of decreasing R-ratios. Introducing an appropriate amount of corrections on the crack opening level onto these individual curves enables the Newman Equation (6.5.1) to be used as a universal normalising function to collapse various da/dN = (ΔK, R) dataset into a representative curve of da/dN–ΔK_{eff}, as illustrated in Figure 6.5.2 [50].

6.5.3 Definition & calibration of ΔK_{eff} in superimposed ΔK_{tot} Range

For the previous superimposed SIF field in Figures 6.4.1(a) & (b), the definition of ΔK_{eff} and the K_{op} – as provided by the crack opening model f, due to secondary plasticity along the crack faces – can be further extended into Figure 6.5.3. However, discussion about Figure 6.4.1(i) is not pursued here presuming that no crack growth is permissible under compression-compression loads.

In Figure 6.5.3 (a) of tension-tension load, for a same value of R_{eff}, two conditions are equally applicable for mean stress and crack closure criteria:

(1) The conditions $\Delta K = \Delta K_{tot\text{-}MS} = \Delta K_{tot\text{-}CC}$ (see Equation (6.4.7a) and Figure 6.5.1(a)) holds at high stress ratio $R > 0.7$ at which crack closure effect disappears.

(2) For $0 < R < 0.7$ the presence of crack closure effect simply reduces Equation (6.4.7a) to $\Delta K_{eff} = \Delta K_{eff\text{-}MS} = \Delta K_{eff\text{-}CC}$.

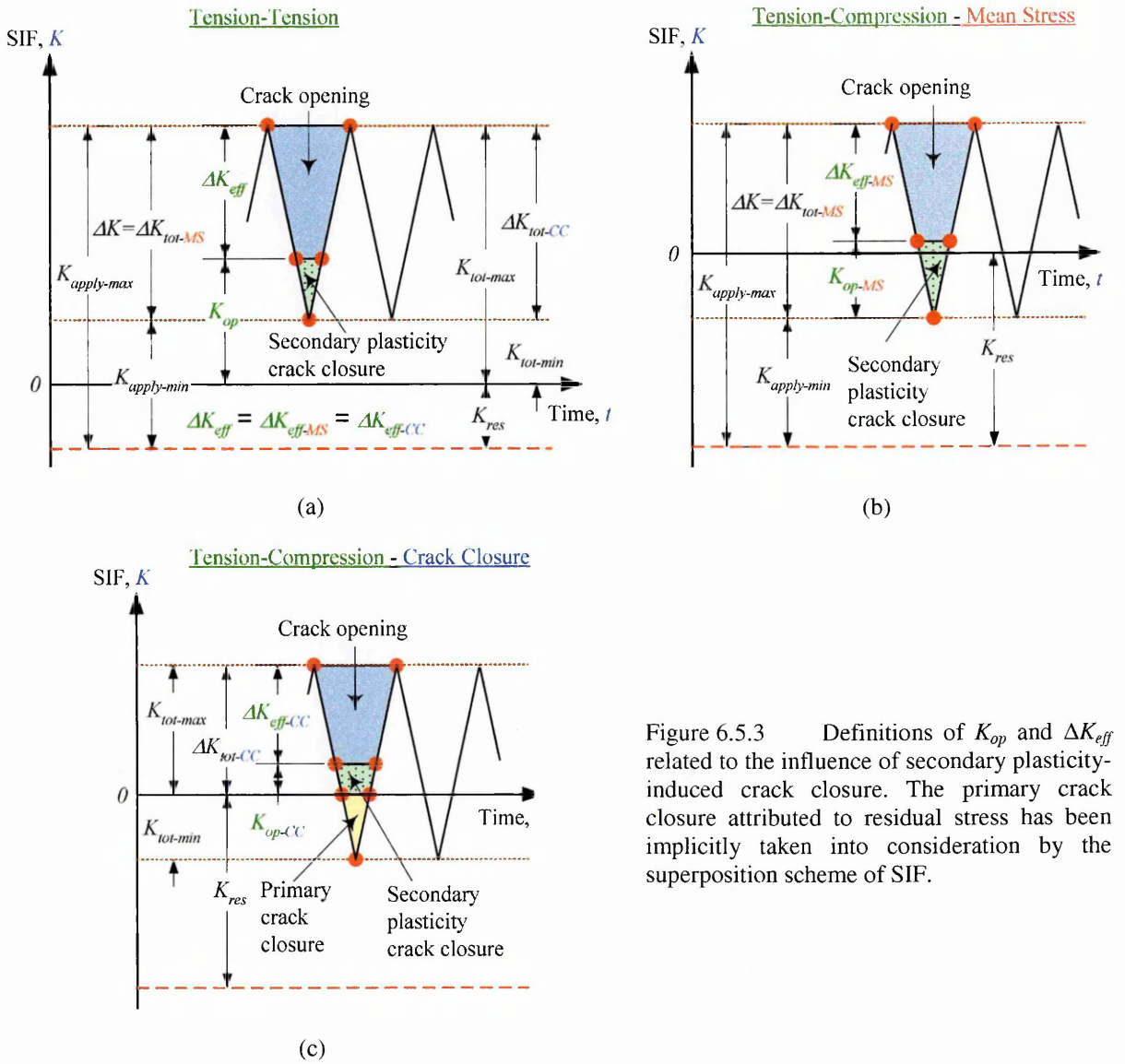

Figure 6.5.3 Definitions of K_{op} and ΔK_{eff} related to the influence of secondary plasticity-induced crack closure. The primary crack closure attributed to residual stress has been implicitly taken into consideration by the superposition scheme of SIF.

However, for tension-compression loading due to differences inherited in both mean stress and crack closure criteria (Figure 6.4.1(f) & (i)), the influence of secondary plasticity crack closure must be described separately in Figures 6.5.3(b) & (c). The mean stress approach (Figure 6.5.3(b)) permits negative or positive values of K_{op}; on the contrary, the crack closure counterpart (Figure 6.5.3(c)) allows only $K_{op} > 0$.

Referring to Figure 6.4.3, the crack opening stress ratio, f against the crack length, c, for the associated R_{eff} variation can be examined by employing relations (6.5.1 & 2) and Figure

6.5.1, and the overall trend is plotted in Figure 6.5.4. As can be observed, the calibrated crack opening ratio f ($=K_{op} / K_{max}$) for both the $R = 0.1$ of remote applied stress and $R = 0.0$ of crack closure criteria is higher than the f-values associated with the mean stress methodology ($R_{lo} = -0.3$ & -0.7). The R-ratio and consequently the f-value is not definable in Equations (6.5.1 & 2) for $R_{eff} < -2.0$ for the present material, as depicted in Figure 6.5.4.

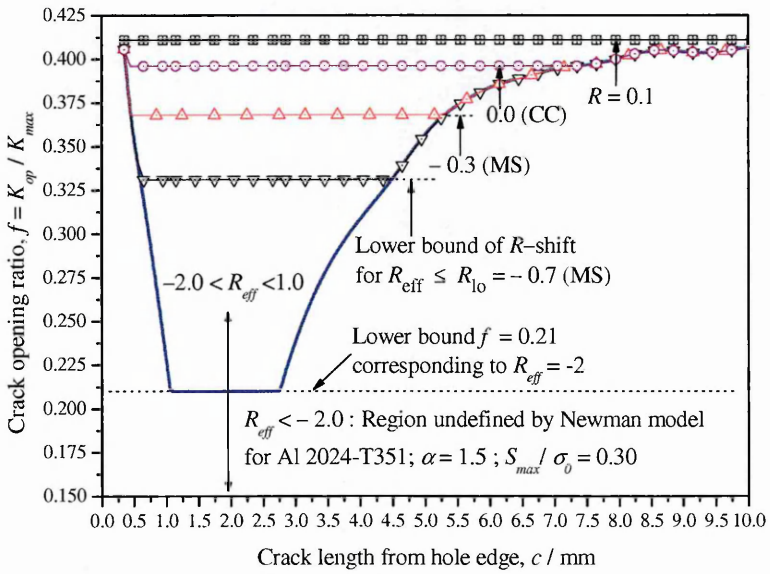

Figure 6.5.4 Newman crack tip opening stress f along prospective crack line, calculated for given R_{eff} variation as a function of crack length, c. CC = crack closure; MS = mean stress.

6.6 Conclusions

This chapter forms a first part of the experimental and theoretical investigation of fatigue crack growth from StressWave cold-worked holes, aimed to produce design data for reliable fatigue life prediction for damage tolerance analysis involving residual stress. Several conclusions may be drawn from this chapter, and are presented as follows:

(a) The knowledge of the residual stress field is an imperative pre-requisite to understand the fatigue crack behaviour required in damage tolerant analysis. The symmetric residual stress at SW hole is found to be useful for growing simple through-thickness crack from pre-cracking EDM notch. Consequently, much analysis complexities due to 2D crack shape problem encountered previously in split-sleeve mandrelized hole previously can be reduced to 1D for SW hole.

(b) To obtain accurate residual SIF for a single through-thickness crack emanating from a hole, we have developed an exact closed-form GF. A geometry correction was also incorporated to include the effect of plate finite width. In comparison, the generic point load SIF solution in AFGROW must be used with caution, especially for longer crack lengths. According to Figure 6.3.2, it is believed that the AFGROW generic model is not suitable for SW cold-worked holes because the actual beneficial effect of compressive residual stress (or SIF) can be overestimated at short crack length and underestimated at longer crack size. The notch introduced at the hole edge also causes a certain degree of SIF relaxation that must be taken into consideration.

(c) A systematic superposition framework of SIF that amalgamates the mean stress and crack closure methodologies, essential for defining and applying the ΔK and R_{eff} in a consistent manner for FCG analysis is proposed. We also introduce a schematic procedure of superposition as an effective means to elucidate the interaction of residual SIF with fatigue loading (see Figures 6.4.1 & 6.5.3). A complete summary of the mathematical treatments involved is also given in Table 6.4.1.

(d) The conditions of compound SIF resulting from applied remote loading and the local residual SIF may be categorized into tension-tension, tension-compression and compression-compression behaviours (Sections 6.4 & 6.5). The calculations based on the present theoretical framework agree with AFGROW computations very well (Figures 6.4.3 & 6.5.4).

(e) The secondary closure effect associated with crack extension-plasticity can be approximated by the Newman crack opening stress function. The amount of crack opening shows strong dependence on the effective stress ratio R_{eff}, crack tip constraint α and the ratio of maximum applied stress to flow stress S_{max}/σ_o. The Newman function covers only $-2 < R_{eff} < 1.0$ (Figure 6.5.1), whereas for the present case the calculated $R_{eff} < -2$ (Figure

6.4.3). In the tension-compression region, the crack opening values corresponding to crack closure criteria are always higher when compared with values of mean stress.

(f) The original mean stress method requires an extensive database of $da/dN = f(\Delta K, R_{eff})$ curves for covering the positive and negative range of R-ratios, which is not efficient and viable; however, this can be solved by the introduction of lower limit of R-shift, R_{lo}. In comparison, the crack closure approach requires only crack growth rate curves for $R \geq 0.0$.

6.7 References

1. StressWave, Technical Report AL-07, Fatigue Testing of 7050-T7451 Aluminum. March 1, 2002.
2. StressWave, Technical Report AL-02 Fatigue Testing of 2024 Low Load Transfer Aluminum Specimens. November 1, 2001.
3. Harter, J.A., AFGROW: Users Guide and Technical Manual. AFRL-VA-WP-TR-2004 (Version 4.0009e.12). 2004: Air Vehicles Directorate, 2790 D Street, Ste 504, Air Force Research Laboratory, WPAFB OH 45433-7542.
4. Lamb, G.J., Jr., A.F.G., and Easterbrook, E.T. Fatigue Performance of an Advanced Hole Cold Working Method. in 2001 USAF Aircraft Structural Integrity Program Conference. 2001. Williamsburg, VA.
5. Ball, D.L. and Lowry, D.R., Experimental investigation on the effects of cold expansion of fastener holes. Fatigue & Fracture of Engineering Materials & Structures, 1998. 21(1): p. 17-34.
6. Stefanescu, D., Measurement and prediction of fatigue crack growth from cold expanded holes Part 1: the effect of fatigue crack growth on cold expansion residual stresses. Journal of Strain Analysis for Engineering Design, 2004. 39(1): p. 25-38.
7. Tan, J.M.L., Fitzpatrick, M.E., and Edwards, L., Stress Intensity Factors for Through-Thickness Cracks in a Wide Plate Under Arbitrary Stress Field, to be submitted to Eng. Frac. Mech.
8. Murakami, Y., ed. Stress Intensity Factors Handbook. 1st ed. 1986, Pergamon.
9. Tada, H., Paris, P.C., and Irwin, G.R., eds. The Stress Analysis of Cracks Handbook. 3rd ed. 2000, American Society of Mechanical Engineers.
10. Schijve, J., Stress Intensity Factors of Hole Edge Cracks-Comparison between One Crack and Two Symmetric Cracks. Int. J. Fracture, 1983. 23: p. R111-R115.

11. Shivakumar, V. and Forman, R.G., Green's Function for a Crack Emanating From a Circular Hole in an Infinite Sheet. International Journal of Fracture, 1980. 16(4): p. 305-316.
12. Wu, X.R. and Carlsson, A.J., Weight Functions and Stress Intensity Factor Solutions. 1991: Pergamon Press, Oxford.
13. Hartranft, R.J. and Sih, G.C., Alternating method applied to edge and surface crack problems, in Method of Analysis and Solutions to Crack Problems, G.C. Sih, Editor. 1973, Noordhoff International Publishing, The Netherlands. p. 177–238.
14. Sih, G.C., ed. Handbook of stress-intensity factors: Stress-intensity factor solutions and formulas for reference. 1973, Institute of Fracture and Solid Mechanics, Lehigh University: Bethlehem, PA.
15. Wawrzynek, P. and Ingraffea, A., FRANC2D: A two-dimensional crack propagation simulator, Version 3.1 User's Guide. 2004.
16. Parker, A.P., Stress intensity factor, crack profiles and fatigue crack growth rates in residual stress fields, in ASTM Special Technical Publication 776: Residual Stress Effects in Fatigue, J.F. Throop and H.S. Reemsnyder, Editors. 1982, American Society for Testing and Materials: Philadelphia, PA. p. 13-31.
17. Beghini, M. and Bertini, L., Fatigue crack propagation through residual stress fields with closure phenomena. Engineering Fracture Mechanics, 1990. 36(3): p. 379-387.
18. Beghini, M. and Bertini, L., Effective stress intensity factor and contact stress for a partially closed Griffith crack in bending. Engineering Fracture Mechanics, 1996. 54(5): p. 667-678.
19. Montenegro, H.L., Cisilino, A., and Otegui, J.L., Application of a weight function based method to assess partially closed cracks. Engineering Fracture Mechanics, 1996. 54(5): p. 679-691.
20. Dann, J.A., Daymond, M.R., Edwards, L., James, J.A., and Santisteban, J.R., A comparison between Engin and Engin-X, a new diffractometer optimized for stress measurement. Physica B: Condensed Matter, 2004. 350(1-3, Supplement 1): p. E511-E514.
21. Newman, J.C.J., FASTRAN-II—A fatigue crack growth structural analysis program, NASA Technical MemorandumTM 104159. 1992, Langley Research Centre: Hampton, Virginia. p. 100.
22. Wang, G.S., A Strip Yield Analysis of Fatigue Crack Growth in the Residual Stress Field. International Journal of Fracture, 1999. 96(3): p. 247-277.
23. Köning, A.U.D., A simple crack closure model for prediction of fatigue crack growth rates under variable-amplitude loading, in Fracture mechanics, ASTM STP 743, R.

Roberts, Editor. 1981, American Society for Testing and Materials: Philadelphia. p. 63–85.

24. Stacey, A. and Webster, G.A., Influence of residual stress on fatigue crack growth in thick-walled cylinder, in ASTM Special Technical Publication 1004: Analytical and Experimental Methods for Residual Stress Effects in Fatigue, R.L. Champoux and J.A. Kapp, Editors. 1988, American Society for Testing and Materials: Philadelphia, PA. p. 107-121.
25. Impellizzeri, L.F. and Rich, D.L., Spectrum fatigue crack growth in lugs, in ASTM Special Technical Publication 595: Fatigue Crack Growth Under Spectrum Loads, R.P. Wei and R.I. Stephen, Editors. 1976, American Society for Testing and Materials: Philadelphia, PA. p. 320-336.
26. Cathey, W.H. and Grandt, A.F.J., Fracture mechanics consideration of residual stresses introduced by coldworking fastener holes. Journal of Engineering Materials and Technology, Transactions of the ASME, 1980. 102(1): p. 85-91.
27. Liu, A.F., Effect of residual stresses on crack growth from a hole. AIAA Journal, 1984. 22(12): p. 1784-1785.
28. Grandt, A.F.J., Stress intensity factors for some through-cracked fastener holes. Int. J. Fracture, 1975. 11(2): p. 283-294.
29. Forman, R.G., Shivakumar, V., Mettu, S., and Newman, J.C., NASGRO Version 3.00 Reference Manual : Fatigue crack growth computer program, NASA Document JSC-22267B. December 2000, Houston, TX: NASA Johnson Space Centre.
30. Chandawanich, N. and Sharpe, J., William N., An experimental study of fatigue crack initiation and growth from coldworked holes. Engineering Fracture Mechanics, 1979. 11(4): p. 609-620.
31. Clark, G., Fatigue crack growth through residual stress fields--theoretical and experimental studies on thick-walled cylinders. Theoretical and Applied Fracture Mechanics, 1984. 2(2): p. 111-125.
32. Grandt, A.F.J. and Hinnerichs, T.D. Stress intensity factor measureaments for flawed fastener holes. in Proceedings of the Army Symposium on Solid Mechanics AMMRC MC 74-8: The Role of Mechanics in Design – Structural Joints. 1974: Army Materials and Mechanics Research Center, Watertown, Massachusetts.
33. Josefson, B.L., Karlsson, S., and Ogeman, R., Influence of residual stresses on fatigue crack growth at stress-coined holes. Engineering Fracture Mechanics, 1994. 47(1): p. 13-27.

34. Toparli, M., Ozel, A., and Aksoy, T., Effect of the residual stresses on the fatigue crack growth behavior at fastener holes. Materials Science and Engineering A, 1997. 225(1-2): p. 196-203.
35. Hsu, T.M., McGee, W.M., and Aberson, J.A., Extended study of flaw growth at fastener holes, AFFDL-TR-82-3073. 1978, Air Force Flight Dynamics Laboratory (AFFDL/FBE), Wright-Patterson AFB: Ohio 45433.
36. Chang, J.B., Prediction of fatigue crack growth at cold-worked fastener holes. J Aircr, 1977. 14(9): p. 903-908.
37. Brot, A. and Nathan, A. Increasing fatigue and crack growth lives of short-edge-margin holes. in Thirteenth ICAF (International Committee on Aeronautical Fatigue) Symposium-Durability and Damage Tolerance in Aircraft Design. 1985. Pisa, Italy: EMAS Publishing, England.
38. Cook, R., Rooke, D.P., Smith, A., and Bowles, R., Residual stress fields at notches: effect on fatigue crack growth. In: RAE Technical Report 85049. 1985, Royal Aircraft Establishment: Farnborough, UK.
39. Leitão, V.M.A., Aliabadi, M.H., Rooke, D.P., and Cook, R. Residual stress fields effect on fatigue crack growth. in Boundary Elements XIV. 1992. Sevilla, Espanha: Computational Mechanics Publications, Southampton.
40. Wieland, D.H., Cutshall, J.T., Burnside, O.H., and Cardinal, J.W. Analysis of cold worked holes for structural life extension. in FAA/NASA International Symposium on Advanced Structural Integrity Methods for Airframe Durability and Damage Tolerance, Conference Publication 3274. 1994: NASA.
41. Buxbaum, O. and Huth, H., Expansion of cracked fastener holes as a measure for extension of lifetime to repair. Engineering Fracture Mechanics, 1987. 28(5-6): p. 689-698.
42. Ball, D.L. and Doerfler, M.T. Experimental and analytical studies of residual stress field evolution and fatigue crack growth at cold expanded holes. in 2003 USAF Aircraft Structural Integrity Program (ASIP) Conference. 2003. Savannah, Georgia.
43. Armen, H., Levy, A., and Eidinoff, H.L., Elastic-plastic behavior of coldworked holes. AIAA Journal of Aircraft, 1984. 21(3): p. 193-201.
44. Vasudevan, A.K. and Sadananda, K., Analysis of fatigue crack growth under compression-compression loading. International Journal of Fatigue, 2001. 23(Supplement 1): p. 365-374.
45. Stefanescu, D., Dutta, M., Wang, D.Q., Edwards, L., and Fitzpatrick, M.E., The effect of high compressive loading on residual stresses and fatigue crack growth at

cold expanded holes. Journal of Strain Analysis for Engineering & Design, 2003. 38: p. 219-225.

46. Nadri, B., Fitzpatrick, M.E., Lodini, A., and Edwards, L., Measurement of residual stresses following overloading of cold expanded holes using the X-ray diffraction technique. J. Neutron Research, 2004. 11: p. 219-225.
47. Elber, W., The significance of fatigue crack closure, in Damage Tolerance in Aircraft Structures, ASTM STP 486. 1971, American Society for Testing and Materials: Philadelphia. p. 230-242.
48. Elber, W., Fatigue crack closure under cyclic tension. Engineering Fracture Mechanics, 1970. 2(1): p. 37-45.
49. Lam, Y.C. and Lian, K.S., The effect of residual stress and its redistribution of fatigue crack growth. Theoretical and Applied Fracture Mechanics, 1989. 12(1): p. 59-66.
50. Newman, J.C.J., A crack opening stress equation for fatigue crack growth. International Journal of Fracture, 1984. 24(3): p. R131-R135.
51. Dugdale, D., S., Yielding of steel sheets containing slits. Journal of the Mechanics and Physics of Solids, 1960. 8: p. 100-104.
52. Newman, J.C.J., ed. A crack-closure model for predicting fatigue crack growth under aircraft spectrum loading. Methods and models for predicting fatigue crack growth under random loading, ASTM STP 748. 1981, American Society for Testing and Materials: Philadelphia. 53–84.
53. Newman, J.R., Prediction fatigue crack growth under variable-amplitude and spectrum loading using a closure model, in Design of fatigue and fracture resistant structure, ASTM STP 761, P.R. Abelkis and C.M. Hudson, Editors. 1982, American Society for Testing and Materials: Philadelphia. p. 255–277.
54. Forman, R.G., Shivakumar, V., Mettu, S., and Newman, J.C., Reference Manual: NASGRO version 3.0 Fracture mechanics and fatigue crack growth analysis software, Document JSC-22267B. 2000, Houston, TX: NASA Johnson Space Centre.
55. Silva, F.S., Crack closure inadequacy at negative stress ratios. International Journal of Fatigue, 2004. 26(3): p. 241-252.
56. Silva, F.S., The importance of compressive stresses on fatigue crack propagation rate. International Journal of Fatigue, 2005. 27(10-12): p. 1441-1452.
57. Yu, M.T., Topper, T.H., DuQuesnay, D.L., and Pompetzki, M., Fatigue crack growth threshold and crack opening of a mild steel. Journal of Testing and Evaluation, 1986. 14(3).

58. Vasudevan, A.K. and Sadananda, K., Application of unified fatigue damage approach to compression-tension region. International Journal of Fatigue, 1999. 21(Supplement 1): p. 263-273.
59. Vasudevan, A.K., Sadananda, K., and Glinka, G., Critical parameters for fatigue damage. International Journal of Fatigue, 2001. 23(Supplement 1): p. 39-53.

Appendix 6–A

Note: The original data were computed to the accuracy of 15 decimal places. However, in the following tables only precisions up to 6 decimal places are presented. These discrete data are deemed sufficiently accurate for most engineering purposes. Tabulated SIF magnification factors: range of crack, 0 < c/R<5 and power of polynomial regression, n = 0 to 10.

c/R	Magnification Factor, $H_n(x/R) = K_n/\sigma_n(x/R)\sqrt{\pi c}$					
	Degree of polynomial expansion, n					
	0	**1**	**2**	**3**	**4**	**5**
0.0	0.000000E+00	0.000000E+00	0.000000E+00	0.000000E+00	0.000000E+00	0.000000E+00
0.1	8.183099E-01	5.683099E-02	4.622066E-03	3.997066E-04	3.572653E-05	3.260153E-06
0.2	8.183099E-01	1.136620E-01	1.848826E-02	3.197653E-03	5.716244E-04	1.043249E-04
0.3	8.183099E-01	1.704930E-01	4.159859E-02	1.079208E-02	2.893849E-03	7.922171E-04
0.4	8.183099E-01	2.273240E-01	7.395305E-02	2.558122E-02	9.145991E-03	3.338396E-03
0.5	8.183099E-01	2.841549E-01	1.155516E-01	4.996332E-02	2.232908E-02	1.018798E-02
0.6	8.183099E-01	3.409859E-01	1.663944E-01	8.633662E-02	4.630158E-02	2.535095E-02
0.7	8.183099E-01	3.978169E-01	2.264812E-01	1.370994E-01	8.577939E-02	5.479339E-02
0.8	8.183099E-01	4.546479E-01	2.958122E-01	2.046498E-01	1.463359E-01	1.068287E-01
0.9	8.183099E-01	5.114789E-01	3.743873E-01	2.913861E-01	2.344017E-01	1.925088E-01
1.0	8.183099E-01	5.683099E-01	4.622066E-01	3.997066E-01	3.572653E-01	3.260153E-01
1.1	8.183099E-01	6.251409E-01	5.592700E-01	5.320095E-01	5.230721E-01	5.250509E-01
1.2	8.183099E-01	6.819719E-01	6.655775E-01	6.906930E-01	7.408253E-01	8.112303E-01
1.3	8.183099E-01	7.388029E-01	7.811291E-01	8.781554E-01	1.020385E+00	1.210472E+00
1.4	8.183099E-01	7.956338E-01	9.059249E-01	1.096795E+00	1.372470E+00	1.753388E+00
1.5	8.183099E-01	8.524648E-01	1.039965E+00	1.349010E+00	1.808655E+00	2.475678E+00
1.6	8.183099E-01	9.092958E-01	1.183249E+00	1.637198E+00	2.341374E+00	3.418518E+00
1.7	8.183099E-01	9.661268E-01	1.335777E+00	1.963758E+00	2.983915E+00	4.628951E+00
1.8	8.183099E-01	1.022958E+00	1.497549E+00	2.331089E+00	3.750428E+00	6.160280E+00
1.9	8.183099E-01	1.079789E+00	1.668566E+00	2.741588E+00	4.655917E+00	8.072461E+00
2.0	8.183099E-01	1.136620E+00	1.848826E+00	3.197653E+00	5.716244E+00	1.043249E+01
2.5	8.183099E-01	1.420775E+00	2.888791E+00	6.245415E+00	1.395567E+01	3.183743E+01
3.0	8.183099E-01	1.704930E+00	4.159859E+00	1.079208E+01	2.893849E+01	7.922171E+01
3.5	8.183099E-01	1.989085E+00	5.662031E+00	1.713742E+01	5.361212E+01	1.712293E+02
4.0	8.183099E-01	2.273240E+00	7.395305E+00	2.558122E+01	9.145991E+01	3.338396E+02
4.5	8.183099E-01	2.557394E+00	9.359683E+00	3.642326E+01	1.465011E+02	6.015899E+02
5.0	8.183099E-01	2.841549E+00	1.155516E+01	4.996332E+01	2.232908E+02	1.018798E+03

Table 6–A1 Magnification factors for kernel Green's function with polynomial type crack face traction acting on a single radial crack (N = 1).

c/R	Magnification Factor, $H_n(x/R) = K_n/\sigma_n(x/R)\sqrt{\pi c}$				
	Degree of polynomial expansion, n				
	6	**7**	**8**	**9**	**10**
0.0	0.000000E+00	0.000000E+00	0.000000E+00	0.000000E+00	0.000000E+00
0.1	3.017631E-07	2.822318E-08	2.660637E-09	2.523918E-10	2.406332E-11
0.2	1.931284E-05	3.612568E-06	6.811231E-07	1.292246E-07	2.464084E-08
0.3	2.199853E-04	6.172410E-05	1.745644E-05	4.967829E-06	1.420915E-06
0.4	1.236022E-03	4.624086E-04	1.743675E-04	6.616301E-05	2.523222E-05
0.5	4.715048E-03	2.204936E-03	1.039311E-03	4.929528E-04	2.349934E-04
0.6	1.407906E-02	7.900685E-03	4.468849E-03	2.543528E-03	1.455017E-03
0.7	3.550213E-02	2.324301E-02	1.533804E-02	1.018492E-02	6.797293E-03
0.8	7.910538E-02	5.918831E-02	4.463808E-02	3.387546E-02	2.583779E-02
0.9	1.603693E-01	1.349906E-01	1.145317E-01	9.778177E-02	8.390361E-02
1.0	3.017631E-01	2.822318E-01	2.660637E-01	2.523918E-01	2.406332E-01
1.1	5.345917E-01	5.499900E-01	5.703312E-01	5.951268E-01	6.241406E-01
1.2	9.010598E-01	1.011288E+00	1.144025E+00	1.302286E+00	1.489937E+00
1.3	1.456553E+00	1.770963E+00	2.170363E+00	2.676489E+00	3.317333E+00
1.4	2.272136E+00	2.975105E+00	3.926539E+00	5.214680E+00	6.960428E+00
1.5	3.437270E+00	4.822196E+00	6.818922E+00	9.702790E+00	1.387612E+01
1.6	5.062745E+00	7.576103E+00	1.142735E+01	1.734424E+01	2.645790E+01
1.7	7.283827E+00	1.158106E+01	1.855996E+01	2.993061E+01	4.851151E+01
1.8	1.026363E+01	1.727880E+01	2.932012E+01	5.006427E+01	8.591730E+01
1.9	1.419671E+01	2.522791E+01	4.518710E+01	8.144374E+01	1.475338E+02
2.0	1.931284E+01	3.612568E+01	6.811231E+01	1.292246E+02	2.464084E+02
2.5	7.367263E+01	1.722606E+02	4.059810E+02	9.627985E+02	2.294857E+03
3.0	2.199853E+02	6.172410E+02	1.745644E+03	4.967829E+03	1.420915E+04
3.5	5.547207E+02	1.815860E+03	5.991423E+03	1.989242E+04	6.637981E+04
4.0	1.236022E+03	4.624086E+03	1.743675E+04	6.616301E+04	2.523222E+05
4.5	2.505770E+03	1.054614E+04	4.473895E+04	1.909800E+05	8.193712E+05
5.0	4.715048E+03	2.204936E+04	1.039311E+05	4.929528E+05	2.349934E+06

Table 6–A2 Magnification factors for kernel Green's function with polynomial type crack face traction acting on a single radial crack (N = 1).

CHAPTER 7: ASSESSMENT OF FATIGUE CRACK GROWTH BEHAVIOUR IN STRESSWAVE COLD-WORKED HOLES: FATIGUE TESTING & LIFE PREDICTION

This chapter describes the experiment and prediction of fatigue crack growth in StressWave cold-worked holes. The *S–N* curve indicated that the life enhancement in StressWave holes consistently outperformed those observed in split-sleeve holes. Fatigue testing also verified uniform crack growth in StressWave specimens because of the highly symmetric residual stress field induced around the hole. AFGROW predictions, using the mean-stress and crack-closure criteria incorporating the residual stress effect, produced encouraging agreement with the experimental crack data. Further study indicated that the prediction could be optimised by systematic calibration of parameters. It is also shown that an appropriate stress intensity factor model is critically for reliable predictions. Accurate prognosis of fatigue crack growth in StressWave holes is a complicated task, and the future efforts necessary to improve the prediction are discussed.

7.1 Introduction

This chapter report a multifaceted initiative carried out in response to the future demands of damage tolerance work for structures containing StressWave (SW) cold-worked holes. This consists of studies of the fatigue performance of SW hole, fatigue crack growth experiment and prediction of fatigue life.

Based on the concepts of linear elastic fracture mechanics (LEFM) and superposition principle discussed earlier in Chapter 6, the mean-stress (MS) and crack-closure (CC) criteria was subsequently incorporated in the present predictive work using AFGROW. Detailed parametric and modelling study in SW holes was also carried out to illustrate how predictive reliability can be maximised in AFGROW. Though the research programme

reported here is devoted mainly to furnish the information gap on the SW method, the information is equally relevant to other hole cold-working techniques [1-4].

7.2 Fatigue Life improvement in StressWave Cold-Worked Holes

The multitude advantages of cost-efficiency and production efficiency associated with SW process [5] has been discussed in Chapter 1. However, the most vital justification of the SW technique in airframe production ultimately lies on the fatigue life enhancement capability of the treated holes when exposed to deleterious fatigue conditions [1, 6].

7.2.1 Stress-life (S–N) curves of plain and cold-worked holes

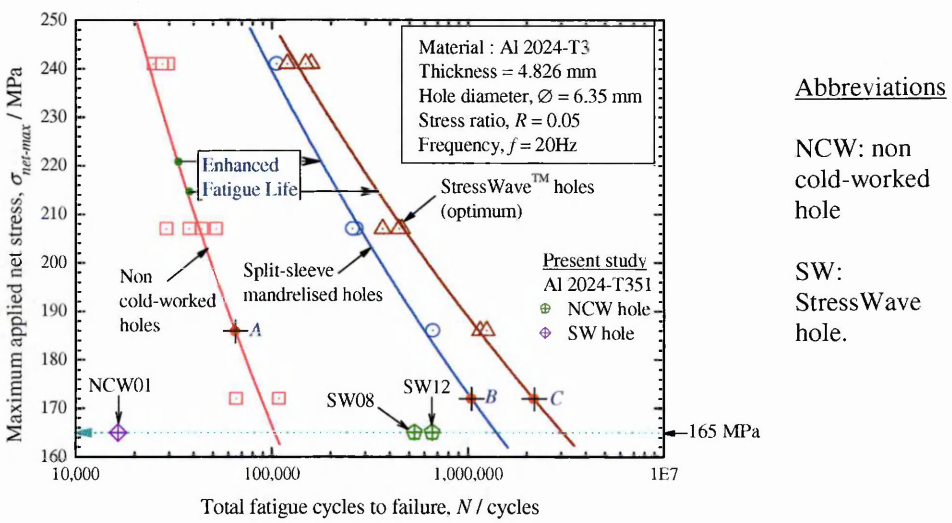

Figure 7.1.1 Comparison of fatigue endurance of specimens containing plain holes, split-sleeve mandrelised holes and StressWave cold-worked holes, adapted from [5]. Plate width, W = 25.4mm and length, L = 152.4mm. Uni-axial fatigue loading applied in the sheet rolling direction. Point A is calculated by interpolation whereas points B and C are extrapolated from the corresponding curves. From present study, the crack sizes of specimens NCW01, SW08 and SW12 are 10.6 mm, 3.2 mm and 6.65 mm, respectively.

Previously, fatigue data describing S–N curves of SW, SSM and non-treated holes in rolled plates have been tested for various materials, e.g. aerospace aluminium alloys 2024–T3/T351 [7, 8], 6061-T6 [9] and 7050–T7451 [10], AISI 4340 steel [11] and 6Al-4V titanium [12]. Regardless of different test conditions, e.g. materials and specimen type, loading level, cold-working methods, both the SW and SSM specimens showed excellent fatigue improvement as contrast to the baseline data (i.e. plain hole). Notably from the

aforementioned studies [7-12], the life extension achieved in pre-stressed holes can be 3 ~ 30 times higher than the those recorded for plain holes.

In order to assess the fatigue resistance between the SSM and SW techniques in a greater detail, a comprehensive fatigue testing by Easterbrook *et al.* [5] is employed. Part of the data is reproduced in Figure 7.1.1 for discussion. Using a central open-hole configuration, Al 2024–T3 plate specimens were fatigued till failure under several load levels. Figure 7.1.1 shows that the SW technique produces comparable or even superior fatigue durability than SSM method.

The SW fatigue result produced in this work, i.e. specimens NCW01, SW08 and SW12, which experiment is explained later in Section 7.3, is superimposed in Figure 7.1.1 for comparison. The data was generated using a constant amplitude loading of maximum net stress, $\sigma_{max-net}$ = 165 MPa. Specimens SW08 and SW12 show excellent life improvement when compared to the baseline curve, though decreased fatigue performance with respect to the other two fatigue curves. Besides the differences in specimen dimensions and heat-treatment, such decline in fatigue endurance is believed largely due to the use of pre-cracking EDM notch in present samples (Figure 6.2.1). Also, the present data correspond only to the partial life of specimen grown to specific crack length without being fractured (Figure 7.1.1).

7.2.2 Life improvement of different hole cold-working techniques

To further explore Figure 7.1.1, the life improvement factor (LIF) is used to assess quantitatively the merit of each cold-working technique. The LIF is simply defined as the ratio of the total fatigue life-to-failure, N /cycles, of the treated holes to that of the plain holes, i.e. LIF = $N_{SW\ or\ SSM\ hole}$ / $N_{plain\ hole}$. Similarly, the relative performance of the two different cold-working techniques is given by $N_{SW\ hole}$ / $N_{SSM\ hole}$. At any given stress level,

the averaged life cycles from individual scattered data is used for analysis. For load levels in which no fatigue data were directly available, interpolated (point *A*) or extrapolated (points *B*, *C*) values were made from the regression curves in Figure 7.1.1.

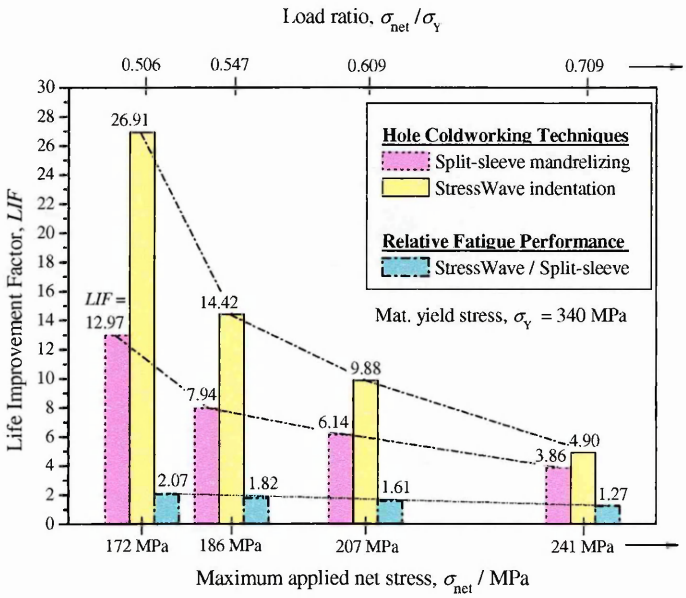

Figure 7.1.2 Comparison in the cold-work life improvement factor (LIF) between SSM holes and StressWave holes with respect to the fatigue life of specimens containing plain holes at four maximum net stress levels of 172, 186, 207 and 241 MPa. Relative performance between SSM and SW is also included.

The LIF chart as a function of maximum applied net-section stress, σ_{net} is given in Figure 7.1.2. Consistent with Figure 7.1.1, it is evident that SW surpassed the performance of its SSM counterpart at all the load levels tested. Also, the degree of effectiveness in cold-worked holes against fatigue diminishes gradually with increasing levels of cyclic stress, and vice versa. A similar trend was also noted for Al 7050–T7451 also involving the study of SW and SSM cold-working methods [10].

7.3 Fatigue Crack Growth Experiments & Results

The *S–N* curve approach in Figure 7.1.1 does not allow us to discriminate explicitly distinct fatigue stages of crack initiation and crack growth in cold-worked holes. However, in the damage tolerance philosophy, allowable crack growth from the assumed initial flaws in cold-worked holes must be analysed for their structural integrity. This requires that the prediction of FCG data be validated experimentally.

In the following, the experimental work related to the fatigue crack growth (FCG) measurement of non-cold worked and SW holes is described. The laboratory crack growth data will be used to validate the FCG predictions later.

7.3.1 Preparation of fatigue specimens and testing

As discussed earlier, the geometry of the Al2024-T351 specimens is depicted in Figure 6.2.1 in Chapter 6. Three fatigue specimens were used for the FCG study: one baseline (i.e. untreated, specimen NCW01) and the remaining two were cold-worked by the SW process (specimens SW08 and SW12), as explained in Chapters 3 & 4.

In all specimens, a crack initiator was introduced at one side of the hole edge perpendicular to the loading axis, using a FANUC ROBOCUT α–O*i*B CNC (computer numerical control) wire electro-discharge machine (EDM). The EDM notch is aimed to produce a known (controlled) site for the growth of a through-thickness crack which could be monitored on both faces concurrently. The notch also allows the crack growth to bypass the high number of fatigue cycles involves in the initiation phase. The dimensions of the through-thickness notch, as measured optically, were shown in Figure 6.2.1 (b) of Chapter 6. Minimum material removal was accomplished using Ø 0.10 mm copper cutting wire.

All the fatigue testing was carried out using an INSTRON servo-hydraulic machine. The test conditions were: room temperature and humidity; constant amplitude of sinusoidal loading; operating frequency f = 4 to 12 Hz; remote stress ratio R = 0.1 with remotely applied peak stress σ_{max} = 138 MPa. The equivalent maximum net-section stress $\sigma_{net\ max}$ = 165 MPa is somewhat lower than the lowest stress level 172 MPa used in Figure 7.1.1. The values of σ_{max} and $\sigma_{net\ max}$ was calibrated from stress concentration factor [13] and validated from a two-dimensional plane-stress finite element analysis [14] to ensure that the locally induced stress level at the hole edge is nominally elastic, i.e. less than the material yield

stress, σ_Y. The assumption made is that the elastic loading will preserve the original residual stress field (Figure 6.2.2) without substantial gross plasticity that causes residual stress redistribution. In turn, the original K_{res} calculated in Figure 6.3.2 remains valid in the framework of LEFM. The crack lengths on both the front and back faces of the specimens were visually monitored using travelling microscopes with eyepieces of 20× magnifications.

7.3.2 Results of fatigue crack growth data

The fatigue crack growth data of plain and SW holes is presented as crack length versus number of fatigue cycles elapsed, i.e. c versus. N curves in Figure 7.3.1. The SW technique enhances the fatigue life dramatically. To illustrate the life improvement gained, for a crack grown to a size c = 6.0 mm in Figure 7.3.1, the corresponding improvement of specimen SW12 is about 57 times higher than that of the baseline specimen.

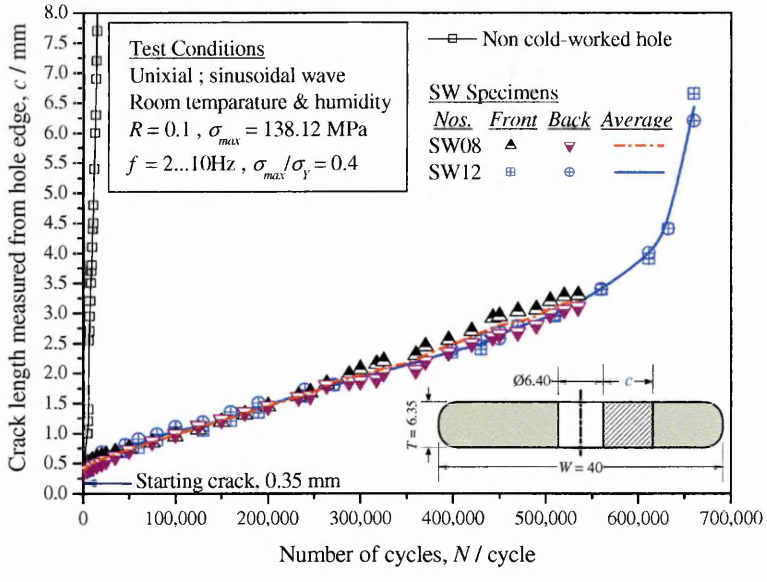

Figure 7.3.1 Comparison of fatigue crack growth for plain holes and StressWave treated holes.

Note also that the crack growth on the front and back faces of the specimen are uniform and repeatable. Though the analysis demonstrated using a through-thickness crack in a hole is somewhat simplified, the behaviour of crack symmetry should significantly increase the fatigue life predictability of SW holes when compared to other cold working techniques. This enables us to explore the MS and CC criteria with confidence without the

complications of non-uniform residual stress field and bulbous corner crack shape frequently encountered in SSM holes [15, 16].

7.4 Fatigue Crack Growth Life Prediction in StressWave Holes

The residual stress data in Figure 6.3.2 can be used to examine the analytical framework proposed in Chapter 6 for the FCG work presented in this chapter. Previous FCG analysis using AFGROW for cold-worked holes has shown mixed success in correlating the laboratory data with prediction [17-20]. In practice, the worst possible case is that AFGROW simulated the crack to be dormant [21] while the physical testing shows otherwise, and such non-conservative estimations are unacceptable.

Further study is indispensable if AFGROW is to be used confidently in these situations. As is shown later, the basic ideas of the MS and CC criteria can provide further clarification in how AFGROW works with K_{res}. Coupled with other facilities available in AFGROW, it will be demonstrated for certain circumstances suitable SIF model, parametric adjustment and new material data are perhaps needed to achieve good agreement with experiment data.

7.4.1 Fatigue crack growth rate model

Several FCG rate models that relate dc/dN–ΔK relation, e.g. Forman Equation, Walker Equation, Tabular lookup, Harter-T Method and NASGRO Equation, have been implemented in AFGROW to calculate crack growth per applied cyclic loading. The effects of R-ratio, crack opening, crack tip constraint factor, threshold region, limiting stress-ratio can be integrated depending on the complexity of these models. In AFGROW, we used the NASGRO Version–3.0 FCG model [22] due to its robustness to capture data trend in all three regions-I, II & III of dc/dN–ΔK curve:

$$\frac{dc}{dN} = C\left[\left(\frac{1-f}{1-R}\right)\Delta K\right]^n \frac{\left(1-\frac{\Delta K_{th}}{\Delta K}\right)^p}{\left(1-\frac{K_{\max}}{K_c}\right)^q} \tag{7.4.1}$$

where N is the number of fatigue cycles, c is the crack length, R is the stress ratio, ΔK is the stress intensity factor range. C, n, p, and q are empirically derived constants through best-fit of laboratory dc/dN–ΔK data.

The notation f is the Newman stress opening function for plasticity-induced crack closure [23] discussed previously in Sections 6.5.1, 6.5.2 & 6.5.3, Chapter 6. In NASGRO Equation (7.4.1), the Newman function, f, is also used to treat the threshold *SIF* range, ΔK_{th} for small crack. The ΔK_{th} relation is empirically defined by

$$\Delta K_{th} = \Delta K_0 \left(\frac{a}{a+a_0}\right)^{0.5} \Bigg/ \left(\frac{1-f}{(1-A_0)(1-R)}\right)^{1+C_{th}R} \tag{7.4.2}$$

ΔK_0 is the threshold *SIF* range at $R = 0.0$; C_{th} is an empirical constant, and a_0 is an intrinsic crack length (fixed at 0.0381 mm). These parametric values are readily provided in the NASGRO–3.0 material database for various types of materials and testing conditions [21]. For completeness, the input parameters for Al 2024-T351 according to AFGROW [21] are tabulated in Table 7.4.1. R_{hi} and R_{lo} are respectively the upper and lower bounds of baseline dc/dN –ΔK curves used to calculate the fatigue crack growth life curve, a versus N subjected to the influence of variable R-ratio loading.

Database ID–Material name: 1000-9000 series aluminium, 2024-T351 Al, [Plt & sht; L-T]

Materials Properties

Coefficient of thermal expansion, $\alpha_T = 2.32\times10^{-5}$ (m/m)/ °C

Young's Modulus, $E = 73084.4$ MPa

Poission's ratio, $\nu = 0.33$ [dimensionless]

Yield Strength $\sigma_Y = 372.317$ MPa

Plane strain fracture toughness $K_{IC} = 37.361$ MPa·m$^{1/2}$

Plane stress fracture toughness $K_C = 74.722$ MPa·m$^{1/2}$

Effective fracture toughness for part-through-the-thickness cracks, $K_C = 52.744$ MPa·m$^{1/2}$

Fitting parameter in ($K_{critical}$ / K_{IC}) versus thickness equation, $A_k = 1$ [dimensionless]

Fitting parameter in ($K_{critical}$ / K_{IC}) versus thickness equation, $B_k = 1$ [dimensionless]

NASGRO Equation 3.0 Constants

Paris crack growth rate constant, $C = 1.7073\times10^{-10}$ (m/cycle)·(MPa·m$^{1/2}$)$^{-n}$

Paris exponent in NASGRO Equation, $n = 3.353$ [dimensionless]

Exponent in NASGRO Equation, $p = 0.5$ [dimensionless]

Exponent in NASGRO Equation, $q = 1.0$ [dimensionless]

Threshold stress intensity factor range at $R = 0.0$, $\Delta K_0 = 2.857$ MPa·m$^{1/2}$

Threshold coefficient, $C_{th} = 1.5$ [dimensionless]

Plane stress /strain constraint factor, $\alpha = 1.5$ [dimensionless]

Ratio of maximum applied stress to the material flow stress, $S_{max} / \sigma_o = 0.3$ [dimensionless]

Upper limit of R-shift, R_{hi} (Max. 1.0) = 0.7 [dimensionless]

Lower limit on R-shift, R_{lo} ($-2.0 = < R_{lo} =< 0$) = –0.3 [dimensionless]

Table 7.4.1 The AFGROW input parameters comprise of material properties and NASGRO constants for Al 2024-T351; all quantities are given in metric units: [m, MN, MPa, °C] [21]. The calculations of life were based on all of the above default values, unless stated otherwise.

7.4.2 Crack model, fatigue spectrum and residual stress data

The other AFGROW inputs for FCG simulation matching the experiment conditions in Section 7.3 are described here:

(1) To simulate the crack problem in Figure 7.3.1, the default AFGROW standard SIF solution for a single through-thickness crack emanating from a central hole in a finite-width plate is used. The starting crack length is assigned equivalent to the EDM notch size, i.e. 0.350 mm (Figure 7.2.1, Chapter 6).

(2) Since the fatigue stressing is simply constant amplitude loading (σ_{max} = 138.12 MPa, R = 0.10), no load-interaction model was considered necessary to account for crack retardation effect related to tensile or compressive overloading.

(3) The residual stress field in SW hole was introduced in AFGROW using the K_{res} data calculated in Figure 6.3.2 with the effect of EDM cutting. Two sets of K_{res} data associated with the GF model (Sections 6.3.1–6.3.3), and AFGROW generic SIF solution (Section 6.3.4), were considered. For FCG analysis, AFGROW employs the elastic superposition principle in which the interaction mechanism between K_{res} and K_{apply} in cracked holes has been explored extensively in Chapter 6.

(4) Parametric adjustment of several elements in NASGRO–3.0 Equation (7.4.1) and Table 7.4.1, e.g. R_{lo}, α, ΔK_0, and C_{th}, was also considered to assess their predictive effect on the FCG life. The elements R_{lo} and α were used to define the MS and CC criteria, whereas ΔK_0, and C_{th}, were mainly concerned with curve-fitting issue of NASGRO–3.0 Equation. Their merits were assessed with respect to the experimental data, and were reported hereafter.

7.4.3 Comparison of AFGROW with experimental results

The experimental FCG curves in Figure 7.3.1 are compared with AFGROW predictions in Figure 7.4.1. As expected, the AFGROW prediction for the plain hole matches the measured FCG data extremely well. Given the first estimate of K_{res} derived from the surface stress data obtained from X-ray technique, fairly good agreement was achieved by AFGROW. The following section discusses AFGROW simulations according to the MS and CC definitions.

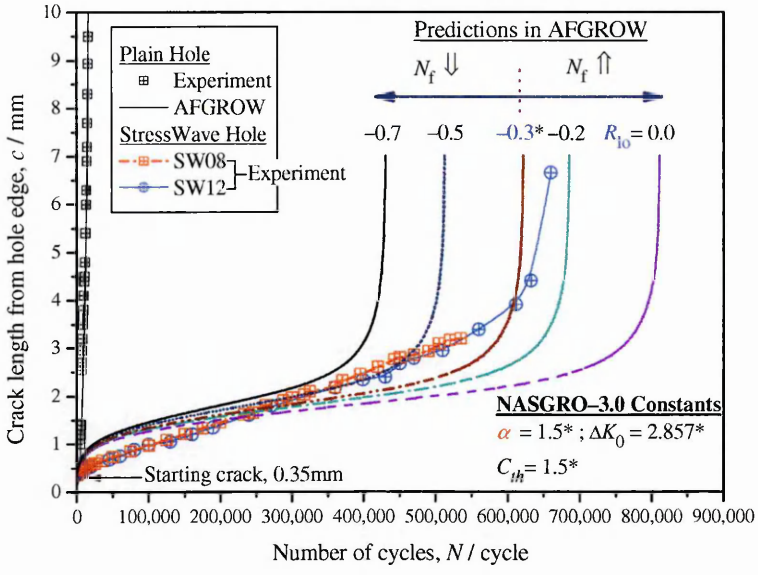

(a) Mean stress criteria

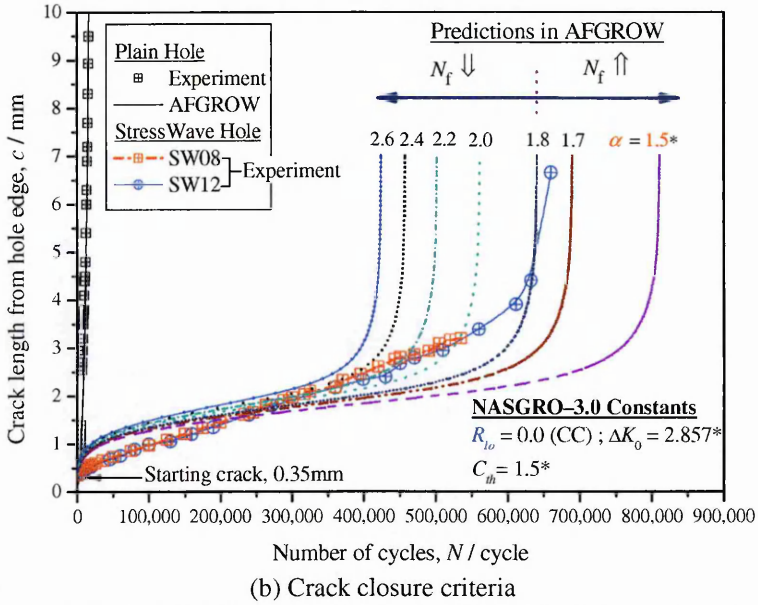

(b) Crack closure criteria

Figure 7.4.1 Experimental and estimated FCG curves for plain holes and SW cold-worked holes. AFGROW estimations are based on the adjustment of the parameters related to mean stress (MS) and crack closure (CC) approaches: (a) lower limit of R–shift for $-0.7 \leq R_{lo} \leq 0.0$, and (b) plane stress/strain constraint factor given $1.5 \leq \alpha \leq 2.6$. *Default AFGROW values defined in equation NASGRO–3.0.

Mean-Stress: Firstly, in Figure 7.4.1(a) the MS (or variable-R) effect was simulated by adjusting the lower cut-off stress ratio, R_{lo}. As explained in Sections 6.5.3 & 7.4.1, the parameter R_{lo} defines the lower R-shift limit in multiple $dc/dN = f(\Delta K, R)$ curves. In other words, R_{lo} controls the permissible range of subzero variation of R_{eff} employed in the FCG computations. In equations (7.4.1) & (7.4.2), the lower and upper bounds of R-shift, viz. R_{hi} and R_{lo} are in fact governed by the limit of the Newman model, i.e. $-2.0 \leq R \leq 1.0$ (see

Section 6.5.1). In AFGROW, these two limits may be separately defined as $0.99 < R_{hi} \leq 0.0$ and $0.0 < R_{lo} \leq -2.0$.

Recalling Figure 6.4.3 of Chapter 6, the effective crack tip stress ratio, R_{eff} was calculated to be between 0.15 and –3.30 for present case. Identifying a suitable R_{hi} (= 0.7) is fairly straightforward because the R_{eff} (< 0.20) is within the range of R_{hi}. In contrast, the selection criteria for R_{lo} at subzero level are not well-defined but differ depending on problem definitions, damage tolerance procedures, and ultimately the reliability of predicted results. The recommended value is typically in the range of $-0.4 \leq R_{lo} \leq -0.2$ [24]. For that reason, it is vital to explore further to obtain suitable values of R_{lo} to match the actual FCG data.

In Figure 7.4.1(a), adjusting $R_{lo} < 0.0$ accelerates the FCG which shortens the total life, whereas setting $R_{lo} = 0.0$ prolongs the fatigue life. The selection of R_{lo}, and in turn the $dc/dN = f(\Delta K, R_{lo})$ curve given by equation NASGRO–3.0, is critical to the prediction associated with MS criteria. The AFGROW default $R_{lo} = -0.3$ incorporating certain degree of MS effect shows reasonable estimation. In contrast, the value $R_{lo} = 0.0$, which strictly represents the CC criteria relating to $\Delta K_{tot\text{-}CC} \geq 0$, overestimated the FCG life in a non-conservative manner.

Crack Closure: Alternatively, it is equally possible to improve the prediction using the CC criteria by altering the crack tip constraint factor α, as illustrated in Figure 7.4.1(b). α represents the state of stress at the crack tip, and by definition $\alpha = 1$ is plane stress and $\alpha = 3$ is plane strain [23]. Overall, setting the α–value between 1.7 and 1.8 has provided fairly good prediction on the final life of specimens approaching fracture (in Figure 7.4.1(b)). Employing $\alpha = 1.7 \sim 1.8$ is comparable to the value ($\alpha = 1.8$) previously calibrated for Al 2024 [23]. It is plausible that the plastic zone size, crack size, thickness and material for a

given loading can affect the stress state surround the crack tip. Here, α is responsible for the crack closure level, f and consequently the crack propagation rates, dc/dN.

From Figures 7.4.1 (a) & (b), it is evident that identical FCG is reproducible by either adjusting the R_{lo} or α, or both simultaneously – capitalising from the fact that both parameters control the amount of ΔK_{eff} calculated for R_{eff} or α in NASGRO–3.0 relation. To demonstrate, referring to Figures 7.4.1 (a) & (b)several pairs of (R_{lo}, α) that provide equal FCG life are (–0.7, 2.6), (–0.5, 2.4) and (0, 1.5). This is the repercussion of the Newman model that permits mixed degree of MS and CC effect to present in the analysis.

7.4.4 Comparison of predicted & experimental "dc/dN versus c data"

Regardless of the R_{lo} and α values used, Figure 7.4.1 discloses that the FCG model predicts a persistent overestimate of crack growth below 0.350 ~ 2.75 mm. The compounded SIF range in AFGROW's prediction is believed to be higher than the amount actually occurred in the testing, which explained premature crack growth. None of the R_{lo} and α value employed accurately duplicates the experimental FCG data in this region.

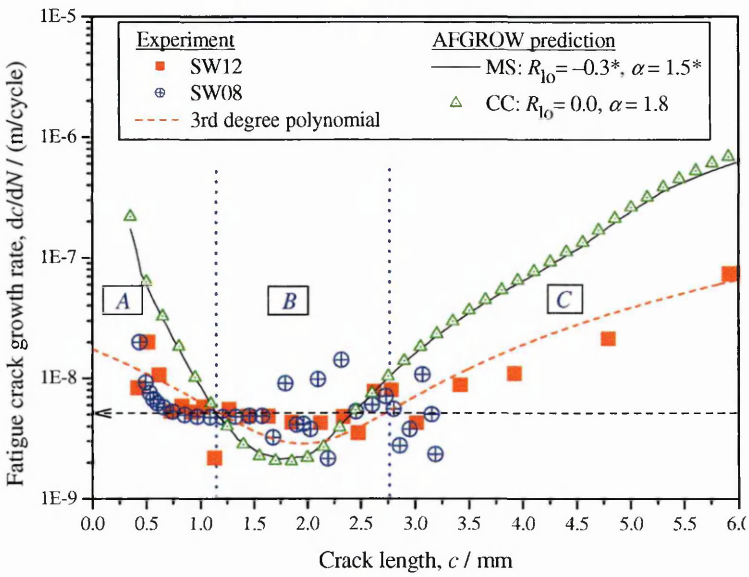

Figure 7.4.2 Fatigue crack propagation rate data derived from fatigue experiment and as estimated by AFGROW. *Default AFGROW values defined in equation NASGRO–3.0.

In Figure 7.4.2, the overall trend of dc/dN vs. c between the prediction and experiment is quite encouraging. The experimental data shows retardation at an average FCG rate of around 5×10^{-9} m/cycle between 0.75 ~ 2.75 mm before accelerates at higher crack length, and this occurs within the compressive zone of the residual stress field (Figure 6.2.2, Chapter 6). On the other hand, the predicted FCG rate is conservative in regions A & C and under-predicted in region B; the observation is consistent to the behaviour of c vs. N plot (Figure 7.4.1).

The "dc/dN versus c" plot of Figure 7.4.2 gives a better depiction of actual cracking behaviour in cold-worked holes, as it is derived directly from the measured data. On the other hand, the SIF representation of ΔK is more inclined to errors/shortcomings in residual stress, superposition technique, plasticity correction, etc, and thus it is advisable to minimise these errors whenever possible. The uncertainty in the determination of ΔK is thought to be partly responsible for the disparity seen in Figure 7.4.2. Further parametric analysis was carried out next to improve the predictive work.

7.5 Parametric Studies in Near-Threshold Region

For cold-worked holes, the majority of life gain occurs under fairly low R_{eff} and ΔK_{eff} when the crack is growing in the compressive region of residual stress. Under such conditions, the crack tips tend to close up and giving reduced FCG rates. According to Grandt & Gallagher [25], long service life may be attained in cold-worked holes providing the operating ΔK_{eff} and dc/dN are comparable to the threshold values. Figure 7.4.2 indicates that the dc/dN is confined between the threshold and stable growth regions.

The NASGRO–3.0 (Equation (7.4.1)) is explored to understand the dc/dN –ΔK curve in these regions. Based on the FCG criteria of MS and CC, the two components ΔK_0 and C_{th}

in relation (7.4.2) will be examined. ΔK_0, the threshold SIF range at R = 0.0 and C_{th}, the threshold coefficient, are both intrinsic properties related to the threshold crack regime.

Another two entities in Equation (7.4.2) were not considered due to the following reasons: a_o is the intrinsic crack size fixed at 0.0381 mm, whilst A_0 is one of the coefficients of Newman's crack opening model, and is dependent on α and S_{max}/σ_0. The parametric study of α was previously explored in Section 7.4; in NASGRO equation the ratio $S_{max}/\sigma_0 = 0.30$ is normally assumed constant for a given set of loading and aluminium alloy used to derive the baseline FCG data, and thus must also remain unaltered.

7.5.1 ΔK_0– Effect on the near-threshold regime

In Figure 7.5.1(a), for different ΔK_0 the NASGRO–3.0 equation shows systematic shift in the dc/dN –ΔK curves at the threshold region–I. However, in regime–II and III all curves of different ΔK_0 associated to MS and CC definitions, blend in and coincide into two very similar curves. In Figure 7.5.1 (b), these curves display a systematic right-shift of the threshold curves for increasing ΔK_0, and also elevation of the dc/dN values correspond to the transition from regime–*I* into regime–*II*, as shown by the dividing line *A*–*A*.

In the present experiment, the SW specimens spend a considerable span of life at FCG rate between 1×10^{-9} and 1×10^{-7} m/cycle. As can be seen in Figure 7.5.1, this range of FCG rate corresponds to the early transition of dc/dN–ΔK curve from the threshold (regime–*I*) to steady crack propagation stage (regime–*II*).

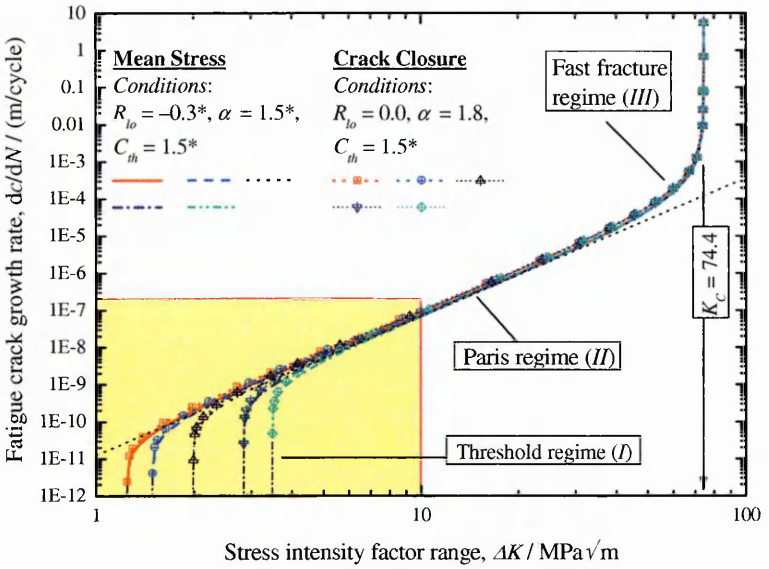

(a)

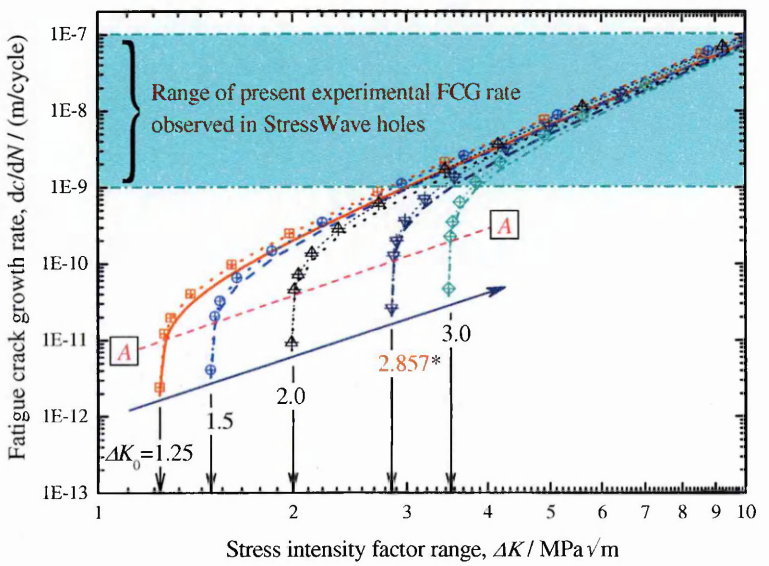

(b)

Figure 7.5.1 The effect of the variation of threshold stress intensity factor range at R = 0.0, ΔK_0 on the behaviour dc/dN– ΔK curves in NASGRO–3.0. model (a) overall behaviour; (b) close look at near-threshold regime (Region-I). *Default AFGROW values.

Despite slight variation calculated by NASGRO–3.0 equation in this transition region, where the experimental FCG rate occurred (Figure 7.5.1 (b)), Figures 7.5.1 & 7.5.2 suggest that the prediction is sensitive to ΔK_0.

(1) While increasing ΔK_0 prolongs the fatigue life and vice-versa, the overall shapes of the FCG curves remain unchanged. The AFGROW default ΔK_0 (= 2.857 MPa·√m) produced a reasonable estimate using the MS criterion (Figure 7.5.1 (a)).

(2) However, for the CC method the prediction is even more sensitive to ΔK_0 (Figure 7.5.2 (b)); and setting ΔK_0 = 2.0 MPa·√m, rather than the default 1.5 MPa·√m, gives a better prediction.

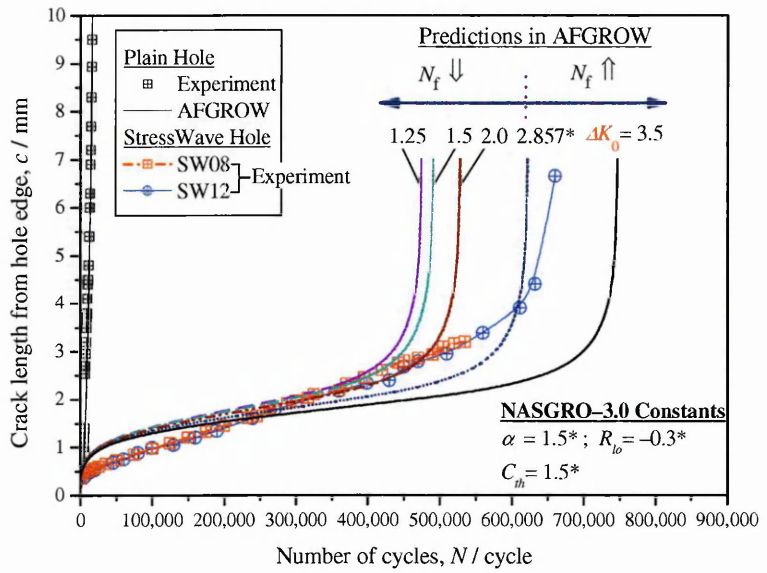

(a) Mean stress with varying ΔK_0

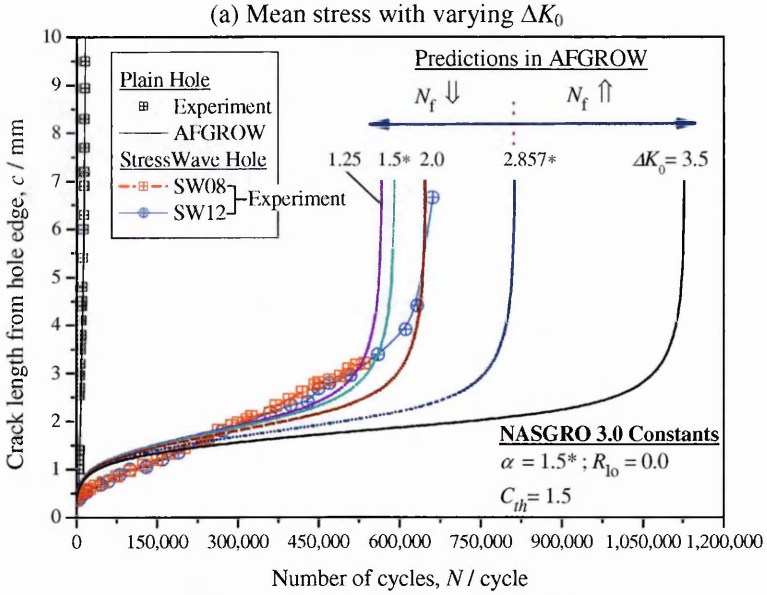

(b) Crack closure with varying ΔK_0

Figure 7.5.2 Effect of threshold SIF range at R = 0.0, ΔK_0 on the prediction of FCG life for dc/dN occur at the near-threshold region. *Default AFGROW values defined in equation NASGRO–3.0.

7.5.2 C_{th}– Effect on the near-threshold regime

For the threshold coefficient C_{th} = 1.0...4.0 studied in Figure 7.5.3, in the Paris regime the dc/dN–ΔK curve defined by the CC criteria is slightly elevated above the MS curve. Otherwise, no significant difference of dc/dN–ΔK curves was noticed for the MS and CC criteria at region–*I* and *III*. Using the dc/dN–ΔK relations plotted in Figure 7.5.3 for

various C_{th}, the AFGROW predictions are shown in Figure 7.5.4, with the following observations:

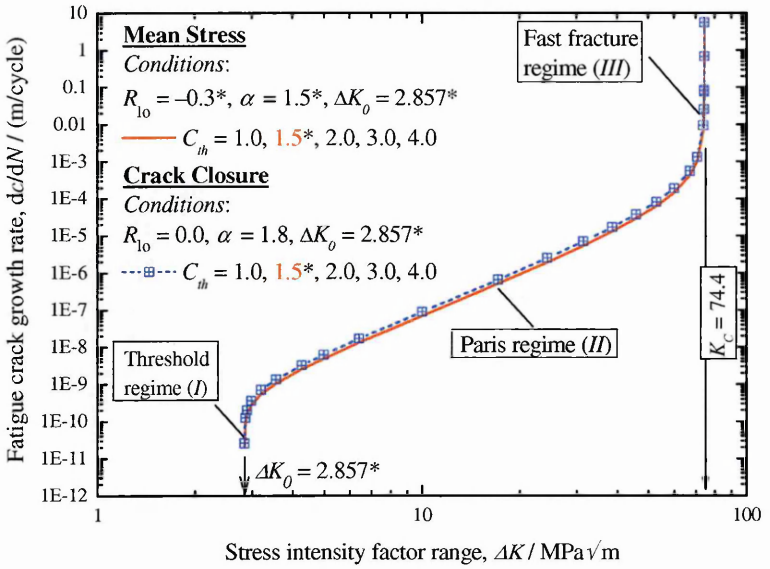

Figure 7.5.3 The effect of the variation of threshold coefficient, C_{th} on the behaviour of dc/dN– ΔK curves in NASGRO model. *Default AFGROW values defined in equation NASGRO–3.0.

(1) For the MS definition (Figure 7.5.4 (a)), a steady rise of fatigue life is observed for decreasing C_{th} = 4.0...1.0. This situation is attributed to the coupling effect between C_{th} and R_{eff} ($\geq R_{lo}$ = –0.3) (see Figure 6.4.3, Chapter 6) that changes the ΔK_0 values, and mathematically this is described by Equation (7.4.2).

(2) Interestingly, under the CC criteria no quantitative changes in the prediction are noticed for varying C_{th} (Figure 7.5.4 (b)). Referring to Figure 6.4.3 of Chapter 6, the entire crack history was spend under single effective stress ratio R_{eff} (= R_{lo} = 0.0, i.e. CC). This condition virtually nullifies the influence of C_{th} and consequently the ΔK_0 = 2.857 MPa·√m is kept undisturbed in AFGROW calculation, as can seen from Equation (7.4.2).

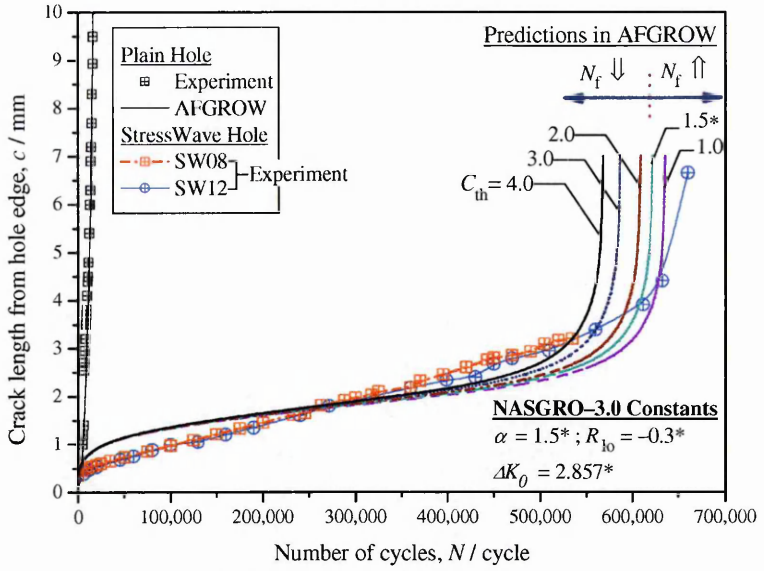

(a) Mean stress with varying C_{th}.

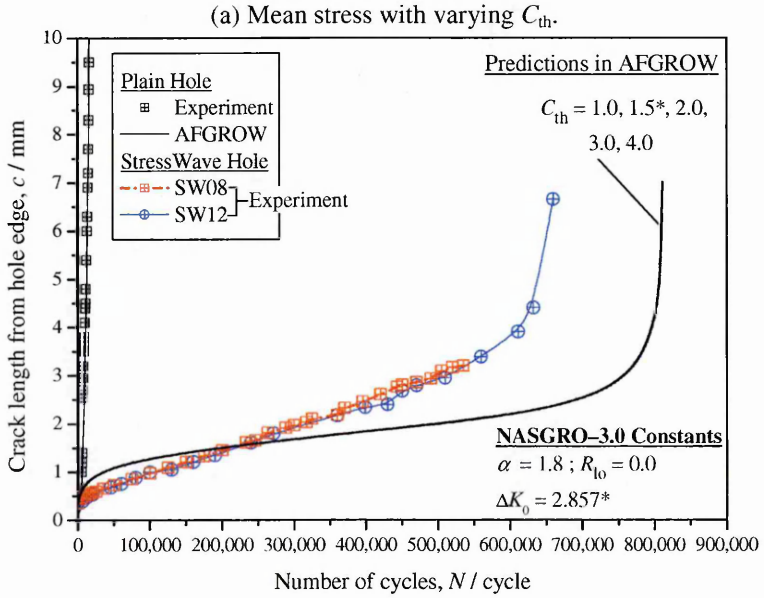

(b) Crack Closure criterion with varying C_{th}.

Figure 7.5.4 Near threshold behaviour. *Default AFGROW values defined in equation NASGRO–3.0.

7.6 Predictability of Fatigue Crack Growth Life in Cold-Worked Holes

The following section will examine some application issues encountered using AFGROW involving cold-worked holes. Suggestions of improving the predictions have been outlined.

7.6.1 AFGROW generic stress intensity factor model

Some success have been reported comparing AFGROW analysis with measured FCG data from cold-worked holes [26-29]. Though excellent correlations were typically achieved for plain holes, much predictive disagreement was observed in cold-worked holes. In prediction, ideally the entire history of the estimated FCG curves should fall within the

scatter band of the test data. Nevertheless, owing to the complexity of FCG modelling for cold-worked holes, the phenomena of over- / under-estimation for certain segments or complete FCG curves are not uncommon. The following summarises some of the undesirable difficulties faced in the fracture control programme of cold-worked holes

Kokaly *et al.* [28] reported that AFGROW predicted either crack arrest or zero crack growth in SSM holes, though in reality the laboratory data [30] showed un-arrested cracking until final fracture. Their analysis also produced an overly-conservative estimation of FCG life which formed only a small fraction of the actual fatigue life.

Facing the same problem, Zhang & Wang [26, 27] resorted to closed-form residual stress models to improve the prediction capability of AFGROW. By modifying several existing residual stress models of cold-expanded holes, and considering the plane stress/strain conditions, work hardening and Bauschinger's effect in materials, some improvement in prediction was gained. The approach can be regarded as streamlining the behaviour of residual stress models to obtained possible optimum results. However, it is concluded that no universal residual stress model fits best for all the fatigue cases studied. As a result, the future FCG analysis of cold-work holes will still need to depend heavily on laboratory fatigue testing for validation.

The use of the AFGROW generic SIF model is a common feature in the work of Kokaly *et al.* [28] and Zhang & Wang [26, 27]. The generic SIF model derived K_{res} from user-defined residual stress data using the Gaussian integration routine implemented in AFGROW [21]. Earlier in Section 6.3, we have addressed that the K_{res} computed by the generic SIF model and the GF are dissimilar (Figure 6.3.2). Although it is an approximate, the generic solution has been claimed to produce fairly good results for specimen without residual stress, particularly at shorter crack lengths, at which majority of the fatigue life is spent

[21]. In this text, it is interesting if similar observation for the generic SIF solution will be seen in SW hole notably with the influence of pronounced residual stress field.

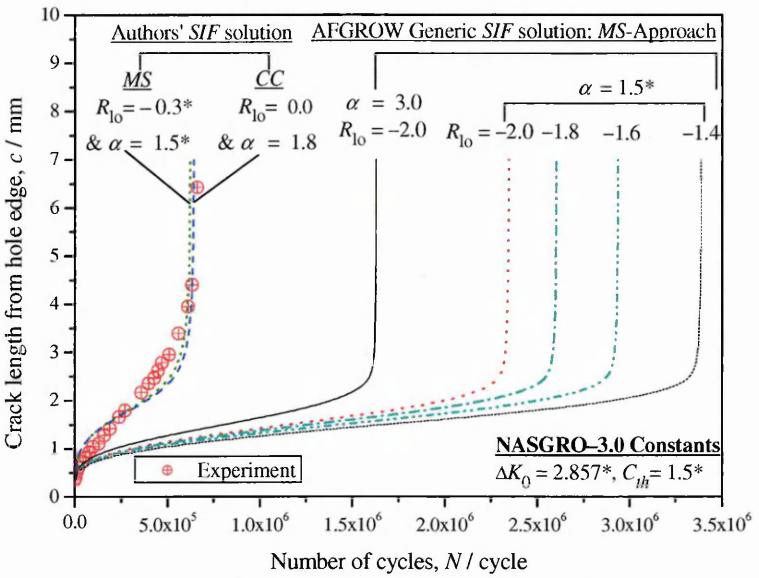

Figure 7.6.1 Comparisons of FCG curves, with respect to the experimental crack data, were made on the basis of the author's *SIF* solution (Green's function) and the AFGROW generic *SIF* model. Prediction criteria, *CC* : crack closure; *MS* : mean stress. *Default AFGROW values defined in equation NASGRO–3.0.

In Figure 7.6.1 & 7.6.2, comparison with the AFGROW generic SIF solution the FCG estimation using the author's GF solution (refer Section 6.3, Chapter 6) is relatively in excellent agreement with the physical data. In contrast, prognosis by the AFGROW generic SIF model is not reliable, and the associated FCG curves behave differently for both the MS (Figure 7.6.1) and CC criteria (Figure 7.6.2).

According to Figure 7.6.1, the combination of generic model and MS approach (α = 1.5 & R_{lo} = –1.4...–2.0) constantly under-predicts the FCG, and the over-estimation is no less than 3.55 times of the actual fatigue life. Despite some improvement being achieved using the extreme values α = 3.0 and R_{lo} = –2.0, the best predicted life is still 2.47 times of the actual data, and thus the results still remained unwarranted for practical applications.

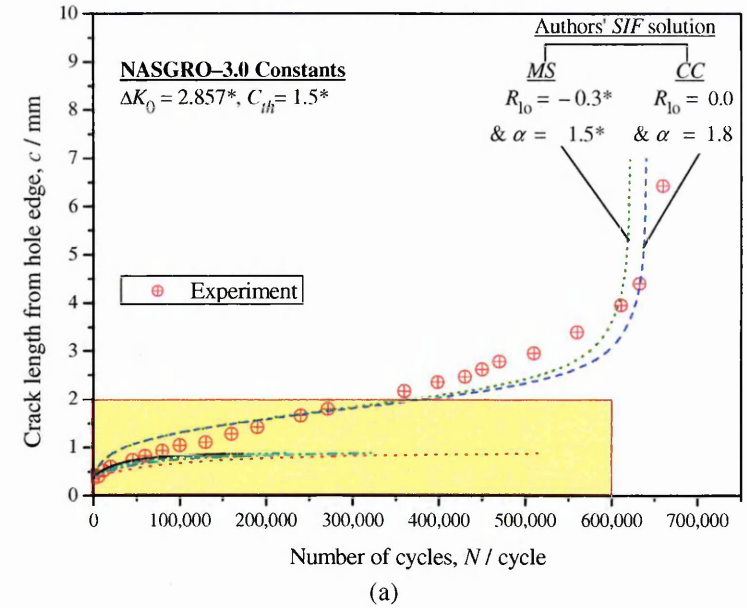

(a)

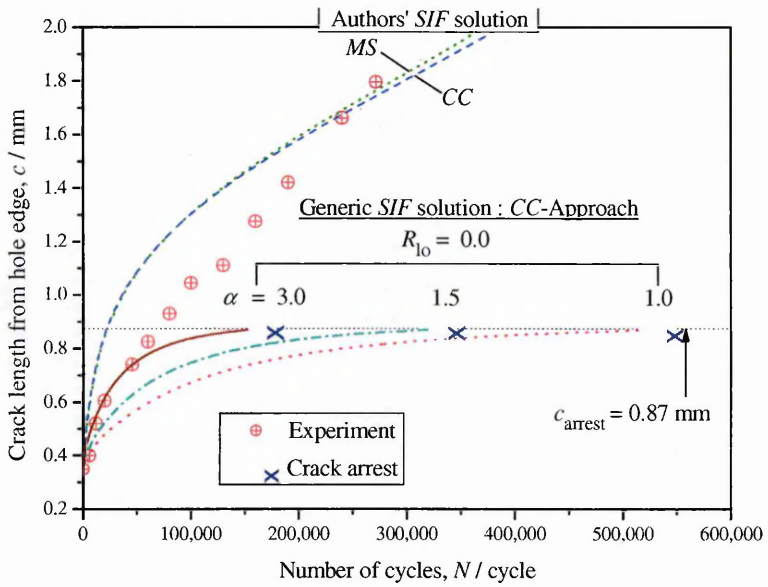

(b)

Figure 7.6.2 Under-prediction of crack-growth i.e. dormant crack, as a consequent of approximated K_{res} computed by the generic SIF model implemented in AFGROW. (a) Overall comparison of FCG curves. The calculation for generic solutions was coupled with *CC*-approach, and (b) detailed view of FCG plot at short crack below 2 mm. Prediction criteria, *CC*: crack closure; *MS*: mean stress. *Default AFGROW values defined in equation NASGRO–3.0.

In Figure 7.6.2(a), the generic SIF model coupled with the CC approach (α = 1.0…3.0 & R_{lo} = 0.0) predicts limited growth of very short cracks, which gives rise to infinite life in SW holes. For all the cases simulated in Figure 7.6.2 (b), the common crack size arrested was predicted to be c_{arrest} = 0.87 mm. In SW holes (Figure 7.2.2 of Chapter 6), this arrested crack length is embedded within the region of maximum compressive residual stress in the reverse yield zone, or inside the domain of minimum K_{res} ahead of the notch tip (see Figure

7.3.2 of Chapter 6). Additional inspection also verifies that for c_{arrest} = 0.87 mm corresponding to the threshold rate $dc/dN < 1\times10^{-12}$ m/cycle, the predicted ΔK_{eff-0} = 2.853 MPa·√m is slightly lower than the material threshold value ΔK_0 = 2.857 MPa·√m at R_{eff} = 0.0. Though the condition for crack arrest complies with the principles outlined by Grandt & Gallagher [31], the predictions nevertheless deviates from the actual testing.

Figures 7.6.1 & 7.6.2 may partially explain some of the problems associated with the AFGROW generic SIF solution when adopted for cold-worked holes. Both Kokaly *et al.* [28] and Zhang & Wang [26, 27] suggested that AFGROW is extremely sensitive to the initial flaw size defined in cold-worked holes. To alleviate the problem, a hypothetical starting crack size rather than the actual values, must be used to improve the prediction. Zhang & Wang [26] also recommended that optimisation for 'correct' Bauschinger's effect and work hardening in stress models was necessary to correlate with measured FCG data. Earlier, Boyd *et al.* [29] concluded that the AFGROW gave better FCG estimations for residual stress data of low interference than the actual higher interference used in their fatigue testing.

Adjusting the initial crack size or residual stress streamlining is, in fact, an empirical means to bypass or reduce the influence of high negative K_{res} associated with generic SIF model. Throughout the present work, an initial crack has been assumed from the 0.350 mm EDM notch. This removes the ambiguity that AFGROW is susceptible to starting crack length. Clearly, an accurate physical description of correct combination of appropriate SIF model and residual stress is central for good life prediction of cold-worked holes.

7.6.2 Enhancing prediction confidence by parametric studies

As has been seen in [4, 16, 18, 26-28, 32-36] and the present results, numerous interweaving issues must be considered to attain a reasonable FCG estimation in cold-

worked holes. Reproducing the actual FCG history (i.e. both laboratory and operational) exactly for cold-worked holes is a formidable task and often impractical, therefore a balanced approach is required to determine a reliable yet economic schedule for inspection and maintenance.

This section deals with the reliability assessment of the parametric approach employed in earlier sections. A method of selecting suitable parameters that relies primarily on the critical information sought is described. The measured and predicted FCG curves given in Figures 7.4.1, 7.5.2 & 7.5.4 will be examined.

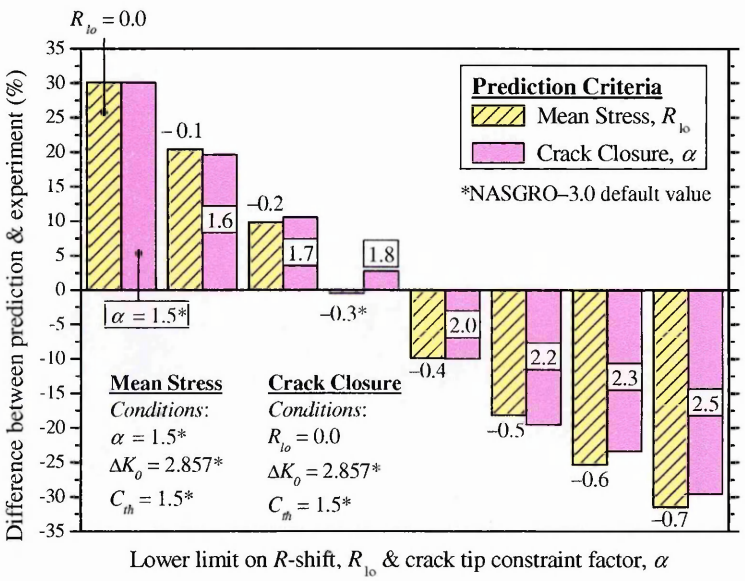

Figure 7.6.3 Reference life based on SW specimen 4 mm crack. *Default AFGROW values defined in equation NASGRO–3.0.

As shown in Figures 7.4.1, 7.5.2 & 7.5.4, none of the parameters R_{lo}, α, ΔK_0 and C_{th} provide an accurate replication of the entire FCG history of SW holes. However, for particular crack range fairly good correlation has been seen from the parameters. For instance, in Figure 7.4.1 the predictions using $R_{lo} = -0.5$ or $\alpha = 2.2$ matches the actual FCG data for crack sizes between 1.0 to 3.0 mm; but the prediction for $c < 1.5$ mm is non-conservative, and for $c > 3.0$ mm the estimation is slightly over-conservative.

A common feature of transition of FCG curve from stable to fast fracture, as shown by the AFGROW prediction in Figures 7.4.1, 7.5.2, 7.5.4, 7.6.1 & 7.6.2, took place soon after the

crack grew to 4 mm. In the present testing, most of the enhancement of fatigue life in SW holes was consumed at short cracks up to 3 ~ 3.5 mm. For illustration of subsequent analysis, the 4 mm crack is hereby hypothetically defined as the upper allowable limit in inspection. This limit necessitates maintenance since at larger crack the SW holes are no longer sustainable by the region of compressive residual stress shown in Figure 6.2.2. For better confidence in prediction, the limiting crack size is also reducible to a more conservative, i.e. shorter crack. Such a procedure generally considers other pessimistic sources of fatigue life knock-down factors, e.g. multiple cracks scenario, materials degradation, lower level of residual stress around the holes, environment, etc [37].

Figures 7.6.3 & 7.6.4 compare the percentage difference between the predictions and experiment, and also summarise the effect of parametric tuning of R_{lo}, α, ΔK_0 and C_{th} on the prediction accuracy, for the MS or CC definitions. For the 4 mm crack limit, Figures 7.6.3 & 7.64 show that optimum range of parameters can be established depends on the degree of conservatism preferred. An exception is the MS condition for $R_{lo} = 0.0$ and C_{th} discussed before in Figure 7.6.4 (b).

Despite the good correlation that can be obtained for particular crack ranges, parametric adjustment must be used with great caution. Any set of parameters is unlikely to be universal for all fatigue cases, and therefore calibration is needed to achieve a satisfactory outcome [37]. Furthermore, while it is preferable to use these parameters according to physical evidence available, reasonable prediction may be gained by using them strictly as fitting parameters.

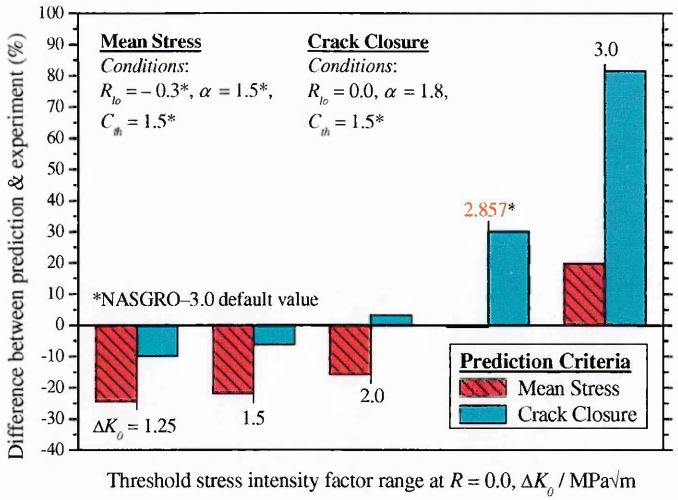

(a)

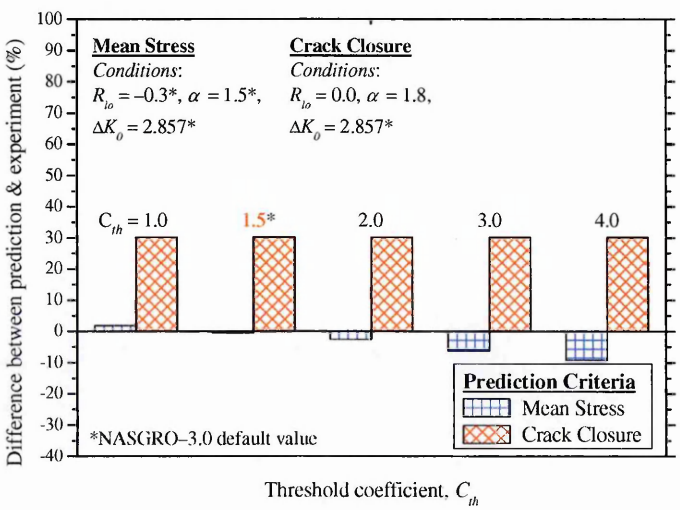

(b)

Figure 7.6.4 Reference life based on SW specimen 4mm crack. *Default AFGROW values defined in equation NASGRO–3.0.

7.7 Discussion

AFGROW [21] incorporates a residual stress effect using the concepts of R_{eff} and α related to the MS and CC approaches, respectively (Section 7.4). Here, user-setting R_{lo} allows either the MS or CC calculation to deal with negative R_{eff}. Albeit distinct in various aspects, it has been shown that both concepts are equally competent in predicting fatigue life. The core requirement lies with the proper calibration of R_{eff} and α in NASGRO–3.0 relation to match the experiment data.

7.7.1 R_{eff} and the requirement of fatigue crack baseline data

AFGROW shows some disparity about how R_{eff} is used to calculate the fatigue life compared to the original MS approach [38]. In AFGROW, the implication of setting the cut-off stress ratio, R_{lo} is that the baseline dc/dN–ΔK curve of R_{lo} is used once the estimated R_{eff} reaches R_{lo}. As seen in Figure 6.4.3 of Chapter 6, the R_{eff} range from 0.1 to –3.26. However, only the baseline curve for $0.1 \geq R_{eff} \geq R_{lo} = -0.7$ or -0.3 or 0.0, in respective to the individual R_{lo} defined, is used in the calculation (see Figure 6.5.4 of Chapter 6).

In contrast, the original MS / variable R_{eff} approach [38] necessitates the use of multiple baseline curves for a wide range of R_{eff}–ratio for FCG estimation. This method is not practical as in a cold-expanded hole the R_{eff} can reach as low as –18 to –25 [39] for given K_{res} and applied loading, and no experimental baseline dc/dN–ΔK data is currently or likely to be ever available for these cases.

In the CC method (see Figure 7.4.2 (a) of Chapter 6), the limit of $R_{lo} = 0.0$ corresponds to a crack length between 0.350 to 7.0 mm. The result implies that for the present case (or perhaps in most cases), only a single dc/dN– ΔK curve derived experimentally for $R_{eff} = 0.0$ is ever needed for CC calculation in AFGROW [35, 40]. Such prerequisite of baseline data is much more economically and practically viable when compared to the requirement of several dc/dN–ΔK curves for various ranges of R-ratios in the MS method.

7.7.2 Derivation of ΔK_{tot} for given R_{eff}

In line with MS theory, two separate algorithms have been used to compute the ΔK_{tot} for positive and negative R_{eff}. For positive R_{eff} (i.e. $0.0 \leq R_{eff} \leq R_{hi} < 1.0$), the d$c$/d$N$–$\Delta K$ curve is defined directly by the NASGRO–3.0 expression (7.4.1). For negative R_{eff} (i.e. $-2.0 \leq R_{lo} \leq R_{eff} < 0.0$), AFGROW internally converts the ΔK_{tot} valued as K_{max}–dependent [21, 24]:

$$\Delta K_{tot} = K_{max} \cdot \left(1 - R_{eff}\right) > 0, \quad -2.0 < R_{lo} < R_{eff} \leq 0.0 \tag{7.7.1}$$

The central notion of relation (7.7.1) is essentially analogous to that of the Walker equation, in which the R–ratio effect on the systematic shift of dc/dN–ΔK can be described mathematically [21, 41]. Moreover, relation (7.7.1) assumes that under negative R_{eff} only the positive part of ΔK_{tot} can cause crack growth; therefore ΔK_{tot} reduces to K_{max}.

For prediction, the dc/dN–ΔK_{tot} relation produced from NASGRO–3.0 equation now, in fact, becomes dc/dN–ΔK_{max}. A unique feature attributed to (7.7.1) is that the reduced dc/dN–ΔK curves for negative R_{eff} have the tendency to shift leftward (see Figure 7.7.1), especially for high negative R-ratios. In contrast, the raw FCG data [38] normally exhibits a constant right-hand shift of dc/dN–ΔK curves for $R_{eff} < 0$, as shown in Figure 7.7.2.

Whilst in the MS theory it is unrealistic to use R_{eff} without the practical restriction of R_{hi} and R_{lo}; however, it is possible to fully simulate the CC approach by setting $R_{lo} = 0.0$ in AFGROW. In this case, only the dc/dN–ΔK curves for zero and positive R_{eff} will be used throughout the computation, and no conversion involving relation (7.7.1) is required.

7.7.3 ΔK_{eff} –Reduction from ΔK_{tot} or K_{max}

Direct use of raw dc/dN– ΔK curves for FCG life prediction must be treated with caution as any secondary plasticity effect has not been accounted for in ΔK_{tot} or K_{max}. To ensure a better result, the crack opening stress associated with secondary plasticity i.e. S_{op}/S_{max} or K_{op}/K_{max} should be used, and hence ΔK_{eff} must be experimentally calibrated from several baseline dc/dN–ΔK dataset of different R-ratios. The is normally done by using the analytical [42-45], or finite element models [46-48].

In this work, the Newman solution [23, 49] was used because it has been fully implemented in NASGRO–3.0 relation; but the principle of secondary plasticity correction remains unchanged if any other suitable model is available.

7.7.4 Comparison of predicted & experiment dc/dN–ΔK_{tot} data

To aid our understanding, the raw data of experiment and prediction is compared in their most basic form of dc/dN–ΔK relation, without the ΔK_{eff} correction. The comparison is made along with other baseline curves at different R-ratios either computed from the NASGRO–3.0 equation (Figure 7.7.1), or extracted directly from the literature (Figure 7.7.2). In Figures 7.7.1 & 2, the experiment (i.e. CC and MS data) and the AFGROW predictions are significantly different.

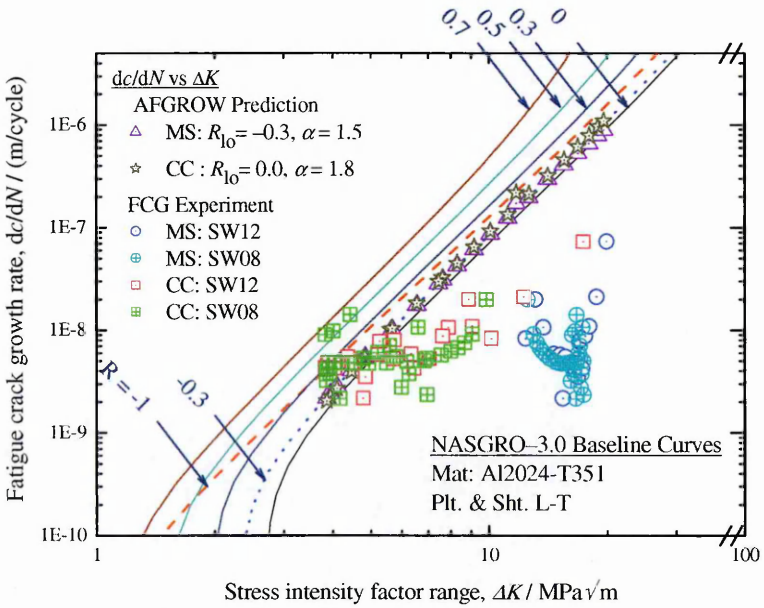

Figure 7.7.1 FCG rate behaviour of SW cold-worked hole: experiment and prediction. Baseline curves taken from AFGROW as defined by NASGRO–3.0. CC = crack closure; MS = mean stress.

In Figure 7.7.1, the range of NASGRO curves associated to MS and CC approaches used for prediction is almost identical (see also Figure 7.4.1). In comparison, only a small population of the experiment CC data matches the NASGRO curves. Moreover, no experimental MS data falls within the range of NASGRO curves prescribed by equation (7.7.1), and hence no direct comparison can be made.

However, in Figure 7.7.2 the trend of MS data passing through the dc/dN–ΔK curves bounded between $-2 < R_{eff} < -1$, were shown to agree quite well with those observed in [38]. Again, the absence of dc/dN–ΔK data lie beyond $R_{eff} < -2$ means there is a practical

constraint if the original variable-R_{eff} (i.e. MS) concept of Liu's [38] is to be used for present FCG prediction.

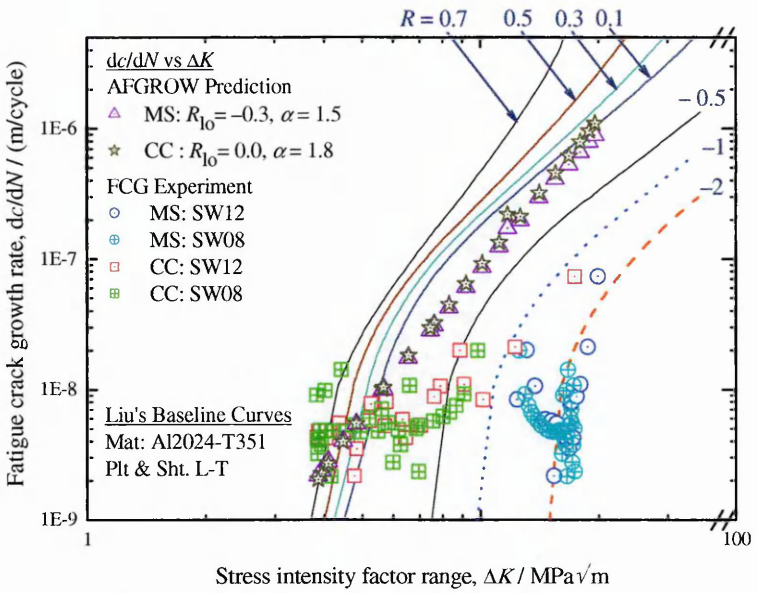

Figure 7.7.2 FCG rate behaviour of SW cold-worked hole: experiment and prediction. Baseline curves taken form Liu's [38]. CC = crack closure; MS = mean stress.

Besides the choice of methodology used, it is worth considering other possibilities of disparities seen in Figures 7.2.1 & 7.7.2, such as the data quality in c vs. N curves, the data reduction of dc/dN, and the computational scheme of ΔK incorporating K_{res} effect. In addition, the NASGRO model (Figures 7.7.1) might not be representative of the material used here, and markedly different than Liu's data (Figures 7.7.2) [38]. Harter [21] also noticed that the FCG rate tend to display a fair amount of scatter, and data for the same material can differ as much as a factor of two in terms of FCG rate. All these possible sources of errors together indicate that predicting FCG life in cold-worked holes with a high degree of reliability and reproducibility is a very delicate and laborious task.

7.8 Conclusion

This article constitutes a comprehensive assessment of fatigue life in cold-worked holes enhanced by SW indentations. This chapter is devoted to explore the practical aspects concerning the actual testing and the FCG prediction in SW holes, which complements the

theoretical foundation laid in Chapter 6. The conclusions of this chapter are arranged as follows:

(a) According to the *S–N* curve methodology, the greatest fatigue benefits in cold-working, as implied from the life improvement factor (LIF), is attained at low-stress level.

(b) In the fatigue testing, symmetric through-thickness crack lengths, as expected, emanated from the EDM-notch tip on both faces of StressWave specimens. The repeatability in the StressWave crack growth data signifies excellent process control was achieved to generate symmetric stress field in the specimen.

(c) The comparison between the crack growth data of AFGROW and experiment showed very favourable agreement using the MS and CC approaches. The prediction for non-cold-worked holes is excellent because the ΔK_{eff} is entirely under the influence of constant *R*-ratio of 0.1, without the complication of residual stress. Conversely, to optimise the prediction reliability in cold-worked holes, it was recognised that calibrating the NASGRO–3.0 parameters such as R_{lo} and α is crucial.

(d) Correct model of stress intensity factor is critical to the K_{res} estimated for cracked hole with residual stress. The present attempt also provides insight to explain certain predictive ambiguities of cold-worked holes in previous work. The approximated AFGROW generic SIF model is susceptible to over-/underestimation the crack growth history. The Green's function developed by the author is shown to be sufficiently accurate for present work.

(e) Parametric study on the NASGRO–3.0 equation in modelling the d*c*/d*N*–ΔK curve is of immediate interest since most of the laboratory FCG rate of SW holes occurred around the transition from the threshold regime into the Paris region. The d*c*/d*N*–ΔK curve

produced from NASGRO model is sensitive to the parameter ΔK_0 and C_{th}, and can be useful as tuning purposes to improve the prediction.

(f) The reliability of AFGROW was also studied in the light of parametric adjustment of R_{lo}, α, ΔK_0 and C_{th} on providing best estimate for a specified limiting crack size. This is important as the accurate replication the actual growth history of the physical crack data is not always sensible. The main idea is to identify some maximum allowable crack lengths in which the intended purposes of cold-working is still effectual.

7.9 References

1. Phillips, J.L., Sleeve coldworking fastener holes, Technical Report AFML-TR-74-10, Vol. I & II. 1974, Air Force Materials Laboratory, Wright-Patterson Air Force Base, OH.
2. Leon, A., Benefits of split mandrel coldworking. International Journal of Fatigue, 1998. 20(1): p. 1-8.
3. Maximov, J.T. and Kalchev, G.M., Modelling of spherical mandrelling manufacturing resistance. International Journal of Machine Tools & Manufacture, 2004. 44(1): p. 95-100.
4. Cook, R., Rooke, D.P., Smith, A., and Bowles, R., Residual stress fields at notches: effect on fatigue crack growth. In: RAE Technical Report 85049. 1985, Royal Aircraft Establishment: Farnborough, UK.
5. Easterbrook, E.T., Flinn, B.D., Meyer, C., and Juhlin, N. The StressWave™ Fatigue life Enhancement Process. in SAE Aerospace Automated Fastening Conference and Exhibition, Proceedings of 2001 Aerospace Congress, Paper No. 2001-01-2578. 2001. Seattle, USA: Society of Automotive Engineers.
6. Fatigue Technology Inc, FTI Process Specification 8101C Cold Expansion of Holes Using the Standard Split Sleeve System and Countersink Cold Expansion™ (CsCx™). 1994: 401 Andover Park East, Seattle, WA 98188-7605 USA.
7. StressWave Inc, Technical Report AL-02 Fatigue Testing of 2024 Low Load Transfer Aluminum Specimens (Nov. 1, 2001). 2001: 6644 South 196th Street, Suite T-106, Kent, WA 98032. p. 8.

8. StressWave Inc, Technical Report AL-06, Fatigue Testing of 0.040 inch thick 2024-T3 Aluminum (Nov. 15, 2001). 2001: 6644 South 196th Street, Suite T-106, Kent, WA 98032. p. 4.
9. StressWave Inc, Technical Report AL-04, Fatigue Testing of 6061-T6 zero load transfer aluminium specimen (Sept. 1, 2001). 2001: 6644 South 196th Street, Suite T-106, Kent, WA 98032. p. 6.
10. StressWave Inc, Technical Report AL-07, Fatigue Testing of 7050-T7451 Aluminum (Mar. 1, 2002). 2002: 6644 South 196th Street, Suite T-106, Kent, WA 98032. p. 3.
11. StressWave Inc, Technical Report ST-01, Fatigue Testing of 4340 Steel (July. 1, 2001). 2001: 6644 South 196th Street, Suite T-106, Kent, WA 98032. p. 3.
12. StressWave Inc, Technical Report TI-01, Fatigue Testing of 6Al-4V Titanium (July 1, 2001). 2001: 6644 South 196th Street, Suite T-106, Kent, WA 98032. p. 3.
13. Pilkey, W.D., Section 4.3.1 Single circular hole in an infinite thin element in uniaxial tension, in Peterson's Stress Concentration Factors, 2nd Ed. 1997, Wiley-Interscience: New York. p. 544.
14. Wawrzynek, P. and Ingraffea, A., FRANC2D: A two-dimensional crack propagation simulator, Version 3.1 User's Guide. 2004.
15. Stefanescu, D., Effect of load history on residual stresses developed at cold expanded fastener holes, PhD Thesis, in Structural Integrity Group, Materials Engineering Department. 2001, The Open University: Milton Keynes.
16. Ball, D.L. and Doerfler, M.T. Experimental and analytical studies of residual stress field evolution and fatigue crack growth at cold expanded holes. in 2003 USAF Aircraft Structural Integrity Program (ASIP) Conference. 2003. Savannah, Georgia.
17. Kokaly, M.T., Restis, J.H., and Reid, L.F. Fatigue crack behaviour and interaction with the residual stress field of a cold worked hole. in Proceedings of the 22nd Symposium of the International Committee on Aeronautical Fatigue: Fatigue of Aeronautical Structures as an Engineering Challenge. 2003. Lucern, Switzerland: EMAS, Cradley Heath, West Midlands.
18. Kokaly, M., Ransom, J., Restis, J., and Reid, L., Predicting fatigue crack growth in the residual stress field of a cold worked hole. Journal of ASTM International, 2005. 2(5): p. 1-13.
19. Wang, Z. and Zhang, X., Predicting fatigue crack growth life for cold-worked holes based on existing closed-form residual stress models. International Journal of Fatigue, 2003. 25(9-11): p. 1285-1291.

20. Zhang, X. and Wang, Z., Fatigue life improvement in fatigue-aged fastener holes using the cold expansion technique. International Journal of Fatigue, 2003. 25(9-11): p. 1249-1257.
21. Harter, J.A., AFGROW: Users Guide and Technical Manual. AFRL-VA-WP-TR-2004 (Version 4.0009e.12). 2004: Air Vehicles Directorate, 2790 D Street, St 504, Air Force Research Laboratory, WPAFB OH 45433-7542.
22. Forman, R.G., Shivakumar, V., Mettu, S., and Newman, J.C., NASGRO Version 3.00 Reference Manual : Fatigue crack growth computer program, NASA Document JSC-22267B. December 2000.
23. Newman, J.C.J., A crack opening stress equation for fatigue crack growth. International Journal of Fracture, 1984. 24(3): p. R131-R135.
24. Boyd, K.L., Jansen, D.A., Krishnan, S., and Harter, J.A., Structural Integrity Analysis & Verification for Aircraft Structures, Volume 2: Effects of Compressive Loading on the Fatigue Crack Growth Rates Of 7075-T651, Report No. WL-TR-97-3017. 1996, Air Force Flight Dynamics Directorate, Wright-Patterson Air Force Base, OH.
25. Grandt, A. and Gallagher, J., Proposed fracture mechanics criteria to select mechanical fasteners for long service lives, in ASTM Special Technical Publication 559: Fracture Toughness and Slow-Stable Cracking. 1974, American Society for Testing and Materials: Philadelphia, PA. p. 13-31.
26. Wang, Z. and Zhang, X., Predicting fatigue crack growth life for cold-worked holes based on existing closed-form residual stress models. Int. J. Fatigue, 2003. 25(9-11): p. 1285-1291.
27. Zhang, X. and Wang, Z., Fatigue life improvement in fatigue-aged fastener holes using the cold expansion technique. Int. J. Fatigue, 2003. 25(9-11): p. 1249-1257.
28. Kokaly, M.T., Restis, J.H., and Reid, L.F. Fatigue Crack Behaviour and Interaction with the Residual Stress Field of a Cold Worked Hole. in Fatigue of Aeronautical Structures as an Engineering Challenge, Proceedings of the 22nd Symposium of the International Committee on Aeronautical Fatigue. 2003. Lucern, Switzerland: EMAS, Cradley Heath, West Midlands.
29. Boyd, K.L., Jansen, D.A., Krishnan, S., and Harter, J.A., Structural Integrity Analysis & Verification for Aircraft Structures, Volume 1: Characterization of 7075-T7351 Aluminum; MODGRO Verification; MODGRO GUI Development, Report No. WL-TR-95-3090. 1996, Air Force Flight Dynamics Directorate, Wright-Patterson Air Force Base, OH.

30. Saunder, T.J. and Jr, A.F.G. The effect of edge distance on coldworking fastener holes. in Proceedings of the Fourth Joint DoD/FAA/NASA Conference on Aging Aircraft. 2000. St. Louis, Missouri.
31. Grandt, A. and Gallagher, J., Proposed fracture mechanics criteria to select mechanical fasteners for long service lives, in Fracture Toughness and Slow-Stable Cracking, ASTM STP 559. 1974, American Society for Testing and Materials: Philadelphia, PA. p. 13-31.
32. Ball, D.L. and Lowry, D.R., Experimental investigation on the effects of cold expansion of fastener holes. Fatigue and Fracture of Engineering Materials & Structures, 1998. 21(1): p. 17-34.
33. Buxbaum, O. and Huth, H., Expansion of cracked fastener holes as a measure for extension of lifetime to repair. Engineering Fracture Mechanics, 1987. 28(5-6): p. 689-698.
34. Clark, G., Fatigue crack growth through residual stress fields--theoretical and experimental studies on thick-walled cylinders. Theoretical and Applied Fracture Mechanics, 1984. 2(2): p. 111-125.
35. Cathey, W.H. and Grandt, A.F.J., Fracture mechanics consideration of residual stresses introduced by coldworking fastener holes. Journal of Engineering Materials and Technology, Transactions of the ASME, 1980. 102(1): p. 85-91.
36. Rich, D.L. and Impellizzeri, L.F., Fatigue analysis of cold-worked and interference fit fastener holes, in ASTM Special Technical Publication 637: Cyclic stress–strain and plastic deformation aspect of fatigue crack growth. 1977, American Society for Testing and Materials: Philadelphia, PA. p. 153–175.
37. Broek, D., The Practical Use of Fracture Mechanics. 1989, Dordrecht, The Netherlands: Kluwer Academic Publishers. 540.
38. Liu, A.F., Effect of residual stresses on crack growth from a hole. AIAA Journal, 1984. 22(12): p. 1784-1785.
39. Stefanescu, D., Effect of load history on residual stresses developed at cold expanded fastener holes, in Structural Integrity Group, Materials Engineering Department, . 2001, The Open University, U.K.
40. Grandt, A.F.J. and Hinnerichs, T.D. Stress intensity factor measureaments for flawed fastener holes. in Proceedings of the Army Symposium on Solid Mechanics AMMRC MC 74-8: The Role of Mechanics in Design – Structural Joints. 1974: Army Materials and Mechanics Research Center, Watertown, Massachusetts.

41. Walker, K., The Effect of Stress Ratio During Crack Propagation and Fatigue for 2024-T3 and 7075-T6 Aluminum, in Effects of Environment and Complex Load History on Fatigue Life, ASTM STP 462. 1970, American Society for Testing and Materials: Philadelphia, PA. p. 1-14.
42. Noroozi, A.H., Glinka, G., and Lambert, S., A two parameter driving force for fatigue crack growth analysis. International Journal of Fatigue, 2005. 27(10-12): p. 1277-1296.
43. Aliaga, D., Davy, A., and Schaff, H., A simple crack closure model for predicting fatigue crack growth under flight simulation loading, in Mechanics of fatigue crack closure, ASTM STP 982, J.C. Newman and W. Elber, Editors. 1988, American Society for Testing and Materials: Philadelphia, PA. p. 491–504.
44. Köning, A.U.D., A simple crack closure model for prediction of fatigue crack growth rates under variable-amplitude loading, in Fracture mechanics, ASTM STP 743, R. Roberts, Editor. 1981, American Society for Testing and Materials: Philadelphia, PA. p. 63–85.
45. Kujawski, D., Utilization of partial crack closure for fatigue crack growth modeling. Engineering Fracture Mechanics, 2002. 69(12): p. 1315-1324.
46. Solanki, K., Daniewicz, S.R., and Newman, J., J. C., A new methodology for computing crack opening values from finite element analyses. Engineering Fracture Mechanics, 2004. 71(7-8): p. 1165-1175.
47. Solanki, K., Daniewicz, S.R., and Newman, J., J. C., Finite element analysis of plasticity-induced fatigue crack closure: an overview. Engineering Fracture Mechanics, 2004. 71(2): p. 149-171.
48. Simandjuntak, S., Alizadeh, H., Pavier, M.J., and Smith, D.J., Fatigue crack closure of a corner crack: A comparison of experimental results with finite element predictions. International Journal of Fatigue, 2005. 27(8): p. 914-919.
49. Newman, J.C.J., ed. A crack-closure model for predicting fatigue crack growth under aircraft spectrum loading. Methods and models for predicting fatigue crack growth under random loading, ASTM STP 748. 1981, American Society for Testing and Materials: Philadelphia. 53–84.

CHAPTER 8: FINAL CONCLUSIONS & SUGGESTIONS FOR FUTURE WORK

The StressWave cold-working method is a typical example of using a favourable residual stress to improve the fatigue durability of mechanical joints. Adoption of StressWave methods in the mass production of fastener holes in the construction of new civil and military airframes is clearly possible. However, large scale implementation of the StressWave process in airframe fabrication procedures, and the associated potentials in fatigue life enhancement, could only be fully realised and justified through detailed investigation.

In response to this requirement, the major impetus of this thesis is the understanding the residual stress imparted around fastener holes treated by the StressWave process, and how the knowledge of residual stress can be utilised in the damage tolerance analysis of cracked holes.

In general, from the information presented in Chapters 3, 4, 5, 6 & 7, it has been shown that accurate measurement and modelling of residual stress, adequate representations of stress intensity factor in crack geometry, methodical comprehension of crack tip interaction with residual stress, as well as the proper assessment of fatigue crack growth rate model, are decisive factors essential in predictive work. Overall, throughout the present work the application of linear elastic fracture mechanics assuming small-scale yielding has produced satisfactory results.

Systematic integration and improved understanding of aforesaid interlinking aspects enable fatigue life predictive models to be performed with greater confidence. If the long-term benefits of the StressWave process are included in the design, manufacturing, safety

inspection and maintenance of aero structures, this could have a significant impact on both safety and economy in aircraft industry.

The following paragraphs provide the short summary of present work coupled with some tentative areas of exploration for future research:

(1) One of the major concerns in this work is the evolution of the residual stress field around a StressWave hole at different stages of the cold-working process. It has been shown that StessWave process generates compressive residual stress that is beneficial to the fatigue durability of hole. To ensure optimum StressWave process in many different applications, a parametric study including material properties, hole size, plate thickness, indenter geometry is needed. Diffraction-based stress measurement is desirable to provide insight on the residual stress distribution, but the high cost and access of experimental resources can be often prohibitive. In this aspect, numerical analysis by finite element modelling is a suitable tool to study the StressWave cold-indentation process.

(2) Both StressWave and split-sleeve mandrel techniques introduce favourable compressive residual stress around fastener holes. The results obtained from neutron and X-ray diffraction measurement together with finite element simulation indicated that different cold-working mechanism is involved in these two different processes. Technically, hole cold-working operates on the mechanism of radial expansion. Nevertheless, the split-sleeve process is also associated with secondary extrusion-type deformation which is responsible for the asymmetric residual stress distribution. The StressWave stress field, on the other hand, is more balanced due to the co-axial indentation from both sides of the plate.

(3) In Chapter 4, the material hardening models for extreme deformation associated with the StressWave deep indenting step was found to be crucial to the accuracy of finite element simulations. Numerical simulations may be further improved by three-dimensional

modelling incorporating material hardening parameters calibrated for a wider range of cyclic stress-strain response. A similar three-dimensional study of the split-sleeve method is also recommended to take account of the presence of gap/slit in the sleeve.

(4) In the current work, the stress intensity factor model developed is a simplification to match the actual physical representation of through-thickness crack geometry in holes adopted for laboratory testing. However, besides the single and double cracks cases reported in the Chapters 5 & 6, the formation and propagation of asymmetric cracks is also commonly encountered in cold-worked hole. Very limited work has been done to study the asymmetric cracks behaviour from hole edge, and the interaction effect between the principal and secondary cracks on the actual fatigue cracking process is still not well-understood. For cold-worked hole, there is also a need to develop a Green's/weight solution for asymmetric cracks, so that the residual stress effect can be included.

(5) The introduction of an EDM notch in the StressWave symmetric stress field is motivated by the controlled growth of through-thickness symmetric cracks. For naturally initiated cracks generally found in actual operating condition, it is more usual to observe corner or semi-elliptical crack shapes at the hole before these flaws transit to through-thickness crack configuration. The formation of these cracks embedded in residual stress field can give rise to different fatigue crack propagation behaviour in cold-worked holes. The present two-dimensional through-thickness crack model cannot fully accommodate the complexity of the three-dimensional residual stress field surrounding cold-worked holes. Hence, a three-dimensional Green's/weight function solution can be useful to study the variation of two-dimensional stress intensity factor along the crack front. When combined with three-dimensional residual stress field, the resulting data may shed new light on the fracture control programme in the future.

(6) Furthermore, the finite-width crack geometry considered and the Green's functions developed for single and double cracks actually corresponds to the elemental hole feature isolated from the global structures containing many holes and crack. The study carried out in this work so far is not fully representative of actual multiple-site damage scenario at cold-worked fastener holes in structures. There are complex issues between the interplay of cracks, local geometry and loading conditions which control the fatigue and fracture characteristic of structures. An inclusive modelling procedure of a full scale structure might be required for this purpose, e.g. an integrated approach of stress solution using a global finite element calculation coupled with present prediction methodology that allows the fatigue crack growth estimation.

(7) For simplicity, so far, the initial residual stress field used in fatigue calculation is assumed to remain undisturbed under cyclic loading and crack growth. Physically, such assumption might not be applicable to cases where drastic redistribution of residual stress takes place after extreme overloading. The propagation of a crack constantly alters the specimen geometry and equilibrium condition in pre-stressed material may also change the residual stress field. Taking account for this fact, some recent work on split-sleeve cold-worked hole has indicated that considering residual stress change on the specimen significantly improved the prediction accuracy. The observation of residual stress evolution has important implications on the variability in prediction task, which required detailed investigation in the future. This includes the fracture modelling of StressWave hole accompanied with residual stress mapping along the crack plane at different crack sizes.

(8) Further research is necessary to improve the prediction of StressWave holes under constant amplitude loading before the task advances to more a complicated flight spectrum environment. Generally, the parametric adjustment primarily governs the total life, but not the overall shape of the fatigue crack growth curves. This leads to the postulation that other

contributing factors should be reassessed in order to match the shape of the experiment curves. Significant progress may possibly be achieved by incorporating the three-dimensional neutron stress data into predictions. Also, as the crack life is spent mainly at the dc/dN ranged between 10^{-9} to 10^{-7} m/cycle more accurate baseline data/ NASGRO–3.0 parameters are needed. This may include the use of long/short crack data in future work, along with recommendations made earlier.